UNIVERSITY OF ZULULAND

Thiosemicarbazone, Xanthate and Dithiocarbamate Single Source Precursors for Cadmium, Lead and Indium Sulfide Nanoparticles

By:

Siphamandla Cecil Masikane

201000941

B.Sc. Pure and Applied Chemistry (UKZN); B.Sc. Hons, M.Sc. Chemistry (UZ)

THESIS

Submitted in fulfilment of the requirements for the degree

DOCTOR OF PHILOSOPHY

In the field of

CHEMISTRY

Faculty of Science and Agriculture

Supervisor: Prof. Neerish Revaprasadu

Department of Chemistry, University of Zululand,

Private bag X1001, KwaDlangezwa, 3886, South Africa

July 2018

DECLARATION

I hereby declare that the work described in this thesis entitled "**Thiosemicarbazone, xanthate and dithiocarbamate single source precursors for metal sulfide nanoparticles**" is my own work and has not been submitted in any form for another degree or qualification of the University of Zululand or any other University/Institution of tertiary education. Information derived from published or unpublished work of others has been acknowledged in the text and a list of references is given.

Name: Siphamandla Cecil Masikane

Signature: ……. Date: ……

CERTIFICATION BY SUPERVISOR

This is to certify that this work was carried out by Mr. Siphamandla Cecil Masikane in the Department of Chemistry, University of Zululand and is approved for submission in fulfilment of the requirements for the degree of Doctor of Philosophy in Chemistry.

……..

Supervisor

Neerish Revaprasadu (Ph.D)

Professor of Inorganic Chemistry

Department of Chemistry, University of Zululand,

KwaDlangezwa, South Africa

Acknowledgements

My utmost appreciation goes to Prof. Neerish Revaprasadu for continued support and mentorship throughout my Ph.D studies. I have been moulded into a good researcher equipped with exceptional skills, through his selflessness and supervision. I would also like to extend my appreciation to Dr Tebogo V. Segapelo (Master's degree supervisor) and Dr. Bongumusa S. Dladla and Dr. Sipho E. Mavundla for motivating me to enrol for Ph.D studies. The RS-DFID Solar Energy consortium is also acknowledged for their support. The DST-NRF and RS-DFID ACBI programme are acknowledged for their financial and related support.

The Department of Chemistry staff and colleagues have played a major role in assisting me with my studies. It would have been too challenging to accomplish the goals set from the beginning of my studies. My special appreciation goes to my colleagues from the Nanotechnology group: Dr S. Mlowe, Dr. M.D. Khan, Mr. C.G. Rufyiriza, Mrs. G.B. Shombe, Mr. S.H. Khoza, Ms. Z. Tshemese, Mr. Z.N.T. Mzimela, Mr. P.W. Zibane, Mr. L.N. Nene, Mr. Z.S. Ncanana and Mr. N. Malima.

Lastly, I would like to extend my heartfelt appreciation to my mom (Mrs J.M. Masikane), dad (Mr. T.J. Masikane) and my siblings (Dr. N.F. Masikane, Mr. M.A. Masikane and Mr. P.L. Masikane) who have provided unconditional love and support since the beginning of my postgraduate studies. A special gratitude goes to Ms. N. Hadebe who has always gone out of her way to be supportive in every aspect, during my Ph.D programme. I would humbly like to dedicate this thesis and years spend behind accomplishing this achievement, to all of you. No words would do justice to express my sincere love and respect I have for all of you. May the Lord bless you abundantly!

Abstract

The work outlined in this thesis entails recent advances in reaction protocols to afford high quality nanoparticles. It also incorporates practices of green chemistry to ascertain that the quality of nanoparticles does not take precedence over environmental impacts, pre and post-synthetic processes. Furthermore, the work has provided a step towards opening new horizons in the research field of nanoparticles and related nanomaterials, particularly on introducing other reaction parameters which have not been either explored or exploited prior to this work. All the aspects mentioned above have, and not limited to, been objectives of the individual studies presented in this work. Thus, they have been easily dealt with following a chapter approach, as outlined below.

In the first chapter, the emphasis is on the fundamental aspects of nanomaterials and nanoscience. The scope of this literature review chapter is narrowed to synthetic protocols which provide access to the manipulation of the properties of the nanomaterials to suit a specific application. The synthetic protocols focus on the use of metal-organic compounds as molecular sources; a similar approach which has been applied in the studies reported in this thesis. Examples on common applications that exploit the properties of the nanomaterials are also outlined briefly.

In the second chapter, eight CdX_2 ($X = Cl^-, I^-$) thiosemicarbazone complexes were prepared and subsequently evaluated as single source molecular precursors towards the fabrication of oleylamine-capped CdS nanoparticles through a solvent thermolysis route. Various reaction parameters were explored with respect to the properties of the nanoparticles obtained. A combination of reaction temperature and the nature of ligands on the Cd(II) centre showed a significant influence on the particle size, morphology and optical absorption properties of the nanoparticles. Different analytical tools were used to establish the properties of the nanoparticles, among them are powder X-ray diffraction, the transmission electron microscopy and UV-Vis spectroscopy. The chapter recognized the crucial importance of facilitating ligand addition reaction as opposed to the common practice of substitution reaction in the preparation of single source molecular precursors. This retains the halide ligands present in the parent metal halide salt used. These halide ligands were found to have

a relatively major influence on the particle size, morphology and absorption optical properties compared to the thiosemicarbazone ligands.

The third chapter reports the work which is a sequel to the second chapter, albeit investigating the broader halide series (i.e. Cl^-, I^- and Br^-) and a non-halogenated counterpart on the material mostly reported to prefer a cubic-like morphology, PbS. Thus, the study focused mainly on the morphology control. For this purpose, one thiosemicarbazone ligand was chosen due to the consistency in trends observed in the previous chapter, while the halide ligands were varied. Four Pb(II) cinnamaldehyde thiosemicarbazone complexes were prepared and used for this study. Morphology control was significantly minor; however, particle shape could easily improve (to perfect cube) or deteriorate (to irregular cube) based on the combination of halide ligands and reaction temperature. Regardless of shape transformation, the particle sizes showed an increase with reaction temperature.

The main aim of the fourth chapter was to devise eco-friendly synthetic protocols to afford non-toxic semiconducting nanoparticles, an alternative to those reported in the previous two chapters. Although the class of thiosemicarbazone compounds used in the previous chapters are famously known for their excellent biological applications, complexation to toxic metal centres and oleylamine-mediation fabrication protocols to obtain CdS and PbS nanoparticles compromised the eco-friendly practice. Thus, in this chapter, non-toxic β-In_2S_3 and $CuInS_2$ nanoparticles were prepared in two eco-friendly alternatives to oleylamine, which are castor oil and olive oil. Different classes of ligands (xanthates and dithiocarbamates) were investigated on their influence in the properties of the nanoparticles, in addition to the choice of capping agent and reaction temperature. Two In(III) and two Cu(II) complexes were used in this work. Very few reports on the use of these castor oil and olive oil capping agents are available, and none of them focus on the fabrication of non-toxic nanoparticles, marking this work a first of its kind.

The fifth chapter reports an additional eco-friendly approach to prepare indium sulfide, a continuation of the work reported in the fourth chapter. In this work, however, the use of capping agents is disregarded. Thus, low decomposition temperatures observed for the In(III) xanthate complexes used were found suitable for the proposed

solventless fabrication route. The route entails the formation of indium sulfide through the thermal decomposition of complexes by solventless thermolysis and melt reaction mechanisms. This practical, inexpensive and a scalable greener route was able to afford various crystallographic phases which were identified through their good quality powder X-ray diffraction patterns. Phase transformation was largely influenced by both decomposition reaction temperature and the nature of the alkyl backbone of the xanthate ligands. Five In(III) xanthate complexes were used in this work, inclusive of one complex used in the fourth chapter. The study provided easy access to investigate the material obtained through mild conditions compared to the earlier traditional practice which used the multielement (indium metal + elemental sulfur) approach at excessive heat (>1000°C) resulting to explosions.

The final, sixth chapter, concludes on the progress outlined in the above-mentioned studies towards the eco-friendly reaction protocols for nanoparticles synthesis. The preparation of CdS and PbS nanoparticles using common reaction parameters was necessary to demonstrate the efficacy of alternative eco-friendly protocols to produce non-toxic β-In_2S_3 and $CuInS_2$ nanoparticles exhibiting similar properties to the former materials. Advantages of using metal-organic as molecular precursors are outlined, based on the experimental results obtained from the studies.

Table of Contents

CHAPTER 1

Table of Figure

List of Tables

List of Scheme

List of abbreviations and symbols

DTA	Differential thermogravimetric analysis
DTC	Dithiocarbamate
EDX	Energy dispersive X-ray
FTIR	Fourier transform infrared
HRTEM	High resolution transmission electron microscopy
IR	Infrared
NMR	Nuclear magnetic resonance
p-XRD	Powder X-ray diffraction
SAED	Selective area electron diffraction
SEM	Scanning Electron Microscopy
SSP	Single source precursor
TEM	Transmission electron microscopy
TGA	Thermogravimetric analysis
TOP	Tri-octylphosphine oxide
XAN	Xanthate
XRD	X-ray diffraction
°C	Degree Celsius
Å	Angstrom
eV	Electron volts
mA	milliamps
nm	Nanometre
θ	Theta
λ	Lambda (wavelength)

CHAPTER 1

1 Introduction and literature review

Recent advances across various science disciplines have largely been dominated by the incorporation and/or applications of functional nanomaterials and nanodevices. This exciting venture follows a few decades-long attention and devotion to harnessing interesting properties from materials engineered at the nanoscale level. Access to these properties has been made possible through a wide range of fabrication protocols whose reaction parameters can be easily manipulated to desired conditions. Significant breakthroughs in this field has broken new grounds towards the development of cutting-edge technology currently available in the commercial marketplace, making the storage of research findings on the shelves as the scientific stigma of the past.

A review by Vance *et al.*[1] brings to attention a number of worldwide inventory databases of nanomaterials-incorporated products in commercial marketplaces. Among these databases is a website[2] which is famous for its extensive entries. Examples of the products which can easily be retrieved by using a user-friendly search function on the website, include: carbon nanotube-incorporated footwear by Adidas and Continental tires, titanium oxide (TiO_2)-incorporated Colgate toothpaste and Dove's antiperspirant deodorants, silicon dioxide-incorporated Samsung flash memory, as well as silver-incorporated washing machines and air conditioning units manufactured by Samsung. These materials are believed to exhibit particle sizes of between 1 nm to 100 nm, an acceptable range for them to be classified as nanomaterials.[3] The examples provided display widespread applications, thus, a motivation for continued search for highly efficient nanomaterials.

Nanomaterials, for a simplistic approach, are usually classified into two groups: nanoparticles and thin films. A compound can be prepared in either a nanoparticle or thin film form, depending on desired applications. For example, TiO_2 nanoparticles can be suspended in mobilised media such as in cosmetics,[4] while the thin film counterpart finds use in solar cell applications.[5] In general, nanoparticles are preferred since most routes to thin films are expensive, sophisticated and sensitive. Furthermore, thin films are limited by few substrates due to compatibility issues and of

course the length of the substrate is limited by the fabrication method.[7] Routes to nanoparticles are however attractive in that they involve relatively more reaction parameters which can be manipulated, as they are mostly wet chemistry techniques. Nanoparticles can be deposited on substrates through different approaches such as drop casting[7] and spin coating techniques,[8] as cheaper and easier means of fabricating thin films.

Regardless of the nanomaterial form or fabrication routes, the synthetic protocols can either use multiple or single source precursors. Triumphs on the use of multiple source precursors can be traced back to the pioneering works of Bawendi and co-workers.[9] However, the use of single source precursors later became popular, in an effort to alleviate disadvantages associated with the multiple precursor route. These disadvantages include tedious reaction steps, challenges in controlling the phase, as well as undesirable contamination. Single source precursors are, essentially, metal-organic compounds with preformed bonds between atoms of preference. The synthesis and use of single source precursors for nanomaterials have been documented thoroughly in book chapters and review articles.[10]

Contributions to the body of knowledge attained from this thesis include new and improved approaches to the fabrication of semiconductor nanoparticles, in both single source precursor and fabrication route context. The latter remained fundamentally important throughout the study, towards the direction of non-toxic nanoparticles obtained from eco-friendly synthetic processes. Various fabrication routes known in literature were considered for this study, preference was subject to reputation associated with high quality nanoparticles.

1.1 Fabrication routes to semiconductor nanoparticles

The scope of the study outlined in this thesis was restricted to metal chalcogenide semiconductor nanoparticles, due to their interesting properties which find use in various applications. The optoelectronic properties are mostly desired, linked to addressing real world problems such as renewable energy (solar energy harvesting)[11] and photocatalytic degradation[12] of organic pollutants in industrial effluents, among others. The choice of fabrication route has a significant influence in

tailoring and fine tuning the properties of the nanoparticles. A desirable route offers many reaction parameters which can be altered, thereby influencing the particle size, shape, morphology and crystallographic phase responsible for the properties obtained.

1.1.1 Precipitation route

The metal and chalcogenide ions in separate solutions instantaneously react upon mixing and thereby forming metal chalcogenide nanoparticles that precipitate due to solvent incompatibility with respect to solubility. The route uses cheaper and simple precursors which dissociate easily in solvents to release ions, e.g. cadmium chloride and sodium sulfide to afford cadmium sulfide nanoparticles.[13] However, the reaction kinetics are too rapid, undesirable for particle size, shape and morphology control. In addition, poor crystallinity is a major deficiency of this route, since heat is ordinarily not applied during the reaction. Heat has become a vital parameter in a majority of fabrication routes to improve the crystallinity of the nanomaterials. Originally, the route does not incorporate capping agents, thus, undesirable polydispersity and agglomeration would result as a consequence, adversely affecting optoelectronic properties of the nanoparticles. It has proven challenging to improve this route without completely modifying the entire reaction protocols. One significant improvement has been the control of particle sizes and narrow particle size distribution, by using cavity-type templates such as zeolites[14] in which restrictive particle growth occurs during the reaction.

1.1.2 Hydrothermal and solvothermal routes

The hydrothermal[15] and solvothermal[16] fabrication routes to nanoparticles are a result of substantial modifications of the precipitation route with an aim of addressing its limitations. Rapid reaction kinetics are alleviated by using other precursors which do not readily dissociate under normal precipitation route reaction protocols. Briefly, the hydrothermal and solvothermal routes involve a sealed reaction conducted at temperatures slightly above the boiling point of the solvent, as means of creating high pressure in the reaction vessel necessary to force solubility and reactivity of the precursors, where applicable. Thus, access to controlling the reaction kinetics is easily

achieved by a choice of solvent and precursors which undergo decomposition and/or dissociation triggered by additional reaction parameters such as heat, pressure and pH, among others. Control over reaction kinetics and the optional incorporation of capping agents enable finetuning of the properties of nanoparticles through particle size, shape and morphology manipulations. It is noteworthy that, as previously mentioned, the heat facilitates the crystallinity of the nanoparticles.

The difference between the hydrothermal and solvothermal routes are obvious: the nature of the solvent used for the reaction. The hydrothermal reactions are conducted in aqueous media, while organic solvents are used in solvothermal reactions.[17] Furthermore, the former is traditionally employed for colloidal metals and metal oxide nanoparticles, while the latter specialises on metal chalcogenide (sulfide, selenide and telluride), phosphide and arsenide nanoparticles synthesis.

1.1.3 Thermal decomposition route

Although the hydrothermal and solvothermal routes afford good quality nanoparticles as compared to the precipitation route, their synthetic protocols however involve long reaction times which span for a couple of hours to a few days. This is primarily due to fewer precursors compatible with these routes, in pursuit of reaction kinetics control. Ideal reaction kinetics is defined by a proper separation between nucleation and growth processes.

The thermal decomposition[18] route (also known as thermolysis) takes precedence over, and not limited to, the fabrication routes mentioned above. The route achieves the separation between the nucleation and growth processes efficiently, as well as crystalline and monodispersed nanoparticles, under reduced reaction time constraints. The reaction time is reduced by using mostly organic-incorporated precursors which easily dissociate with temperature and/or capping agent via various mechanisms. The common practices involve either the heat-up treatment of the contents (precursors and solvents) in a reaction vessel or injection of the precursors in preheated solvents at desired temperatures.[19] The latter, commonly known as the hot injection method, is mostly preferred due to its design which promotes a short-burst nucleation as a result of an instantaneous decomposition upon injection in a hot

solvent. This enables the subsequent growth processes to favour monodispersity which is interlinked to particle size-dependant features such as optical properties,[20] magnetism[21] and catalytic efficacy[22].

The hot injection and heat-up methods vary significantly, they however have close similarities pertaining to the mechanisms behind the formation of nanoparticles.[19b] More on this is elaborated in the subsections 1.1.3.1 and 1.1.3.2.

1.1.3.1 Hot injection method

The diversity of the suitable precursors is among many attributes for the hot injection synthesis of nanoparticles. Generally, the chalcogenide source-type precursors receive the most attention, while metal sources remain as common laboratory salts (i.e. metal halides, nitrates, acetates, etc). For example, in the case of metal sulfide nanoparticles, three prominent sulfur source approaches are commonly utilised: 1) commercial compounds such as thioacetamide,[23] 2) laboratory-made compounds such as tri-*n*-octylphosphine sulfide (TOPS),[24] and 3) thiolated solvents such as dodecanethiol[25] used primarily as a capping agent which releases sulfide ions through decomposition at higher temperatures.

The general procedure of the hot injection method utilising a configuration similar to Figure 1.1, involves two steps which include: 1) a preparation of a solution or suspension of precursor/s, 2) subsequent injection of solution/suspension in a preheated solvent of choice. In the first step, a precursor may be formed *in-situ*, e.g. TOPS solution formed by reacting elemental sulfur with tri-*n*-octylphosphine which acts as both reactant and dispersion medium. In some instances, the suspension would be warmed to moderate temperatures with the aim of inducing solubility and/or low viscosity. Excessive heating should however be avoided as the precursors may decompose prematurely before the injection step. Low viscosity is desirable in achieving fast injection rates.

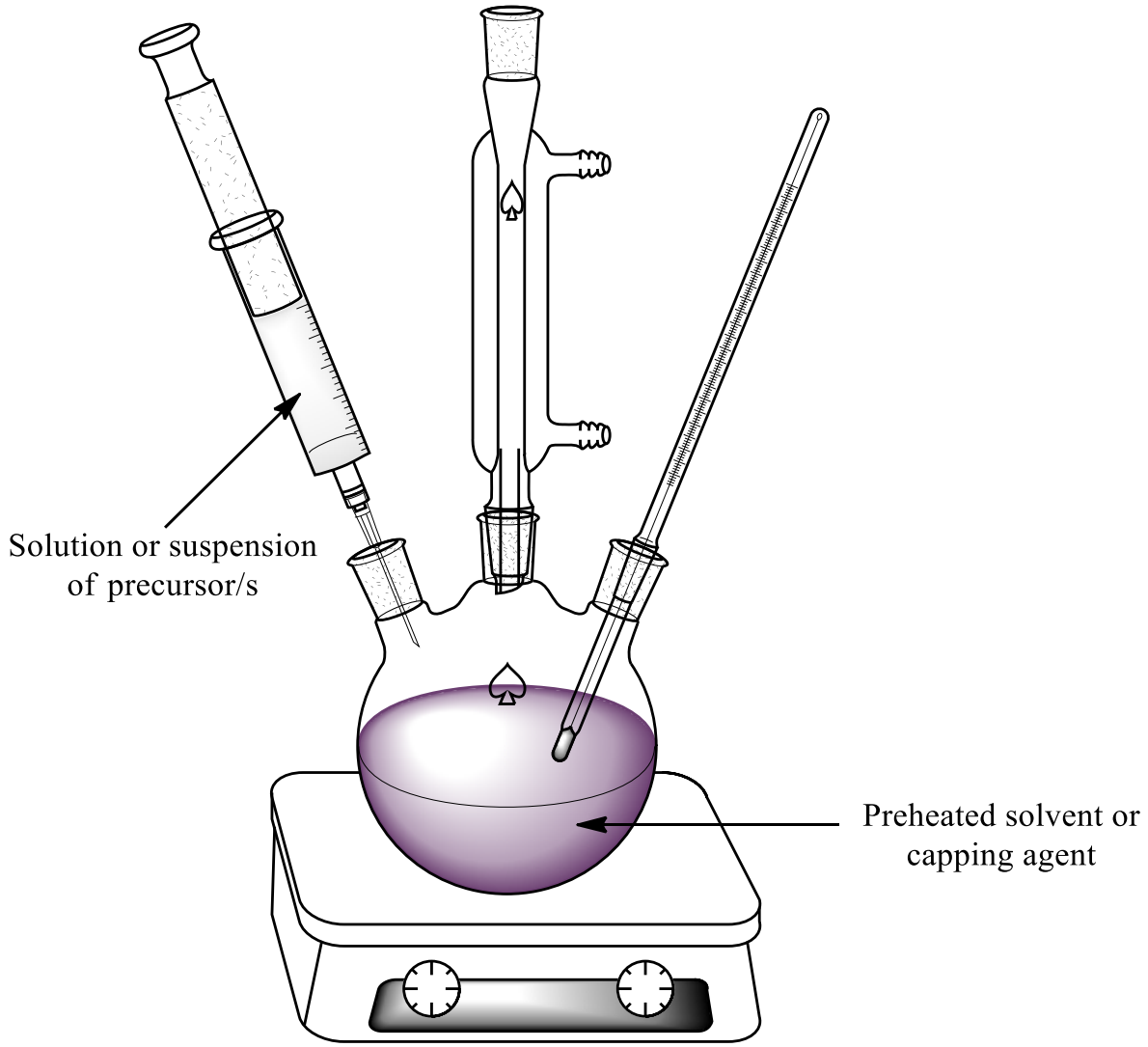

Figure 1.1: Graphic representation of a typical hot injection reaction setup.

The philosophy behind fast injection rate is achieving the immediate decomposition of the precursor molecules to yield a high concentration of nuclei which together grow to monodispersed nanoparticles, Figure 1.2a. However, this is experimentally challenging and usually proceeds via random nucleation leading to uncontrolled growth of nanoparticles which exhibit broad size distribution, Figure 1.2b. The broad size distribution can be solved by prolonging the reaction time (Figure 1.2c and d), thus allowing particles to grow further through size focusing[26] and Ostwald ripening[27] processes.

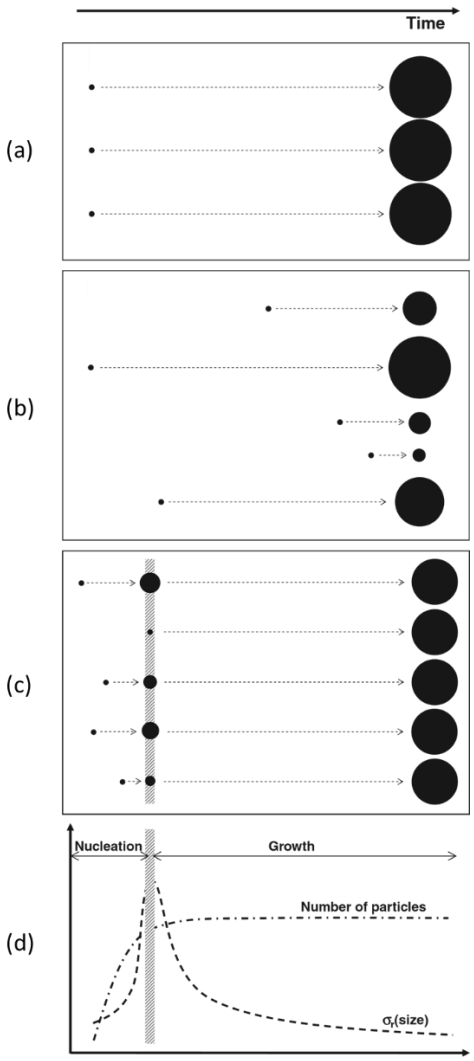

Figure 1.2: Nanoparticle formation through a) ideal theoretical growth, b) common experimental growth, c) prolonged experimental growth and d) plots depicting prolonged experimental growth.[19b]

1.1.3.2 Heat-up method

The difference between the hot injection and heat-up methods is how the precursor is introduced to the solvent or capping agent media. Unlike the hot injection method, the heat up method involves the direct addition of the precursor to the solvent or capping agent, removing the need of a supplementary dispersing agent (Figure 1.3). This is normally conducted at room temperature. The resulting solution or suspension is gradually heated to and held at a desired temperature for a certain period of time.

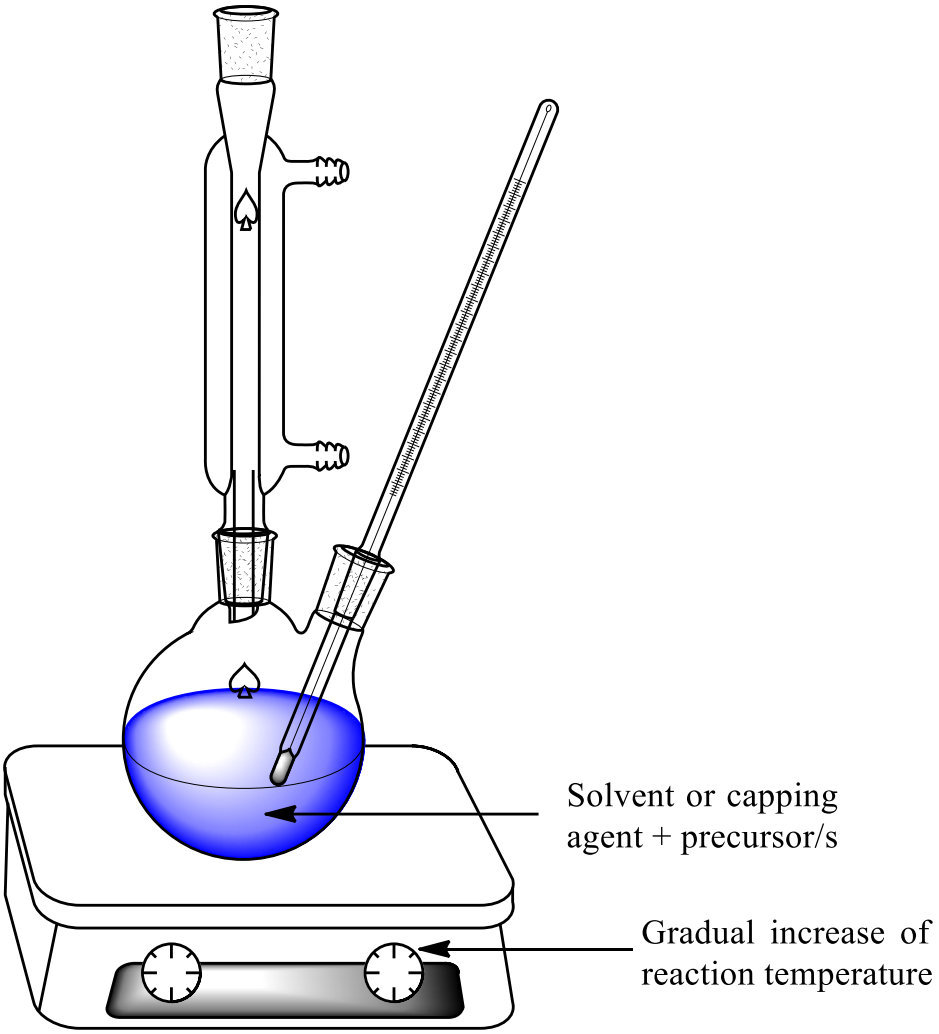

Figure 1.3: Graphic representation of a typical heat-up reaction setup.

Regardless of the differences between the hot injection and heat-up methods, they share similar particle growth processes, i.e. nucleation and growth stages, Figure 1.4. The heat-up method has an additional stage, accumulation, where the precursor/s gradually decompose to yield monomers, Figure 1.4b. In this accumulation stage, the concentration of the monomers increases to a saturation point which approaches the activation energy barrier for the subsequent stage, nucleation. The particle size distribution improves with reaction time similar to the hot injection method, i.e. through size focusing and Ostwald ripening processes. The heat-up method can be graphically summarised through the LaMer[28] diagram which, originally, was used to propose the concept of burst nucleation, Figure 1.5.

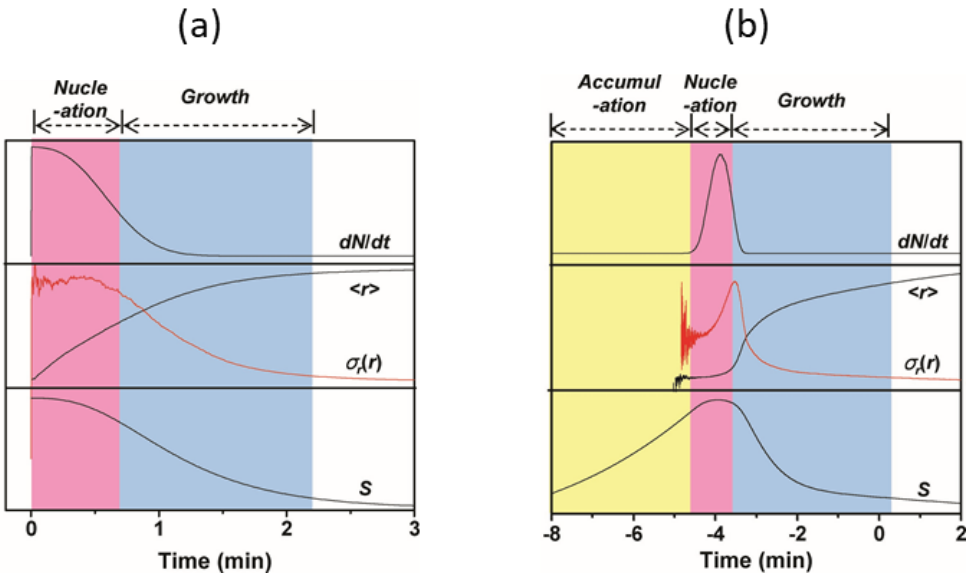

Figure 1.4: The simulated formation of nanoparticles from (a) hot injection and (b) heat-up processes, as a function of dN/dt, <r>, σ_r(r), and s which denote nucleation rate, mean radius of particles, relative standard deviation of the particles' radii and supersaturation level, respectively.[19b]

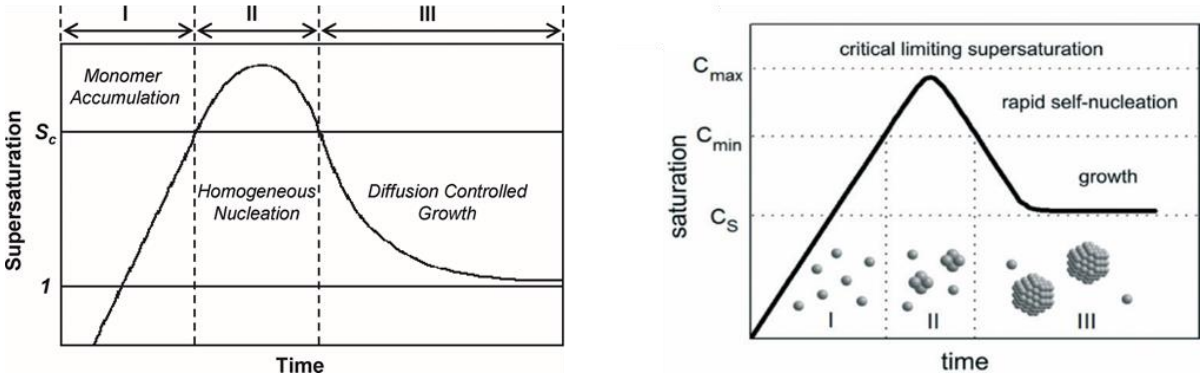

Figure 1.5: A typical LaMer diagram depicting nanoparticle growth.[28]

Both hot injection and heat-up methods are complimentary with respect to the nature of the precursor and solvents used. However, the heat-up reactions proceed for a relatively longer time. It is for this apparent reason that the hot injection method is usually preferred, although both methods are capable of producing high quality monodispersed nanoparticles.

1.1.3.3 Solvents in the synthesis of nanoparticles

The diversity in the precursors generally used in the thermal decomposition routes discussed above is however confronted by the alteration of numerous reaction parameters, to accommodate the chemical differences. This applies mostly to the multiple source precursor approach, where the precursors decompose/dissociate in different mechanisms and rates. Therefore, the choice of solvent (coordinative or non-coordinative) through its functional groups and boiling point range then becomes of paramount importance.[29] A mixed solvent system is usually employed when the reaction is threatened by the chemical differences of the precursors, where an individual solvent is targeted to control the decomposition dynamics of a specific precursor.

The choice of the solvent, coordinative or non-coordinative, depends on the sought-after properties of the nanoparticles. The coordinative solvents are mostly preferred due to the role they play during and post-synthesis of nanoparticles. The coordinative solvents' primary objective is to control the growth (incl. shape and morphology) and stability of the nanoparticles during the fabrication stage. Shape and morphology control occurs as a result of a solvent binding to and subsequently restricting growth in a specific plane of a nanoparticle. It is for this reason that these solvents are generally referred to as capping agents/ligands. The capping agents also prevent agglomeration of the nanoparticles, thus retaining attractive features such as optical properties. The other requirement of a capping agent, in addition to functional group, is the bulkiness.

Capping agents are easily classified by their functional groups, the most common being outlined in a review by Green[30], Figure 1.6. The "R" backbones in Figure 1.6 are usually long alkyl chain, ideal for achieving efficient passivation of nanoparticles. In the early years of the hot injection technique, the octyl derivative of phosphine oxide **1**, tri-*n*-octylphosphine oxide, was the preferred capping agent due to its high boiling point and presumed compatibility with tri-*n*-octylphosphine chalcogenides due to similarities in their chemical structures. However, it has undesirable limitations such as strong emission in the visible region during photoluminescence studies on semiconductor nanoparticles, when heated above 260

°C.[31] As a result of this, long alkyl chain amines such as hexadecylamine, dodecylamine and oleylamine became the preferred capping agents over tri-*n*-octylphosphine oxide.

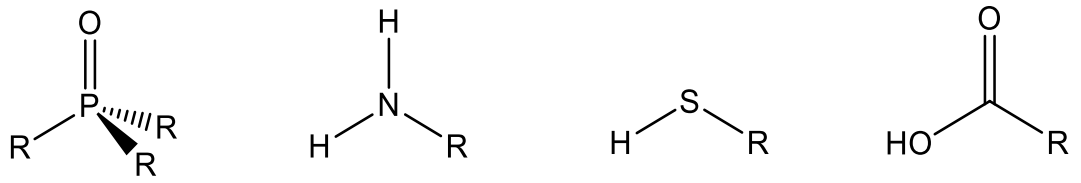

1 **2** **3** **4**

Figure 1.6: Phosphine oxide **1**, amine **2**, thiol **3** and carboxylic acid **4** functional groups common among capping agents.

Long alkyl chain amines have similar chemical attributes to tri-*n*-octylphosphine oxide and tri-*n*-octylphosphine combined, i.e. high boiling point and can form chalcogenide derivatives, respectively. In the latter, Joo *et al*.,[32] demonstrated the synthesis of CdS and CdSe nanomaterials using the sulfide and selenide amine-type precursors prepared from the proposed reaction Scheme 1.1. This was inspired by the earlier works of Davis and Nakshbendi[33] which depict the sulfur + amine reactions, as well as selenium + amine reactions by Sonoda *et al*.[34] Generally, long alkyl chain amine-capped nanoparticles are found to have improved emission quantum yields compared to tri-*n*-octylphosphine oxide-capped nanoparticles, due to large surface coverage and electron contribution from the amine functional group, among other factors.[35]

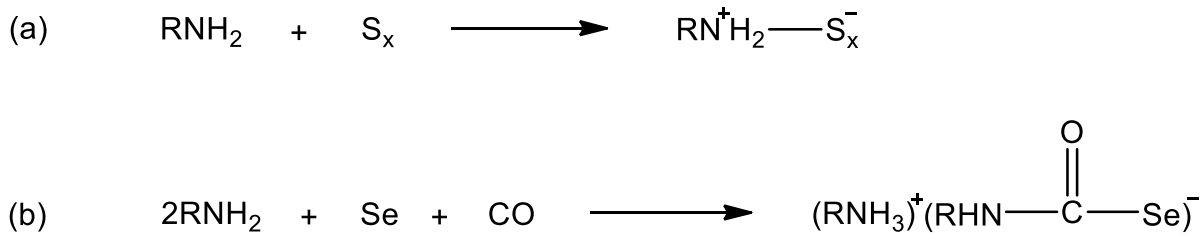

Scheme 1.1: Amine-derived (a) sulfur and (b) selenium precursors.

The use of thiols as capping agents have made a major contribution in the synthesis and functionalisation of light-emitting nanoparticles for use in various

applications, although primarily in the biological sector.[36, 37] Highly luminescent CdSe/ZnS core/shell nanoparticles have always attracted a lot of attention as better fluorophores for biological imaging. [37] However, good quality and tuneable properties could be accessed through the hot injection method which uses tri-*n*-octylphosphine oxide as a capping agent. Unfortunately, tri-*n*-octylphosphine oxide-capped nanoparticles have inherent solubility difficulties in aqueous media. Breakthrough in achieving solubility in aqueous media involved the substitution of the tri-*n*-octylphosphine oxide ligands with thiol ligands.[38] Futhermore, Rogach *et al*.,[39] reported that the room-temperature photoluminescence quantum efficiency of the aqueous synthesized CdTe nanoparticles drastically increased when capped with thiols. It is however reported in the review article by Parak *et al*.[40] that thiol-capped CdSe/ZnS nanoparticles have a short shelf life as a result of dynamic bonding (binding and unbinding in equilibrium) existing between thiol ligand and ZnS shell. It has been demonstrated that the stability can be significantly improved by rather using multidentate thiol ligands,[41] e.g. the proposed explanation on the observed stability in the dithiothreitol-capped CdSe/ZnS is attributed to the S-S distance (~3.6 Å) in the bidentate ligand being theoretically close to the Zn-Zn distance (3.82 Å) in the ZnS shell.[42] Surprisingly, the experimental evidence obtained by Aldana *et al*.[43] suggests the opposite, although photostability of the nanoparticles improved with an increase in the alkyl chain length of the ligands instead. Recent literature reports have identified thiols as shape-directing agents. [44-46] The shape-directing abilities are attributed to a combination of factors including the lowering the energy barrier for nucleation and growth processes, the thiol functional group binding to specific facets on the nanoparticles' surface, as well as the chemical structure which has an influence in the thermal stability of the thiol ligand.

1.1.3.3.1 Carboxylic acids and 'green' capping agents

Long alkyl chain carboxylic acids are probably the first capping agents reported in literature, the earliest example being oleic acid used to stabilize magnetite (Fe_3O_4) colloids.[47] There are several features that make oleic acid the most preferred over other carboxylic acid capping agents, these include: 1) ability to coordinate in a bidentate manner through both oxygen atoms,[48] and 2) coordination can also occur

through the double bond.[49, 50] The importance of the double bond in oleic acid has been reported in literature; Tadmor *et al.*[51] confirmed that oleic acid (Figure 1.7a) displays efficient capping over stearic acid (Figure 1.7b) due to the existence and absence of the double bond, respectively. The three features, namely, 1) carboxylate functional group, 2) double bond and 3) long alky groups enables oleic acid-capped nanoparticles to be soluble and/or transferable between polar and non-polar without usage of a phase transfer reagent.[52] Furthermore, Bala *et al.*[53] commented that a *trans* isomer of oleic acid (Figure 1.7c) has poor capping capabilities.

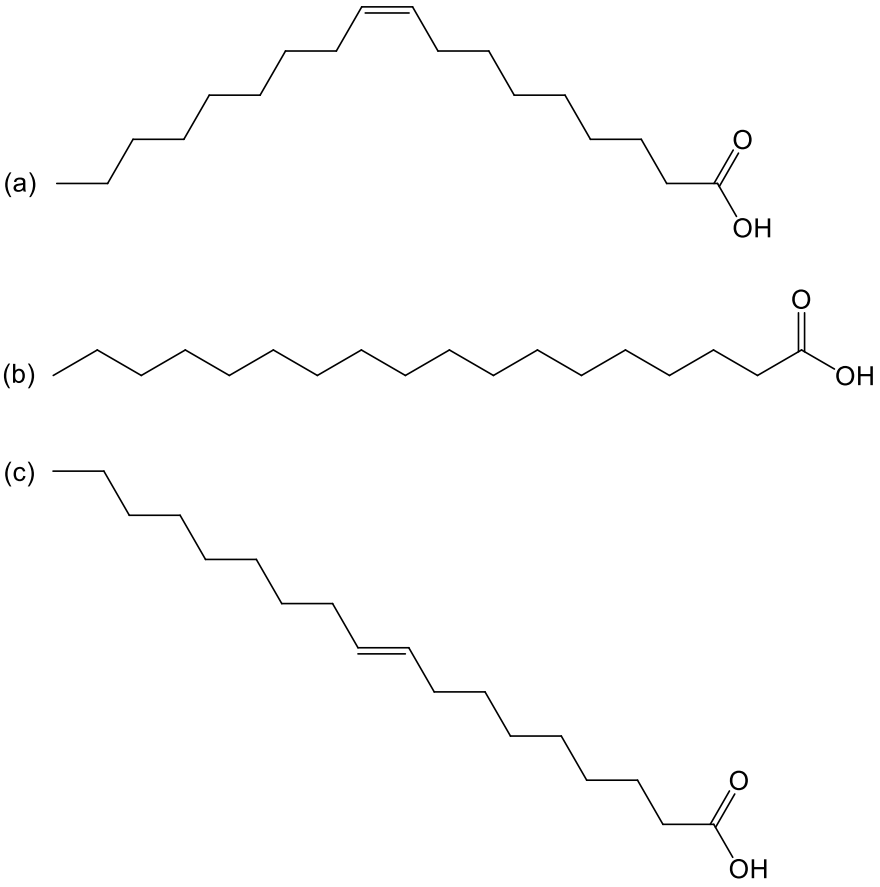

Figure 1.7: The chemical structures of (a) oleic acid in its *cis* (oleyl) form, (b) stearic acid and (c) oleic acid in its *trans* (elaidyl) form.

The 'green' capping agents, specifically in the context of natural occurrence/origin, have received considerable interest in the synthesis and stabilization of nanoparticles. They are predominantly fatty acids, sharing structural similarities with oleic acid (i.e. composed of mainly carboxylic acid functional group and long alkyl chain). Common examples include palmitic acid,[54] linoleic acid,[55]

ricinoleic acid,[56] and anacardic acids,[57] among others. Their chemical structures are provided in Figure 1.8. They have been used as both pure extracts and as mixtures in naturally occurring oils such as olive oil,[58] castor oil[59] and cashew nut shell liquid,[60] among others. Compositions in these oils are provided in Table 1.1. It should however be noted that factors such as geographical areas, climate and soil quality have an impact in the chemical compositions (qualitative and quantitative) of an individual plant.

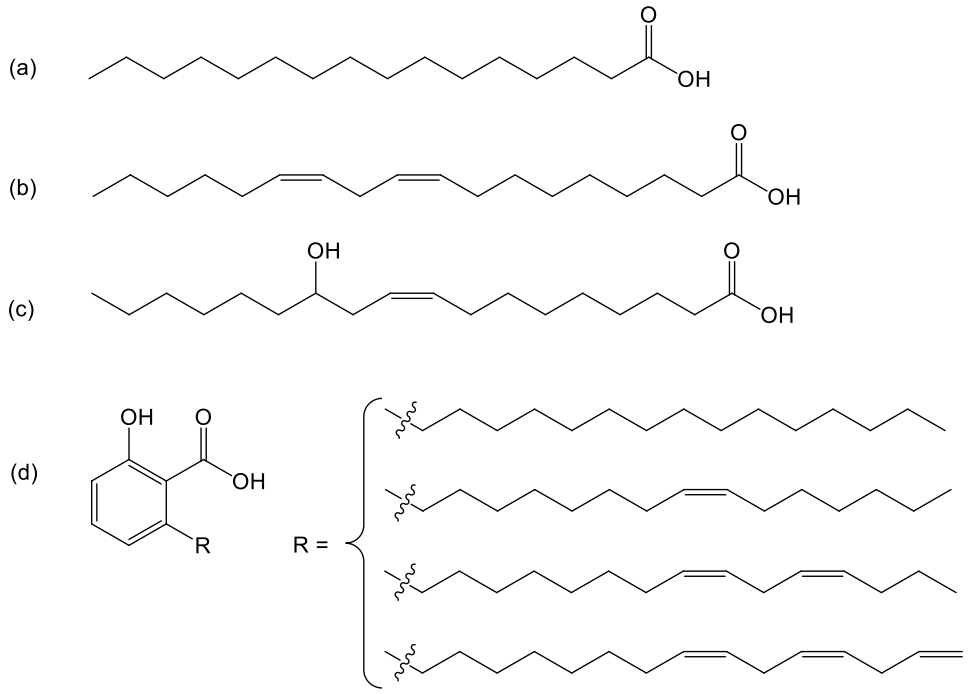

Figure 1.8: Chemical structures of (a) palmitic acid, (b) linoleic acid, (c) ricinoleic acid and (d) anacardic acid.

Table 1.1: Three major components of olive oil, castor oil and cashew nut shell liquid (CNSL).

	Olive oil[61]	**Castor oil**[62]	**CNSL**[63]
Compound (%)	Oleic acid (55-83)	Ricinoleic acid (92)	Anacardic acid (72)
	Linoleic acid (3-21)	Linoleic acid (5)	Cardol (22)
	Palmitic (7-20)	Oleic acid (2)	Cardanol (5)

Other interests on green synthetic methods focus on the incorporation of biological processes which include the use of bacteria, yeasts, fungi and algae, among

others. These are outlined in detailed review articles by Iravani[64] and Kharissova *et al.*[65] Other methods would be of unique or peculiar nature, such as the synthesis of honey-stabilized silver nanoparticles reported by Philip.[66]

1.2 Single source molecular precursors for metal sulfide nanomaterials

The incorporation of single source molecular precursors (SSPs) in various synthetic methods has been of great convenience to synthetic scientists and engineers, providing easy access to nanoparticles and their properties. Some of the SSPs are already commercially available such as Zn(II) diethyldithiocarbamate for ZnS nanoparticles,[67] while the majority are easily prepared from classical methods of chemical synthesis. Ideal SSPs are those that can be prepared in few reaction steps using readily available starting materials, preferably inexpensive as well. Low toxicity and stability that extends to longer shelf life are advantageous qualities. Other features such as low temperature decomposition and volatility are dependant on the desired fabrication route for nanoparticles.

The SSPs, similarly to capping agents, are grouped according to their functional groups. Different functional groups, as well as derivatisation of the backbone of the structure, have a significant influence on the chemical behaviour of the SSP thus imparting different decomposition/dissociation rate and mechanisms. Generally, dichalcogenato complexes are mostly used as SSPs for the fabrication of metal chalcogenide nanomaterials. For metal sulfide nanomaterials, they include:

- Dithiophosphinato complexes of the general formula $[M(S_2PR_2)_n]$ in Figure 1.9 normally obtained by a reaction of a metal salt with a dithiophosphinate ligand **DTP**.[68] The ligand is synthesized as shown in Scheme 1.2. The complex $[Zn(S_2P^iBu_2)_2]$ is an example of the SSP which has been used to synthesize ZnS[69] nanomaterials. Analogous to dithiophosphinato complexes are dithiophosphato complexes, $[M\{S_2P(OR)_2\}_n]$, obtained from dithiophosphato ligands synthesized from the reaction of alcohols with phosphorus pentasulfide.[70] The complex $[Cd\{S_2P(OEt)_2\}_2]$ is an example of the dithiophosphato class which has been used as a SSP to fabricate CdS nanoparticles.[71]

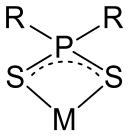

Figure 1.9: Structural example of dichalcogenophosphinato complexes.

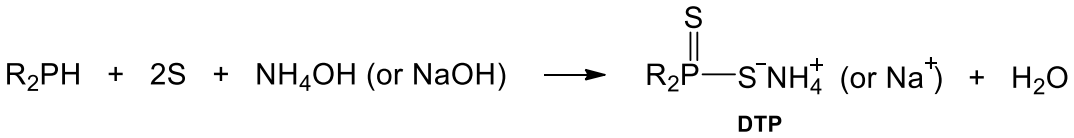

Scheme 1.2: Preparation of thiophosphinate ligand **DTP**.[68]

- Dithioimidodiphosphinato complexes, $[M\{(SPR_2)_2N\}_n]$, shown in Figure 1.10, are synthesized from the dithioimidodiphosphinato ligand **DIP** prepared following the reaction Scheme 1.3.[72] Complexation with metal requires deprotonation with strong bases such as sodium alkoxides. The dithioimidodiphosphinato complexes are however mostly used as SSPs for thin films; PbS[73] and β-In_2S_3[74] thin films have been fabricated from $[Pb\{(SP^iPr_2)_2N\}_2]$ and $[In\{(SP^iPr_2)_2N\}_2Cl]$, respectively.

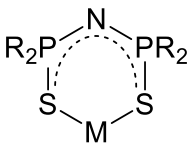

Figure 1.10: Structural example of dithioimidodiphosphinato complexes.

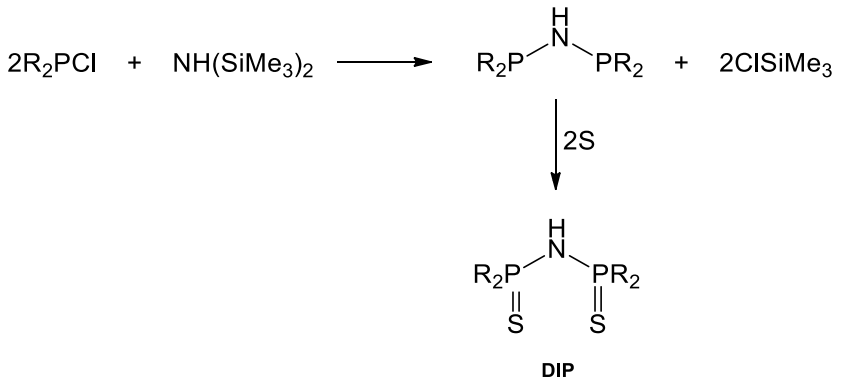

Scheme 1.3: Preparation of dithioimidodiphosphinato ligand **DIP**.[72]

- Dithiobiuret complexes, [M{(SCNR$_2$)$_2$N}$_n$], shown in Figure 1.11, display similar coordination mode to the dichalcogenophosphinato complexes. The complexes are formed through complexation with the dithiobiuret ligand **DTB** synthesized according to Scheme 1.4.[75] Metal acetates are usually used, thereby deprotonating the ligand to give off acetic acid as a by-product. The use of triethylamine base would then be advised in instances where the reaction is slow or does not occur. An exemplary complex [Co{(SCNMe$_2$)$_2$N}$_3$] has been used as a SSP to prepare Co$_{1-x}$S nanoparticles.[76]

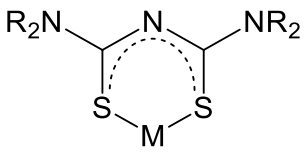

Figure 1.11: Structural example of dithiobiuret complexes.

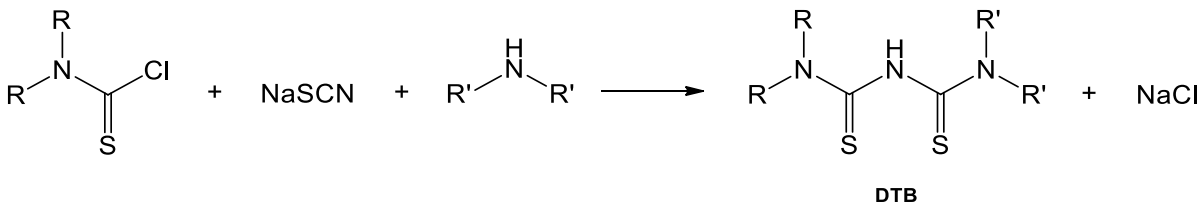

Scheme 1.4: Preparation of dithiobiuret ligand **DTB**.[75]

- Dithiocarbamato complexes, [M(S_2CNR_2)$_n$], shown in Figure 1.12, are mostly prepared for the reaction of a metal salt with an anionic dithiocarbamato ligand **DTC** usually stabilized by a cationic sodium. The ligand is commonly prepared following the reaction Scheme 1.5.[77] This group of complexes have been of great interest over the years, particularly due to the diversity through the symmetric and asymmetric amines, which can either be of alkyl, aryl or heterocyclic nature. Furthermore, they are usually more stable at ambient conditions. Iron sulfide nanoparticles, for example, have been synthesized from [Fe(S_2CNMe_2)$_2$] and [Fe($S_2CNC_3H_3N$)$_2$] complexes synthesized from alkyl and heterocyclic amines, respectively.[78] Dithiocarbamate complexes from primary amines are also known in literature, although it is mentioned elsewhere that they rarely receive a lot of attention due to the stigma of poor stability and low volatility,[10a] rendering it challenging to use in thin film fabrication methods such as the chemical vapour deposition. Paca and Ajibade,[78] among few research groups, were able to prepare complexes such as [Fe($S_2CNHC_6H_5$)$_2$] from a primary amine, and subsequently used as SSP for the fabrication of iron sulfide nanoparticles.

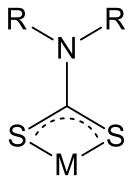

Figure 1.12: Structural example of dithiocarbamato complexes.

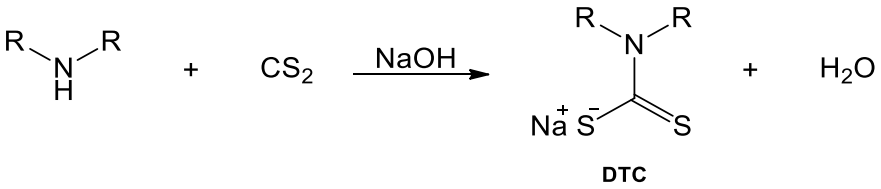

Scheme 1.5: Preparation of dithiocarbamato ligand **DTC**.[77]

- Xanthato complexes, [M(S_2COR)$_n$], shown in Figure 1.13, share both structural and synthetic protocols with dithiocarbamato complexes. The ligands are synthesized in a similar manner to Scheme 1.5, albeit using alcohols in place

of amines and KOH as a preferred base.[79] Xathate complexes have a lot of interesting features which make them more desirable over other classes of SSPs. They undergo a clean decomposition, via a Chugaev elimination pathway (*viz*. decomposition of alkylxanthato Pb(II) complex[80] in Scheme 1.6), where the by-products are highly volatile by-products (alkene, carbonyl sulfide and hydrogen sulfide). This reduces or eliminates sources of contamination to the final product. Tshemese *et al.*[81] have conducted a comparative study on the synthesis of PbS nanoparticles from $[Pb(S_2OEt)_2]$ SSP route and multiple precursor $\{Pb(COOCH_3)_2$ + 1-dodecanethiol or $Na_2S\}$ route; SSP route produced relatively well-defined nanoparticles.

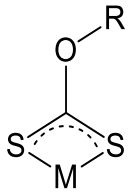

Figure 1.13: Structural example of xanthato complexes.

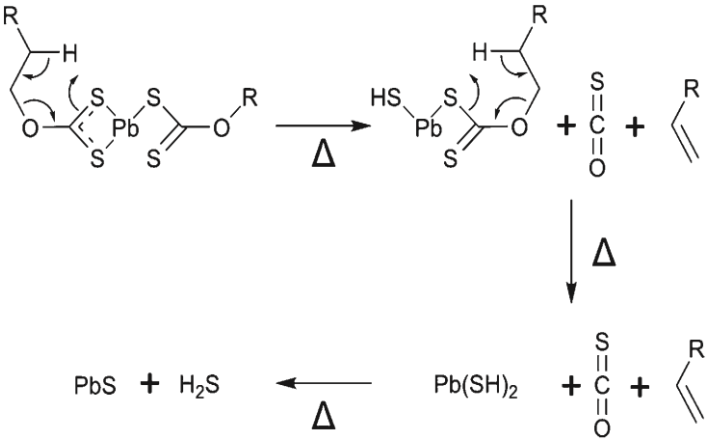

Scheme 1.6: The decomposition of alkylxanthato Pb(II) via the Chugaev elimination pathway.[80]

1.3 Statement of the research problem

Metal-organic compounds have attracted an unprecedented amount of attention as single source precursors (SSPs) for metal chalcogenide semiconductor nanoparticles. The merits have motivated a pursuit on the modification of current, or

design of novel SSPs, as means of establishing access to desirable properties and the discovery of new features of the nanoparticles. The design of new SSPs requires the knowledge and expertise of classical methods of synthesis coupled with organometallics. To date, there are no modelling or computational methods to predict the properties of the nanoparticles through the decomposition of the SSPs. Thus, the synthesis and evaluation of new SSPs is important in this context. This is by far the cost-efficient and mostly robust approach to good quality nanoparticles. However, the majority of the fabrication protocols for nanoparticles still use and produce toxic substances. The quality of the nanoparticles frequently takes precedence over environmental concerns and eco-friendly practices.

This work explores the use of new various SSPs for the fabrication of nanoparticles. Other environmentally-conscious reaction parameters, in addition to the chemical structure of the SSPs, were examined to map optimum conditions to afford nanoparticles exhibiting interesting properties.

1.4 Scope of the work

The work has been structured into three parts, towards the green synthesis of non-toxic nanoparticles. The first part includes the hot injection synthesis of well-known CdS and PbS nanoparticles using oleylamine as a capping agent, following an approach incorporating single source precursors constituting non-toxic thiosemicarbazone ligands. Furthermore, the study explores the influence of the halogen ligands present in the single source precursors, which has been overlooked in literature. The second part presents alternative green approaches to obtain non-toxic β-In_2S_3 and $CuInS_2$ nanoparticles, exhibiting improved optoelectronic properties to CdS and PbS nanoparticles, respectively. The route used hot injection reaction protocols incorporating In(III) and Cu(II) ethyl xanthate molecular precursors, using castor oil and olive oil as capping agents. The third part, reports a relatively greener method of preparing non-toxic indium sulfide nanoparticles exhibiting different crystallographic phases. The route uses solventless thermolytic reaction protocols where various In(III) xanthate complexes were used as single source precursors.

In addition to toxicity awareness, other features were also subjects of interest, which include particle size, shape and morphology control, as well as tuning the energy band gaps of the nanoparticles through manipulation of reaction parameters.

1.5 Aim and objectives of the work

The main aim of the study is to devise reaction protocols towards the green synthesis of non-toxic nanoparticles, using metal complexes as molecular precursors.

The objectives of the work include:

- The synthesis and characterisation of halogenated Cd(II) and Pb(II) thiosemicarbazone complexes, as well as In(III) and Cu(II) xanthate and dithiocarbamate complexes.
- The hot injection synthesis and characterisation of oleylamine-capped CdS and PbS nanoparticles.
- The hot injection synthesis and characterisation of castor oil and olive oil-capped β-In_2S_3 and $CuInS_2$ nanoparticles.
- The synthesis and characterisation of indium sulfide nanoparticles using solventless thermolysis.

1.6 Thesis layout

Chapter	Title	Description
1	Introduction	The summary of the current advances in the exploitation of nanomaterials in both laboratory and commercial marketplace. Synthetic methods for functional nanoparticles are reviewed.

2	The influence of both organic and halide ligands on Cd(II) thiosemicarbazone complexes in determining the properties of oleylamine-capped CdS nanoparticles	Detailed study on the synthesis of halogenated complexes and their use as single source precursors for the fabrication of nanoparticles. Morphological and optoelectronic properties are evaluated.
3	The influence of the halide ligands in Pb(II) thiosemicarbazone complexes on the properties of PbS nanoparticles	
4	Castor oil and olive oil as green capping agents towards the synthesis of non-toxic β-In_2S_3 and $CuInS_2$ nanoparticles from molecular precursors	Efforts in devising eco-friendly hot injection synthetic protocols to afford non-toxic nanoparticles. The effect of using different classes of molecular precursors on the properties of the nanoparticles is studied.
5	Solventless synthesis of indium sulfide nanoparticles and aggregrates from the thermal decomposition of indium(III) complexes	Crystallographic and phase control of nanoparticles from solventless decomposition of single source precursors.
6	Conclusion	The summary of the overall work reported in this thesis.

References

[1] M. A. Vance, T. Kuiken, E. P. Vejerano, S. P. McGinnis, M. F. Hochella Jr., D. Rejeski, M. S. Hull, *Beilstein J. Nanotechnol.* **2015**, *6*, 1769, and references therein.

[2] http://www.nanotechproject.org, last visited on 25 June 2018.

[3] I. Khan, K. Saeed, I. Khan, *Arabian J. Chem.* **2017**, http://dx.doi.org/10.1016/j.arabjc.2017.05.011.

[4] J. F. Jacobs, I. van de Poel, P. Osseweijer, *Nanoethics*, **2010**, *4*, 103.

[5] E. Hernández-Rodríguez, V. Rejón, R. Mis-Fernández, J. L. Pena, *Solar Energy*, **2016**, *132*, 64.

[6] Seshan, K. (Ed.). (2012). *Handbook of thin film deposition*. William Andrew.

[7] Q. Guo, H. W. Hillhouse, R. Agrawal, *J. Am. Chem. Soc.* **2009**, *131*, 11672.

[8] J. Meyer, R. Khalandovsky, P. Görrn, A, Kahn, *Adv. Mater.* **2011**, *23*, 70.

[9] C. B. Murray, D. J. Norris, M. G. Bawendi, *J. Am. Chem. Soc.* **1993**, *115*, 8706.

[10] (a) M.A. Malik, M. Afzaal, P. O'Brien, *Chem. Rev*. **2010**, *110*, 4417. (b) V. Bessergenev, *J. Phys.: Condens, Matter* **2004**, *16*, S531. (c) Malik, M. A., O'Brien, P. (2008). Basic Chemistry of CVD and ALD Precursors. In *Chemical Vapour Deposition* (pp.207-271). (d) Green, M. (2014). The Use of Single-Source Precursors in Nanoparticle Synthesis. In *Semiconductor Quantum Dots: Organometallic and Inorganic Synthesis* (pp. 224-251).

[11] M.-R. Gao, Y.-F. Xu, J. Jiang, S.-H. Yu, *Chem. Soc. Rev.* **2013**, *42*, 2986.

[12] M. D. Regulacio, M.-Y. Han, *Acc. Chem. Res.* **2016**, *49*, 511.

[13] E. Esakkiraj, S. P. Sheik Abdul Kadhar, J. Herry, K. Mohanraj, S. Kanaan, S. Barathan, G. Sivakumar, *Optik* **2013**, *124*, 5229.

[14] M. Sathish, B. Viswanathan, R. P. Viswanath, *Int. J. Hydrog. Energy* **2006**, *31*, 891.

[15] X. Chen, R. Fan, *Chem. Mater.* **2001**, *13*, 802.

[16] W.-C. Huang, C.-H. Tseng, S.-H. Chang, H.-Y. Tuan, C.-C. Chiang, L.-M. Lyu, M.-H. Huang, *Langmuir* **2012**, *28*, 8496.

[17] Y. Zhu, T. Mei, Y. Wang, Y. Qian, *J. Mater. Chem.* **2011**, *21*, 11457.

[18] J. Park, B. Koo, Y. Hwang, C. Bae, K. An, J.-G. Park, H. M. Park, T. Hyeon, *Angew. Chem.* **2004**, *116*, 2332.

[19] (a) J. van Embden, A.S.R. Chesman, J.J. Jasieniak, *Chem. Mater.* **2015**, *27*, 2246. (b) S.G. Kwon, T. Hyeon, *Small* **2011**, *7*, 2685.

[20] S. Eustis, M.A. El-Sayed, *Chem. Soc. Rev.* **2006**, *35*, 209.

[21] A.H. Lu,E.L. Salabas, F. Schüth, *Angew. Chem. Int. Ed.* **2007**, *46*, 1222.

[22] A.T. Bell, *Science* **2003**, *299*, 1688.

[23] T. Wu, X. Zhou, H. Zhang, X. Xhong, *Nano Res.* **2010**, *3*, 379.

[24] W. Wichiansee, M.N. Nordin, M. Green, R.J. Curry, *J. Mater. Chem.* **2011**, *21*, 7331.

[25] M. Michalska, A. Florczak, H. Dams-Kozlowska, J. Gapinski, S. Jurga, R. Schneider, *Acta Biomater.* **2016**, *35*, 293.

[26] X. Peng, J. Wickham, A.P. Alivisatos, *J. Am. Chem. Soc.* **1998**, *120*, 5343.

[27] J.A. Marqusee, J. Ross, *J. Chem. Phys*. **1984**, *80*, 536.

[28] V.K. LaMer, R.H. Dinegar, *J. Am. Chem. Soc.* **1950**, *72*, 4847.

[29] N. Al-Salim, A.G. Young, R.D. Tilley, A.J. McQuillan, J. Xia, *Chem. Mater.* **2007**, *19*, 5185.

[30] M. Green, *J. Mater. Chem.* **2010**, *20*, 5797.

[31] O.I. Mićić, J.R. Sprague, C.J. Curtis, K.M. Jones, J.L. Machol, A.J. Nozik, H. Giessen, B. Fluegel, G. Mohs, N. Peyghambarian, *J. Phys. Chem.* **1995**, *99*, 7754.

[32] (a) J. Joo, H.B. Na, T. Yu, J.H. Yu, Y.W. Kim, F. Wu, J.Z. Zhang, T. Hyeon, *J. Am. Chem. Soc.* **2003**, *125*, 11100. (b) J. Joo, J.S. Son, S.G. Kwon, J.H. Yu, T. Hyeon, *J. Am. Chem. Soc.* **2006**, *128*, 5632.

[33] R.E. Davis, H.F. Nakshbendi, *J. Am. Chem. Soc.* **1962**, *84*, 2085.

[34] N. Sonoda, T. Yasuhara, K. Kondo, T. Ikeda, S. Tsutsuma, *J. Am. Chem. Soc.* **1971**, *93*, 6344.

[35] D.V. Talapin, A.L. Rogach, A. Kornowski, M. Haase, H. Weller, *Nano Lett.* **2001**, *1*, 207.

[36] N. Gaponik, *J. Mater. Chem.* **2010**, *20*, 5174.

[37] I.L. Medintz, H.T. Uyeda, E.R. Goldman, H. Mattoussi, *Nat. Mater.* **2005**, *4*, 435.

[38] X.G. Peng, T.E. Wilson, A.P. Alivisatos, P.G. Schultz, *Angew. Chem. Int. Ed. Engl.* **1997**, *36*, 145.

[39] A.L. Rogach, T. Franzl, T.A. Klar, J. Feldmann, N. Gaponik, V. Lesnyak, A. Shavel, A. Eychmüller, Y.P. Rakovich, J.F. Donegan, *J. Phys. Chem. C* **2007**, *111*, 14628.

[40] W.J. Parak, D. Gerion, T. Pellegrino, D. Zanchet, C. Micheel, S.C. Williams, R. Boudreau, M.A. Le Gros, C.A. Larabell, A.P. Alivisatos, *Nanotech.* **2003**, *14*, R15.

[41] H.T. Uyeda, I.L. Medintz, J.K. Jaiswal, S.M. Simon, H. Mattoussi, *J. Am. Chem. Soc.* **2005**, *127*, 3870.

[42] S. Pathak, S.-K. Choi, N. Arnheim, M.E. Thompson, *J. Am. Chem. Soc.* **2001**, *123*, 4103.

[43] J. Aldana, Y.A. Wang, X. Peng, *J. Am. Chem. Soc.* **2001**, *123*, 8844.

[44] G.J. Leong, M.C. Schulze, M.B. Strand, D. Maloney, S.L. Frisco, H.N. Dinh, B. Pivovar, R.M. Richards, *Appl. Organometal. Chem.* **2014**, *28*, 1.

[45] W. van der Stam, S. Gradmann, T. Atlantzis, X. Ke, M. Baldus, S. Bals, C. de Mello Donega, *Chem. Mater.* **2016**, *28*, 6705.

[46] M.D. Khan, M. Akhtar, M.A. Malik, N. Revaprasadu, P. O'Brien, *ChemistrySelect* **2018**, *3*, 2943.

[47] S.E. Khalafalla, G.W. Reimers, *Sep. Sci.* **1973**, *8*, 161.

[48] N. Wu, L. Fu, M. Su, M. Aslam, K.C. Wong, V.P. Dravid, *Nano Lett.* **2004**, *4*, 383.

[49] H. Hirai, H. Aizawa, *J. Colloid Interface Sci.* **1993**, *161*, 471.

[50] W. Wang, S. Efrima, O. Regev, *Langmuir* **1998**, *14*, 602.

[51] R. Tadmor, R.E. Rosensweig, J. Frey, J. Klein, *Langmuir* **2000**, *16*, 9117.

[52] A. Prakash, H. Zhu, C.J. Jones, D.N. Benolt, A.Z. Ellsworth, E.L. Bryant, V.L. Colvin, *ACS Nano* **2009**, *3*, 2139.

[53] T. Bala, A. Swami, B.L.V. Prasad, M. Sastry, *J. Colloid Interface Sci.* **2005**, *283*, 422.

[54] Z. Paulsen, M.O. Onani, G.R.J. Allard, A. Kiplagat, J.O. Okil, F.B. Dejene, G.M. Mahanga, *Physica B* **2016**, *480*, 156.

[55] R. Das, S.S. Nath, R. Bhattacharjee, *J. Fluoresc.* **2011**, *21*, 1165.

[56] B. Meesaragandla, S. Sarkar, C. Hazra, V. Mahalingam, *ChemPlusChem* **2013**, *78*, 1338.

[57] S. Mlowe, R. Pullabhotla, E. Mubofu, F. Ngassapa, N. Revaprasadu, *Int. Nano. Lett*. **2014**, *4*, 106.

[58] S.J.O. Hardman, D.M. Graham, S.K. Stubbs, B.F. Spencer, E.A. Seddon, H.-T. Fung, S. Gardonio, F. Sirotti, M.G. Silly, J. Akhtar, P. O'Brien, D.J. Binks, W.R. Flavell, *Phys. Chem. Chem. Phys.* **2011**, *13*, 20275.

[59] G.B. Shombe, E.B. Mubofu, S. Mlowe, N. Revaprasadu, *Mater. Sci. Semicond*. *Process*. **2016**, *43*, 230.

[60] P. Velmurugan, M. Iydroose, S.-M. Lee, M. Cho, J.-H. Park, V. Balachandar, B.-T. Oh, *Indian. J. Microbiol.* **2014**, *54*, 196.

[61] Boskou, D., Blekas, G., & Tsimidou, M. (2006). Olive oil composition. In *Olive Oil (Second Edition)* (pp. 41-72).

[62] S.S. Gupta, T.P. Hilditch, J.P. Riley, *J. Sci. Food Agric.* **1951**, *2*, 245.

[63] Lomonaco, D., Mele, G., & Mazzetto, S. E. (2017). Cashew nutshell liquid (CNSL): from an agro-industrial waste to a sustainable alternative to petrochemical resources. In *Cashew Nut Shell Liquid* (pp. 19-38). Springer, Cham.

[64] S. Iravani, *Green Chem.* **2011**, *13*, 2638.

[65] O.V. Kharissova, H.V. Rasika Dias, B.I. Kharisov, B.O. Pérez, V.M. Jiménez Pérez, *Trends Biotechnol.* **2013**, *31*, 240.

[66] D. Philip, *Spectrochim. Acta, Part A* **2010**, *75*, 1078.

[67] https://www.sigmaaldrich.com/catalog/product/aldrich/329703?lang=en&region=ZA, last visited on 25 June 2018.

[68] M.M. Rauhut, H.A. Currier, V.P. Wystrach, *J. Org. Chem.* **1961**, *26*, 5133.

[69] C. Byrom, M.A. Malik, P. O'Brien, A.J.P. White, D.J. Williams, *Polyhedron* **2000**, *19*, 211.

[70] H.P.S. Chauhan, C.P. Bhasin, G. Srivastava, R.C. Mehrotra, *Phosphorus, Sulfur, Relat. Elem.* **1983**, *15*, 99.

[71] B. Kaboudin, A. Ghaderian, *Appl. Surf. Sci.* **2013**, *282*, 396.

[72] J.D. Woollins, *J. Chem. Soc., Dalton Trans*. **1996**, 2893.

[73] M. Afzaal, K. Ellwood, N.L. Pickett, P. O'Brien, J. Raftery, J. Waters, *J. Mater. Chem.* **2004**, *14*, 1310.

[74] M. Afzaal, D. Crouch, P. O'Brien, J.-H. Park, *J. Mater. Sci. Mater. Electron*. **2003**, *14*, 555.

[75] K. Ramasamy, M.A. Malik, P. O'Brien, J. Raftery, *Dalton Trans.* **2010**, *39*, 1460.

[76] K. Ramasamy, W. Maneerprakorn, M.A. Malik, P. O'Brien, *Phil. Trans. R. Soc. A* **2010**, *368*, 4249.

[77] A. Uhlin, S. Åkerström, *Acta Chem. Scand.* **1971**, *25*, 393.

[78] A.M. Paca, P.A. Ajibade, *Nanomaterials* **2018**, *8*, 187.

[79] F. Mazzi, C. Tadini, *Z. Krist.* **1963**, *118*, 378.

[80] P.D. McNaughter, S.A. Saah, M. Akhtar, K. Abdulwahab, M.A. Malik, J. Raftery, J.A.M. Awudza, P. O'Brien, *Dalton Trans.*, **2016**, *45*, 16345.

[81] Z. Tshemese, M.D. Khan, S. Mlowe, N. Revaprasadu, *Mater. Sci. Eng. B-Adv.* **2018**, *227*, 116.

CHAPTER 2

2 The influence of both organic and halide ligands on Cd(II) thiosemicarbazone complexes in determining the properties of oleylamine-capped CdS nanoparticles

2.1 Introduction

Cadmium sulfide (CdS), a II–VI semiconductor with a direct band gap of 2.42 eV, has been identified as an important device material which can be exploited, for example, in solar cells,[1] light-emitting diodes for flat-panel displays,[2] gas sensors,[3] luminescence devices[4] and heterogeneous photocatalysis.[5]

One of the principal routes to high-quality CdS nanoparticles is the thermolysis of metal complexes as single-source precursors in high-boiling solvents. This route allows for the control of particle size and shape by varying reaction conditions such as temperature, precursor concentration and capping group. Other advantages of using complexes include their air stability, low toxicity, limited pre-reaction protocols and control over stoichiometry.

Various classes of complexes have been employed to create CdS nanomaterials. Extensive work on dithiocarbamates,[6] xanthates,[7] thiourea,[8] dithiophosphinates[9] and dithioimidodiphosphinates[10] has been reported. The control of the CdS morphology in the form of spheres, rods, bipods and tetrapods has been achieved by using these classes of complexes. There has been no clear evidence, however, of the influence of the precursor composition on the morphology of the particles, although it has been inferred that the alkyl chain length of the capping groups plays a role in the final shape of the particles. Initially, phosphine-based capping groups such as tri-*n*-octylphosphine oxide were used for passivation. Alkylamine capping agents, such as hexadecylamine and oleylamine, superseded phosphine-based capping agents, due to the efficiency with which they can be adsorbed by the CdS nanoparticle core, which allows for shape manipulation.[11,12]

Recent work has shown that halogens can influence the shape of nanoparticles, improve their optical properties and influence charge transport between particles.[13–

[17] Halide ions have been shown to be effective in the passivation of PbS and CdSe nanoparticle systems[13,15,17] through subsequent formation of complexes with metal chalcogenides that alter the nucleation and growth kinetics. Chloride ions can induce structural transformation in CdSe and CdTe nanoparticles.[13] The presence of halogens can be regarded as a new parameter for shape control. The manipulation of particle shape and properties can improve the performance of nanoparticle-based optoelectronic devices.

The use of metal complexes as single-source precursors for the hot-injection route is well-established for the preparation of nanosized materials. Although many of the precursors contain halogens, there has not been a systematic study of the effect of using halogenated complexes on nanoparticle morphology. Thiosemicarbazones are versatile chelating ligands with the ability to form complexes with transition metal cations. As a result of their inherent metal–sulfur bond, the complexes have been identified as potential single-source precursors for the preparation of metal sulfide nanoparticles and thin films.[18,19]

In this chapter, a synthetic protocol for the formation of CdS nanoparticles by solvothermal decomposition of cadmium-based thiosemicarbazone complexes is reported. The effect of the nature of the metal complexes, particularly the incorporation of halogen ligands to the Cd(II) centre, and the reaction temperature was investigated in this work. Since this is the first study of its kind, based on our current knowledge, restrictions have been imposed resulting to the selection of two halogen ligands to avoid a large data set and tedious experiments. In the halogen group, Cl, Br and I are common ligands which are easily incorporated in the SSPs. Thus, halogens displaying a broad or significant difference in their properties (e.g. ionic radii) have been chosen, i.e. Cl and I.

2.2 Experimental

2.2.1 Materials

Tri-*n*-octylphosphine and oleylamine were purchased from Sigma-Aldrich. Acetone, methanol, cyclohexane and hexane were obtained from Shalom

Laboratories. Cadmium chloride and cadmium iodide were purchased from S D Fine-Chem. Limited. All chemicals were used as received.

2.2.2 Synthesis of complexes

2.2.2.1 Synthesis of ligands

Ligands were prepared by methods reported elsewhere,[20] and the synthesis of the corresponding Cd(II)X complexes are detailed in the following subsections.

2.2.2.2 Preparation of Bis(cinnamaldehyde thiosemicarbazone) cadmium(II) chloride (1)

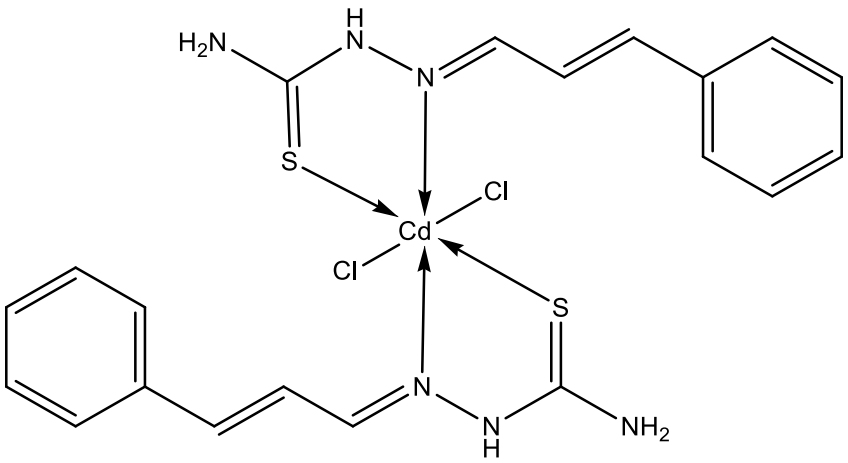

To a round-bottom flask was added cinnamaldehyde thiosemicarbazone (1.17 g, 5.70 mmol) dissolved in anhydrous methanol (20 mL). To this, a solution of $CdCl_2$ (523 mg, 2.85 mmol) dissolved in anhydrous methanol (20 mL) was added with constant stirring which was continued for 36 h at room temperature. The solvent was evaporated *in vacuo* and yellow coloured solids were obtained. The solids were washed with 3 x 10 mL of cyclohexane, followed by 2 x 10 mL of n-hexane, to remove impurities present. The washed solids were then dried under vacuum to afford an analytically pure product (**1**). Yield: 1.31 g (77%), m.p. 195 °C.

Elemental analyses (%) for $CdCl_2C_{20}H_{22}N_6S_2$ found (calcd): C: 40.72 (40.44). H: 3.48 (3.73). N: 14.48 (14.15). S:10.52 (10.79).

IR: 3436 cm^{-1}, 3285 cm^{-1} (υ_{NH2} asymm. and symm.), 3158 cm^{-1} (υ_{N-H}), 1581 cm^{-1} (υ_{C-N}), 982 cm^{-1} (υ_{C-S}).

NMR (δ in ppm) ^{1}H: 6.82-8.19 (m, NH_2 + C_6H_5-CH=CH-CH=N), 11.42 (s, NH). $^{13}C\{^{1}H\}$: 177.31 (C=S), 144.98 (CH=N), 138.99, 135.80 (CH=CH), 128.84, 127.72, 126.91, 124.95 (aromatic carbons).

2.2.2.3 Preparation of Bis(4-fluoro-acetophenone thiosemicarbazone) cadmium(II) chloride (2)

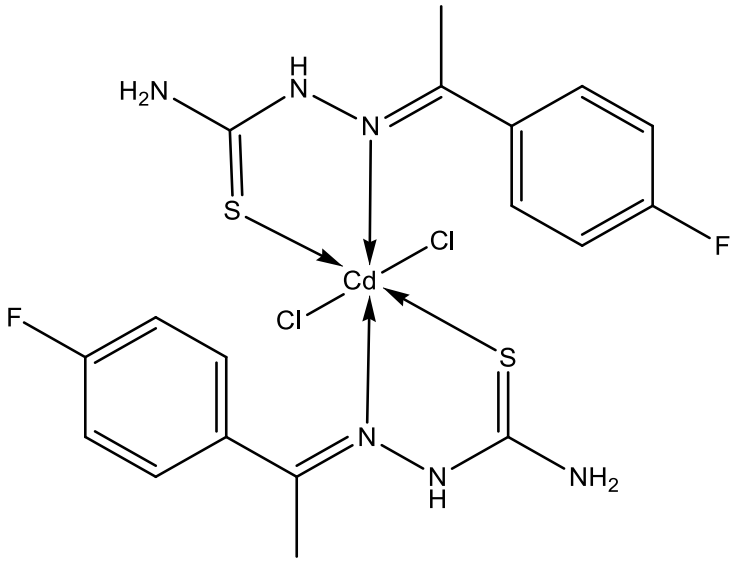

The reaction protocol used for the preparation of (**1**) was followed. The ligand, 4-fluoro-acetophenone thiosemicarbazone (1.06 g, 4.99 mmol) and $CdCl_2$ (458 mg, 2.49 mmol) gave a white precipitate of (**2**). Yield: 1.35 g (89%), m.p. 153 °C.

Elemental analyses (%) for $CdCl_2C_{18}H_{20}N_6F_2S_2$ found (calcd): C: 35.96 (35.68). H: 3.48 (3.32). N: 13.53 (13.87). S: 10.29 (10.58).

IR: 3416 cm^{-1}, 3306 cm^{-1} (υ_{NH2} asymm. and symm.), 3165 cm^{-1} (υ_{N-H}), 1582 cm^{-1} (υ_{C-N}), 966 cm^{-1} (υ_{C-S}).

NMR (δ in ppm) ^{1}H: 7.16-8.42 (m, NH_2 + C_6H_5-C=N), 10.31 (s, NH), 3.38 (CH_3). $^{13}C\{^{1}H\}$: 177.65 (C=S), 148.06 (C=N), 14.20 (CH_3), 133.91, 129.03, 128.92, 114.87 (aromatic carbons).

2.2.2.4 Preparation of Bis(4-chlorobenzaldehyde thiosemicarbazone) cadmium(II) chloride (3)

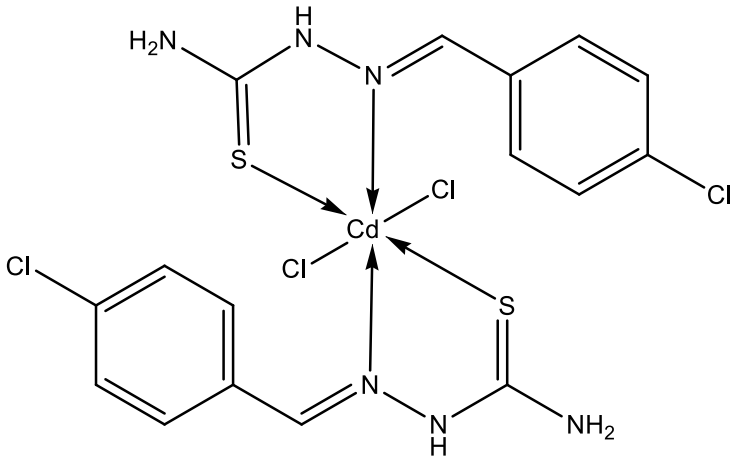

The reaction protocol used for the preparation of (**1**) was followed. The ligand, 4-chlorobenzaldehyde thiosemicarbazone ligand (946 mg, 4.42 mmol) and $CdCl_2$ (406 mg, 2.21 mmol) gave a white precipitate of (**3**). Yield 1.16 g (86%), m.p. 221 °C.

Elemental analyses (%) for $CdCl_4C_{16}H_{16}N_6S_2$ found (calcd): Cd: 18.73 (18.40). C: 31.76 (31.46). H: 2.48 (2.64). N: 13.49 (13.76). S: 10.22 (10.50). Cl: 23.01 (23.21).

IR: 3451 cm^{-1},3296 cm^{-1} (υ_{NH2} asymm. and symm.), 3188 cm^{-1} (υ_{N-H}), 1589 cm^{-1} (υ_{C-N}), 957 cm^{-1} (υ_{C-S}).

NMR (δ in ppm) ^{1}H: 7.42-8.31 (s, NH_2, mC_6H_5-CH=N),11.57 (s, NH). $^{13}C\{^{1}H\}$: 177.47 (C=S), 141.41 (CH=N), 134.32,133.01,128.95,128.66 (aromatic carbons).

2.2.2.5 Preparation of Bis(benzophenone thiosemicarbazone) cadmium(II) chloride (4)

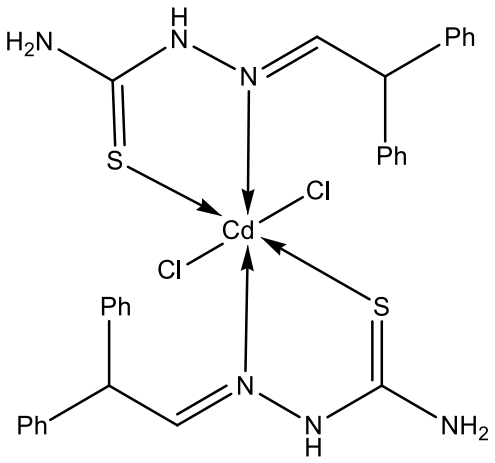

The reaction protocol for the preparation of (**1**) was followed. Benzophenone thiosemicarbazone (1.317 g, 5.16 mmol) and $CdCl_2$ (473 mg, 2.58 mmol) gave a white precipitate of (**4**). Yield 1.61 g (90%), m.p. 194 °C.

Elemental analyses (%) for $CdCl_2C_{28}H_{26}N_6S_2$ found (calcd): Cd: 16.53 (16.19). C: 48.77 (48.45). H: 3.52 (3.77). N:12.29 (12.10). S:9.05 (9.24). Cl: 10.42 (10.21).

IR: 3399cm^{-1}, 3287cm^{-1} (υ_{NH2} asymm. and symm.), 3167cm^{-1} (υ_{N-H}), 1602cm^{-1} (υ_{C-N}), 837cm^{-1} (υ_{C-S}).

NMR (δ in ppm) ^{1}H: 7.30 - 8.53 (s, NH_2, mC_6H_5-C=N), 8.63 (s, NH). $^{13}C\{^{1}H\}$: 177.56 (C=S), 149.54 (C=N), 136.25, 131.17, 129.97, 129.77, 128.32, 128.25, 127.57 (aromatic carbons).

2.2.2.6 Preparation of Bis(cinnamaldehyde thiosemicarbazone) cadmium(II) iodide (5)

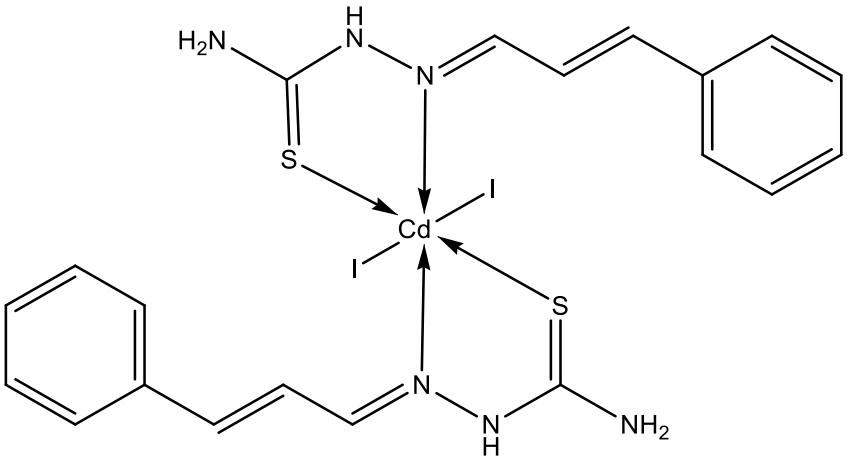

The reaction protocol used for the preparation of (**1**) was followed. Cinnamaldehyde thiosemicarbazone (1.11 g, 5.41 mmol) and CdI_2 (991 mg, 2.70 mmol) gave a yellow precipitate of (**5**). Yield: 1.84 g (87%), m.p. 149 °C.

Elemental analyses (%) for $CdI_2C_{20}H_{22}N_6S_2$ found (calcd): C: 31.14 (30.92). H: 2.68 (2.85). N: 10.68 (10.81). S: 8.10 (8.25).

IR: 3407 cm^{-1}, 3283 cm^{-1} (υ_{NH2} asymm. and symm.), 3165 cm^{-1} (υ_{N-H}), 1579 cm^{-1} (υ_{C-N}), 972 cm^{-1} (υ_{C-S}).

NMR (δ in ppm) ^{1}H: 6.82-8.17 (m, NH_2 + C_6H_5-CH=CH-CH=N), 11.42 (s, NH). $^{13}C\{^{1}H\}$: 177.24 (C=S), 145.05 (CH=N), 139.02, 135.78 (CH=CH), 128.85, 127.71, 126.90, 124.94 (aromatic carbons).

2.2.2.7 Preparation of Bis(4-fluoro-acetophenone thiosemicarbazone) cadmium(II) iodide (6)

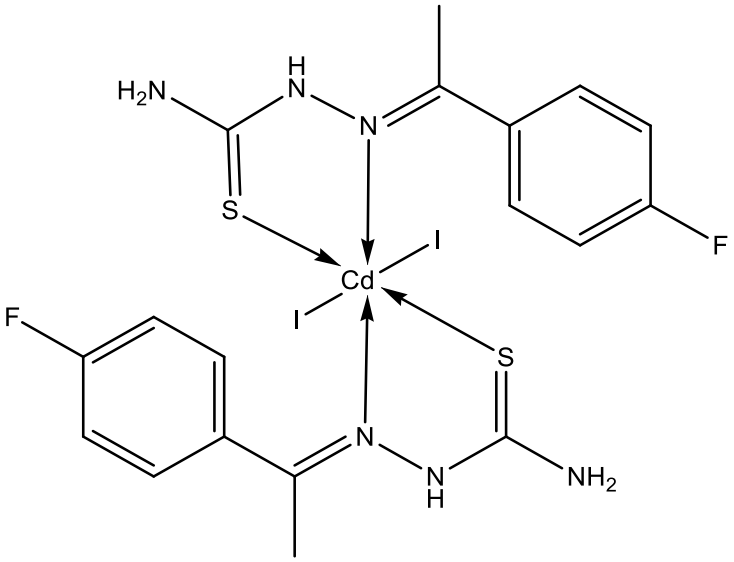

The reaction protocol used for the preparation of (**1**) was followed. The ligand, 4-fluoro-acetophenone thiosemicarbazone (874 mg, 4.13 mmol) and CdI_2 (758 mg, 2.06 mmol) gave a white precipitate of (**6**). Yield: 1.51 g (92%), m.p. 150 °C.

Elemental analyses (%) for $CdI_2C_{18}H_{20}N_6F_2S_2$ found (calcd): C: 27.68 (27.40). H: 2.32 (2.55). N: 10.36 (10.65). S: 8.44 (8.13)

IR: 3429 cm^{-1}, 3300 cm^{-1} (υ_{NH2} asymm. and symm.), 3086 cm^{-1} (υ_{N-H}), 1588 cm^{-1} (υ_{C-N}), 1009 cm^{-1} (υ_{C-S}).

NMR (δ in ppm) ^{1}H: 7.16-8.34 (m, NH_2 + C_6H_5-C=N), 10.24 (s, NH), 3.37 (CH_3), $^{13}C\{^{1}H\}$: 177.91 (C=S), 147.81 (C=N), 14.17 (CH_3), 133.94, 128.99, 128.88, 115.15 (aromatic carbons).

2.2.2.8 Preparation of Bis(4-chlorobenzaldehyde thiosemicarbazone) cadmium(II) iodide (7)

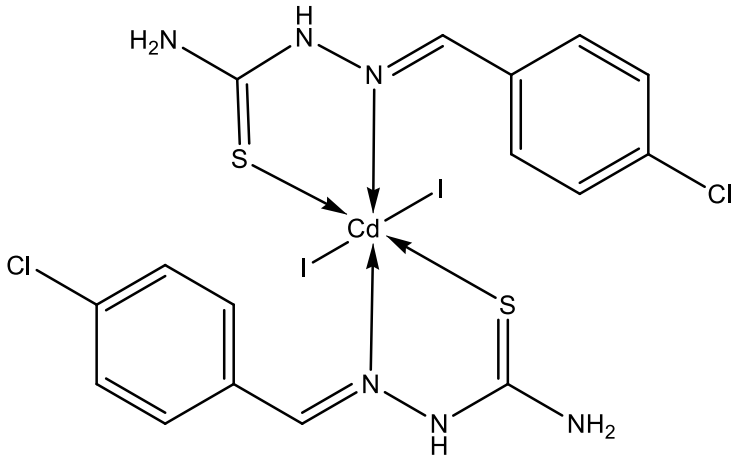

The reaction protocol for the preparation of (**1**) was followed. 4-chlorobenzaldehyde thiosemicarbazone (869 mg, 4.06 mmol) and CdI_2 (745 mg, 2.03 mmol) gave a white precipitate of (**7**). Yield 1.48 g (92%), m.p. 218 °C.

Elemental analyses (%) for $CdI_2Cl_2C_{16}H_{16}N_6S_2$ found (calcd): Cd: 14.32 (14.16).C: 24.56 (24.21). H: 2.28 (2.03). N:10.32 (10.58). S:7.85 (8.08). Cl: 8.64 (8.93).

IR: 3412 cm^{-1}, 3262cm^{-1} (υ_{NH2} asymm. and symm.), 3156 cm^{-1} (υ_{N-H}), 1588 cm^{-1} (υ_{C-N}), 955 cm^{-1} (υ_{C-S}).

NMR (δ in ppm) ^1H: 7.44-8.22 (s, NH_2, m C_6H_5-CH=N),11.49 (s, NH). $^{13}C\{^1H\}$: 177.81 (C=S),141.14 (CH=N),134.26, 133.08, 128.91, 128.65 (aromatic carbon).

2.2.2.9 Preparation of Bis(benzophenone thiosemicarbazone) cadmium(II) iodide (8)

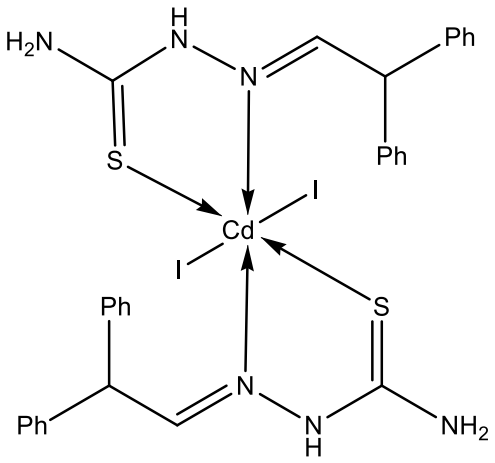

The reaction protocol used for the preparation of (**1**) was followed. Benzophenone thiosemicarbazone (935 mg, 3.66 mmol) and CdI_2 (671 mg, 1.83 mmol) gave a white precipitate of (**8**). Yield 1.57 g (97%), m.p. 91 °C.

Elemental analyses (%) for $CdI_2C_{28}H_{26}N_6S_2$ found (calcd): Cd: 12.97 (12.81). C: 38.54 (38.35). H: 2.84 (2.98). N:9.28 (9.58). S:7.14 (7.31).

IR: 3406 cm^{-1}, 3286 cm^{-1} (υ_{NH2} asymm. and symm.), 3192 cm^{-1} (υ_{N-H}), 1592 cm^{-1} (υ_{C-N}), 832 cm^{-1} (υ_{C-S}).

NMR (δ in ppm) ^{1}H: 7.32 - 8.48 (s, NH_2; m, C_6H_5-C=N), 8.63 (s, NH). $^{13}C\{^{1}H\}$: 177.64 (C=S), 149.03 (C=N), 136.26, 131.17, 129.96, 129.77, 128.31, 128.25, 127.56 (aromatic carbons).

2.2.3 Synthesis of nanoparticles

A three-necked flask equipped with a reflux condenser, thermometer and a rubber septum was charged with oleylamine (3.00 g), which was subsequently heated and maintained at an appropriate temperature (190 °C, 230 °C or 270 °C). A suspension of a precursor (250 mg) dispersed in tri-*n*-octylphosphine (6 mL) was injected into the heated oleylamine with a glass syringe. The reaction was stopped after 1 h and cooled to ~100 °C. Excess methanol was added to the cooled reaction, where the resulting yellow to orange coloured precipitate was removed by

centrifugation; the supernatant was discarded. The washing process of the precipitate was repeated thrice with methanol. The washed precipitate (CdS nanoparticles) was suspended in hexane prior to spectroscopic and TEM analyses.

2.2.4 Characterisation techniques

2.2.4.1 Microelemental analysis

The microelemental analysis technique was used to accurately measure the atomic composition of the synthesized compounds. The analyses of carbon, hydrogen, nitrogen and sulfur were carried out with a Thermo Finnigan Italy Model FLASH EA 1112 Series elemental analyser. Quantitative determination of cadmium and chloride contents were performed by complexometric and Volhard titration methods, respectively.

2.2.4.2 Infra-red (IR) spectroscopy

The IR spectroscopy was used to elucidate the chemical structure of the synthesized compounds through identification of their functional groups. The IR spectra were recorded on a PerkinElmer Spectrum One FTIR Spectrometer in the range 4000–400 cm^{-1}.

2.2.4.3 Molar conductance

Molar conductance measurements were made to determine the bonding mode and ionic character of the complexes. The measurements were made in dimethylformamide solutions (10^{-3} mol L^{-1}) using a Toshniwal conductivity meter.

2.2.4.4 Melting point

Melting point measurements were conducted to determine temperatures at which complexes melt; a traditional and quick method used to compliment microelemental analysis on the purity of compounds. Measurements were carried out on a Centrofix Scientific sales syndicate melting point apparatus.

2.2.4.5 ^{1}H and ^{13}C nuclear magnetic resonance (NMR) spectroscopy

Similar to the IR spectroscopy, the NMR spectroscopic technique was used to elucidate the chemical structure of the synthesized compounds, albeit through identification of proton and carbon equivalents. The ^{1}H and $^{13}C\{^{1}H\}$ NMR spectra were recorded with a Bruker 300 MHz spectrometer at room temperature using DMSO-d_6 as a solvent and TMS as an internal reference.

2.2.4.6 Thermogravimetric analysis (TGA)

The TGA was used to determine thermal stability of the synthesized compounds by measuring their weights against change in temperature. Furthermore, the TGA was used to determine the decomposition pattern of the compounds. The TGA measurements were performed using a PerkinElmer Pyris Diamond TG/DTA model from 30°C to 900°C at a heating rate of 10 °C min^{-1} under nitrogen atmosphere.

2.2.4.7 Optical absorbance measurements

The optical absorbance measurements were performed to estimate the optical band gap energies of the as-prepared CdS nanoparticles. Thus, the measurements were conducted at the UV-Vis spectral range on a Varian Cary 50 UV/Vis spectrophotometer using a quartz cuvette (1 cm path length) and hexane as a dispersing solvent.

2.2.4.8 Powder X-ray diffraction (p-XRD)

The p-XRD technique was used to determine the crystallographic phase of the as-prepared CdS nanoparticles. Powder XRD patterns were recorded at room temperature using a Bruker AXS D8 Advance diffractometer equipped with nickel-filtered Cu-Kα radiation (λ = 1.5418 Å) at 40 kV and 40 mA. The samples were dried *in vacuo* prior to analyses.

2.2.4.9 Transmission electron microscopy (TEM) and high resolution TEM (HRTEM)

The TEM and HRTEM imaging techniques were collectively used to determine the morphological features (particle size and shape) and crystallinity of the as-prepared CdS nanoparticles. Imaging was performed on a JEOL 1400 TEM and JEOL 2100 HRTEM, at accelerating voltages of 120 kV and 200 kV, respectively. Dilute suspensions of CdS nanoparticles were evaporated on Formvar-coated Cu grids (150 mesh) for TEM and holey carbon grids for HRTEM analyses, prior to analyses. The acquired images were further processed using Soft Imaging Systems iTEM software (TEM), and Gatan camera with Gatan software (HRTEM).

2.2.4.10 Energy dispersive X-ray (EDX) spectroscopy

The EDX spectroscopic technique was used for the microelemental analysis of CdS nanoparticles, to determine existence of halogenated species in the samples. The analysis was performed on CdS nanoparticles sprinkled on copper tape, using a Zeiss Ultra Plus FEG SEM equipped with an Oxford detector EDX operated at 20 kV, using Aztec software for microelemental analysis.

2.3 Results and discussion

Precursor design was identified as the primary objective for the study, crucial for tuning the properties of the CdS nanoparticles in a different, single source molecular precursor (SSP) approach. Synthetic protocols to afford SSPs involved the use of three commercial starting materials in a two-step reaction conducted at room temperature; reaction parameters recognized as the implementation of green chemistry principles.[21] The first reaction step involves the preparation of the ligands, thiosemicarbazones, while the second is the preparation of the corresponding Cd(II) SSPs. The phenyl analogues of the thiosemicarbazone ligands were preferred, thus, providing easy access to derivatise the compound in both electronic and steric approach. Theoretically, the two features influence the decomposition kinetics of the precursor which may lead to nanoparticles possessing unique properties. The second reaction step affords Cd(II) thiosemicarbazone SSPs which are obtained analytically

pure, at very good yields between 77-97%. The SSPs, *Bis*(cinnamaldehyde thiosemicarbazone) cadmium(II) chloride (**1**), *Bis*(4-fluoro-acetophenone thiosemicarbazone) cadmium(II) chloride (**2**), *Bis*(4-chlorobenzaldehyde thiosemicarbazone)cadmium(II) chloride (**3**), *Bis*(benzophenone thiosemicarbazone)cadmium(II) chloride (**4**), *Bis*(cinnamaldehyde thiosemicarbazone) cadmium(II) iodide (**5**), Preparation of *Bis*(4-fluoro-acetophenone thiosemicarbazone) cadmium(II) iodide (**6**), *Bis*(4-chlorobenzaldehyde thiosemicarbazone)cadmium(II) iodide (**7**), *Bis*(benzophenone thiosemicarbazone)cadmium(II) iodide (**8**), were confirmed mostly by elemental analysis, Fourier transform infrared (FTIR) and nuclear magnetic resonance (NMR) spectroscopy techniques. The NMR spectra are provided in Figure A1-16 Appendix section.

Due to the nature of the study, it was of crucial importance to retain the halogen ligands from the parent metal source to be present in the SSP structure. As such, three analytical techniques were used to ascertain complexation by addition, as opposed to a substitution reaction. These techniques include: 1) the elemental analyser instrument which quantifies organic constituents *i.e.* C, H and S elements, 2) complexometric experiments to quantify Cd atoms, and 3) the Volhard method to determine the amount of the halogens. In addition to this, molar conductivities (Ω^{-1} cm^2 mol^{-1}) of 21.5, 13.0, 17.65 and 12.8 were measured from the DMF solutions (10^{-3} mol L^{-1}) of four representative SSPs (**1**), (**2**), (**5**) and (**6**), respectively. This confirms that the SSPs are neutral metal-organic compounds, since high molar conductivity values are typical of ionic compounds and electrolytes. Furthermore, the positive test for halogens atoms by the Volhard method and the presence of N-H functional group provided in Table 2.1 suggests that deprotonation did not occur, which is an indication that synthetic route towards the SSPs did not proceed through the substitution mechanism. Thus, the overall analyses data conforms to the proposed chemical structures presented in section 2.2.2.

Table 2.1: The FTIR and ^{1}H NMR data on the N-H functional group in all SSPs.

SSP	FTIR	^{1}H NMR
	υ_{N-H} / cm^{-1}	δ –N(H)- / ppm
(**1**)	3158	11.42
(**2**)	3165	10.31
(**3**)	3188	11.57
(**4**)	3167	8.63
(**5**)	3165	11.42
(**6**)	3086	10.24
(**7**)	3156	11.49
(**8**)	3192	8.63

The data in Table 2.1 is also intended to demonstrate the influence of varying the phenyl moieties in the chemical structure of the SSP. Similar observation noted for the halogen ligands directly attached to the Cd(II) metal centre. This is indicative of unique chemical environments in individual SSPs, as such, different chemical behaviour with respect to decomposition is anticipated. This hypothesis was confirmed by the TGA where the SSPs showed different decomposition profiles *viz.* various decomposition steps at different temperatures (Figure 2.1). The decomposition patterns however look similar, as a result of similarities in the chemical structures of the SSPs. It is clear that the halogen ligands on the metal centre are a major influence on the decomposition pathway of the SSPs; the iodide class gives a cleaner decomposition pattern (i.e. steep decomposition curves typical of fast decomposition) relative to the chloride counterpart. This may be attributed to larger ionic diameter of the halogen; bulkier compounds decompose effortlessly. Nevertheless, the SSPs were found to be thermally stable up to 175 °C where they undergo two or three decomposition steps. The first decomposition step in SSPs (**1**) and (**8**) at 100 °C is generally attributed to either water of crystallisation or moisture adsorbed on the compound. The latter is a possible explanation for the two SSPs, which suggests they are hydroscopic in nature.

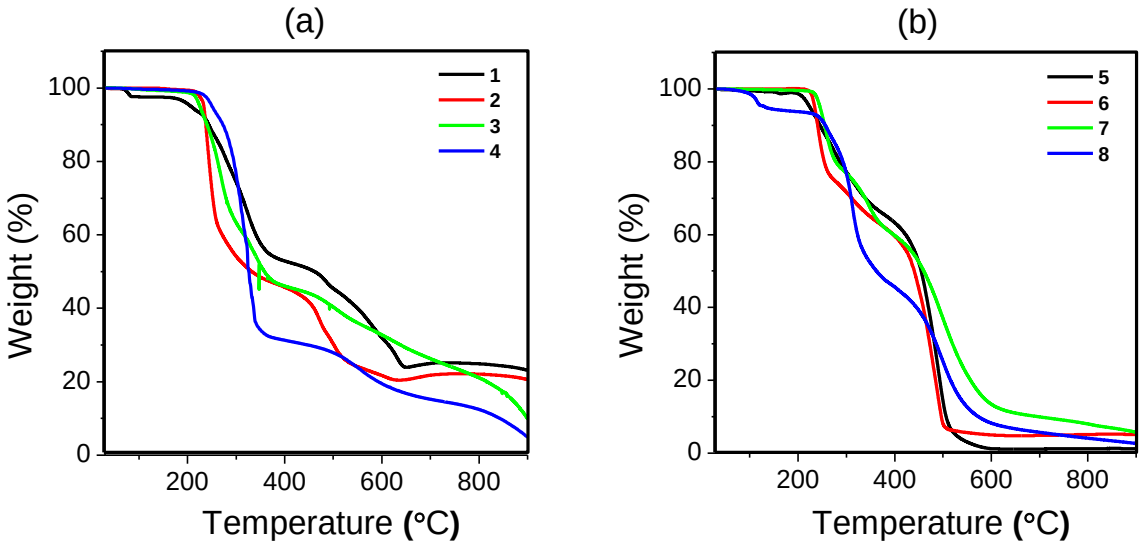

Figure 2.1: The TGA profiles for (a) $[Cd(L_2)Cl_2]$, and (b) $[Cd(L_2)I_2]$ SPPs, where L = thiosemicarbazone ligand.

Although the TGA is intended to study the thermal stability of the compounds, it has become a common practice to be used as a tool to determine whether the SSP decomposes to afford residue corresponding to a desired inorganic compound. This approach should only be used as a guide since its reliability depends on the nature of the compound. For example, in this work it is expected that the residue weights obtained from the TGA would correspond to CdS. However, few SSPs conform to this anticipation as seen in Table 2.2. The discrepancies in other SSPs would be a result of carbonaceous material strongly adsorbed on CdS or loss of CdS through sublimation mechanisms assisted by volatile organic components, where the residue weight is relatively higher or lower to theoretical CdS, respectively. Evidence to this was observed on heavier residues obtained mostly at 600 °C displaying a tint of black colour in addition to yellow or orange colour for pure CdS, while yellow or orange coloured material would be deposited on the ventilation lid of the TGA instrument with only black residue remaining on the sample pan at 800 °C. The yellow coloured deposits could have been CdS or elemental sulfur. The TGA data was not found conclusive with respect to appropriate decomposition temperature to afford CdS. Regardless of this, there are examples of transition metal complexes of thiosemicarbazones which have been used as versatile SSPs for synthesizing metal sulfide nanoparticles.[22,23] This work included a solvent-assisted thermal

decomposition of the SSPs. The method has been established to facilitate decomposition of SSPs at relatively lower temperatures through a different mechanism.

Table 2.2: Comparison of residues obtained from TGA data to corresponding theoretical CdS.

SSP	Residue %	Theoretical CdS %
(**1**)	24.10	24.33
(**2**)	20.52	23.85
(**3**)	10.70	23.70
(**4**)	5.08	20.82
(**5**)	1.30	18.6
(**6**)	5.29	18.32
(**7**)	5.79	18.20
(**8**)	2.95	16.5

This report extends the scope of the previously published work in which a cadmium(II) acetophenone thiosemicarbazone with iodido ligands was used as a SSP.[19] Sphere-like CdS nanocrystallites were obtained by a solvothermal technique in refluxing ethylene glycol. It was observed that an increase in reaction time improved the uniformity of the distribution of nanocrystallites. However, the study overlooked a possible influence of the halide ligands on the properties of the prepared nanocrystallites. Furthermore, the influence of temperature was not explored. Therefore, the current study was designed such that it included investigation of the parameters ignored in the earlier work. The SSPs were then thermally decomposed in the presence of an organic capping agent, namely, oleylamine, in pursuit of good-quality CdS nanocrystals. We observed that the chemical structure of the SSP and reaction temperature had a significant influence on the crystallographic, morphological and electronic properties of the CdS nanoparticles. The influence of the reaction time was found to be negligible, that is, there was no significant difference in the

experimental results obtained after 1 and 2 h. These observations were conducted in a typical reaction protocol provided in section 2.2.2.2.

The thermolysis of the SSPs produced oleylamine-capped solids which exhibited yellow to orange colours, which intensify with an increase in reaction temperature. The solids were matched to wurtzite hexagonal CdS (card no. 03-065-3414) through powder X-ray diffraction (p-XRD) technique. The reaction parameters had no influence on the crystallographic phase of the nanoparticles, however, the crystallinity mostly improved with increase in reaction temperature (Figure 2.2-2.9). This phenomenon is common in the field, attributed to an increase in crystallite size as a result of less broadening of reflection peaks in the p-XRD patterns with temperature.

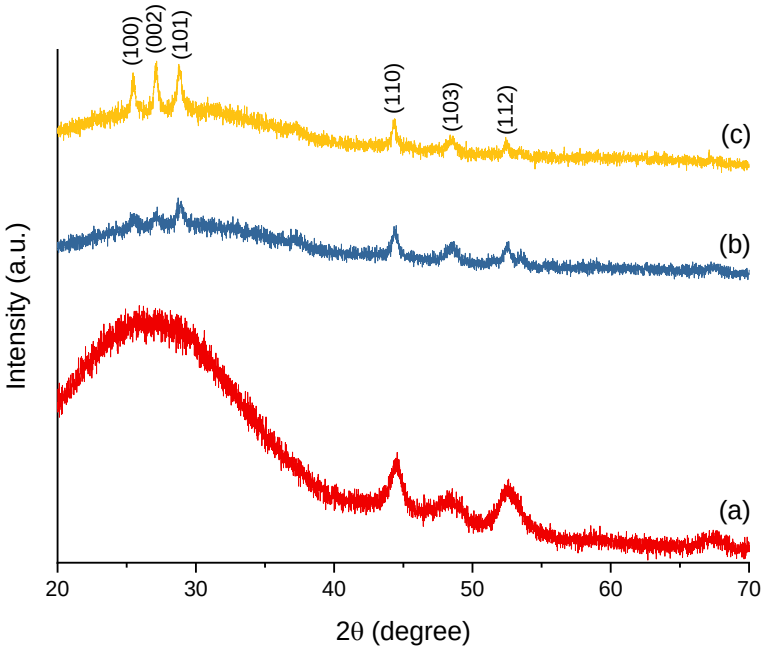

Figure 2.2: The p-XRD patterns of CdS nanoparticles synthesized from SSP (**1**) at (a) 190 °C, (b) 230 °C and (c) 270 °C.

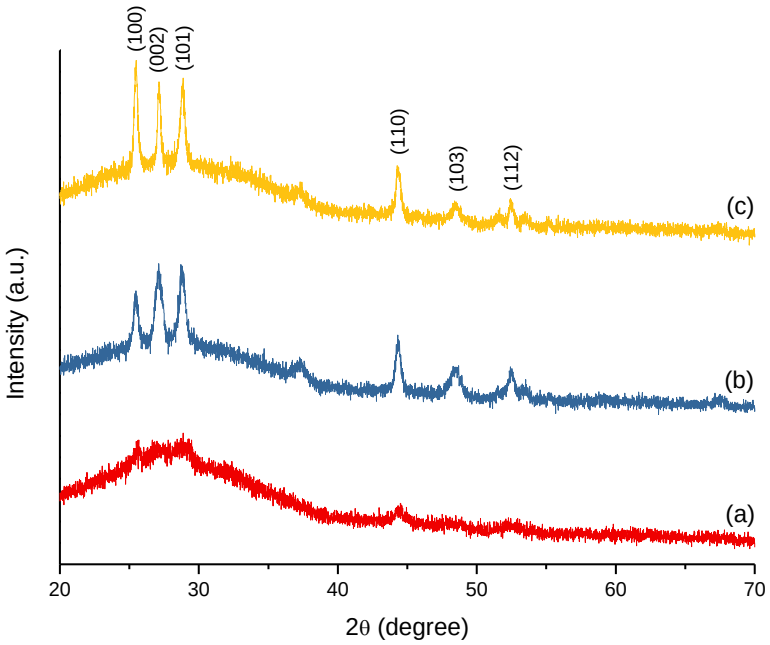

Figure 2.3: The p-XRD patterns of CdS nanoparticles synthesized from SSP (**2**) at (a) 190 °C, (b) 230 °C and (c) 270 °C.

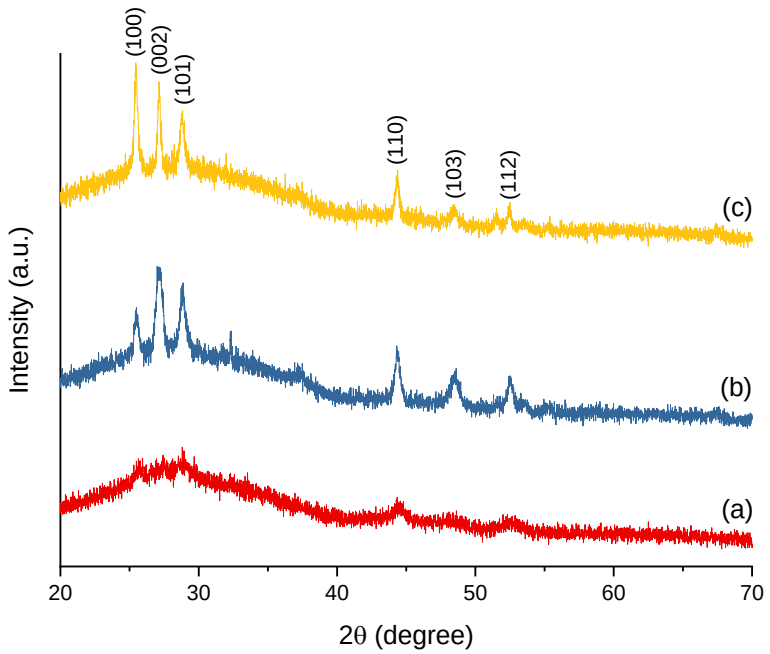

Figure 2.4: The p-XRD patterns of CdS nanoparticles synthesized from SSP (**3**) at (a) 190 °C, (b) 230 °C and (c) 270 °C.

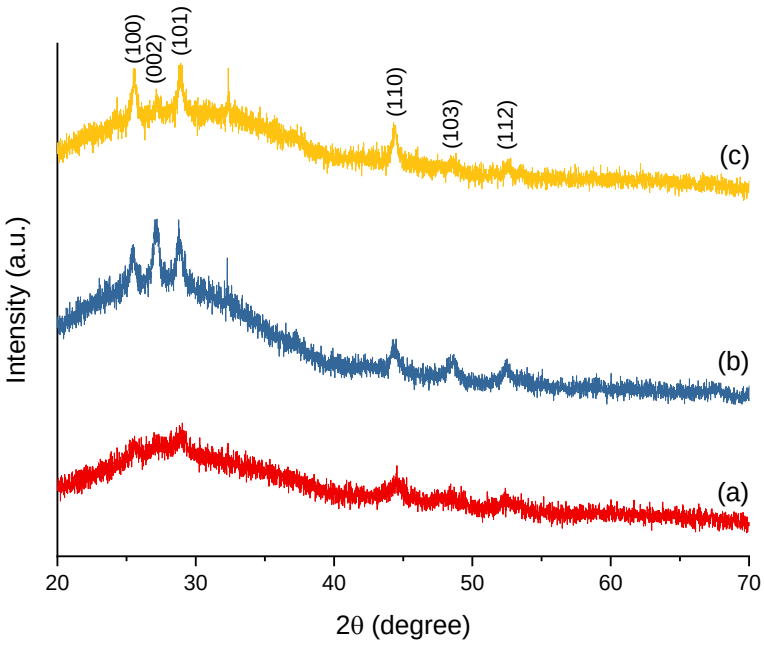

Figure 2.5: The p-XRD patterns of CdS nanoparticles synthesized from SSP (**4**) at (a) 190 °C, (b) 230 °C and (c) 270 °C.

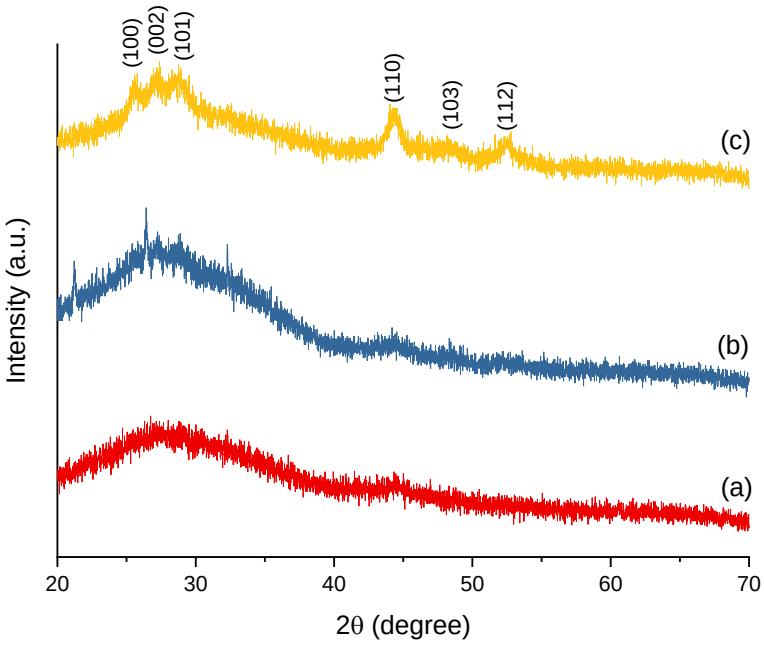

Figure 2.6: The p-XRD patterns of CdS nanoparticles synthesized from SSP (**5**) at (a) 190 °C, (b) 230 °C and (c) 270 °C.

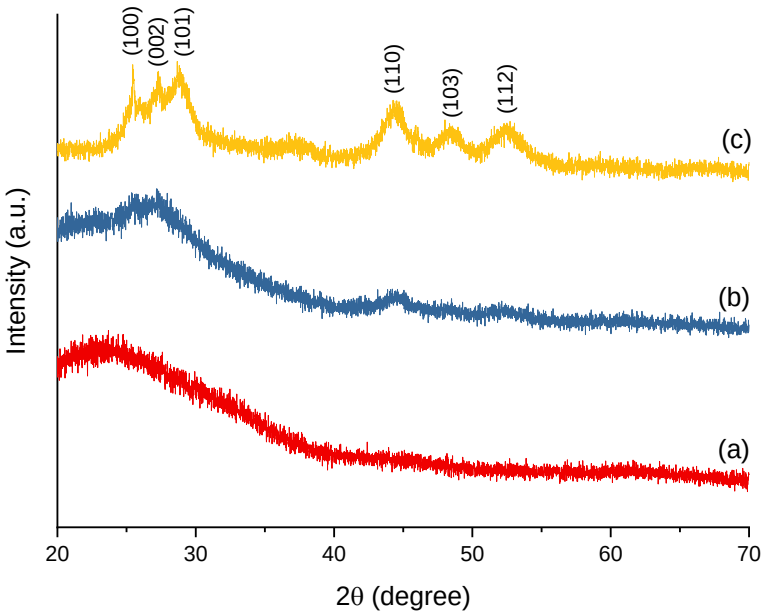

Figure 2.7: The p-XRD patterns of CdS nanoparticles synthesized from SSP (**6**) at (a) 190 °C, (b) 230 °C and (c) 270 °C.

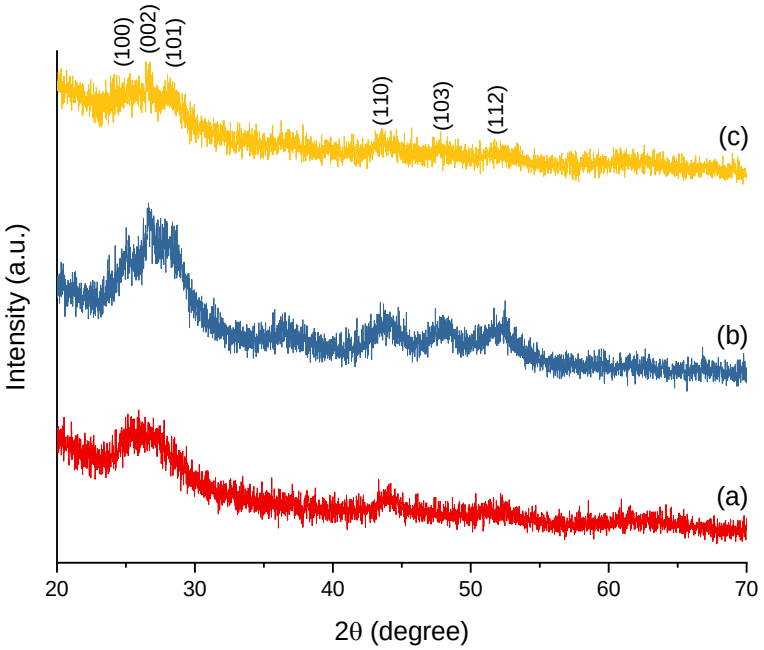

Figure 2.8: The p-XRD patterns of CdS nanoparticles synthesized from SSP (**7**) at (a) 190 °C, (b) 230 °C and (c) 270 °C.

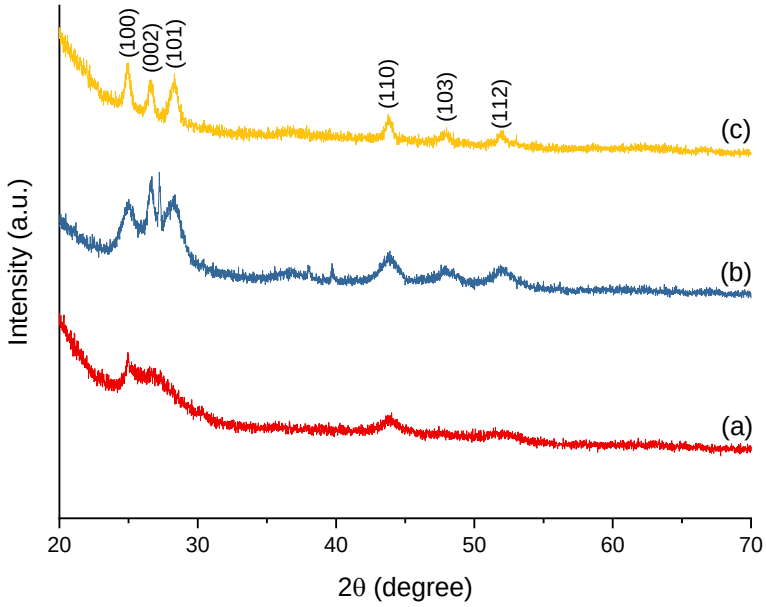

Figure 2.9: The p-XRD patterns of CdS nanoparticles synthesized from SSP (**8**) at (a) 190 °C, (b) 230 °C and (c) 270 °C.

The influence of changing the SSP was also observed on crystallinity-based features such as preferred orientation growth of the crystallite which is normally observed through the reflection peak of high intensity, as seen in Figure 2.10. It was clear from this point that both the thiosemicarbazone ligands and reaction temperature are the key role parameters towards this. In addition to this observation, it was found that the nanoparticles from the CdI_2 SSPs exhibited poor crystallinity relative to the $CdCl_2$ counterparts, although they displayed faster decomposition patterns in their TGA profiles. Thus, this proved that the decomposition pathway is different in the presence of a capping agent, and to some extent, the halide ligands impose an interference with the capping agent to effectively produce highly crystalline nanoparticles.

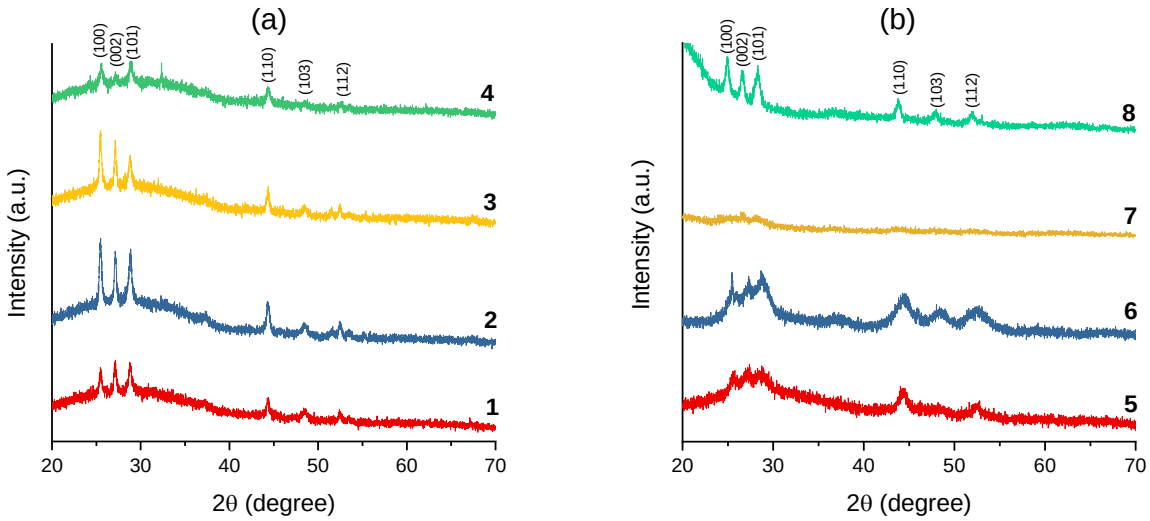

Figure 2.10: The p-XRD patterns of CdS nanoparticles synthesized at 270°C from (a) $[Cd(L_2)Cl_2]$ (**1**)-(**4**), and (b) $[Cd(L_2)I_2]$ (**5**)-(**8**) SSPs, where L = thiosemicarbazone ligand.

The effects of reaction temperature and type of ligand on the morphology of the CdS nanoparticles were also studied. The shape transformation is unique per group of SSPs, i.e. $CdCl_2$ and CdI_2 groups. In the former, the nanoparticles mostly start as either irregular cubes or spheres at 190°C, which transform into short rods or rectangular nanoparticles at 230 °C, then finally as irregular cubes at 270 °C reaction temperature. This is illustrated by a representative example in Figure 2.11. The trend is observed throughout the $CdCl_2$ series as seen in Figures 2.11-2.14. The rod-like particles obtained at 230 °C closely resembled the CdS quantum platelets reported by Buhro and co-workers.[24] The particle sizes are reasonably similar, although the quantum platelets exhibited two absorption peaks (337 and 375 nm), which were significantly blueshifted as compared to the single peak observed for the rod-like nanoparticles. This was regarded as an indication that the two morphologies being compared are distinctively different.

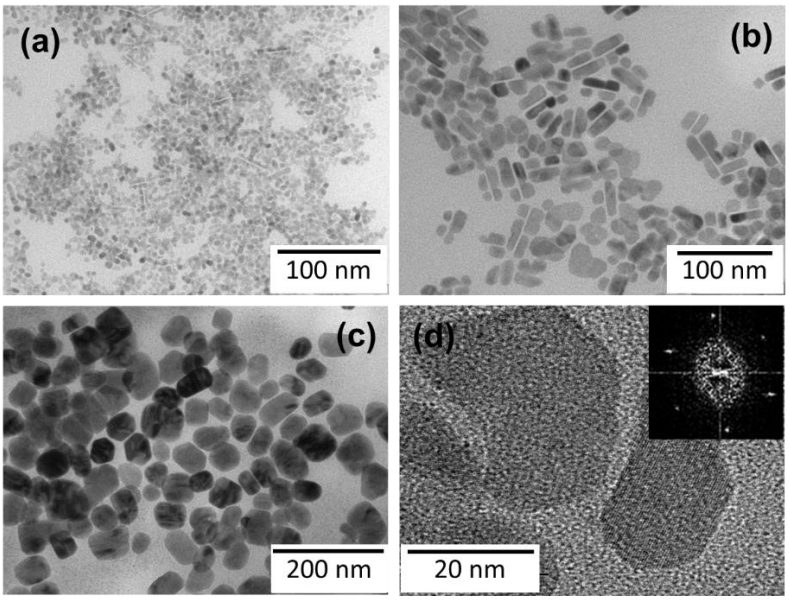

Figure 2.11: TEM images of CdS nanoparticles synthesized using SSP (**1**) at (a) 190 °C, (b) 230 °C and (c) 270 °C reaction temperatures; (d) HRTEM image of nanoparticles prepared at 270 °C (inset: SAED image) of CdS nanoparticles.

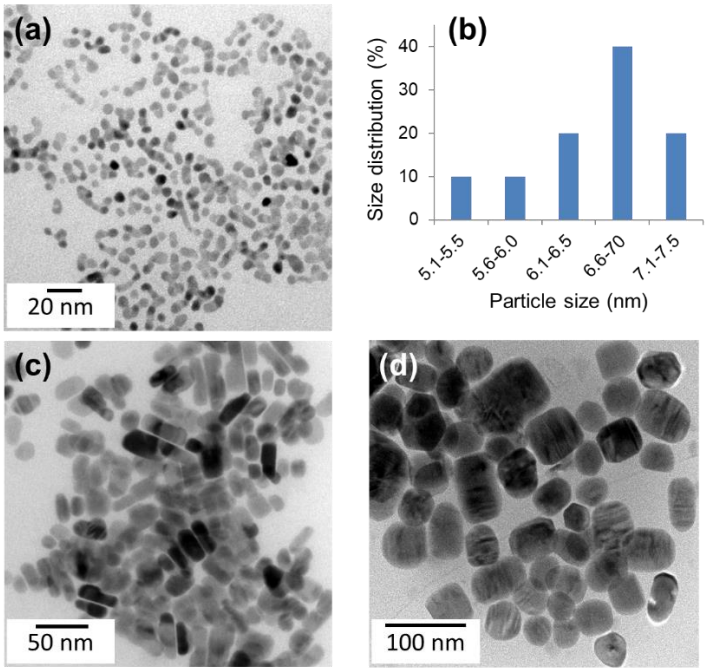

Figure 2.12: TEM images of CdS nanoparticles synthesized using SSP (**2**) at (a) 190 °C, (c) 230 °C and (d) 270 °C reaction temperatures; (b) particle size distribution of particles synthesized at 190 °C.

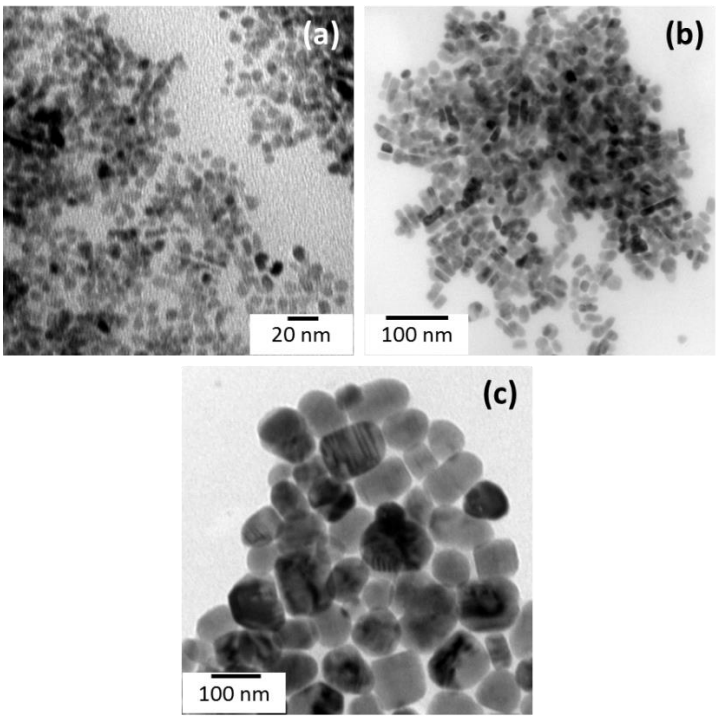

Figure 2.13: TEM images of CdS nanoparticles synthesized using SSP (**3**) at (a) 190 °C, (b) 230 °C, and (c) 270 °C reaction temperatures.

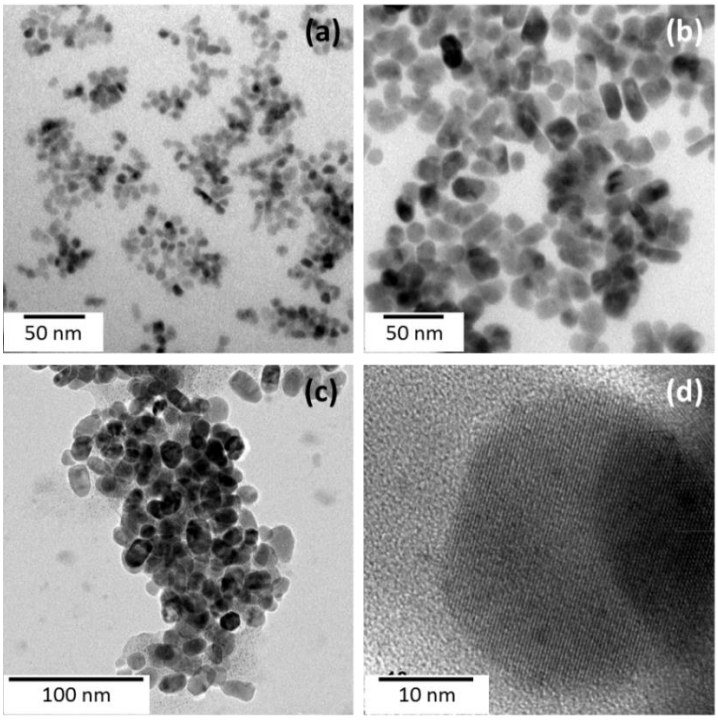

Figure 2.14: TEM images of CdS nanoparticles synthesized using SSP (**4**) at (a) 190 °C, (b) 230 °C, (c) 270 °C reaction temperatures, and the HR-TEM micrograph for nanoparticles obtained at 270 °C.

The morphologies observed in the nanoparticles obtained from the $CdCl_2$ series are common for CdS nanoparticles. The CdI_2 series, however, displayed interesting morphological features which are either rare or have not been encountered in previous CdS literature reports. The nanoparticles mostly formed nanodendrites which proceed to form chain-like structures at higher temperatures, 230 °C and 270 °C, Figure 2.15-2.18. These nanodendrites were constructed of nanoparticles exhibiting cubic and rod-like shapes. The difference in morphological features of the nanoparticles obtained from $CdCl_2$ and CdI_2 groups can be seen clearly in Figure 2.19. SSP (**8**) deviates from the nanodendrite trend, however, there is evidence of orientated attachment where irregular nanocubes predominately formed short chains.

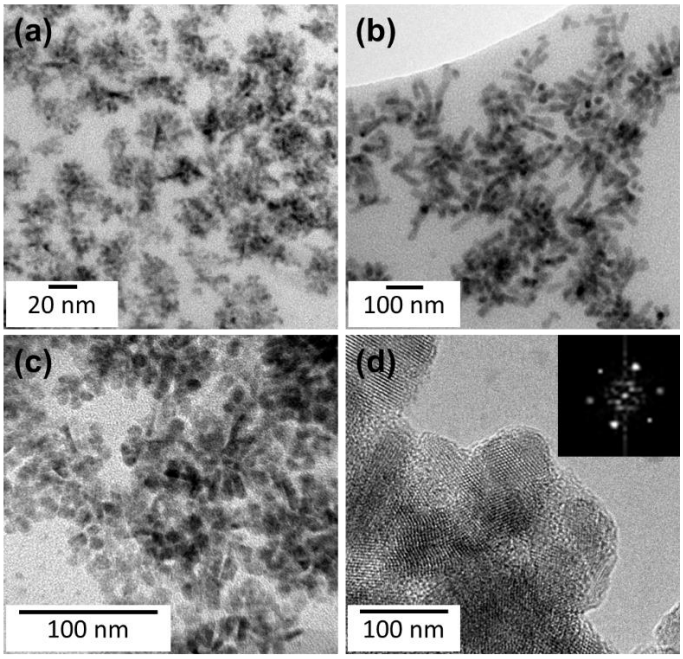

Figure 2.15: TEM images of CdS nanoparticles synthesized using SSP (**5**) at (a) 190 °C, (b) 230 °C and (c) 270 °C reaction temperatures; (d) HRTEM image (inset: SAED image) show the highly crystalline nature of CdS synthesized at 270 °C.

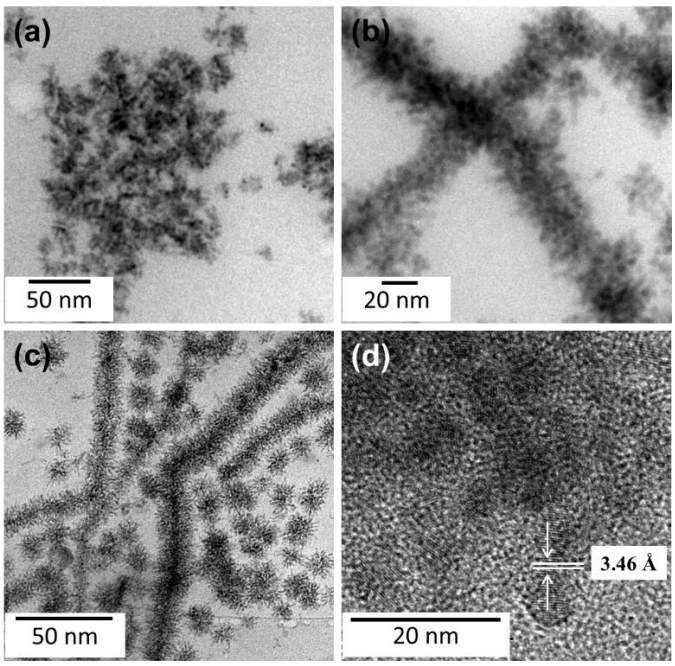

Figure 2.16: TEM images of CdS nanoparticles synthesized using SSP (**6**) at (a) 190 °C, (b) 230 °C and (c) 270 °C reaction temperatures; (d) HRTEM image of nanoparticles synthesized at 270 °C.

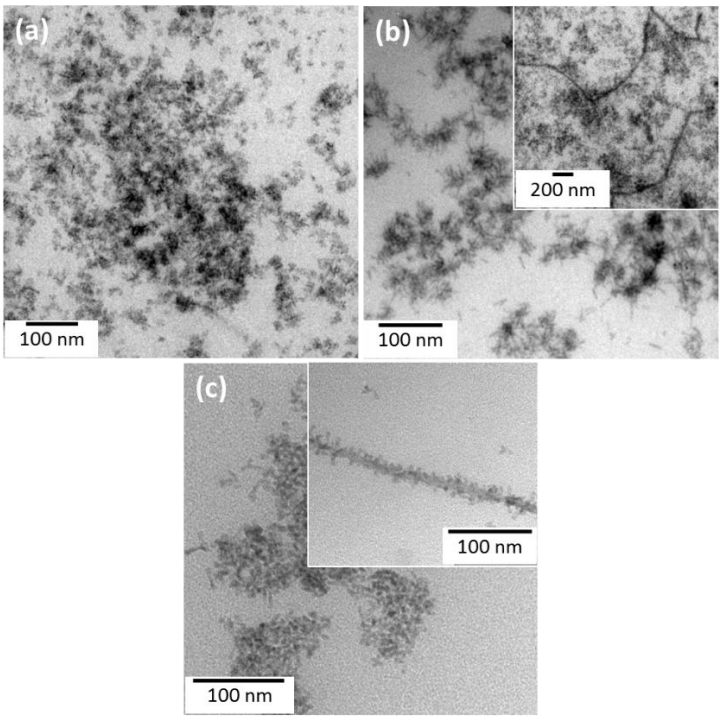

Figure 2.17: TEM images of CdS nanoparticles synthesized using SSP (**7**) at (a) 190 °C, (b) 230 °C, and (c) 270 °C reaction temperatures.

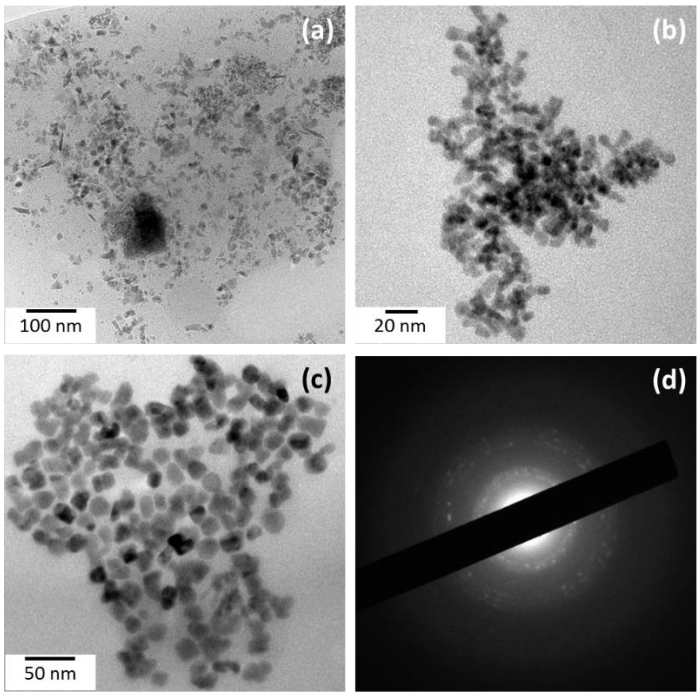

Figure 2.18: TEM images of CdS nanoparticles synthesized using SSP (**8**) at (a) 190 °C, (b) 230 °C, (c) 270 °C reaction temperatures, and the (d) SAED image for nanoparticles obtained at 270 °C.

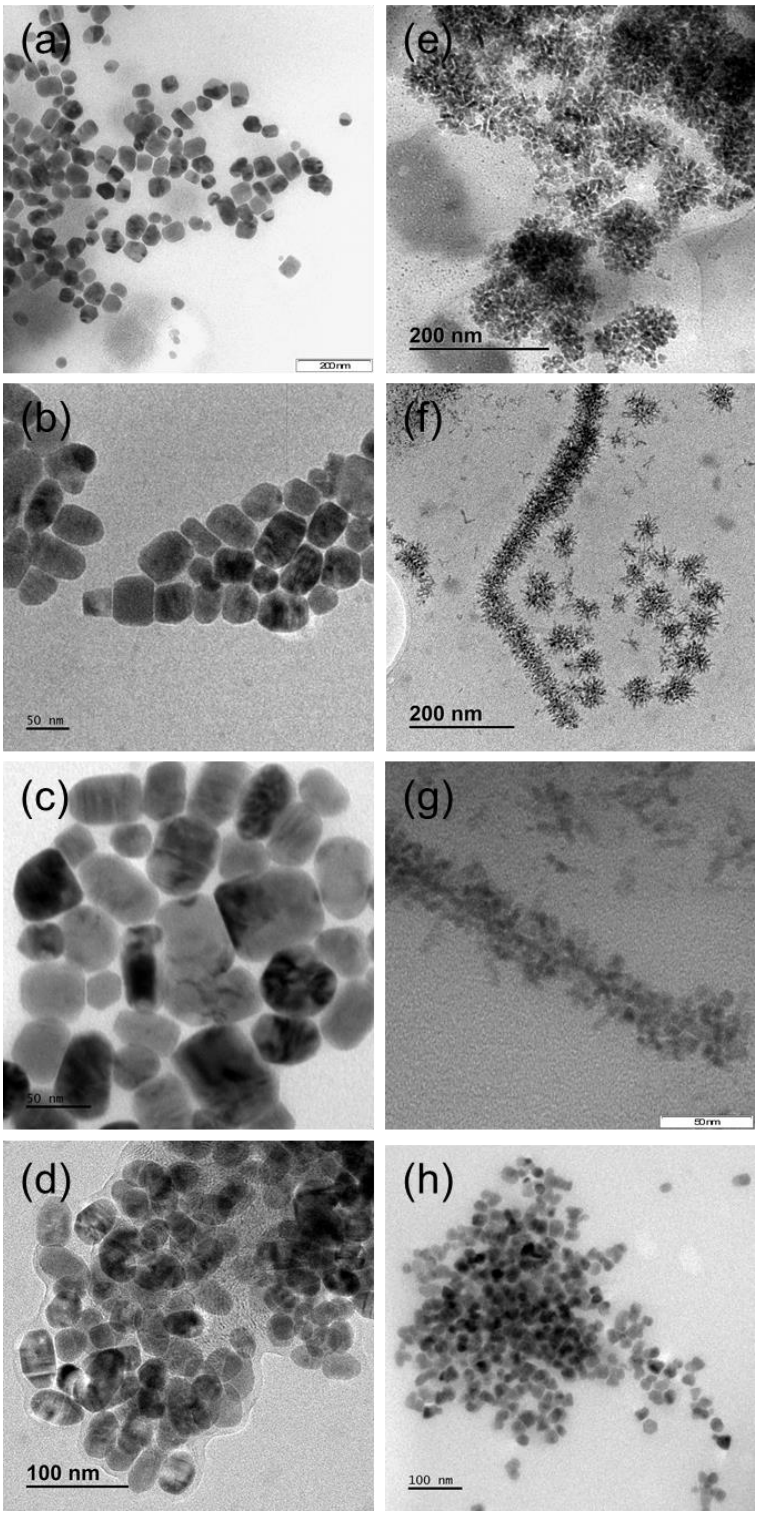

Figure 2.19: TEM images of CdS nanoparticles obtained at 270 °C from the $CdCl_2$ group (a) SSP (**1**), (b) SSP (**2**), (c) SSP (**3**) and (d) SSP (**4**), as well as the corresponding CdI_2 group (e) SSP (**5**), (f) SSP (**6**), (g) SSP (**7**) and (h) SSP (**8**).

The observed features of the particles could be a result of the presence, and possible influence, of the halide ions in the SSPs. It has been reported that halide ions are capable of capping CdE (E = Se, Te) and PbSe particles, by simply etching and replacing the chalcogenide atoms on the surface.[25] Other reports suggest that the incorporation of halogens in the capping ligands greatly influences the structural transformation of nanoparticles. Meyns *et al*.[15] reported the evolution of CdSe nanorods into hexagonal pyramids when halogenated additives were present. The halogenated additives facilitate the dynamic adsorption/desorption processes of the ligands. The changes in the surface energy of the particles promote the formation of pyramidal structures. In this work, however, there was no evidence of halogen capping in the as-prepared CdS nanomaterials, according to HRTEM and energy-dispersive X-ray (EDX) spectroscopy, Figure 2.20. It could be argued that the observed properties, in particular the morphology, may also be influenced by the difference in dissociation energies of the Cd–X bonds.[26] Alternatively and/or additionally, the morphological changes may have resulted from the influence of the halogen incorporated in the organic ligands in the case of SSPs (**2**), (**3**), (**6**) and (**7**). The steric factors imposed by the thiosemicarbazone ligands (especially the phenyl moieties) cannot be ignored as they also play a role in the decomposition of the SSP. Nevertheless, it is the ions that cause changes to the surface energy though adsorption and desorption, and thereby influence anisotropic growth.

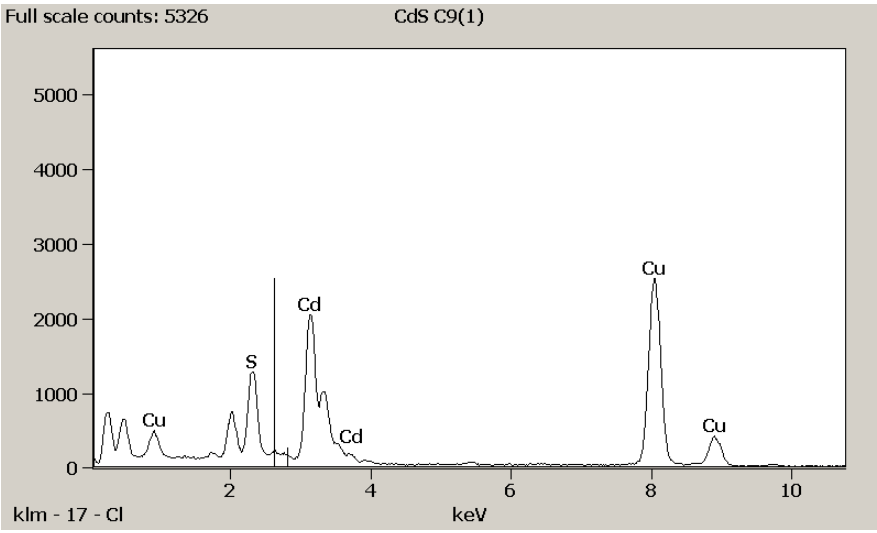

Figure 2.20. EDX spectrum of CdS nanoparticles synthesized from SSP (**6**) at 270 °C.

In correlation to the morphological properties and the particle sizes from the TEM images, the CdI_2 group affords relatively smaller nanoparticles. Regardless of this, both $CdCl_2$ and CdI_2 groups showed a common trend which instigated an increase in particle size with temperature. High reaction temperatures favour the activation energy for nucleation rather than for particle growth. As a result, higher nucleation rates produce a larger population of nuclei, which subsequently compete for the remaining SSP in growth processes. Owing to faster depletion of the SSP, the high temperature conditions promote the Ostwald ripening process, in which larger nanoparticles grow at the expense of smaller ones, and thereby both the average size and the size distribution of the particles are increased. This phenomenon is a common particle growth mechanism, especially in the hot-injection method and related.

The size-dependant optical properties theory is well known, and perhaps the main motivation towards the field. The band gap of the material increases with a decrease in particle size, due to quantum confinement effects. There are other factors that play a crucial role in the electronic properties of the nanoparticles, such as the morphology, as previously stated in this report in the case of QP's versus short rod-like nanoparticles. As such, this work studied the effect of reaction temperature and type of SSP on the optical properties of the as-prepared nanoparticles. An ideal trend in optical properties is illustrated in Figure 2.21 (i) and (ii) where the nanoparticles obtained from SSP (**3**) exhibit absorption edges (and corresponding estimated band gap energies) of 517 nm (2.60 eV), 769 nm (1.98 eV) and >800 nm (1.92 eV) at increasing reaction temperatures of 190 °C and 230 °C and 270 °C, respectively. However, there are cases where the nanoparticles deviate from the trend, as observed from SSP (**4**) in Figure 2.21 (iii) and (iv) where 510 nm (2.51 eV), 566 nm (2.35 eV) and 528 nm (2.44 eV) are observed at 190 °C and 230 °C and 270 °C, respectively. The spectra obtained from the nanoparticles synthesized from other SSPs are provided in Figure 2.22 and the corresponding estimated band gap energies in Table 2.3.

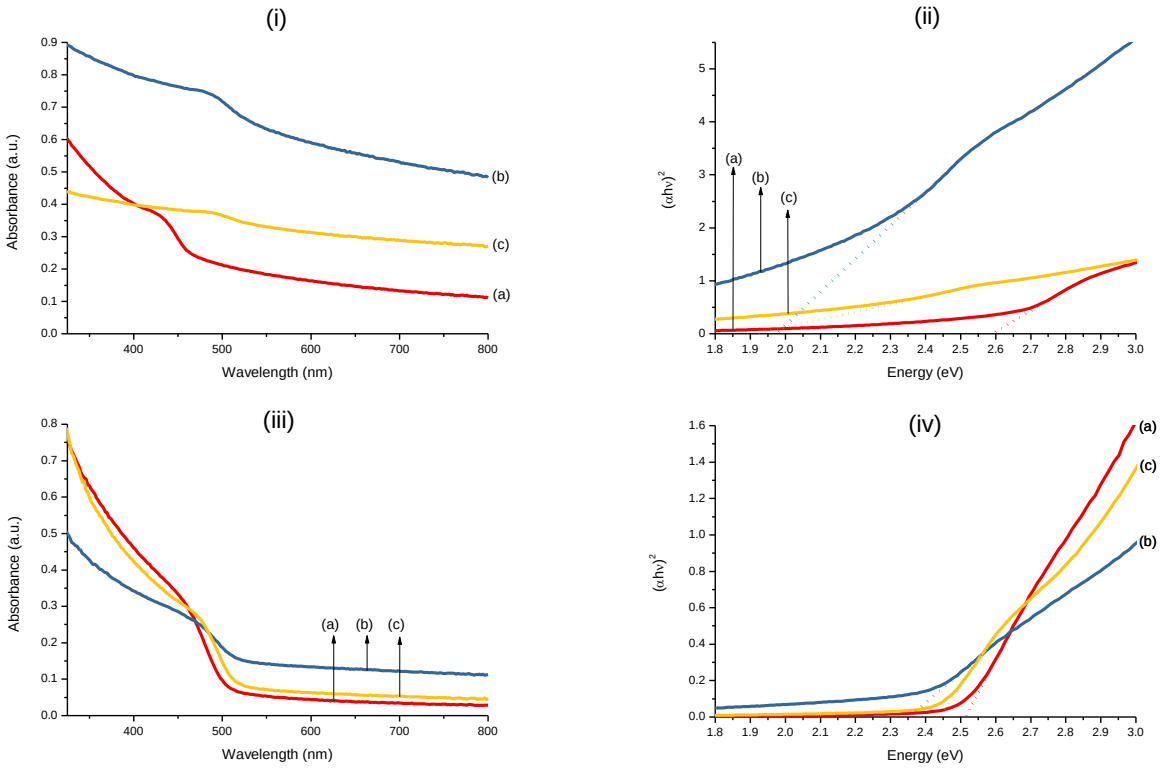

Figure 2.21: (i) The UV-Vis spectra and (ii) corresponding Tauc plots obtained from SSP (**3**), as well as (iii) the UV-Vis spectra and (iv) corresponding Tauc plots obtained from SSP (**4**) at (a) 190 °C, (b) 230 °C and (c) 270 °C reaction temperatures.

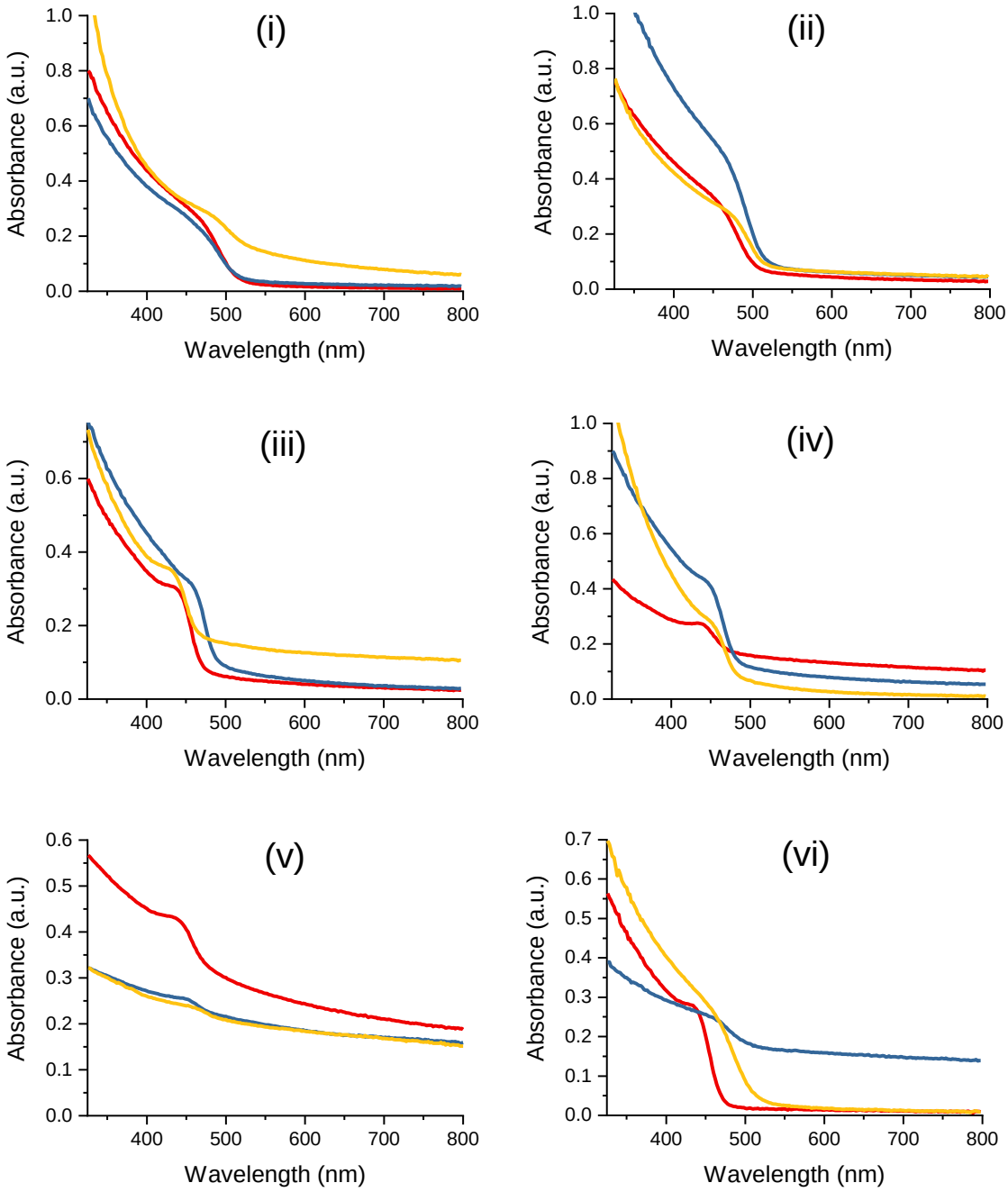

Figure 2.22: The UV-Vis spectra of oleylamine-capped CdS nanoparticles obtained from (i) SSP (**1**), (ii) SSP (**2**), (iii) SSP (**5**), (iv) SSP (**6**), (v) SSP (**7**) and (vi) SSP (**8**) at 190°C (red), 230 °C (blue) and 270 °C (orange) reaction temperatures.

Apart from particle size, there are other factors that influence the optical properties, such as an inefficient passivation of the nanoparticles by a capping agent which consequently results to undesirable agglomeration. Inconsistent injection rate of the SSP, or even the nature of the SSP may be contributing factors. Regardless of this, the band gap of the material is tailored for a specific application. With CdS, a wider band gap is mostly pursued, due to exploitation in optoelectronic applications such as solar cells. From our study, we observed that wider (or in appropriate terms, blueshifted from bulk CdS) band gap energies predominate at 190 °C reaction temperature. It was clearly demonstrated in Figure 2.23 that the nature of the phenyl moiety influences the optical properties. However, the halide ligands display a pronounced influence as compared to the thiosemicarbazone ligands, i.e. the CdI_2 (**5**)-(**8**) SSPs produce nanoparticles that exhibit absorption edges at higher energy region of 483 ± 21 nm compared to 519 ± 5 nm the $CdCl_2$ (**1**)-(**4**) SSP. Furthermore, the narrower bands observed in the CdI_2 series is typical of monodispersity or narrow particle size distribution.

The complete analyses on particle size from TEM images and optical properties of the nanoparticles are provided in Table 2.3.

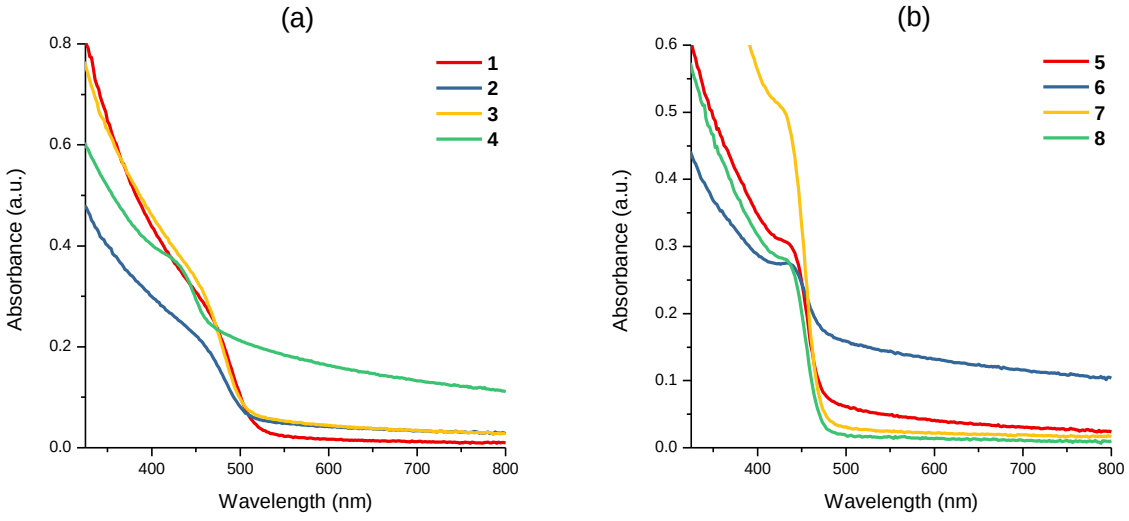

Figure 2.23: The UV-Vis spectra of oleylamine-capped CdS nanoparticles synthesized at 270 °C from (a) $CdCl_2$ (**1**)-(**4**), and (b) CdI_2 (**5**)-(**8**) SSPs.

Table 2.3: The properties of oleylamine-capped nanoparticles estimated from UV-Vis spectroscopy and TEM imaging.

SSP	Reaction temperature [°C]	Absorption edge [nm]	Absorption band gap [eV]	Particle length (width or diameter) from TEM [nm]
	190	506	2.45	17.0 (6.81)
(**1**)	230	521	2.38	43.4 (15.0)
	270	521	2.38	– (48.9)
	190	500	2.48	– (6.52)
(**2**)	230	512	2.42	32.6 (11.2)
	270	528	2.35	– (36.2)
	190	517	2.60	– (6.60)
(**3**)	230	769	1.98	32.2 (12.1)
	270	>800	1.92	– (56.8)
	190	510	2.51	– (8.64)
(**4**)	230	566	2.35	28.3 (13.5)
	270	528	2.44	– (44.6)
	190	472	2.63	–
(**5**)	230	472	2.63	35.2 (5.68)
	270	488	2.54	–
	190	469	2.64	–
(**6**)	230	481	2.58	–
	270	481	2.58	16.8 (4.20)
	190	556	2.46	–
(**7**)	230	644	2.26	–
	270	720	2.16	– (21.3)
	190	471	2.68	–
(**8**)	230	589	2.37	– (7.26)
	270	518	2.50	– (19.2)

Following the interesting influence of the halide ligands, a pilot study was conducted whereby iodide-containing compounds were deliberately added to SSP (**3**), in pursuit of understanding the formation of nanodendrite structures in SSP (**7**) and all other CdI_2 SSPs used. Two iodide sources were used: the inorganic potassium iodide (KI), and organic methyl iodide (MeI) compounds. The reaction protocols used to prepare the nanoparticles are similar to those outlined in section 2.2.3, with minor modifications which entail the dispersion of SSP (**3**) together with either KI or MeI (four moles equivalent) in tri-*n*-octylphosphine. The resulting mixture was then injected in oleylamine preheated at mid-temperature 230 °C.

The pilot study did not produce nanodendrite structures. The nanoparticles from the MeI-incorporated reaction exhibit smaller (irregular spheres) and larger (hexagonal) particle sizes, while the KI reaction produces irregular spheres of similar dimensions to the ones from MeI. Additionally, these morphologies observed in Figure 2.24 are still different from the rod-like morphology observed in SSP (**3**) alone at the same reaction temperature. Therefore, it can be concluded that the formation of the nanodendrite structures prefer the iodido species to be bonded to the Cd(II) centre rather than ionic species in the reaction, assuming both KI and MeI dissociate to release I^- anions.

Interestingly, the p-XRD patterns of the KI-incorporated reaction reveals that KCl by-product is formed in addition to the anticipated CdS. The evidence is provided in Figure 2.25 (i), where the peaks denoted with * are indexed to KCl (card no. 00-041-1476). However, it could not be deduced whether KCl forms through ligand exchange mechanism or by simply scavenging the Cl^- anions. In the case of the latter, it presented an additional uncertainty on the origins of these Cl^- anions, which could be from the dissociation of the chloride ligands bonded to Cd(II) and/or decomposition of the 4-chlorobenzyl moiety in the thiosemicarbazone ligands. The p-XRD pattern of the MeI-incorporated reaction displayed similar characteristics to the nanoparticles obtained from SSP (**3**).

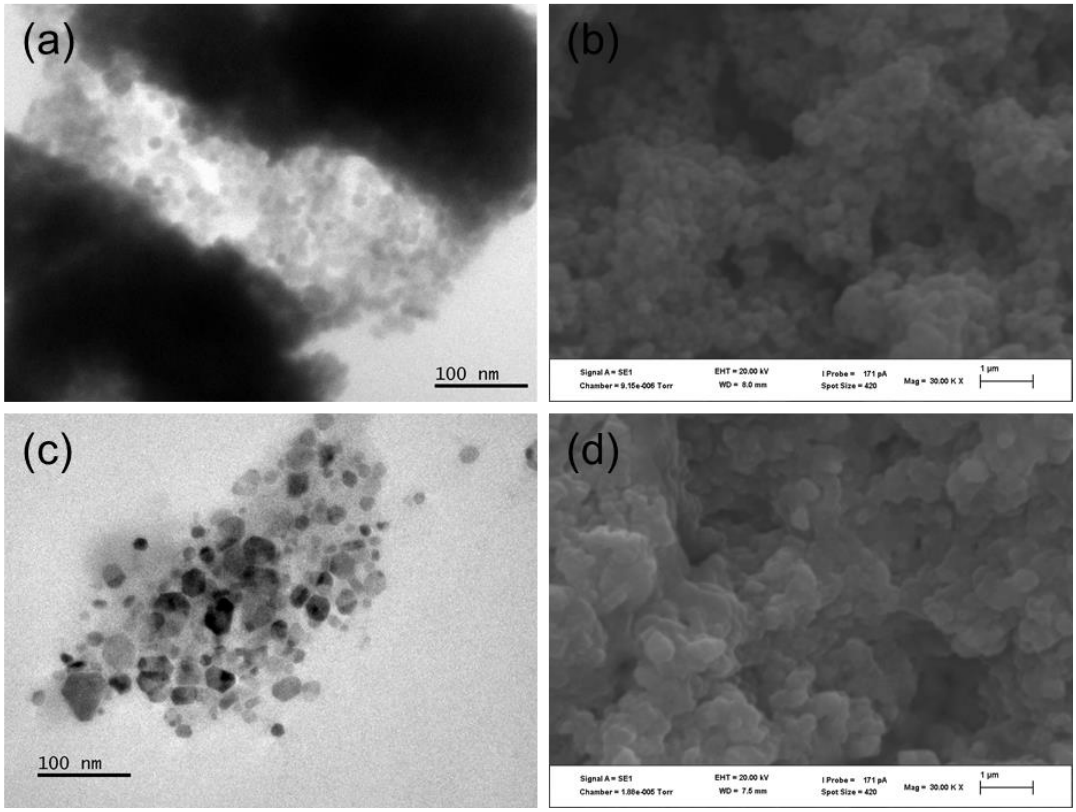

Figure 2.24: The (a) TEM and (b) scanning electron microscopy images of CdS nanoparticles prepared from SSP (**3**) with four-mole equivalent of KI, as well as four-mole equivalent of MeI in (c) and (d) images.

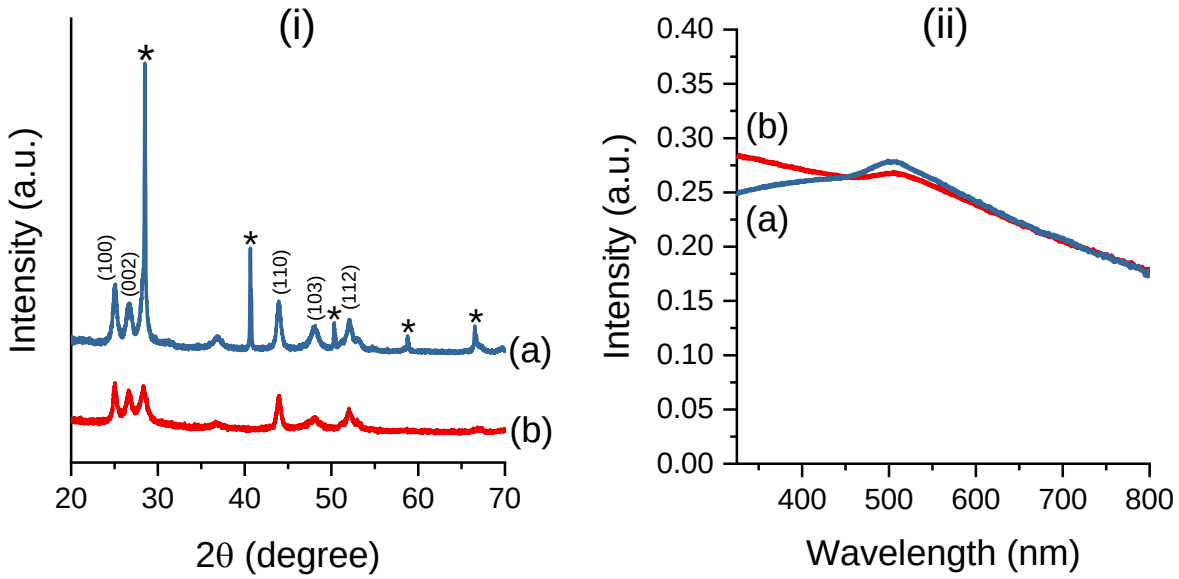

Figure 2.25: The (i) p-XRD patterns and (ii) UV-Vis spectra of CdS nanoparticles prepared from SSP (**3**) with four-mole equivalent of (a) KI and (b) MeI. * denotes reflection peaks identified as KCl (card no. 00-041-1476).

The optical properties of the nanoparticles from KI and MeI incorporated reactions were deemed inconclusive. The absorption edges could not be estimated from the UV-Vis spectra provided in Figure 2.25 (ii). The absorption edges seem to be >800 nm. What could be extracted is the absorption maxima which were found at 500 nm and 508 nm for KI and MeI reactions, respectively.

2.4 Conclusions

The work in this chapter has presented a route to oleylamine-capped CdS nanoparticles through solvothermal decomposition of eight Cd(II) thiosemicarbazone complexes as single-source precursors (SSPs). It was also demonstrated that both nanoparticle size and morphology control are temperature and structure-dependent, and a plausible growth mechanism has been discussed. The CdS products were analyzed by UV/Vis spectroscopy, TEM, HRTEM, EDX spectroscopy and powder XRD for determination of phase, crystallinity, composition, size and morphology. Blueshifted absorptions were consistently observed, analysis of which revealed quantum confinement phenomena of the CdS particles. The dependence of their shape and size variation on reaction temperature and SSP composition was also studied. For the first time, to the best of our knowledge, this work further presented the influence of halide ligands on the formation of nanoparticles, in the context of SSPs. The presence of iodido ligands in SSPs (**5**)-(**8**) resulted in clusters of rod-shaped and branched strands of rod-like nanodendrite morphologies, whereas transformation from rod-like to cubic nanocrystals was achieved by using chlorido SSPs (**1**)-(**4**). The preliminary study of introducing external sources of iodide anions also presented a window of opportunity to tailor the properties, morphology and optical-based, among others.

References

[1] a) L. X. Reynolds, T. Lutz, S. Dowland, A. MacLachlan, S. King, S. A. Haque, *Nanoscale* **2012**, *4*, 1561. b) P.-F. Yin, T. Ling, Y.-R. Lu, Z.-W. Xu, S.Z. Qiao, X.-W. Du, *Adv. Mater.* **2015**, *27*, 740. c) F. Cao, H. Wang, Z. Xia, X. Dai, S. Cong, C. Dong, B. Sun, Y. Lou, Y. Sun, J. Zhao, G. Zou, *Mater. Chem. Phys.* **2015**, *149–150*, 124–128.

[2] a) S. Nizamoglu, E. Mutlugun, O. Akyuz, N. K. Perkgoz, H. V. Demir, L. Liebscher, S. Sapra, N. Gaponik, A. Eychmüller, *New J. Phys.* **2008**, *10*, 023026. b) J. I. Wong, N. Mishra, G. Xing, M. Li, S. Chakrabortty, T. C. Sum, Y. Shi, Y. Chan, H. Y. Yang, *ACS Nano* **2014**, *8*, 2873. c) E. V. Kolobkova, D. S. Kukushkin, N. V. Nikonorov, A. I. Sidorov, T. A. Shakhverdov, *Glass Phys. Chem.* **2015**, *41*, 104.

[3] a) X. Fu, J. Liu, Y. Wan, X. Zhang, F. Meng, J. Liu, *J. Mater. Chem.* **2012**, *22*, 17782. b) S. T. Navale, A. T. Mane, M. A. Chougule, N. M. Shinde, J. Kim, V. B. Patil, *RSC Adv.* **2014**, *4*, 44547. c) L. Maserati, I. Moreels, M. Prato, R. Krahne, L. Manna, Y. Zhang, *ACS Appl. Mater. Interfaces* **2014**, *6*, 9517.

[4] a) K.-J. Wu, K.-C. Chu, C.-Y. Chao, Y.-F. Chen, *Nano Lett.* **2007**, *7*, 1908. b) K. Deng, L. Li, *Adv. Mater.* **2014**, *26*, 2619. c) K. Yuan, L. Chen, Y. Chen, *Chem. Eur. J.* **2014**, *20*, 11488.

[5] a) Y. Zhang, N. Zhang, Z.-R. Tang, Y.-J. Xu, *Chem. Sci.* **2012**, *3*, 2812. b) A. Girbeti, B. Fabbri, A. Gaiardo, V. Guidi, C. Malagù, *Appl. Phys. Lett.* **2014**, *104*, 222102. c) J. Xiong, W. Wu, Y. Liu, L. Shen, L. Wu, *J. Nanopart. Res.* **2015**, *17*, 55.

[6] a) T. Trindade, P. O'Brien, *Chem. Mater.* **1997**, *9*, 523530. b) B. Ludolph, M. A. Malik, P. O'Brien, N. Revaprasadu, *Chem. Commun.* **1998**, 1849. c) L. D. Nyamen, V. S. R. Pullabhotla, A. A. Nejo, P. Ndifon, N. Revaprasadu, *New J. Chem.* **2011**, *35*, 1133. d) L. D. Nyamen, N. Revaprasadu, R. V. S. R. Pullabhotla, A. A. Nejo, P. T. Ndifon, M. A. Malik, P. O'Brien, *Polyhedron* **2013**, *56*, 62. e) S. Mlowe, D. J. Lewis, M. A. Malik, J. Raftery, E. B. Mubofu, P. O'Brien, N. Revaprasadu, *New J. Chem.* **2014**, *38*, 6073.

[7] a) D. Barreca, A. Gasparotto, C. Maragno, R. Seraglia, E. Tondello, A. Venzo, V. Krishnan, H. Bertagnolli, *Appl. Organomet. Chem.* **2005**, *19*, 59. b) D. C. Onwudiwe, A. D. Mohammed, C. A. Strydom, D. A. Young, A. Jordaan, *Superlattices Microstruct.* **2014**, *70*, 98. c) L. Stroea, A. K. Bansal, I. D. W. Samuel, S. Kowalski, S. Allard, U. Scherf, L. Ortolani, S. Cavallini, S. Toffanin, F. Antolini, *Sci. Adv. Mater.* **2015**, *7*, 1.

[8] a) M. J. Moloto, P. O'Brien, M. A. Malik, N. Revaprasadu, *J. Mater. Sci. Mater. Electron.* **2004**, *15*, 313. b) N. Moloto, N. Revaprasadu, M. J. Moloto, P. O'Brien,

M. Helliwell, *Polyhedron* **2007**, *26*, 3947. c) J. D. Patel, F. Mighri, A. Ajji, T. K. Chaudhuri, *J. Nanosci. Nanotechnol.* **2015**, *15*, 2733.

[9] C. Byrom, M. A. Malik, P. O'Brien, A. J. P. White, D. J. Williams, *Polyhedron* **2000**, *19*, 211.

[10] D. Fan, M. Afzaal, M. A. Malik, C. Q. Nguyen, P. O'Brien, P. J. Thomas, *Coord. Chem. Rev.* **2007**, *251*, 1878.

[11] M. Green, *J. Mater. Chem.* **2010**, *20*, 5797.

[12] Y. Yin, A. P. Alivisatos, *Nature* **2005**, *437*, 664.

[13] M. Saruyama, M. Kanehara, T. Teranishi, *J. Am. Chem. Soc.* **2010**, *132*, 3280.

[14] M. J. Greaney, E. Couderc, J. Zhao, B. A. Nail, M. Mecklenburg, W. Thornbury, F. E. Osterloh, S. E. Bradforth, R. L. Brutchey, *Chem. Mater.* **2015**, *27*, 744.

[15] M. Meyns, F. Iacono, C. Palentia, J. Geweke, M. D. Coderch, U. E. A. Fittschen, J. M. Gallego, R. Otero, B. H. Juárez, C. Klinke, *Chem. Mater.* **2014**, *26*, 1813.

[16] F. Lacono, C. Palencia, L. de la Cueva, M. Meyns, L. Terracciano, A. Vollmer, M. de la Mata, C. Klinke, J. M. Gallego, H. B. Juárez, R. Otero, *ACS Nano* **2013**, *7*, 2559.

[17] J. Tang, K. W. Kemp, S. Hoogland, K. S. Jeong, H. Liu, L. Levina, M. Furukawa, X. Wang, R. Debnath, D. Cha, K. W. Chou, A. Fischer, A. Amassian, J. B. Asbury, E. H. Sargent, *Nat. Mater.* **2011**, *10*, 765.

[18] S. D. Disale, S. S. Garje, *Adv. Sci. Lett.* **2010**, *3*, 80.

[19] A. M. Palve, S. S. Garje, *Polyhedron* **2013**, *61*, 195.

[20] P. Anastas, N. Eghbali, *Chem. Soc. Rev.* **2010**, *39*, 301.

[21] F. E. Anderson, C. J. Duca, J. V. Scudi, *J. Am. Chem. Soc.* **1951**, *73*, 4967.

[22] S. D. Disale, S. S. Garje, *Adv. Sci. Lett.* **2010**, *3*, 80.

[23] A. M. Palve, S. S. Garje, *Polyhedron* **2013**, *61*, 195.

[24] Y. Wang, Y. Zhou, Y. Zhang, W. Buhro, *Inorg. Chem.* **2015**, *54*, 1165.

[25] a) K. Bae, J. Joo, L. A. Padilha, J. Won, D. C. Lee, Q. Lin, W.-K. Koh, H. Luo, V. I. Klimov, J. M. Pietryga, *J. Am. Chem. Soc.* **2012**, *134*, 20160. b) R. C. Page, D. Espinobarro-Velazquez, M. A. Leontiadou, C. Smith, E. A. Lewis, S. J. Haigh, C. Li, H. Radtke, A. Pengpad, F. Bondino, E. Magnano, I. Pis, W. R. Flavell, P. O'Brien, D. J. Binks, *Small* **2014**, *11*, 1548.

[26] J. A. Dean, *Lange's Handbook of Chemistry*, 15th ed., McGraw-Hill, New York, **1999**, p 4.42.

CHAPTER 3

3 The influence of the halide ligands in Pb(II) thiosemicarbazone complexes on the properties of PbS nanoparticles

3.1 Introduction

Lead sulfide (PbS) is a group IV–VI semiconducting material which has received unprecedented attention over the last decade, owing to its tunable electronic and morphological properties.[1–3] Regardless of its toxic nature,[4] PbS has unique quantization effects, properties which are accompanied by a direct band gap of 0.41 eV at 300 K, and a large excitonic Bohr radius of 18 nm.[5–7] These interesting properties have captured the attention of researchers, who have explored many synthetic routes and applications of this material.[8–10] PbS in the nano-size regime also exhibits interesting physical and chemical properties. A good example is the tuning of its broad, near infrared band edge to the ultra violet range through the engineering of the particle size and morphology. This is an important feature for optoelectronic devices which allows the material to harness energy within this broad range.[11] For this purpose, PbS nanomaterials have potential applications in solar cells,[12] NIR communications,[11, 13] thermal and biological imaging,[14] tuneable near infrared detectors[15] and light emitting diodes[16].

Synthesis protocols for PbS nanostructures, can utilize either multiple or single source precursors (SSPs).[6, 17–25] Joo *et al*.[21], for example used lead chloride and sulfur dissolved in oleylamine as dual sources to synthesize PbS particles. The use of SSPs has recently been preferred for size and shape-control, due to high quality materials obtained previously.[6, 22–25] This is easily achieved through the decomposition or disintegration of the SSP, which is usually a metal–organic compound bearing the preformed metal–chalcogen bonds. Furthermore, the SSPs have the advantage of ascertained purity and stability under ambient conditions, as well as the omission of pre-reactions prior to nanomaterial-based fabrication processes. The majority of the work on lead complexes used as SSPs for PbS nanostructures has been dominated by thiolates such as dithiocarbamates, xanthates and thiosermicarbazides.[6, 19, 25, 26] Other similar compounds continue to receive

considerable attention mainly in other fields of research. For example, thiosemicarbazones which predominate in biological applications.[27, 28] Garje and co-workers have explored the use of these compounds as ligands for various metal complexes.[29–33]

Although diverse fabrication protocols have been established for PbS nanomaterials,[20, 23, 24, 34–37] very few allow easy access to size, shape and morphology control. As a result, solvent-based fabrication protocols such as the solvothermal method,[38–40] address this issue by employing coordinating solvents which play a major role in: (i) lowering the decomposition temperature, and (ii) stabilizing nanomaterials during and after fabrication. Many coordinated solvents have been explored to achieve this, including non-toxic cetytrimethylammonium bromide (CTAB) and polyethylene glycol 400 (PEG-400).[38] Long alkyl chain amines such as hexadecylamine and oleylamine, have taken precedence due to high efficiency in producing good quality nanostructures.[41, 42]

Size and morphology control, in the context of SSPs, has mainly focused on organic ligands which can either be constituents within the SSPs or the capping agents.[2, 43, 44] Recent work has identified the addition of halogenated compounds to synthesis protocols as a means to control size, shape and phase of nanoparticles.[45, 46] Klinke *et al*.[46] investigated the morphology, size and phase of CdSe nanoparticles through the influence of the chemical structure and type of halogen atom introduced into the reaction. Very few reports have focused on inorganic ligands incorporated in the chemical structures of SSPs. To the best of the our knowledge, these reports have been restricted to common anionic ligands such as Cl^-, CH_3COO^-, NO_3^-, SO_4^{2-}, PF_6^-, BPh_4^- and BF_4^- on Zn^{2+}, Ni^{2+}, Ce^{2+}, In^{3+}, Co^{2+}, Cu^+, Rh^0 and Cd^{2+} metal centres ([47], and references therein). However, studies that concentrate on the halogen series are rare, hence the work outline in chapter 2 and a recent report[48] provided an opportunity towards this direction. Both sources demonstrated the size, shape and morphology control on CdS nanoparticles by altering the organic and halogen (Cl^- and I^-) components of the Cd(II)-thiosemicarbazone complexes.

The work outlined in this chapter was thus extended from chapter 2 and published work[48] to further study the morphological evolution and possible effect on

the properties of PbS nanoparticles, focusing on the broader halogen series (Cl^-, Br^- and I^-) complimented by a nonhalogenated precursor. The nanoparticles were prepared by the solvothermal decomposition of halogenated and non-halogenated Pb(II)-cinnamaldehyde thiosemicarbazone complexes in oleylamine at different reaction temperatures.

3.2 Experimental

3.2.1 Materials

Tri-*n*-octylphosphine and oleylamine were purchased from Sigma-Aldrich. Acetone, methanol, cyclohexane and hexane were purchased from Merck. Lead(II) acetate trihydrate and lead(II) iodide were procured from S D Fine-Chem, while lead(II) chloride and lead(II) bromide were procured from Alfa-Aesar. All chemicals were used as received.

3.2.2 Synthesis of complexes

The cinnamaldehyde thiosemicarbazone ligand and complexes were synthesized by previous methods outlined in references [48, 49] and section 2.2.2 of chapter 2, with minor modifications.

3.2.2.1 Preparation of bis(cinnamaldehyde thiosemicarbazone) lead(II) (9)

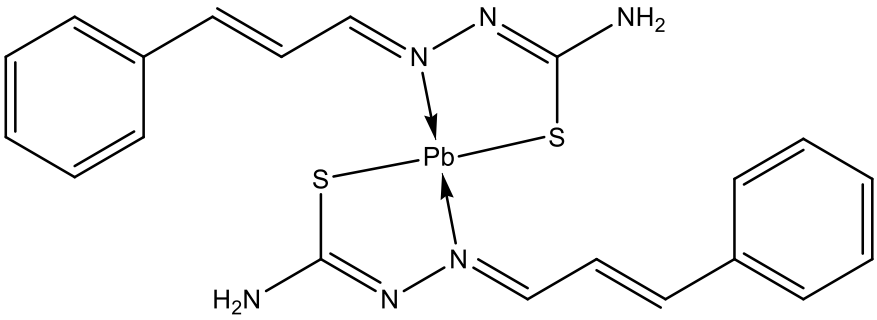

In a round-bottom flask, was dissolved $Pb(OAc)_2 \cdot 3H_2O$ (966 mg, 2.54 mmol) in dry methanol (15.0 mL). To this colourless solution, was added a solution of cinnamaldehyde thiosemicarbazone (1.04 g, 5.09 mmol) in dry methanol (25.0 mL), under vigorous stirring. The resulting pale green-coloured mixture was refluxed while stirring for 10 h. The mixture was then cooled to room temperature, prior to evaporating

the solvent under vacuum. The pale green solids were repeatedly washed with copious amounts of cyclohexane and n-hexane, in this order. The solid, complex (**9**), were dried under vacuum at room temperature. Yield: 1.16 g, 73.9%. m.p. 136 °C.

Elemental analyses for $PbC_{20}H_{20}N_6S_2$, % found (calcd): Pb: 33.90 (33.64). C: 39.32 (39.00). H: 3.14 (3.27). N: 13.38 (13.64). S: 10.18 (10.41).

IR: 3480, 3355 cm^{-1} (υ_{NH2} asym. and sym.), 1556 cm^{-1} (υ_{C-N}), 973 cm^{-1} (υ_{C-S}), 503 cm^{-1} (υ_{Pb-N}).

NMR (δ in ppm) ^{1}H: 6.89–8.05 (m, NH_2 + C_6H_5–CH=CH–CH=N), ^{13}C: 177.53 (C=S), 146.24 (CH=N), 138.00, 136.01 (CH=CH), 128.80, 128.59, 126.76, 125.65 (aromatic carbons).

3.2.2.2 Preparation of Bis(cinnamaldehyde thiosemicarbazone)lead(II) chloride (10)

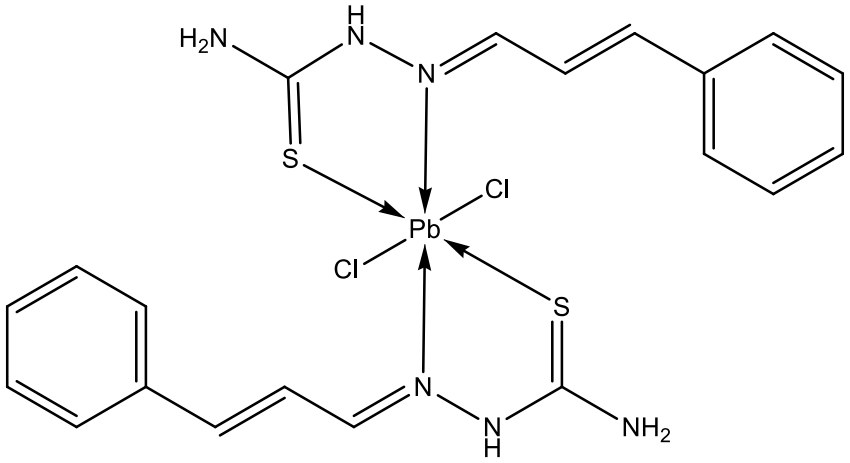

The reaction protocol used for the preparation of (**1**) in section 2.2.2.2 of chapter 2 was followed. The ligand, cinnamaldehyde thiosemicarbazone (1.19 g, 5.80 mmol) and $PbCl_2$ (807 mg, 2.90 mmol) were used. A yellow coloured complex (**10**) was formed, filtered, washed with copious amounts of deionised water, and then finally dried under vacuum. Yield: 1.46 g, 73.0%. m.p. 165 °C.

Elemental analyses for $PbCl_2C_{20}H_{22}N_6S_2$ (%) found (calcd): Pb: 30.47 (30.08). C: 35.10 (34.88). H: 3.42 (3.21). N: 12.08 (12.20). S: 9.18 (9.31). Cl: 10.54 (10.29).

IR: 3413 cm^{-1}, 3271 cm^{-1} (υ_{NH2} asymm. and symm.), 3161 cm^{-1} (υ_{N-H}), 1607 cm^{-1} (υ_{C-N}), 972 cm^{-1} (υ_{C-S}), 513 cm^{-1} (υ_{Pb-N}).

NMR (δ in ppm) ^{1}H: 6.82–8.16 (m, NH_2 + C_6H_5–CH=CH–CH=N), 11.39 (s, NH), $^{13}C\{^{1}H\}$: 177.63 (C=S), 144.70 (CH=N), 138.83, 135.83 (CH=CH), 128.84, 128.80, 126.88, 125.03 (aromatic carbons).

3.2.2.3 Preparation of Bis(cinnamaldehyde thiosemicarbazone)lead(II) bromide (11)

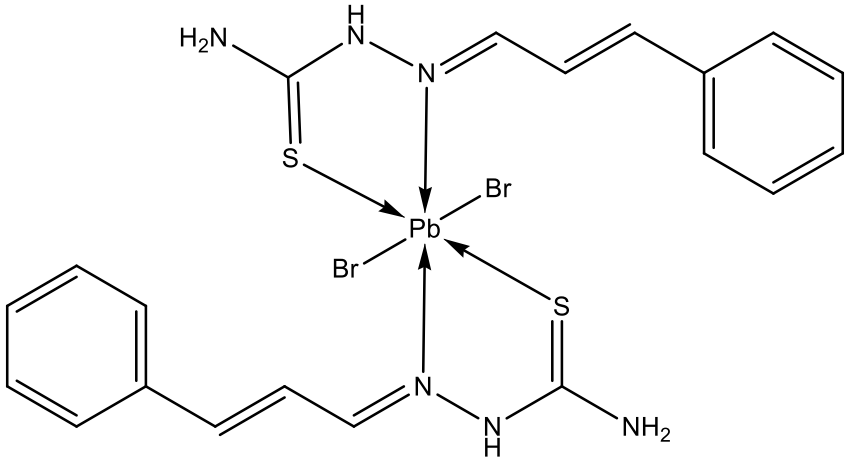

The reaction protocol used for the preparation of (**1**) in section 2.2.2.2 of chapter 2 was followed. Cinnamaldehyde thiosemicarbazone (1.41 g, 6.84 mmol) and $PbBr_2$ (1.26 g, 3.42 mmol) were used. A yellow coloured complex (**11**) was obtained. Yield: 2.19 g, 82.2%. m.p. 172 °C.

Elemental analyses for $PbBr_2C_{20}H_{22}N_6S_2$ (%) found (calcd): Pb: 26.79 (26.64), $C\{^{1}H\}$: 30.97 (30.89), H: 2.64 (2.85), N: 10.67 (10.80), S: 8.08 (8.24).

IR: 3422, 3276 cm^{-1} (u_{NH2} asym. and sym.), 3165 cm^{-1} (u_{N-H}), 1607 cm^{-1} (u_{C-N}), 973 cm^{-1} (u_{C-S}); 508 cm^{-1} (u_{Pb-N}).

NMR (δ in ppm) ^{1}H 6.82–8.17 (m, NH_2 + C_6H_5–CH=CH–CH=N), 11.39 (s, NH), ^{13}C: 177.61 (C=S), 144.71 (CH=N), 138.83, 135.82 (CH=CH), 128.84, 128.80, 126.88, 125.01 (aromatic carbons).

3.2.2.4 Preparation of Bis(cinnamaldehyde thiosemicarbazone)lead(II) iodide (12)

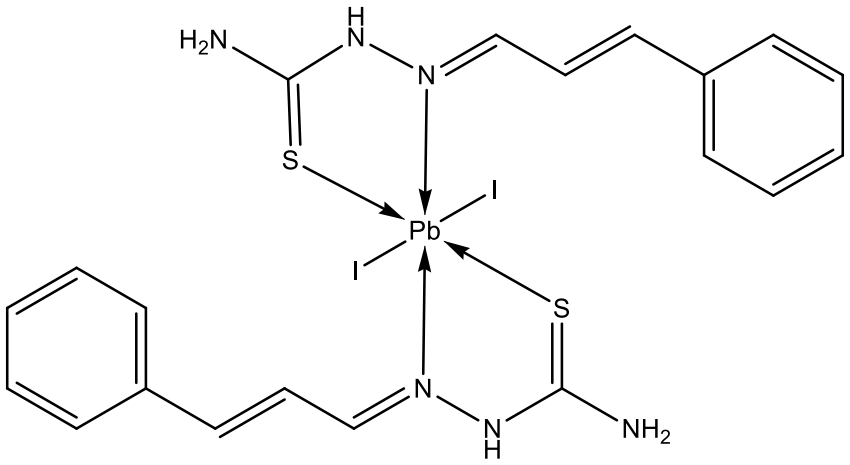

The reaction protocol used for the preparation of (**1**) in section 2.2.2.2 of chapter 2 was followed. Cinnamaldehyde thiosemicarbazone (1.11 g, 5.40 mmol) and PbI_2 (1.25 g, 2.70 mmol) were used. A yellow coloured complex (**12**) was obtained. Yield: 1.70 g, 72.0%. m.p. 224 °C.

Elemental analyses for $PbI_2C_{20}H_{22}N_6S_2$ (%) found (calcd): Pb: 23.25 (23.77).C: 27.94 (27.56). H: 2.24 (2.54). N: 9.32 (9.64). S: 7.12 (7.35).

IR: 3419, 3287 cm^{-1} (υ_{NH2} asymm. and symm.), 3181 cm^{-1} (υ_{N-H}), 1579 cm^{-1} (υ_{C-N}), 978 cm^{-1} (υ_{C-S}), 499 cm^{-1} (υ_{Pb-N}).

NMR (δ in ppm) ^{1}H: 6.82–8.16 (m, NH_2 + C_6H_5–CH=CH–CH=N), 11.39 (s, NH), $^{13}C\{^{1}H\}$: 177.60 (C=S), 144.69 (CH=N), 138.83, 135.83 (CH=CH), 128.85, 128.80, 126.88, 125.01 (aromatic carbons).

3.2.3 Synthesis of nanoparticles

The reaction protocol used in section 2.2.3 of chapter 2 was followed.

3.2.4 Characterisation techniques

The characterisation techniques and instrument specifications used in this chapter are outlined in detail in section 2.2.4 of chapter 2, with minor modifications as follows:

- TGA measurements were performed from 30 °C to 700 °C.
- Optical absorbance measurements were conducted at the UV-Vis-NIR spectral range on a Perkin-Elmer Lambda 1050 NIR UV-Visible spectrophotometer.
- EDX spectroscopy was performed on nanoparticles drop-casted on glass slides and subsequently carbon-coated using Quorum coater (Model Q150TE) prior to analyses.

3.3 Results and discussion

The study investigates the influence of halogen ligands on the decomposition behaviour of the Pb(II)-cinnamaldehyde thiosemicarbazone complexes (herein used as single-source molecular precursors, SSPs), which is subsequently monitored through size and morphology of PbS nanoparticles produced. Complementary to this, the SSPs were prepared from the PbX_2 (X = Cl, Br and I) series, as illustrated in Scheme 3.1a. The preparation protocols are adapted from the procedures which previously afforded the Cd(II) counterparts,[48] where the 1:2 (ligand to metal salt) is essential to form structurally-stable compounds. The hydrated lead acetate salt, $Pb(OAc)_2 \cdot 3H_2O$, was used to prepare a nonhalogenated SSP which would serve as a reference material, Scheme 3.1b. The structures of the SSPs were elucidated through the use of FT-IR and ^{1}H and $^{13}C\{^{1}H\}$ NMR spectroscopic data acquired from the SSPs (Figures A17–31 Appendix section).

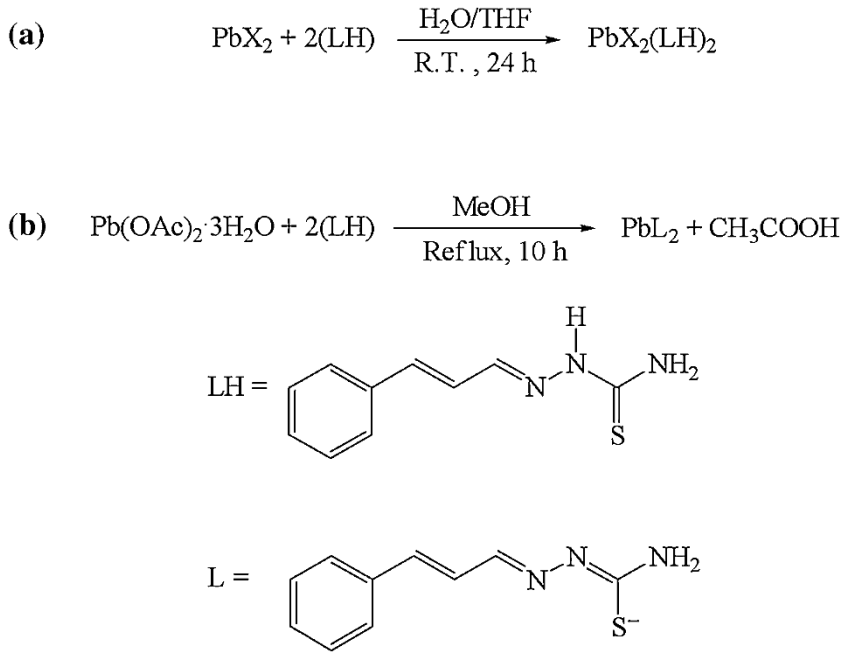

Scheme 3.1: The synthesis of (a) $[Pb(LH)_2X_2]$ and (b) $[PbL_2]$ SSPs.

A prominent band appearing at around 1625 cm^{-1} is typical of the azomethine (C=N) functional group.[50, 51] This is indicative of a successful condensation between the aldehyde and amino moieties, thus forming the desired cinnamaldehyde thiosemicarbazone ligand (Scheme 3.1). When the ligand is complexed to Pb salts, the υ(C=N) band shifts to lower wavenumbers by 10–15 cm^{-1}. This decrease in the wavenumbers for the azomethine group is attributed to metal ion chelation; [52–54] the electron deficient metal centre removing electron density from the ligand and lowering the bond order and hence vibrational frequency. A similar trend is observed for the secondary amine functional group which appears at 3156 cm^{-1} in the ligand. Interestingly, this υ(NH) band is absent in nonhalogenated-(**9**) SSP which thus prompts deprotonation. Due to this observation, accompanied by the absence of the acetate component in non-halogenated-(**9**) SSP (Figures A17 and A18 Appendix section), it was proposed that an acetic acid by-product is formed. A plausible mechanism is illustrated in Scheme 3.2.

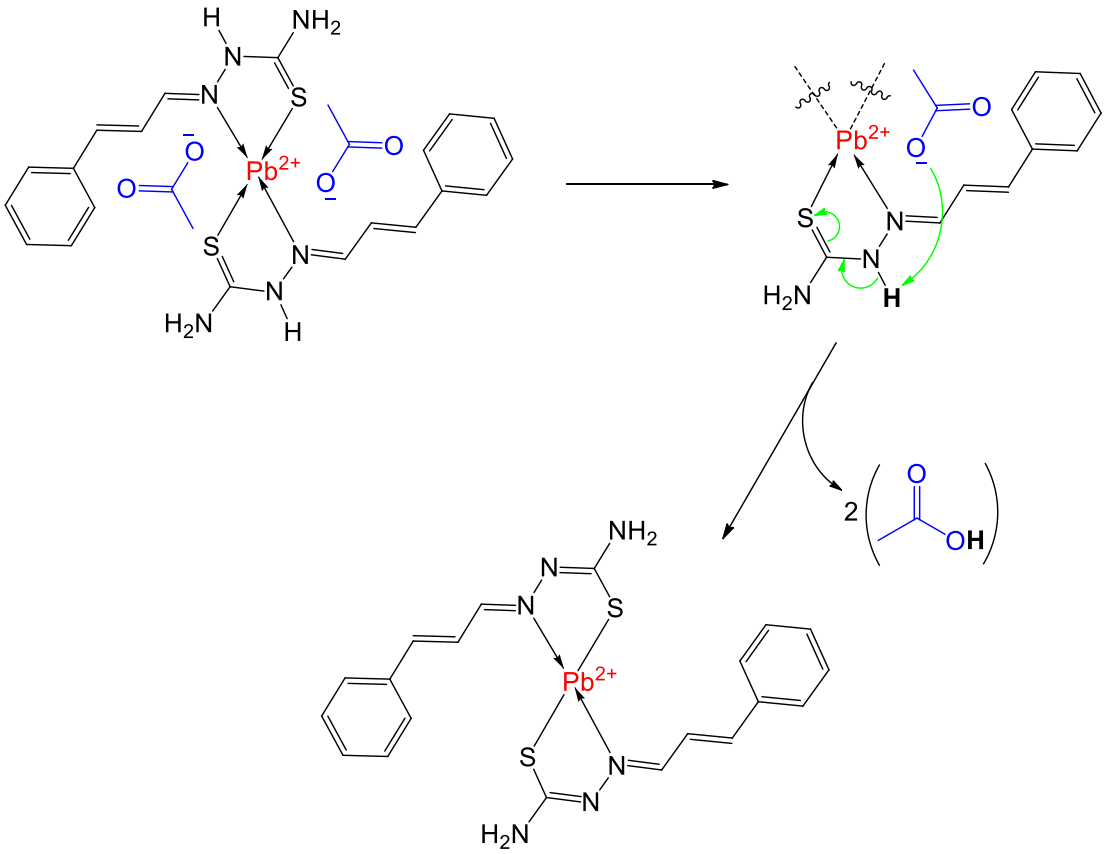

Scheme 3.2: Mechanism illustrating the formation of a nonhalogenated-(**9**) SSP.

The results from the elemental analysis and molar conductance studies on the SSPs corroborated with the spectroscopic data. The SSPs were found to be relatively pure, and the anticipated 1:2 metal to ligand stoichiometry was confirmed, as suggested by the elemental analysis data. Molar conductance readings were taken from the pre-made 10^{-3} M solutions of SSPs in dimethylformamide, and were recorded to be 13.5, 25.4, 19.5, and 14.8 Ω^{-1} cm^2 mol^{-1} for SSPs (**9**), (**10**), (**11**) and (**12**), respectively. These molar conductance readings are consistent with non-ionic adducts or uncharged complexes, i.e. nonelectrolyte properties.[55]

The halogen ligands have been found to exert an influence on the thermal stability of the SSPs, although no specific trend is observed (Figure 3.1a). The chlorido-(**10**) and iodido-(**12**) SSPs show two relatively clean decomposition patterns, whereas those of the remaining SSPs are undefined. Nonetheless, the solid residues retained from this thermogravimetric analysis study were matched to the PbS (card number: 00-005-0592) as shown in Figure 3.1b.

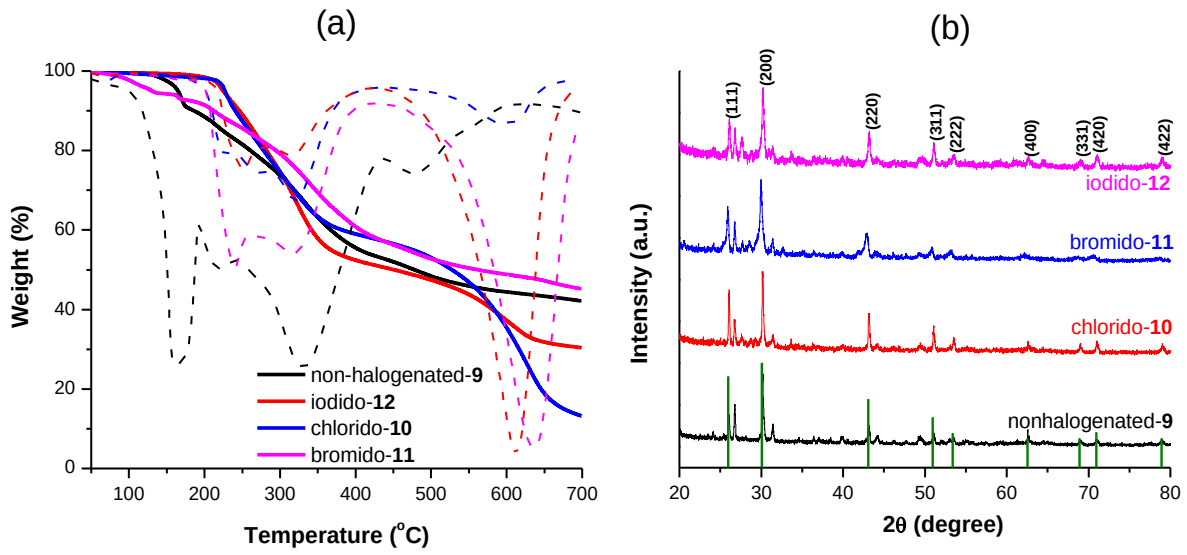

Figure 3.1: (a) Thermogravimetric (solid line) and differential thermogravimetric (dash line) decomposition profiles of the SSPs, with the corresponding (b) p-XRD patterns of the residues obtained from thermogravimetric analysis.

The morphological properties of the PbS nanoparticles, are influenced by both the thermolytic reaction temperature and the type of halogen ligand incorporated within the Pb(II) SSPs. The investigated halogen series consist of chloride, bromide and iodide-incorporated SSPs, where the SSP obtained from lead acetate serves as a reference material. Prior to this investigation, it was necessary to confirm whether PbS nanoparticles had formed after thermolytic processes. For this purpose, p-XRD and scanning electron microscopy energy dispersive X-ray (SEM-EDX) studies were conducted.

The p-XRD patterns confirmed that the products of the thermolytic reactions correspond to PbS (Figure 3.2). The patterns also reveal the formation of face centered cubic (FCC) rock-salt structure (card number: 00-005-0592) of PbS. This was observed for the PbS nanoparticles obtained from all the precursors, there was no phase change observed when temperature was varied. The additional unindexed peaks observed in the diffraction patterns on Figure 3.1b compared to those of Figure 3.2, can be attributed to impurities resulting from high decomposition temperatures in the absence of a capping agent. This clearly demonstrates the advantages and/or

capabilities of a capping agent in lowering the decomposition energy of the SSP to afford phase-pure nanomaterials.

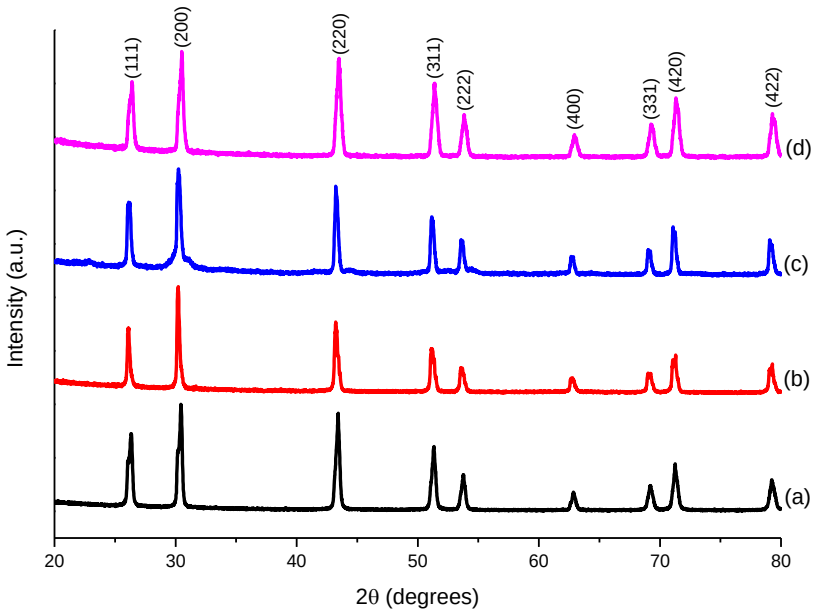

Figure 3.2: The p-XRD patterns of PbS nanoparticles synthesized at 270 °C using lead thiosemicarbazone SSPs made from (a) lead acetate (b) lead chloride (c) lead bromide and (d) lead iodide metal salts.

The SEM-EDX studies also confirmed the material to have Pb and S components; C component is attributed to carbon coating used to supress surface charging during imaging (Figures 3.3–3.7). Interestingly, substantial amounts of halogen content were detected in some of the samples. Due to the nature of the study, no further investigations were conducted to determine in what chemical form the halogen species exist in/within the material. However, the elemental mapping images suggest homogeneity throughout the samples (Figure 3.6 and 3.7). This could indicate either halogen-PbS solid solution or adhesion by the halogens on the PbS surfaces, similarly to inorganic capping groups reported elsewhere.[56–58]

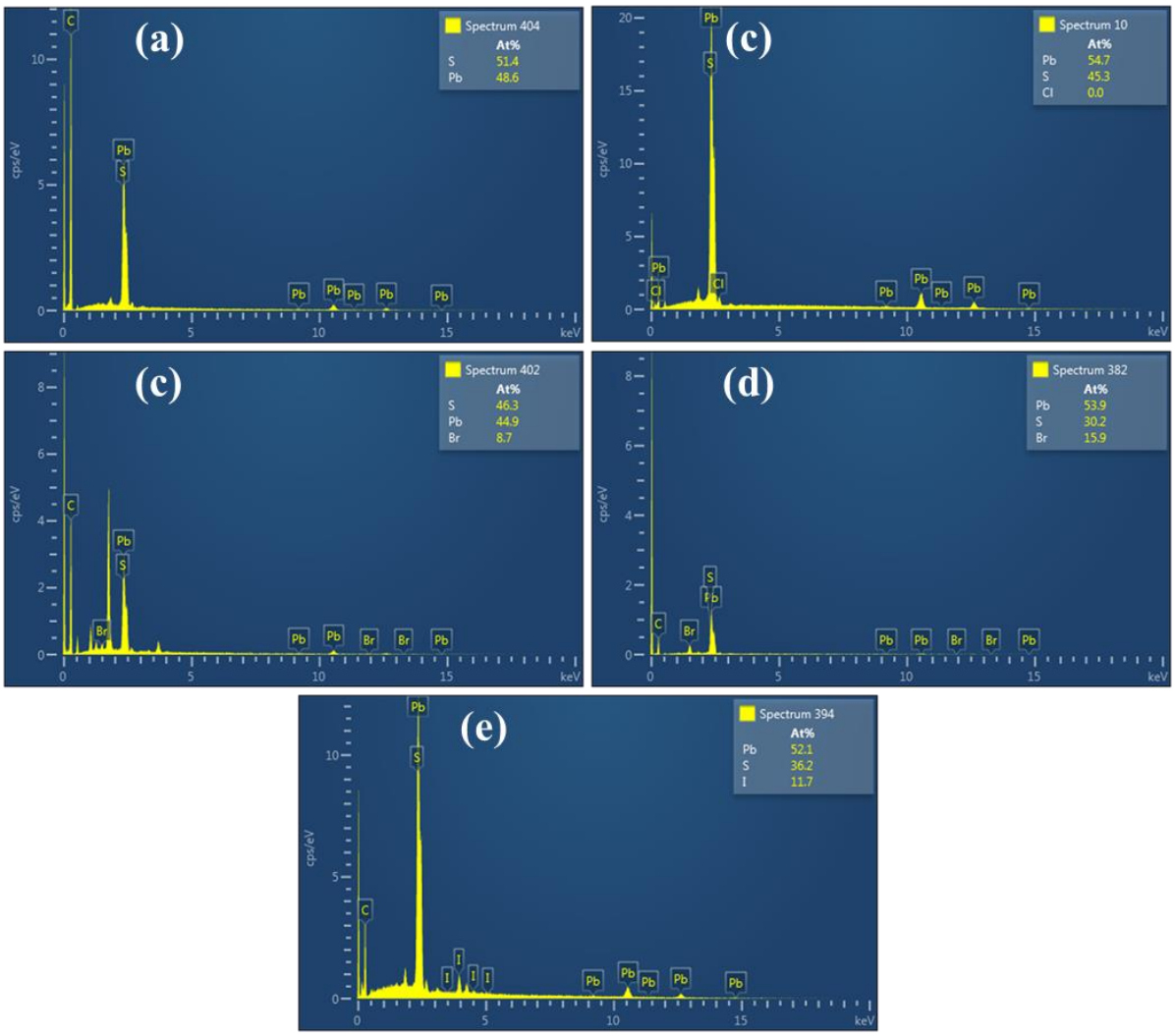

Figure 3.3: The EDX spectra of PbS nanoparticles obtained from (a) non-halogentaed-(**9**) at 270 °C, (b) chlorido-(**10**) at 270 °C, (c) bromido-(**11**) at 190 °C, (d) bromido-(**11**) at 270 °C, and (e) iodido-(**12**) at 270 °C.

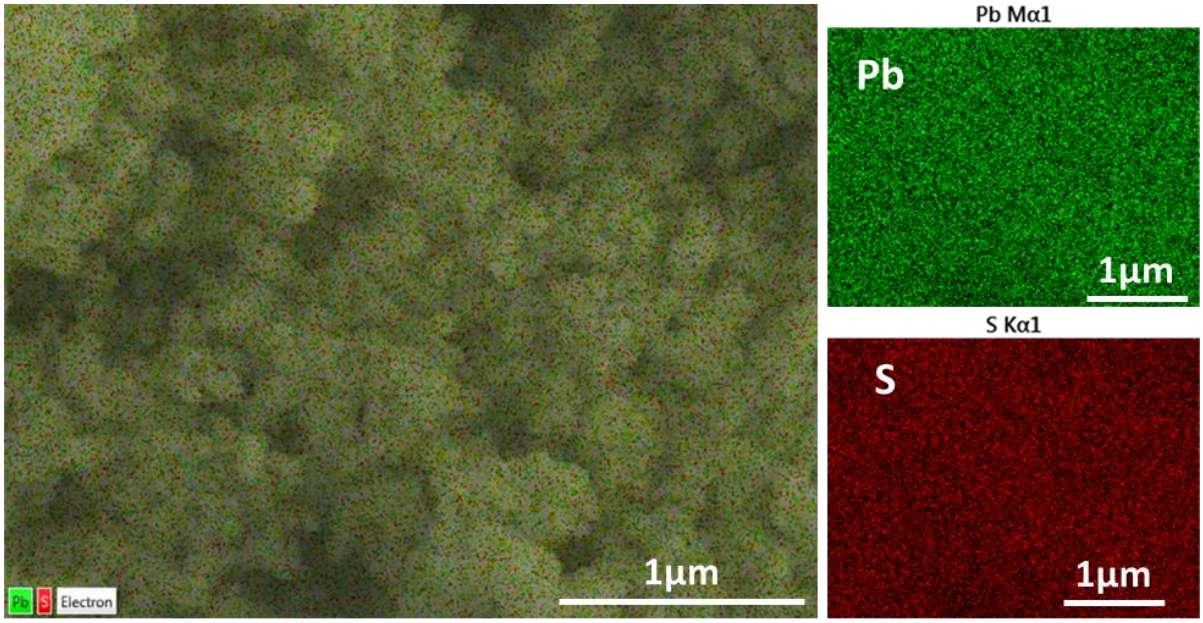

Figure 3.4: Elemental mapping for PbS nanoparticles obtained from non-halogenated-(**9**) at 270 °C.

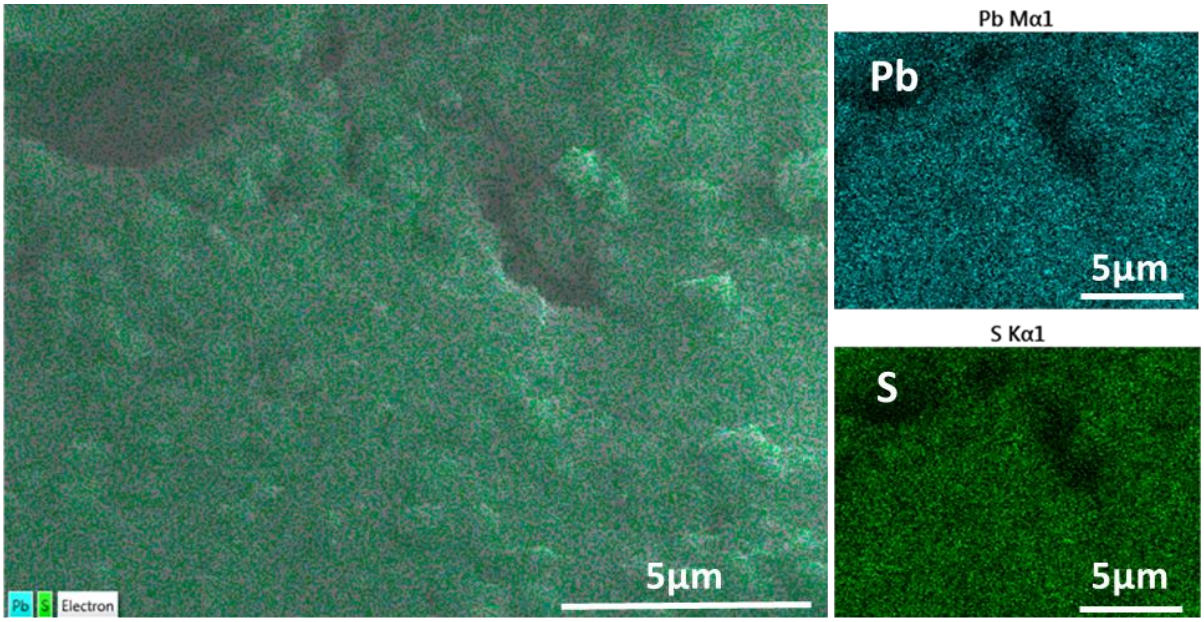

Figure 3.5: Elemental mapping for PbS nanoparticles obtained from chlorido-(**10**) at 270 °C.

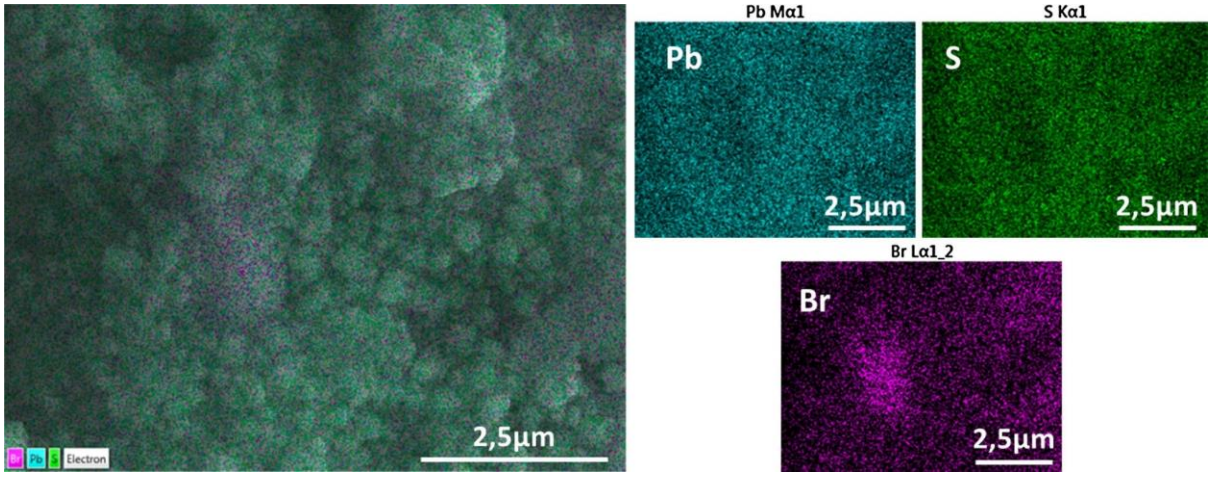

Figure 3.6: **E**lemental mapping images for PbS nanoparticles obtained from bromido-(**11**) at 270 °C.

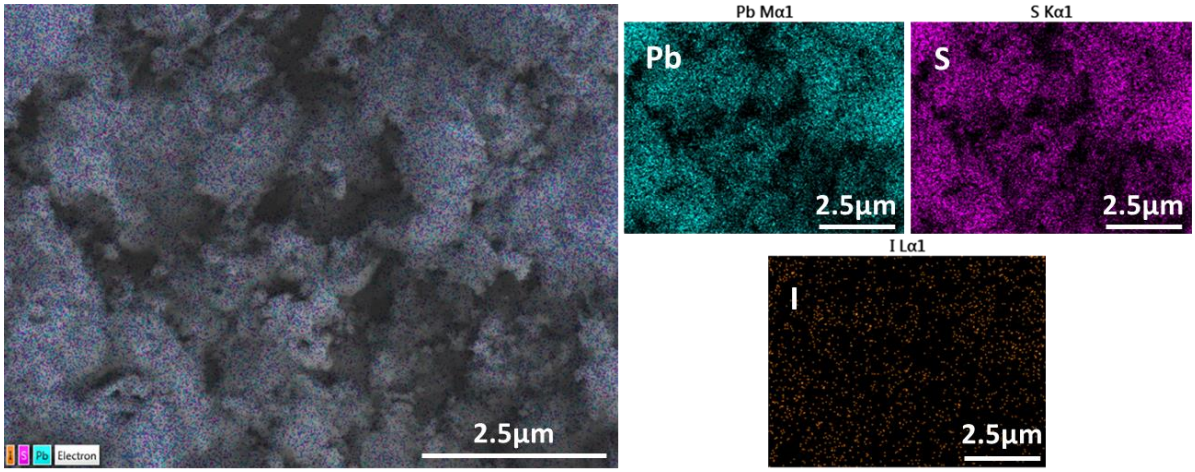

Figure 3.7: Elemental mapping for PbS nanoparticles obtained from iodido-(**12**) at 270 °C.

From the TEM studies, it was evident that the size of the nanoparticles increases with reaction temperature from 190 °C to 270 °C. This is generally attributed to the Ostwald ripening growth process. At relatively lower reaction temperature (190 °C), close to uniform particle sizes are obtained from the halogenated SSPs (**10**), (**11**) and (**12**) in Figures 3.8a, 3.9a and 3.9c, respectively. An increase to 230 °C adversely affects the monodispersity, for example, the nanoparticles obtained from chlorido-(**10**) exhibits a mixture of three average sizes where the largest particles are ± 100 nm (Figure 3.8b). A similar trend was observed for the bromido-(**11**) and iodido-(**12**) SSPs (Figures 3.10a and 3.10c). A further increase to 270 °C showed an interesting observation, the largest particle sizes obtained from chlorido-(**10**) (Figure 3.8c),

bromido-(**11**) (Figure 3.10b) and iodido-(**12**) (Figure 3.10d) are found to be ± 100, ± 200 and ± 400 nm, respectively. Coincidently, this observation coincides with an increasing trend in atomic diameter of elements in the group VII halogen series. Furthermore, improvement in monodispersity drops significantly down the halogen series. At this point, there is insufficient evidence to conclude if this observation is as a result of either electronic or steric differences exerted by the halogens on the decomposition of the complex.

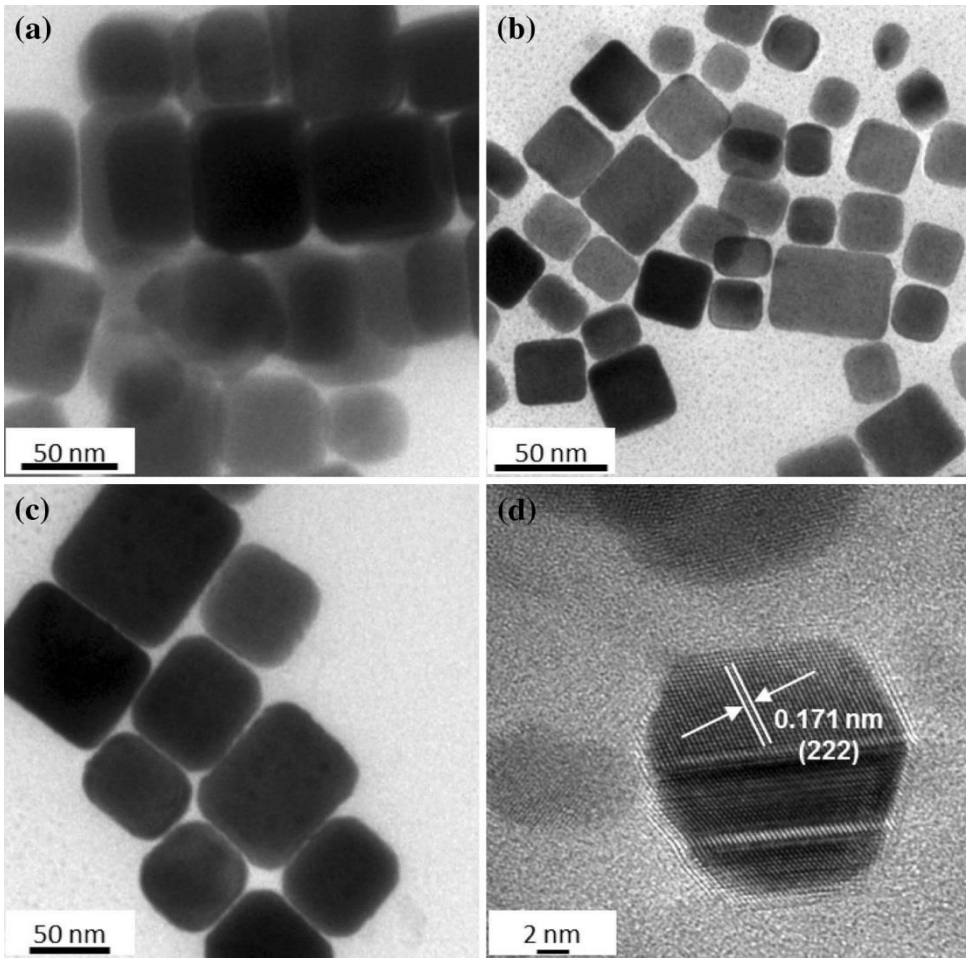

Figure 3.8: TEM images of PbS nanoparticles obtained from the thermolysis of chlorido-(**10**) SSP in oleylamine at (a) 190 °C, (b) 230 °C, (c) 270 °C, as well as (d) the HRTEM image obtained at 230 °C decomposition temperature.

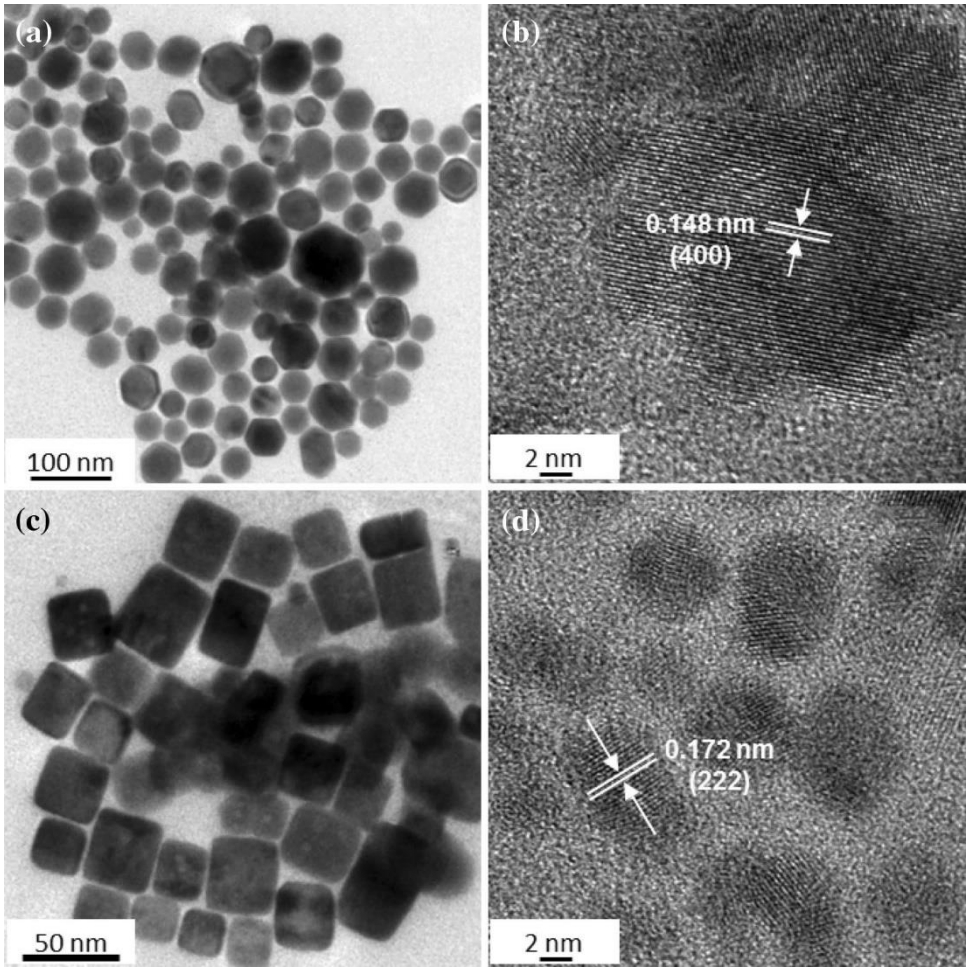

Figure 3.9: TEM images of PbS nanoparticles obtained from the thermolysis of (a) bromido-(**11**) at 190 °C, and (c) iodido-(**12**) at 190 °C, with the corresponding HRTEM images obtained at (b) 190 °C and (d) 270 °C decomposition temperatures, respectively.

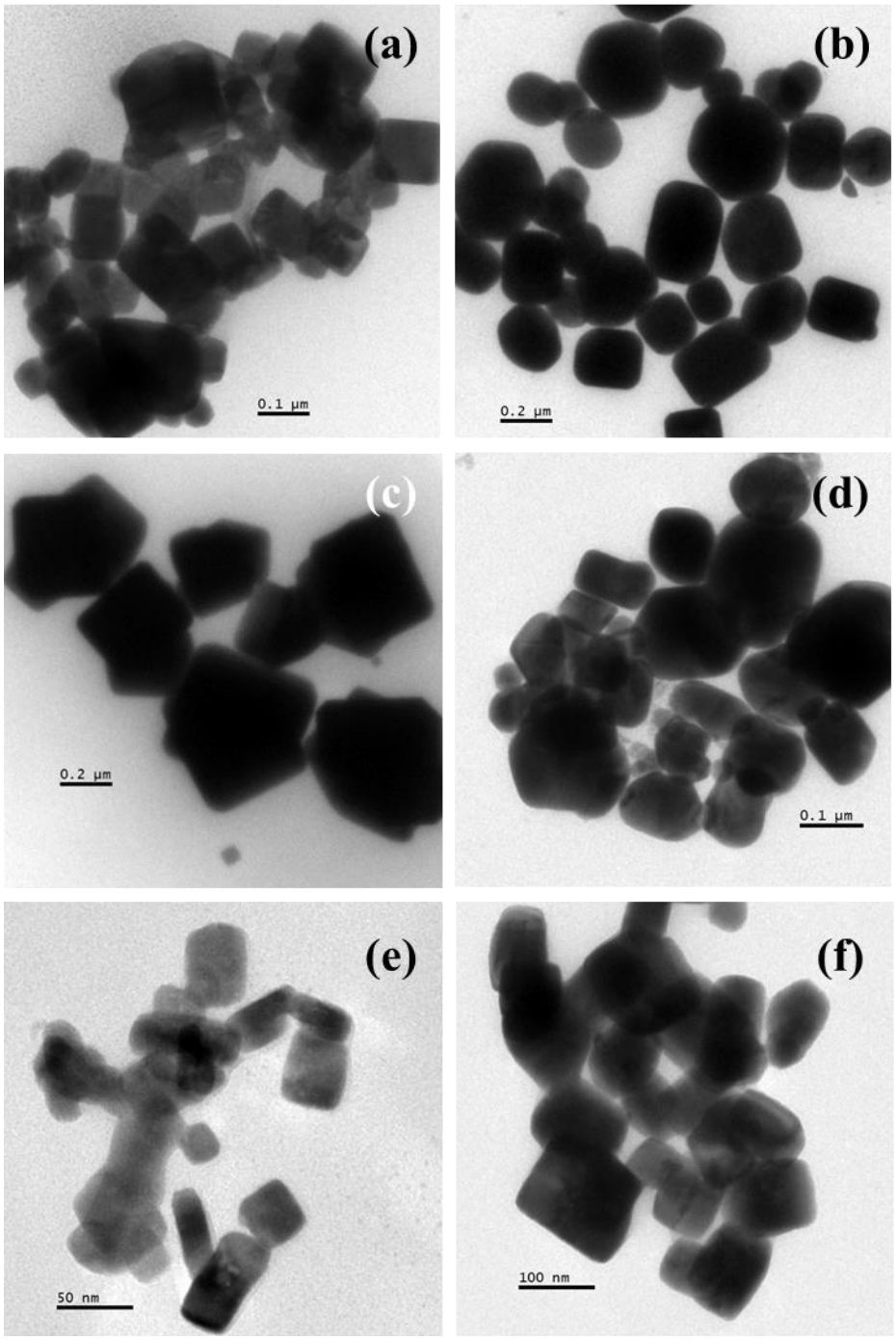

Figure 3.10: TEM images of PbS nanoparticles obtained from the thermolysis of bromido-(**11**) at (a) 230 °C and (b) 270 °C, iodido-(**12**) at (c) 230 °C and (d) 270 °C, as well as non-halogenated-(**9**) at (e) 190 °C and (f) 230 °C decomposition temperatures.

The non-halogenated-(**9**) SSP, on the other hand, exhibits different behaviour to that of the halogen derivatives. The nanoparticles agglomerate at lower-to-moderate reaction temperatures, 190 °C and 230 °C, thus making it difficult to investigate and

conclude on the sizes of the as-prepared nanoparticles (Figure 3.10e and 3.10f). However, as the temperature is raised to 270 °C, pronounced and almost uniform cubic-shaped nanoparticles are obtained (Figure 3.11a).

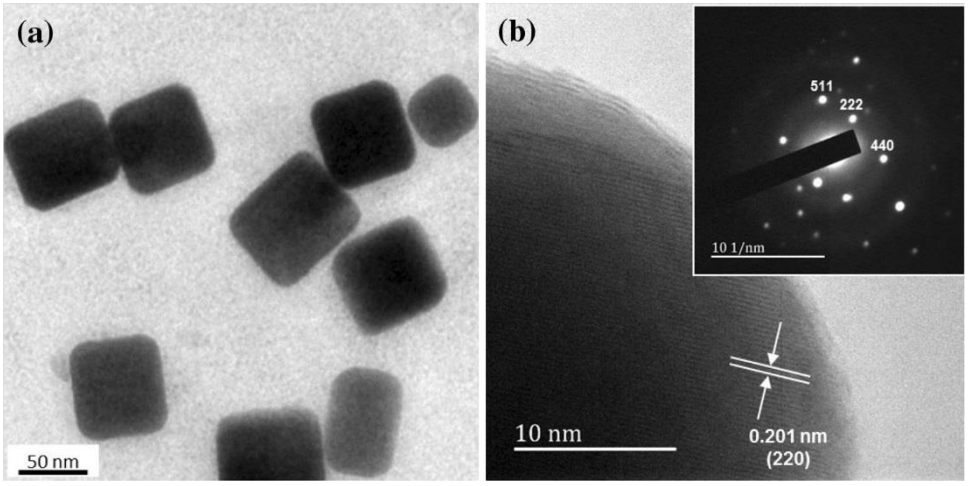

Figure 3.11: The (a) TEM image of PbS nanoparticles obtained from the thermolysis of nonhalogenated-(**9**) at 270 °C, and the corresponding (b) HRTEM image (insert: SAED image)

Although the study has failed to achieve a uniform and controlled size of the nanoparticles, the opposite was observed with regards to their shape. The work by Cao *et al*.[38] has established a detailed growth mechanism for PbS nanoparticles. Briefly, the mechanism involves the nucleation where growth starts from the rock salt like seed crystal of PbS. These seed crystals are responsible for the final morphology of the material obtained. It is known that the PbS seeds are tetradecahedrons, i.e. truncated cubes with exposing [100] and [111] facets. The growth along <100> facet would lead to pods, whereas, preferential growth along <111> direction would lead to cubes. Therefore, the final shape of the PbS nanoparticles will depend on relative growth along <100> and <111> directions. Crystallographic [111] facets of the rock salt structure have high intrinsic surface energy. This leads to higher growth rate along <111> direction resulting into cubes. Thus, stabilizing surfactants which can block or enhance growth of certain facet, temperature and concentration of precursor are among reaction parameters used to manipulate the morphology of the materials prepared. Certain stabilizing agents like amines are known to stabilise [100] facets, thus indirectly enhancing growth along <111> direction. This leads to growth of octopods along <111> direction, the further repining, i.e. space filling between

octopods results into final cubes. In this work, it was observed that the role of the halogen ligands incorporated within the SSPs, as well as a choice of reaction temperature, have an influence on the morphology of the nanoparticles. Interestingly, the shape of the nanoparticles become more pronounced as the reaction temperature increases, when the non-halogenated-(**9**) and chlorido-(**10**) SSPs are used. However, the opposite is observed for the bromido-(**11**) and iodido-(**12**) SSPs. Additionally, the nanoparticles obtained from the bromido-(**11**) SSP exhibit truncated cubic-like shape at a relatively lower temperature (190 °C), which is different from the cubes observed at other temperatures across all SSPs (Figure 3.9a). The clearly visible lattice fringes observed from the HRTEM images confirmed that the nanoparticles are crystalline, regardless of the morphology (Figures 3.9b and Figure 3.12). It was further noted that nanoparticles obtained from the chlorido-(**10**) and iodido-(**12**) SSPs were disintegrating into smaller nanoparticles, while acquiring images showing lattice fringes (Figures 3.8d and Figure 3.9d, respectively). The absence of the chloride content in the nanoparticles obtained from chlorido-(**10**) ruled out the possibility of the role of halogens in such a phenomenon.

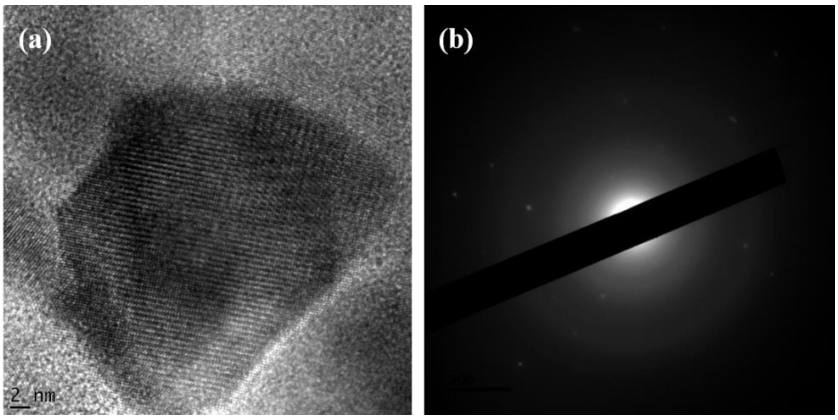

Figure 3.12: The (a) HRTEM image and (b) SAED image of PbS nanoparticles obtained from bromido-(**11**) SSP at 270 °C.

As a result of the relatively varied morphology of PbS nanoparticles obtained from bromido-(**11**), further studies were carried out. For this purpose, UV-Vis-NIR optical absorption studies were conducted. As shown in Figure 3.13, these nanoparticles absorb strongly in Visible-NIR region due to their strong size quantization.[59] Remarkably, the influence of temperature gave a strong absorption band 715 nm (1.73 eV) from truncated cube-shaped nanoparticles synthesized at 190

°C. At relatively higher reaction temperatures, 230 °C and 270 °C, the samples exhibited strong absorption peaks at much lower wavelength 395 nm (3.14 eV), progressively blue shifted from both the bulk material and nanoparticles obtained at 190 °C. The absorption spectra wavelength for the 190 °C sample is consistent with literature reports, however, a decrease in absorption wavelength (blue shift) at higher reaction temperatures is not commonly reported.

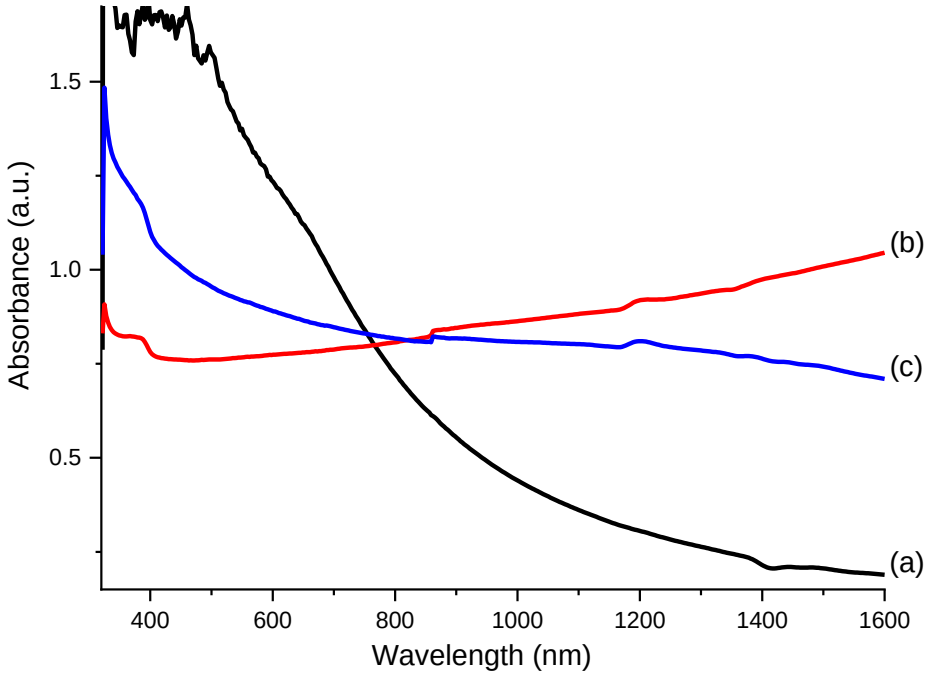

Figure 3.13: The UV-Vis-NIR absorption spectra of oleylamine-capped PbS nanoparticles synthesized using bromido-(**11**) SSP at (a) 190 °C, (b) 230 °C and (c) 270 °C.

Further absorption measurements of nanoparticles obtained from other SSPs were conducted. As a result of the interesting observation made from bromido-(**11**) at higher temperatures, focus was only in absorption studies on nanoparticles synthesized at 270 °C (Figure 3.14). The PbS nanoparticles obtained from the iodido-(**12**) SSP showed a broad absorption in the NIR region around 1150 nm (1.08 eV) and an excitonic absorption peak at 390 nm (3.18 eV). The nanoparticles obtained from the non-halogenated-(**9**) and chlorido-(**10**) SSPs showed absorption bands around

500 nm (2.48 eV) and 1100 nm (1.13 eV), respectively. The bromido-(**11**) SSP showed an excitonic absorption peak at around 390 nm (3.18 eV). The absorption band energies observed here are typical of PbS nanoparticles, attributed to features such as particle size and shape.[60] The differences in band-edge excitonic features could be due to the structural differences in the SSPs.

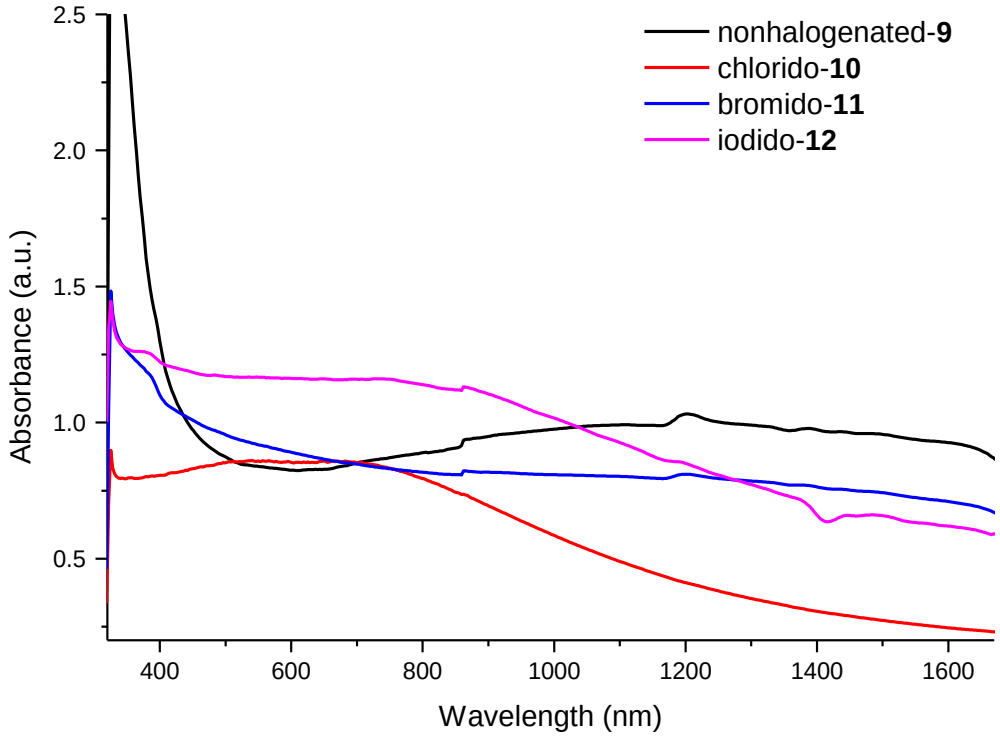

Figure 3.14: The UV-Vis-NIR absorption spectra of oleylamine-capped PbS nanoparticles synthesized at 270 °C.

3.4 Conclusion

In this study, PbX_2 (X = Cl, Br, I) and non-halogenated Pb(II) cinnamaldehyde thiosemicarbazone complexes have been prepared in good yields and characterized fully by elemental analysis, FT-IR and ^{1}H and $^{13}C\{^{1}H\}$ NMR spectroscopy techniques. The thermogravimetric analysis confirmed that the complexes are suitable for use as single source molecular precursors (SSPs) towards the synthesis of PbS, albeit at moderate decomposition temperatures. Thus, the SSPs were used to demonstrate the role of the halide ligands on the size and shape of the PbS nanoparticles, as well as their optical absorption properties. The formation of PbS material (card number: 00-005-0592) through the oleylamine-mediated hot-injection reaction was confirmed

using powder X-ray diffraction and energy dispersive X-ray (EDX) spectroscopy. Significant amounts of the bromide and iodide elements were detected in nanoparticles obtained from the corresponding SSPs. Average particle sizes are found to be in the 50–400 nm range, were estimated using transmission electron microscopy imaging; increase in reaction temperature results in an increase in particle size. Furthermore, the dominant cubic-shape morphology becomes less pronounced down the halogen series. Interestingly, the bromide-incorporated SSP produced truncated cube-shaped nanoparticles at relatively lower temperatures. The optical absorbance for all nanoparticles were found to be blue-shifted when compared to the bulk material; band gaps of between 1.08 to 3.18 eV were obtained.

References

[1] M. Salavati-Niasari, A. Sobhani, F. Davar, *J. Alloys Compd*. **2010**, *507*, 77.

[2] N. Reilly, M. Wehrung, R. Andrew, O. Dell, L. Sun, *Mater. Chem. Phys*. **2014**, *147*, 1.

[3] K.T. Yong, Y. Sahoo, K.R. Choudhury, M.T. Swihart, J.R. Minter, P.N. Prasad, *Chem. Mater*. **2006**, *18*, 5965.

[4] J.T. Zelikoff, J.H. Li, A. Hartwig, X.W. Wang, M. Costa, T.G. Rossman, *Carcinogenesis* **1988**, *9*, 1727.

[5] I. Chakraborty, S.P. Moulik, *J. Nanoparticle Res*. **2005**, *7*, 237.

[6] L.D. Nyamen, V.S.R. Rajasekhar Pullabhotla, A.A. Nejo, P.T. Ndifon, J.H. Warner, N. Revaprasadu, *Dalton Trans*. **2012**, *41*, 8297.

[7] H. Karami, M. Ghasemi, S. Matini, *Int. J. Electrochem. Sci.* **2013**, *8*, 11661.

[8] K. Ramasamy, M.A. Malik, N. Revaprasadu, P. O'Brien, *Chem. Mater*. **2013**, *25*, 3551.

[9] K.C. Preetha, T.L. Remadevi, *Mater. Sci. Semicond. Process*. **2013**, *16*, 605.

[10] M. Corricelli, D. Altamura, L. De Caro, A. Guagliardi, A. Falqui, A. Genovese, A. Agostiano, C. Giannini, M. Striccoli, M.L. Curri, *Cryst. Eng. Comm*. **2011**, *13*, 3988.

[11] K.N. Bourdakos, D.M.N.M. Dissanayake, T. Lutz, S.R.P. Silva, R.J. Curry, *Appl. Phys. Lett*. **2008**, *92*, 2008.

[12] S. Günes, K.P. Fritz, H. Neugebauer, N.S. Sariciftci, S. Kumar, G.D. Scholes, *Sol. Energy Mater. Sol. Cells* **2007**, *91*, 420.

[13] F.C.J.M. Van Veggel, *Chem. Mater*. **2014**, *26*, 111.

[14] J.D. Patel, *Mater. Sci. Appl*. **2012**, *03*, 125.

[15] M. Asad, M. Fathipour, M.H. Sheikhi, M. Pourfath, *Sens. Actuators A* **2014**, *220*, 213.

[16] L. Sun, J.J. Choi, D. Stachnik, A.C. Bartnik, B.-R. Hyun, G.G. Malliaras, T. Hanrath, F.W. Wise, *Nat. Nanotechnol*. **2012**, *7*, 369.

[17] A.O. Nejo, A.A. Nejo, R.V.S.R. Pullabhotla, N. Revaprasadu, *J. Alloys Compd*. **2012**, *537*, 19.

[18] C. Gervas, S. Mlowe, M.P. Akerman, I. Ezekiel, T. Moyo, N. Revaprasadu, *Polyhedron* **2017**, *122*, 16.

[19] S. Ye, Y. Ye, Y. Ni, Z. Wu, *J. Cryst. Growth* **2005**, *284*, 172.

[20] T. Trindade, P. O'Brien, X. Zhang, M. Motevalli, *J. Mater. Chem*. **1997**, *7*, 1011.

[21] J. Joo, H.B. Na, T.Y. Yu, J.H. Yu, Y.W. Kim, F. Wu, J.Z. Zhang, T. Hyeon, *J. Am. Chem. Soc*. **2003**, *125*, 11100.

[22] G.B. Shombe, E.B. Mubofu, S. Mlowe, N. Revaprasadu, *Mater. Lett*. **2016**, *185*, 17.

[23] D. Berhanu, K. Govender, D. Smyth-Boyle, M. Archbold, D.P. Halliday, P. O'Brien, *Chem. Commun*. **2016**, *0*, 4709.

[24] I. Jen-La Plante, T.W. Zeid, P. Yang, T. Mokari, *J. Mater. Chem*. **2010**, *20*, 6612.

[25] N.O. Boadi, M.A. Malik, P. O'Brien, J.A.M. Awudza, *Dalton Trans*. **2012**, *41*, 10497.

[26] M.A. Malik, M. Afzaal, P. O'Brien, *Chem. Rev*. **2010**, *110*, 4417.

[27] S. Bhakat, A. Chakraborty, S.P. Dash, A.K. Panda, R. Acharyya, A. Biswas, S. Mukhopadhyay, S. Bhutia, A. Crochet, Y.P. Patil, M. Nethaji, R. Dinda, *Dalton Trans*. **2015**, *44*, 6140.

[28] E. Pahontu, F. Julea, T. Rosu, V. Purcarea, Y. Chumakov, P. Petrenco, A. Gulea, *J. Cell. Mol. Med*. **2015**, *19*, 865.

[29] B.P. Bade, S.S. Garje, Y.S. Niwate, M. Afzaal, P. O'Brien, *Chem. Vap. Depos*. **2008**, *14*, 292.

[30] S.D. Disale, S.S. Garje, *Appl. Organometal. Chem*. **2010**, *24*, 734.

[31] J.B. Biswal, S.S. Garje, *Synth. React. Inorg. Met.-Org. Nano-Met. Chem*. **2013**, *43*, 461.

[32] A.S. Pawar, S.S. Garje, *Bull. Mater. Sci*. **2015**, *38*, 1843.

[33] A.S. Pawar, S. Mlowe, S.S. Garje, M.P. Akerman, N. Revaprasadu, *Inorg. Chim. Acta* **2017**, *463*, 7.

[34] S. Axnanda, M. Scheele, E. Crumlin, B.H. Mao, R. Chang, S. Rani, M. Faiz, S.D. Wang, A.P. Alivisatos, Z. Liu, *Nano Lett*. **2013**, *13*, 6176.

[35] Y. Zhao, X.H. Liao, J.M. Hong, J.J. Zhu, *Mater. Chem. Phys*. **2004**, *87*, 149.

[36] M.R. Karim, M.D. Aktaruzzaman, M. Ashrafuzzaman, M.D.B. Zaman, *Chalcogenide Lett*. **2014**, *11*, 531.

[37] M. Behboudnia, M. Behboudnia, A. Habibi-Yangjeh, A. Khodayari, A. Khodayari, Y. Jafari-Tarzanag, *Bull. Korean Chem. Soc*. **2008**, *29*, 53.

[38] Y. Cao, P. Hu, D. Jia, *Nanoscale Res. Lett*. **2012**, *7*, 668.

[39] N. Wang, X. Cao, L. Guo, S. Yang, Z. Wu, *ACS Nano* **2008**, *2*, 184.

[40] Y. Ji, D. Yang, H. Zhang, X. Ma, J. Xu, D. Que, *Solid State Phenom*. **2004**, *197*, 99–100.

[41] M. Green, *J. Mater. Chem*. **2010**, *20*, 5797.

[42] Y. Yin, A.P. Alivisatos, *Nature* **2005**, *437*, 664.

[43] P.S. Nair, G.D. Scholes, *J. Mater. Chem*. **2006**, *16*, 467.

[44] M.S. Bakshi, *Cryst. Growth Des*. **2016**, *16*, 1104.

[45] J. Zhang, J. Gao, E.M. Miller, J.M. Luther, M.C. Beard, *ACS Nano* **2014**, *8*, 614.

[46] F. Gerdes, C. Navío, B.H. Juárez, C. Klinke, *Nano Lett*. **2017**, *17*, 4165.

[47] R. Gaur, P. Jeevanandam, *New J. Chem*. **2015**, *39*, 9442.

[48] A.S. Pawar, S.C. Masikane, S. Mlowe, S.S. Garje, N. Revaprasadu, Eur. *J. Inorg. Chem*. **2016**, *2016*, 366.

[49] F.E. Anderson, C.J. Duca, J.V. Scudi, *J. Am. Chem. Soc*. **1951**, *73*, 4967.

[50] C.H. Collins, A.M. Lyne, J.M. Grange, *Microbiological Methods*, 6th edn. (Butterworths, Oxford, **1989**)

[51] M.A. Ali, S.E. Livingstone, D.J. Philips, *Inorg. Chim. Acta* **1973**, *7*, 179.

[52] A. Saxena, J.K. Koacher, J.P. Tandon, *Inorg. Nucl. Chem. Lett*. **1981**, *17*, 229.

[53] A. Saxena, J.P. Tandon, K.C. Molloy, J.J. Zuckerman, *Inorg.Chim. Acta* **1982**, *63*, 71.

[54] A.K. Varshney, S. Varshney, H.L. Singh, *Bull. Pol. Acad. Sci. Chem*. **1997**, *45*, 373.

[55] W.J. Geary, *Coord. Chem. Rev*. **1971**, *7*, 81.

[56] M. Saruyama, M. Kanehara, T. Teranishi, *J. Am. Chem. Soc*. **2010**, *132*, 3280.

[57] M. Meyns, F. Iacono, C. Palentia, J. Geweke, M.D. Coderch, U.E.A. Fitt-schen, J.M. Gallego, R. Otero, B.H. Juárez, C. Klinke, *Chem. Mater*. **2014**, *26*, 1813.

[58] J. Tang, K.W. Kemp, S. Hoogland, K.S. Jeong, H. Liu, L. Levina, M. Fu-rukawa, X. Wang, R. Debnath, D. Cha, K.W. Chou, A. Fischer, A. Amassian, J.B. Asbury, E.H. Sargent, *Nat. Mater*. **2011**, *10*, 765.

[59] Y. Wang, A. Suna, W. Mahler, R. Kasowski, *J. Chem. Phys*. **1987**, *87*, 7315.

[60] F. Jähnig, D. Bozyigit, O. Yarema, V. Wood, *APL Mater*. **2015**, *3*, 01.

CHAPTER 4

4 Castor oil and olive oil as green capping agents towards the synthesis of non-toxic β-In_2S_3 and $CuInS_2$ nanoparticles from molecular precursors

4.1 Introduction

Literature reports have provided access in attaining nanomaterials exhibiting desired properties, through various synthetic protocols. However, the design of most protocols raises concerns related to their efficiency in producing high quality nanomaterials taking precedence over financial and environmental impacts. Semiconductor nanoparticles are a typical example of nanomaterials which are generally prepared using toxic solvents that aid in preserving the attractive properties of the nanoparticles during and post-synthesis processes. Green[1] reviewed the chemistry and passivation mechanisms of common solvents such as trioctylphosphine oxide, amines and thiols. Recent efforts have focused on the use of alternative eco-friendly solvents as a first step towards the greener fabrication of semiconductor nanoparticles. Castor oil, olive oil and anacardic acid extracts are among alternative eco-friendly passivating solvents which have been reported, for the preparation of various metal sulfide semiconductor nanoparticles.[2–5] Other reports such as the concise review by Iravani[6] also outline advances in the organism and plant-mediated biosynthesis of metal nanoparticles.

In_2S_3 and $CuInS_2$ compounds have received attention as potential materials in solar cell applications. The In_2S_3 phase is the most common amongst InS, In_3S_4 and In_6S_7 in the In-S binary system.[7,8] It is a non-toxic semiconductor (direct band gap of 2.0–2.8 eV), with potential as an alternative to the toxic CdS buffer in cadmium gallium indium selenide solar cells.[9] Its exploitation in catalysis[10,11] and optoelectronic applications[12,13] has been reported. The In_2S_3 phase exists in the α (cubic), β (tetragonal) and γ (trigonal) polymorphic forms because of defects responsible for vacancies within the structure.[14] The widely reported β-In_2S_3 and the less reported γ-In_2S_3 a two dimensional material at the atomic level such as InS, are stable at room temperature.[15] Access to thin films and nanoparticles of β-In_2S_3 through a synthetic approach, can follow either the multiple precursor route or single source molecular

precursor (SSP) route. Generally, the use of SSPs is preferred due to clean decomposition of an organometallic compound with preformed bonds (e.g. In-S bonds) at practical temperatures. A variety of In(III) complexes as SSPs for the preparation of β-In_2S_3 nanomaterials have been explored. The nature of the ligand, choice of synthetic method and tweaking of reaction parameters have been identified as having a significant influence on the crystallographic and morphological preference of the indium sulfide material produced. The In(III)-trisdiethyldithiocarbamate complex, [$In(S_2CNEt_2)_3$], has produced β-In_2S_3 urchin-like microspheres composed of nanoflakes via the hydrothermal route,[16] sub-nanometer to micrometer β-In_2S_3 sheets through the long alkyl chain amine-mediated thermolysis route,[17,18] and InS quantum dots through the TOPO-mediated thermolysis route.[19] The organo-In(III) complexes with the same diethyldithiocarbamate ligand, [$RIn(S_2CNEt_2)$] where R = dimethyl, diethyl and neopentyl produce films exhibiting different phases (InS, In_6S_7 and β-In_2S_3) which result from the influence of both type of ligand and temperature used in the low-pressure metal organic chemical vapour deposition (LP-MOCVD) reaction.[20] Mixed alkydithiocarbamates [$In(S_2CNMeR)_3$] where R = n-Butyl and n-Hexyl, gave α-In_2S_3 thin films by LP-MOCVD.[21] Organo-In(III) complex with a mixed alkydithiocarbamate ligand [$Et_2In(S_2CNMe^nBu)$], produced β-In_2S_3 thin films using the standard MOCVD method.[22,23] Xanthate complexes are preferred as SSPs due to their advantages which include low decomposition temperatures, and cost-effective synthetic protocols. From previous reports, methyl, ethyl, iso-propyl, sec-butyl xanthate compounds have been used to study the In-S system.[24–26] Alkyl thiolates,[27–29] thiobenzoates,[30] thiocarbazates,[31] thiobiurets,[32] thiophosphinates [33] and thiocarboxylates [34,35] have also been reported as SSPs for the synthesis of indium sulfide nanoparticles and thin films exhibiting different phases and morphologies.

$CuInS_2$ represents a class of non-toxic I-III-VI_2 ternary semiconductors exhibiting interesting properties similarly to group II-VI and IV-VI semiconductors. Wet-chemical fabrication protocols allow the tuning of its direct band gap of 1.5 eV in the visible region through variation of the Cu:In:S stoichiometric ratio, in addition to particle size and shape. The synthesis of $CuInS_2$ nanoparticles is mostly achieved through colloidal synthesis routes such as the hot-injection and solvothermal methods. A review by Kolny-Olesiak and Weller covers a thorough scope on the synthesis

methods and applications of colloidal $CuInS_2$ nanoparticles.[36] Briefly, the multiple precursor route is widely used, although the reactivity of the Cu^+ and In^{3+} cations differ significantly towards S^{2-} anions. The reactivity of In^{3+} is relatively slower due to its hard Lewis acid character, as opposed to the soft chemical character of Cu^+ similarly to S^{2-}. Thus, thiols and carboxylic acid stabilisers are required to promote a balanced release of the Cu^+ and for In^{3+} cations, respectively. An alternative is the simultaneous release which is achieved through the use of SSPs.[37–39] Common SSPs reported have the general formula $[(PR'_3)_2CuIn(SR'')_4]$, where R′ = octyl, i-Bu and Ph while R″ = Et, n-Pr, and t-Bu.[40–42] Reaction temperature and time, as well as the type of coordinating solvents have been identified to influence the morphological and optical properties of $CuInS_2$ nanoparticles.

Few notable attempts have been reported on the green synthetic approach for $CuInS_2$ nanoparticles, however with limitations. Zhong *et al*.[43] followed a multiple precursor route using octadecene as a non-toxic solvent; the heat-up method however uses a toxic sulfur source (1-dodecanethiol) although at minor quantities. Furthermore, improving crystallinity by extending the reaction time has adverse effects on the purity of the desired material, as noted from the unindexed peaks in the powder X-ray diffraction patterns. Kharkwal *et al*.[44] then reported an improved, low-temperature approach using a copper indium xanthate as a precursor. The precursor is obtained by a one-pot reaction protocol, as co-precipitated complexes of unknown composition nor purity. In addition, the reaction protocol involves the use of dichlorobenzene, oleylamine and trioctylphosphine which do not qualify as non-toxic eco-friendly chemicals. An alternative approach by Buchmaier *et al*.[45] involves the room temperature reaction approach, using pre-synthesized indium and copper xanthate complexes as molecular precursors. However, oleylamine is essential to initiate the reaction which is conducted in nitrogen atmosphere in a glove box for three days. In this chapter, another green synthesis approach that eliminates the likes of toxic chemicals such as those mentioned above is reported. The sole use of castor oil and olive oil as potential non-toxic and eco-friendly passivating agents towards the synthesis of non-toxic In_2S_3 and $CuInS_2$ nanoparticles is demonstrated. Furthermore, the green aspect of using xanthate ligands is already outlined in chapter, concerning

clean decomposition at low temperatures through the Chugaev elimination mechanism.

4.2 Experimental

4.2.1 Materials

The indium(III) chloride, copper(II) chloride dihydrate, potassium ethyl xanthogenate, anhydrous magnesium sulfate and dichloromethane chemicals were purchased from Sigma-Aldrich, while ethanol was purchased from Shalom Laboratories. All chemicals were used as received.

4.2.2 Synthesis of precursors

4.2.2.1. General Procedure: Preparation of tris-ethyl xanthato indium(III) (13)

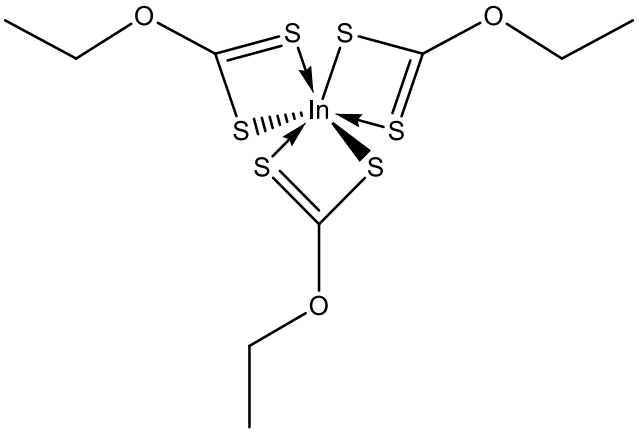

In a 250 mL two-neck flask was dissolved potassium ethyl xanthogenate (4.95 g, 30.9 mmol) in ethanol (100 mL). A colourless aqueous solution of Indium(III) chloride (2.28 g, 10.3 mmol) in ethanol (5.0 mL) was added drop-wise to the resulting pale-yellow solution. The solvent of a turbid, white coloured mixture was then removed under vacuum. The residue was dissolved in chloroform, washed with deionised water, and the organic fraction was dried with anhydrous magnesium sulfate prior to slow evaporation in open air. Colourless crystals were obtained; Yield: 4.50 g, 91%.

Anal. Calc. % (obtained) for $C_9H_{15}S_6O_3In$: C, 22.60 (22.95); H, 3.16 (2.94); S, 40.21 (39.84); In, 24.00 (23.64).

^{1}H NMR δ: 4.53 ($CH_3C\underline{H}_2$-, q), 1.51 ($C\underline{H}_3CH_2$-, t). ^{13}C(^{1}H) δ: 229.76, 76.03, 13.88.

4.2.2.2. Preparation of bis-ethyl xanthato copper(II) (14)

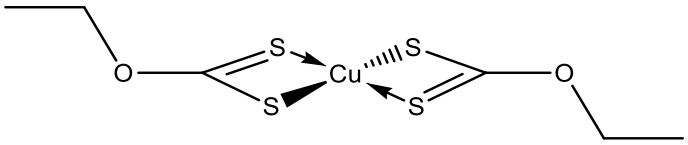

The copper(II) chloride dihydrate salt (2.00 g, 11.7 mmol) and potassium ethyl xanthogenate (3.75 g, 23.4 mmol) were used. Yellow coloured powder was obtained without further purification. Yield 3.84 g (71%).

Anal. Calc. % (obtained) for $C_6H_{10}S_4O_2Cu$: C, 23.55 (23.81); H, 3.29 (3.15).

^{1}H NMR δ: 4.72 ($CH_3C\underline{H}_2$-, q), 1.45 ($C\underline{H}_3CH_2$-, t). ^{13}C(^{1}H) δ: 207.51, 71.66, 13.63.

4.2.3 Synthesis of nanoparticles

The complexes used in this study have been prepared per modified methods reported previously.[46] They are preferred for their ease of accessibility, i.e. commercial availability of the ethyl xanthate ligand or simple preparation thereof following known reaction protocols. They were then used as starting materials for the synthesis of β-In_2S_3 and $CuInS_2$ nanoparticles.

4.2.3.1 Preparation of β-In_2S_3 nanoparticles

In a typical experiment, 250 mg of the complex is dispersed in 1octadecene (3.0 mL) and then injected into a 3.00 g of pre-heated coordinating solvent (castor oil or olive oil) at a desired temperature (200 °C, 250 °C or 300 °C). After an hour, the reaction is cooled down to ~60 °C and excess ethanol is charged into the reaction flask. The solids are separated by centrifugation, washed three times with acetone then dried in a vacuum desiccator at 30 °C overnight. The powder X-ray diffraction measurements were done on a dried sample, while TEM and ultraviolet-visible-near infrared absorption measurements were done on samples dispersed in ethanol and dichloromethane, respectively.

4.2.3.2. Preparation of $CuInS_2$ nanoparticles

Prior to the thermolysis experiments, equimolar amounts of the same-class complexes are ground in a pestle and mortar until a uniform powder is obtained. Then, 250 mg of the resulting powder is used following the thermolytic experiment outlined for β-In_2S_3 nanoparticles above.

4.2.4 Characterisation techniques

The characterisation techniques and instrument specifications used in this chapter are outlined in detail in section 2.2.4 of chapter 2, with minor modifications as follows:

- Microelemental analyses were conducted on a Carlo Erba EA 1108 elemental analyzer attached to an Edwards E2M8 vacuum pump, and a PerkinElmer automated model 2400 series II CHNS/O analyzer.
- The NMR spectra were recorded on a Bruker 500 spectrometer.
- Optical absorbance measurements were conducted at the UV-Vis-NIR spectral range on a Perkin-Elmer Lambda 1050 NIR UV-Visible spectrophotometer.
- The EDX and scanning electron microscopy imaging were performed on nanoparticles supported directly on the carbon tape; imaging was conducted at 15 kV.

4.3 Results and discussion

4.3.1 β-In_2S_3 nanoparticles

The solid products obtained through the thermolytic decomposition of In(III) ethyl xanthate (**13**) exhibit yellow colour which intensifies as the reaction temperature is increased. This observation is characteristic of indium sulfide materials.

The broad bands in the powder X-ray diffraction (p-XRD) patterns for the products obtained at lower temperatures of 200 °C, are suggestive of an amorphous crystallographic nature of the material, Figure 4.1A-a. The crystallinity of the nanoparticles is enhanced as the reaction temperature is raised to 250 °C and 300 °C, where the diffraction patterns are matched to the cubic β-In_2S_3 (card no. 00-025-0390),

Figure 4.1A-b and 4.1A-c, respectively. Similar diffraction patterns were obtained for castor oil-capped nanoparticles. It is observed that the crystallinity of the olive oil-capped nanoparticles improves significantly as compared to the castor oil-capped nanoparticles, Figure 4.1B. The reflection peaks are however still broad, thus, making it a challenge to calculate and compare the lattice parameters.

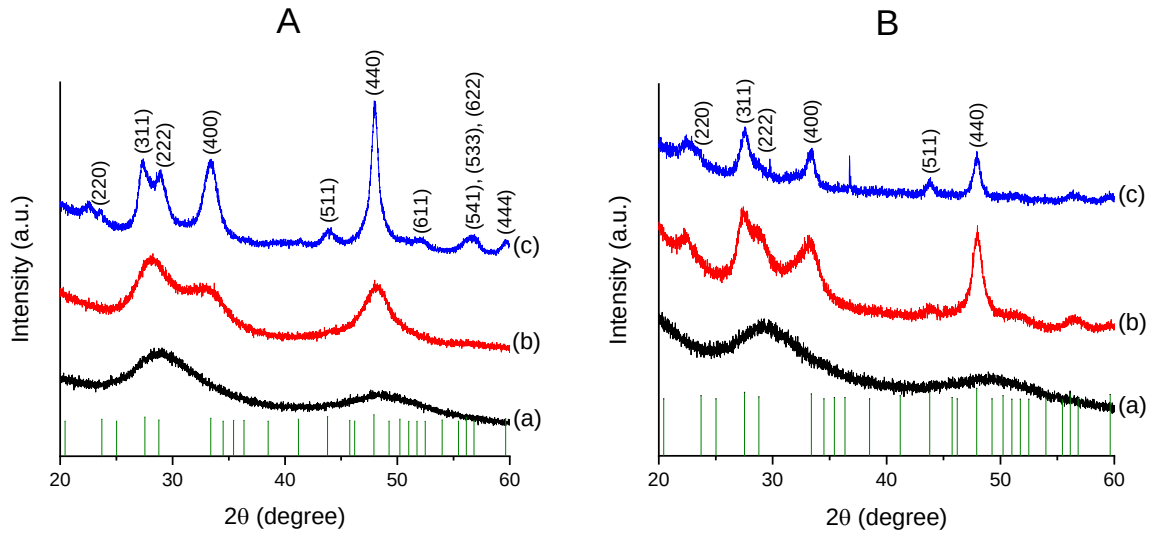

Figure 4.1: The p-XRD patterns for (A) olive oil-capped and (B) castor oil-capped β-In_2S_3 nanoparticles synthesized from (**13**) at (a) 200 °C, (b) 250 °C and (c) 300 °C, indexed to β-In_2S_3 (card no. 00-025-0390).

The broadness of the peaks generally implies smaller crystallites sizes, which is also confirmed by the transmission electron microscopy (TEM) images. For both coordinating solvents, the imaging technique was considered inefficient to estimate the size of the nanoparticles synthesized at 200 °C, Figure 4.2a and Figure 4.2d. Interesting features are however observed with an increase in reaction temperature. At 250 °C, both castor oil and olive oil coordinating solvents produce nanoparticles that exhibit a rod-like morphology, Figure 4.2b and Figure 4.2e, respectively. However, the average particle size of the castor oil-capped nanoparticles is relatively smaller (length: 12.2 ± 3.1 nm, diameter: 1.97 ± 0.49 nm), as compared to those obtained from the olive oil-capped particles (length: 30.1 ±6.9 nm, diameter: 3.99 ± 0.66 nm). An increase to 300 °C results in irregular shaped, elongated castor oil-capped nanoparticles (14.5 ± 3.1 nm), whereas olive oil-capped nanoparticles retain their rod-like morphology (length: 35.1 ± 6.8 nm, diameter: 5.16 ± 1.42 nm), Figure 4.2c and Figure 4.2f, respectively.

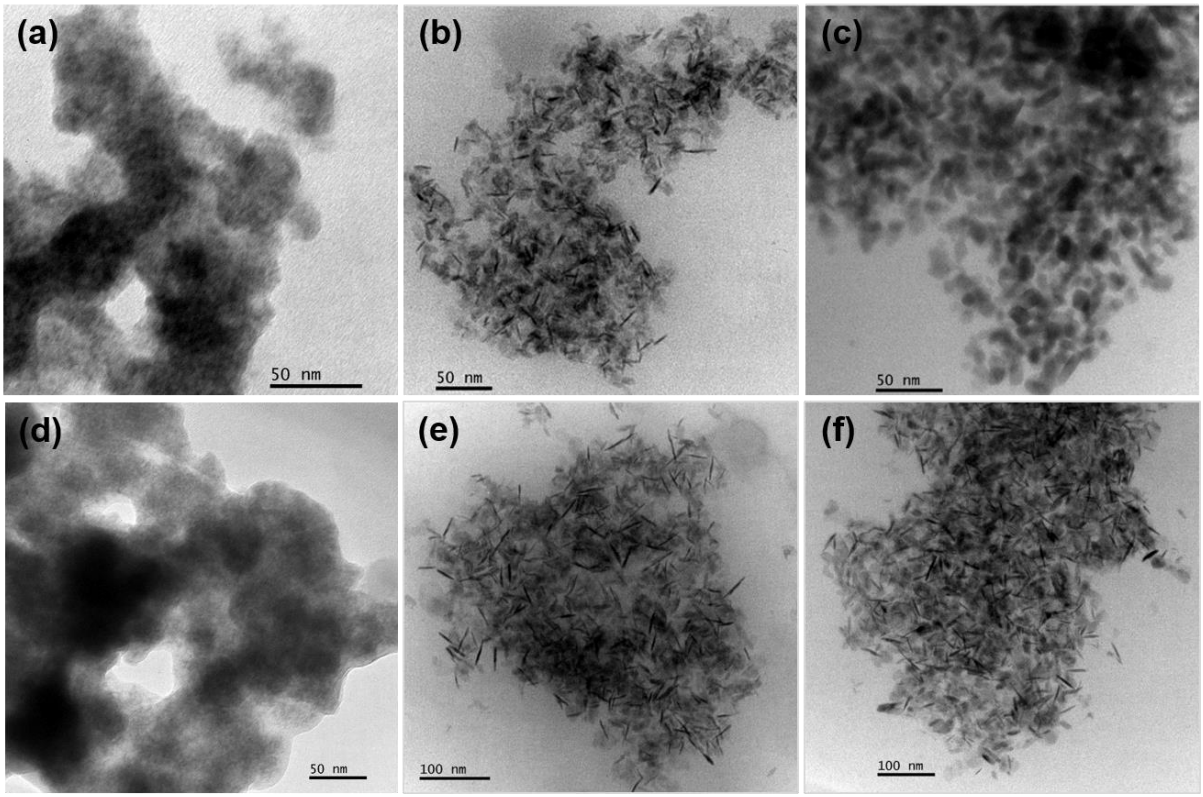

Figure 4.2: The TEM images of castor oil-capped β-In_2S_3 nanoparticles obtained at (a) 200 °C, (b) 250 °C, and (c) 300 °C. Olive oil-capped β-In_2S_3 nanoparticles obtained at (d) 200 °C, (e) 250 °C, and (f) 300 °C.

The optical properties of the nanoparticles through the ultraviolet-visible-near infrared (UV–Vis–NIR) absorption measurements corroborate observations from the p-XRD and TEM data. The nature of the capping agent and reaction temperature have an influence on the optical properties of the β-In_2S_3 nanoparticles produced. The former however does not provide adequate information for the amorphous materials produced at 200 °C, Figure 4.3.

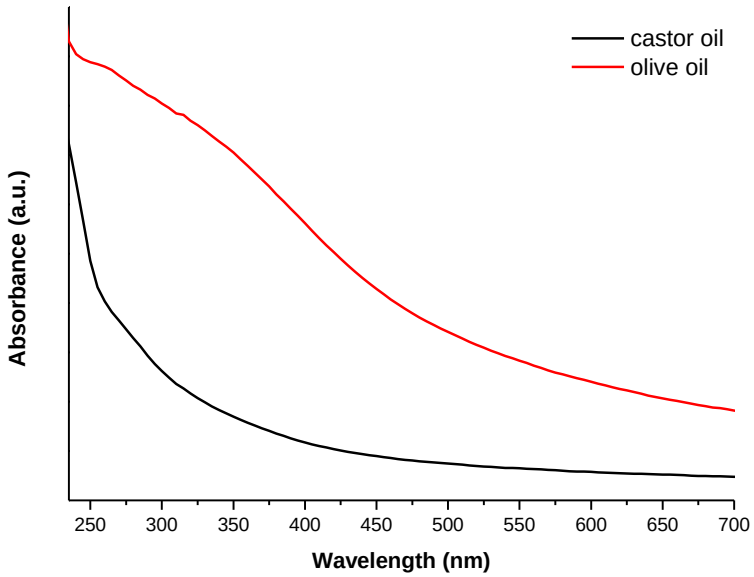

Figure 4.3: The UV-Vis-NIR absorption spectra of In_2S_3 nanoparticles obtained at 200 °C.

At higher temperatures, the absorption spectra exhibit less pronounced absorption onsets, Figure 4.4a and Figure 4.4c. This observation is commonly attributed to poor particle size distribution. In accordance with the TEM images, the dual absorption band observed in Figure 4.4c for 300°C can be explained by a transverse and longitudinal absorption feature known to occur in particles with a rod-like morphology.[47–49] An increase in reaction temperature results in a decrease in estimated band gap energies, owing to conditions that favour the formation of relatively larger particles due to the Ostwald ripening process.[50] The process entails the thermodynamic-assisted fast nucleation rate at the expense of the precursor concentration; the resulting smaller particles attach to larger particles as means of reducing their high surface energy. Regardless of this, the castor oil-capped nanoparticles are found to exhibit higher band gap energies relative to olive oil-capped nanoparticles. This is a common observation ascribed to an inverse proportionality of band gap energy to the particle size as it approaches the Bohr exciton diameter, a phenomenon known as the quantum confinement effect.[51] Band gap energies of 4.3 eV and 4.0 eV are estimated for castor oil-capped nanoparticles at 250 °C and 300 °C reaction temperatures, respectively, Figure 4.4b. Olive oil-capped nanoparticles

display band gap energies of 3.7 eV and 3.5 eV at 250 °C and 300 °C, respectively, Figure 4.4d. The band gap energies are found to be blue-shifted to that of the bulk counterpart (2.0–2.8 eV).[52]

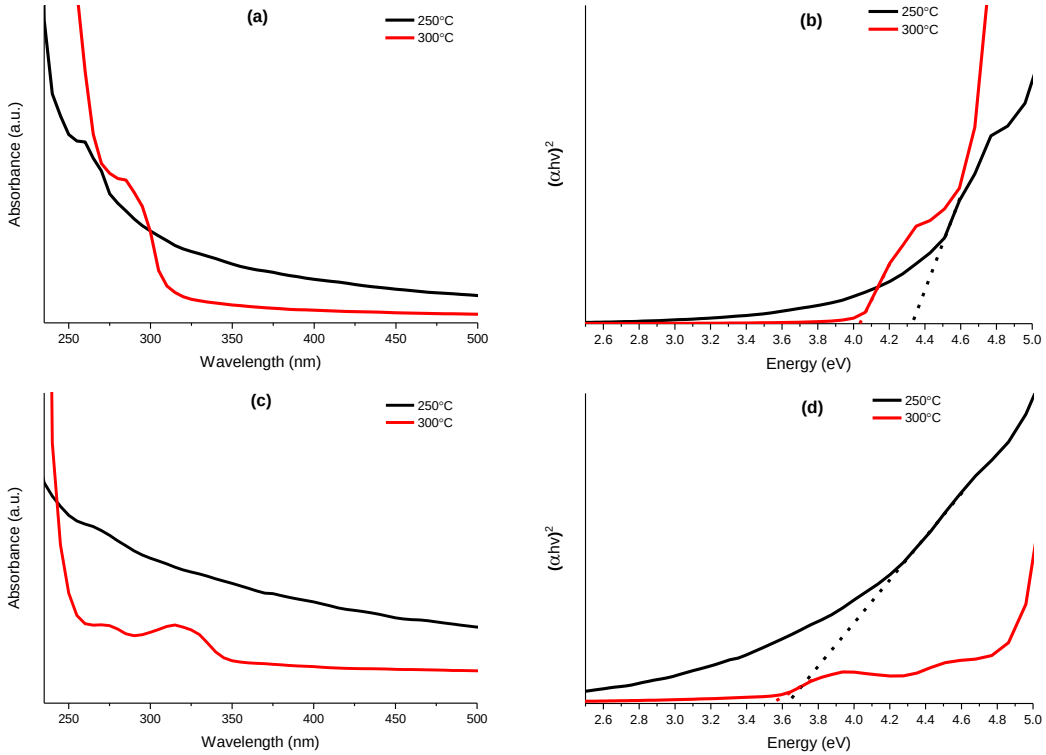

Figure 4.4: The (a) UV-Vis-NIR spectra and the corresponding (b) Tauc plots for the castor oil-capped β-In_2S_3 nanoparticles. The (c) UV-Vis spectra and the corresponding (d) Tauc plots for the olive oil-capped β-In_2S_3 nanoparticles.

4.3.2 $CuInS_2$ nanoparticles

The dual-molecular source fabrication approach utilizing equimolar In(III) ethyl xanthate (**13**) and Cu(II) ethyl xanthate (**14**) complexes affords black-coloured solids typical of $CuInS_2$. Observations were similar for both castor oil and olive oil-mediated reactions, regardless of the type of the ligand used.

The crystallographic nature of $CuInS_2$ is well known.[36,53] Three crystallographic phases, namely: chalcopyrite, zinc blende and wurtzite are stable at room temperature, *ca.* 980 °C and ca.1045 °C, respectively. All these phases are stable at room temperature for nanomaterial-based counterparts, dependant on the reaction

parameters used. However, distinguishing the chalcopyrite phase from the identical zinc blende phase becomes challenging at the nanometer scale, due to the broadness of the peaks. In this study, the p-XRD patterns of all nanoparticles were identical and well-matched to the roquesite mineral, $CuInS_2$ (card no.: 01-075-0106) exhibiting a chalcopyrite phase, Figure 4.5. This standard pattern was simulated from the single crystal X-ray data acquisition for ICSD 28739 and exists in a tetragonal crystallographic system. The lattice parameters *a* and *c* calculated for the as-prepared $CuInS_2$ nanoparticles were found to be within range *a* = 5.517(5) Å and *c* = 11.06(1) Å of the standard pattern, Figure 4.6 and Figure 4.7, respectively. The errors and trends observed in the calculations using the Celref software possibly result from the relative poor crystallinity of the nanoparticles which improves with increase in reaction temperature and coordinating solvent.

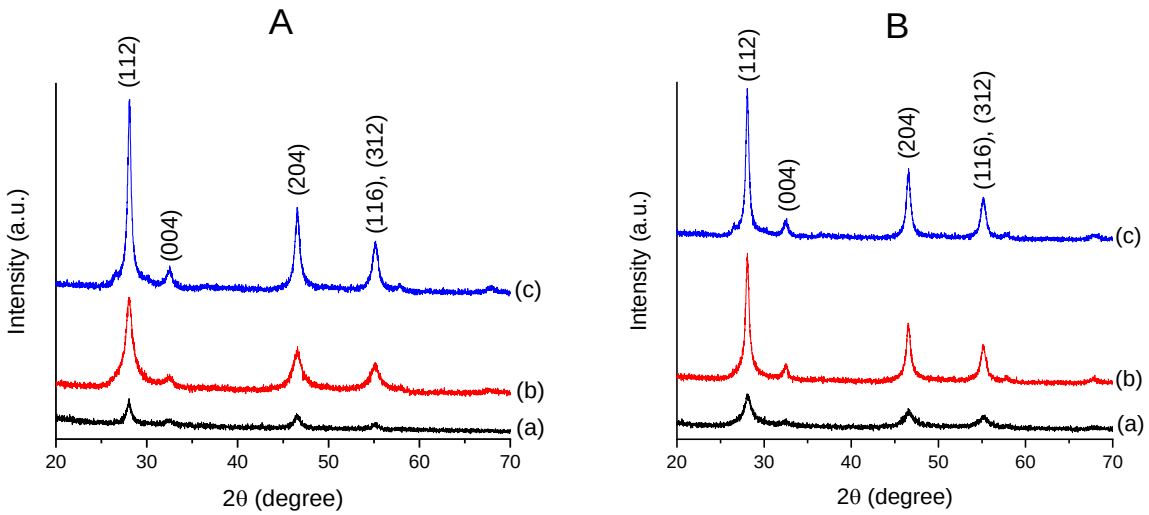

Figure 4.5: The p-XRD patterns for (A) castor oil-capped and (B) olive oil-capped chalcopyrite $CuInS_2$ nanoparticles (card no.: 01-075-0106) synthesized from (**13**) + (**14**) at (a) 200 °C, (b) 250 °C and 300 °C.

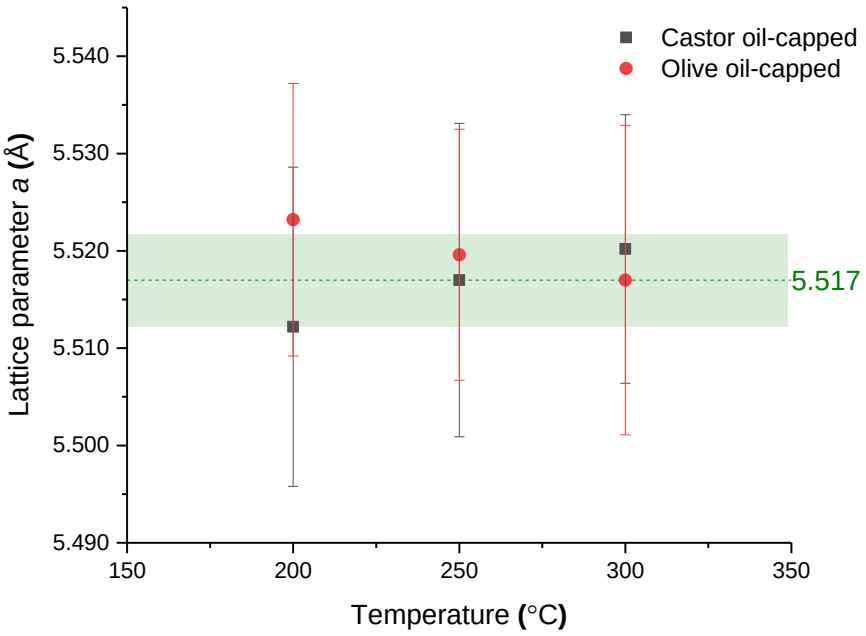

Figure 4.6: Calculated lattice parameter *a* for $CuInS_2$ nanoparticles compared to 5.517(5) Å for the $CuInS_2$ standard pattern 01-075-0106.

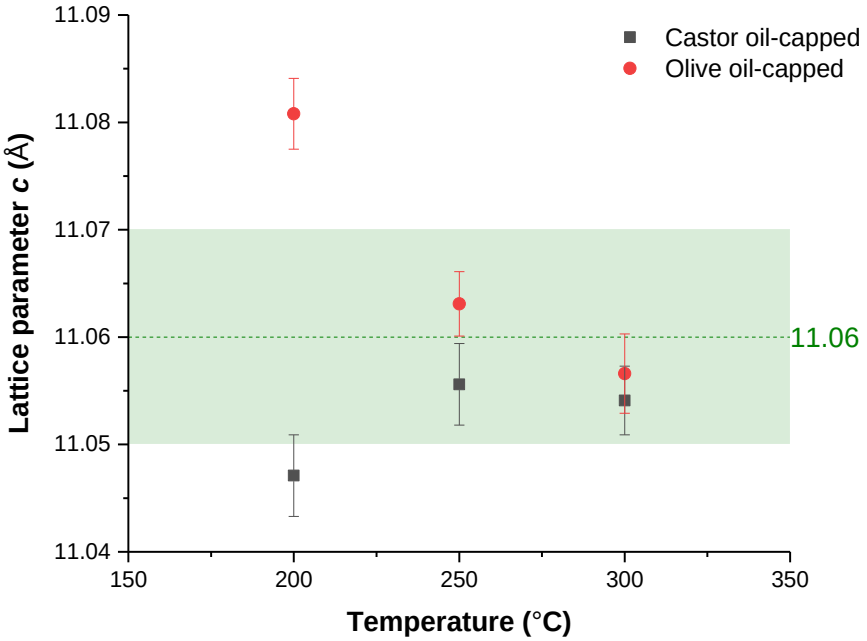

Figure 4.7: Calculated lattice parameter *c* for $CuInS_2$ nanoparticles compared to 11.06(1) Å for the $CuInS_2$ standard pattern 01-075-0106.

Although xanthates are desirable for their low decomposition temperature, the dual source system has no control on the morphology of the nanoparticles produced, regardless of the coordinating solvent used. The nanoparticles appear irregularly shaped, thus morphology and particle size determination proved to be a challenge. However, the nanoparticles appear anisotropic in nature with predominant cubic-like morphology, Figure 4.8. The high resolution TEM image shows lattice fringes with the inter-lattice spacing of 1.67 Å corresponding to the (116) plane, Figure 4.8d.

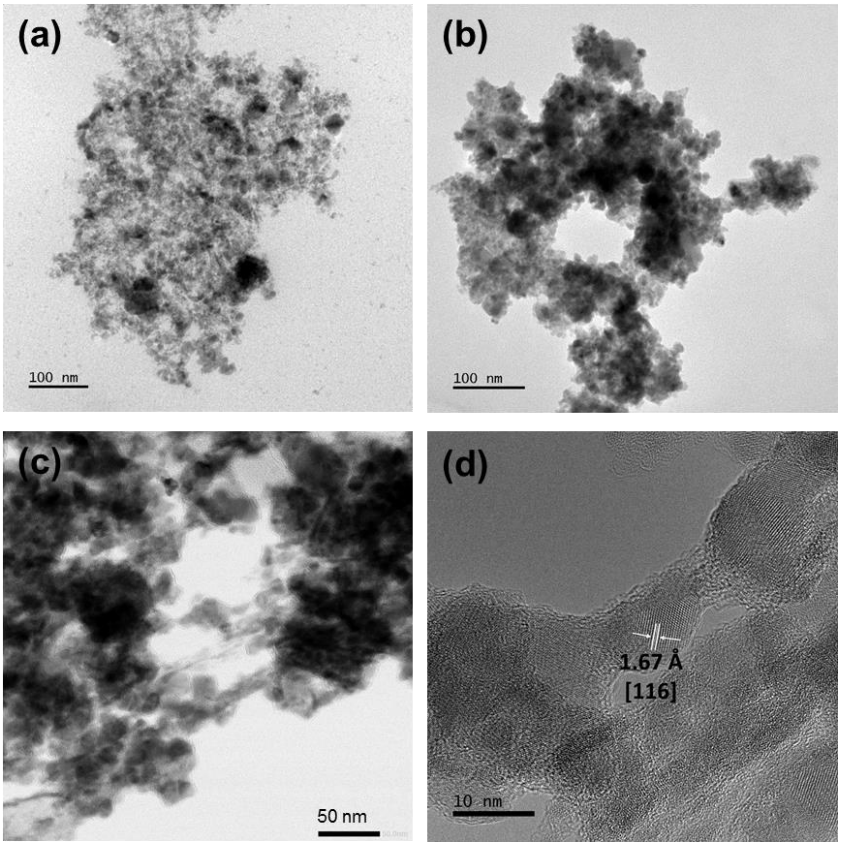

Figure 4.8: TEM images of castor oil-capped $CuInS_2$ nanoparticles synthesized from (**13**) + (**14**) at (a) 200 °C, (b) 250 °C, (c) 300 °C, and (d) a high resolution TEM image for 300 °C.

The scanning electron microscopy images reveal similar observations made from the TEM images; the irregular shaped nanoparticles appear small in size, Figures 4.9a, c and e. Interestingly, the corresponding energy dispersive X-ray (EDX) spectra show a high Cu:In ratio at lower reaction temperatures, which gradually decreases with an increase in temperature, Figure 4.9b, d and f. This observation may be attributed to the general growth mechanism which follows the formation of copper

sulfide intermediate to which $CuInS_2$ emanates.[54] According to Xie *et al*.[55] the reactivity of the soft Lewis acid Cu^+ ions cannot be suppressed by the hard Lewis bases such as fatty acids, thus promoting the initial formation of copper sulfide nanophases. Similarly, current work uses castor oil and olive oil which contain ricinoleic acid and oleic acid as major fatty acid components, respectively. Regardless of this, the current approach entails the use of metal-organic precursors to which upon the hot-injection experiment their combined rapid decomposition is assumed, as the reaction temperatures are slightly above their thermal decomposition temperatures. However, this approach seems not to be effective in seeking alternative means relative to the controlled release of metal cations especially at lower reaction temperatures. The evidence to this is observed through the EDX spectrum of the olive oil-capped nanoparticles synthesized at 200 °C, where the Cu:In:S atomic ratio of 38.6:23.7:37.7 is suggestive of a $Cu_{2-x}S$- $CuInS_2$ system similarly to that observed by Connor *et al*.[54] According to their work, full conversion to attain ratios close to 1:1:2 is facilitated by the high mobility of the Cu^+ ions and lattice distortion at moderate temperatures. This may explain the similar observation on the castor oil-capped nanoparticles synthesized at 250 °C and 300 °C reaction temperatures. The trend is however negligible in the olive oil series, Figure 4.10. This suggests that the capping agents play a major role in the decomposition and subsequent reactivity of the precursors.

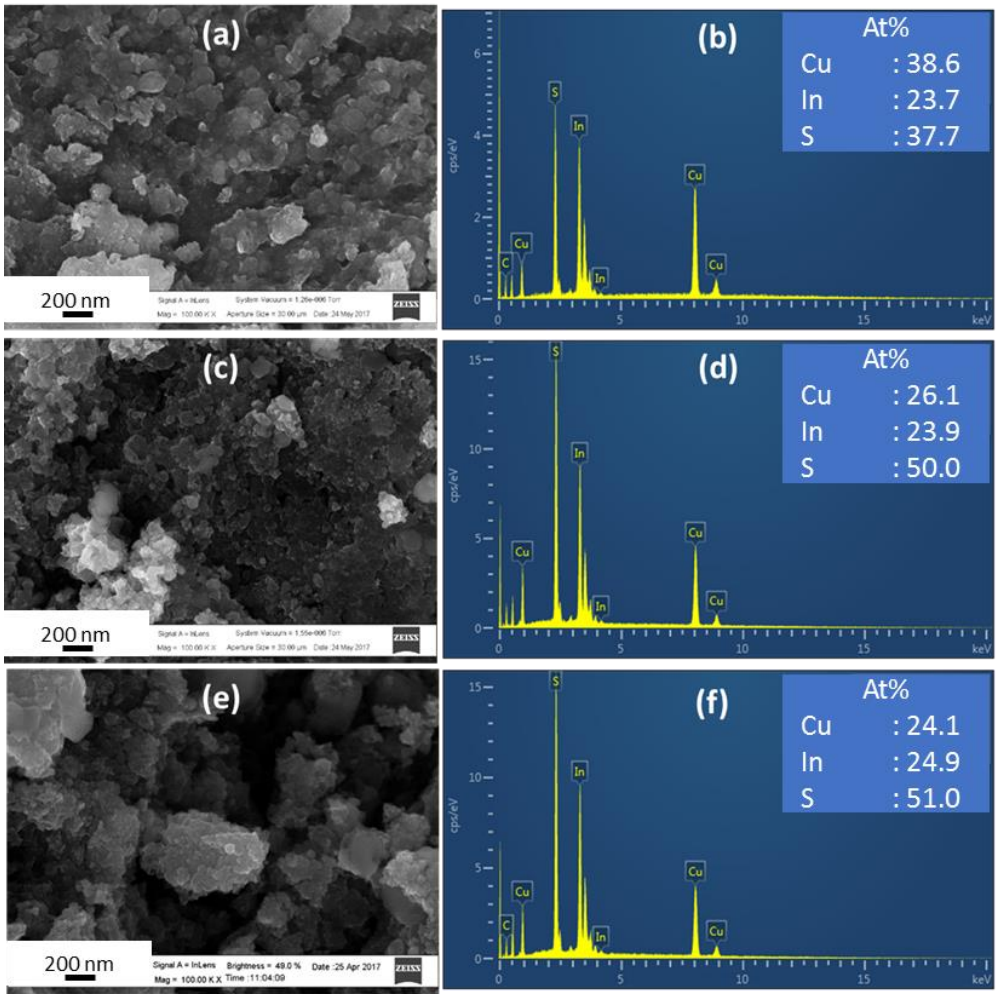

Figure 4.9: The scanning electron microscopy (SEM) images and the corresponding EDX spectra of the castor oil-capped $CuInS_2$ nanoparticles obtained in the ascending order of 200 °C, 250 °C and 300 °C reaction temperatures.

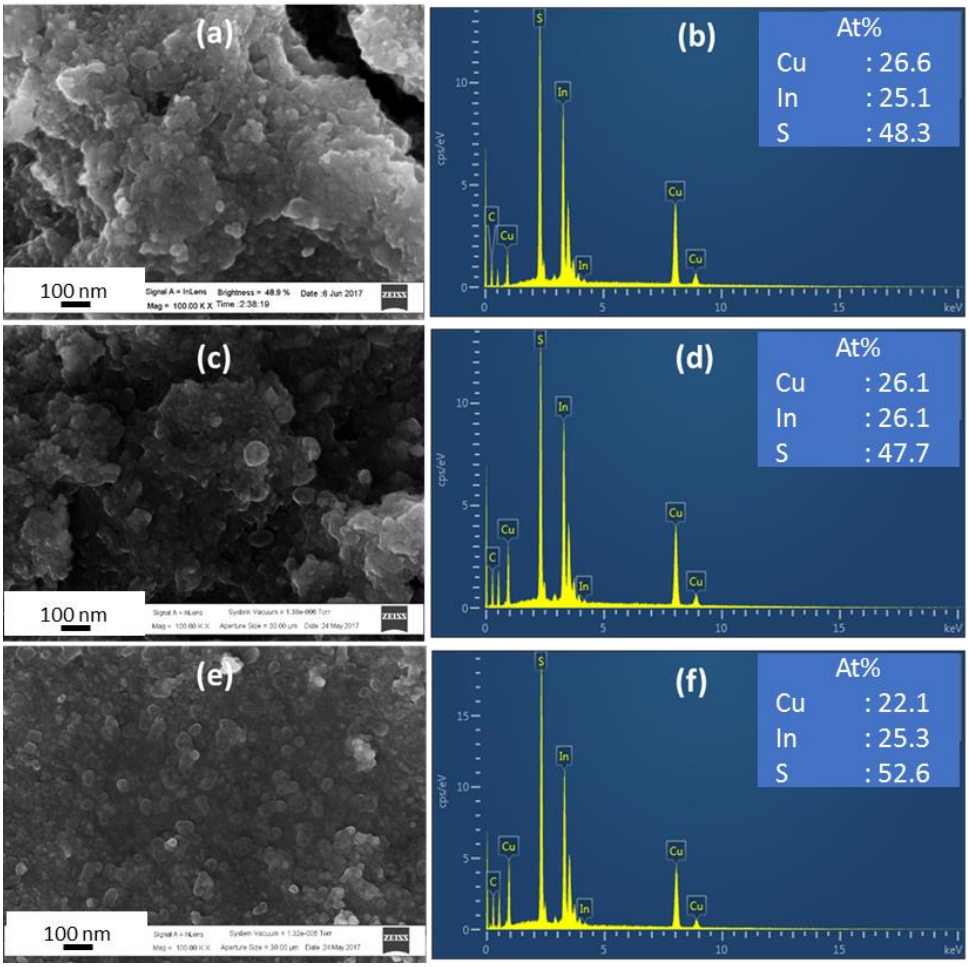

Figure 4.10: SEM images and the corresponding EDX spectra of the olive oil-capped $CuInS_2$ nanoparticles obtained in the ascending order of 200 °C, 250 °C and 300 °C reaction temperatures.

The UV–Vis–NIR absorption spectra of the nanoparticles display different absorption curves across the Vis-NIR region, complimentary to the difference in crystallographic phases observed in their p-XRD patterns. The castor oil-capped nanoparticles show estimated band gaps of 1.37 eV, 1.4 eV and 1.15 eV (Figure 4.11), whereas the olive oil-capped nanoparticles show 1.5 eV, 1.38 eV and 1.2 eV (Figure 4.12) at reaction temperatures of 200 °C, 250 °C and 300 °C, respectively. The absorption spectra were identical to both capping agents. However, there is some degree of uncertainty in the estimated band gap energies, owing to the low linear profiles in the Tauc plots.

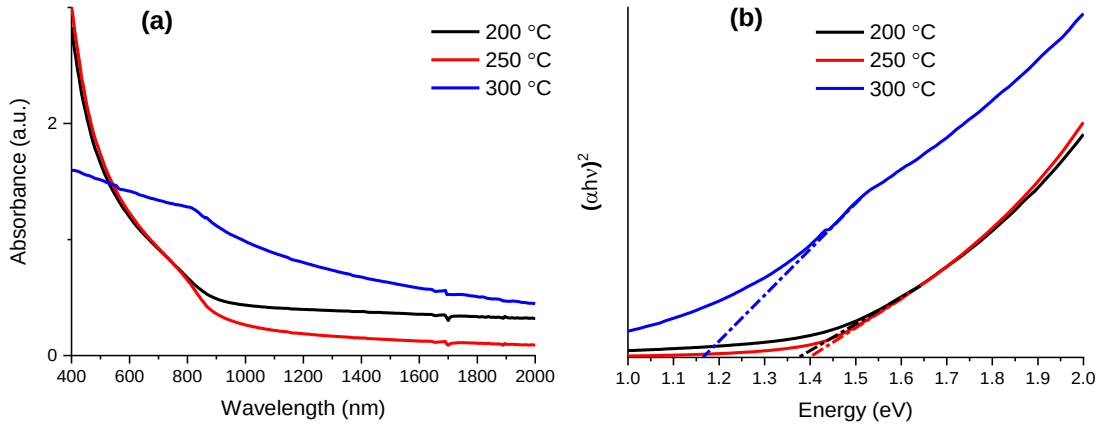

Figure 4.11: The (a) UV-Vis-NIR spectra and the corresponding (b) Tauc plots for the castor oil-capped $CuInS_2$ nanoparticles synthesized from (**13**) + (**14**).

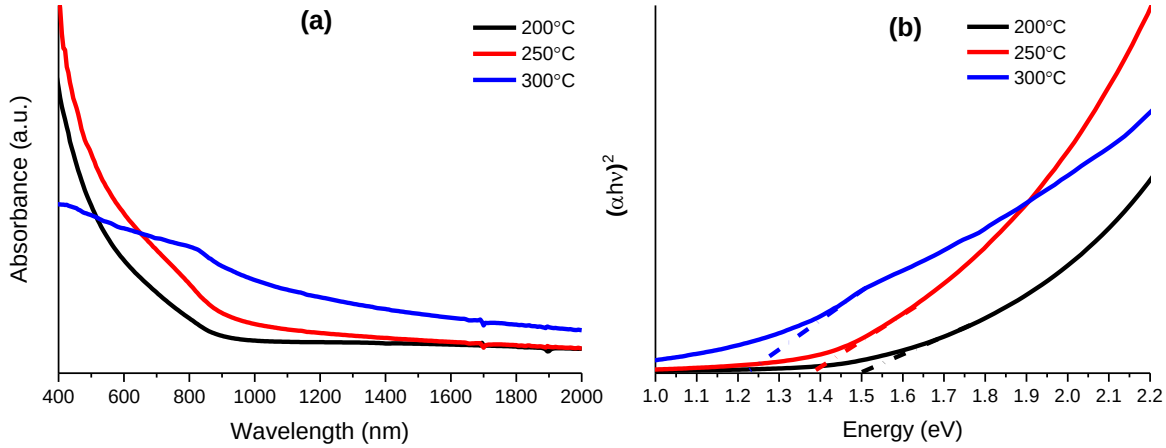

Figure 4.12: The (a) UV-Vis-NIR spectra and the corresponding (b) Tauc plots for the olive oil-capped $CuInS_2$ nanoparticles synthesized from (**13**) + (**14**).

4.3.3 The diethyl dithiocarbamate precursors approach

As a result of the core objective of the study, evaluation of castor oil and olive oil as green solvents for the production of non-toxic nanoparticles, the scope was extended to use an alternative class of precursors. Dithiocarbamates (DTCs) were then identified as appropriate precursors due to structural similarities to xanthates (XANs), thus ruling out possibilities of the solvents being selective towards specific precursors. As a result, this section aimed at introducing another parameter: the influence of the class of precursor on the properties of the castor oil and olive oil-capped β-In_2S_3 and $CuInS_2$ nanoparticles. The DTC precursors were prepared

following the synthetic protocols outlined in section 4.2.2.1 using commercial sodium diethyl dithiocarbamate trihydrate as a ligand. The precursors, *tris*-ethyldithiocarbamato indium(III) (**13D**) and *tris*-ethyldithiocarbamato copper(II) (**14D**), were obtained analytically pure as light-grey and brown crystal, respectively, from chloroform mother liquor.

The p-XRD patterns of the nanoparticles obtained from (**13D**) display a similar trend to that observed from (**13**) reactions. However, the proficiency of the coordinating solvents to produce crystalline nanoparticles was relatively lower in (**13D**). Clear evidence to this is observed in the diffraction patterns of olive oil-capped nanoparticles which suggest non-decomposed and incomplete decomposition of the precursor at 200 °C and 250 °C reaction temperatures, respectively, Figure 4.13. Regardless of this, TEM studies reveal morphological transformation which is both temperature and coordinating solvent-dependant. In the castor oil-mediated reaction, irregular sphere-like nanoparticles (5.16 ± 1.47 nm) are obtained at 200 °C, Figure 4.14a, which transform to irregular shaped nanosheets of average lengths of (33.3 ± 3.99 nm) and (435 ± 82.3 nm) at 250 °C and 300 °C, Figure 4.14b and c, respectively. The nanosheets obtained at 300 °C resemble characteristics of the In_2S_3 sheets reported in literature, obtained from the hot-injection of the same complex in oleylamine.[17] When olive oil is used, the nanoparticles display rod-like features similarly to the castor oil-capped nanoparticles, although they are less pronounced. These features are observed at 200 °C (10.8 ± 1.09 nm) and 250°C (28.6 ± 6.23 nm), Figure 4.15a and Figure 4.15b, respectively. Flower-like or urchin-like microstructures are obtained at 300 °C, Figure 4.15c, similarly to those reported by Chen *et al.*[16]

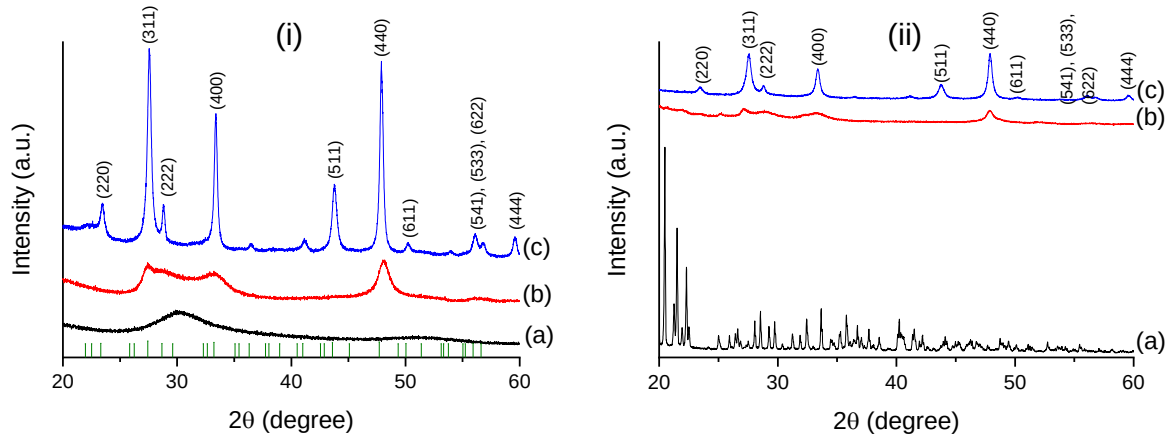

Figure 4.13: The p-XRD patterns for (i) castor oil-capped and (ii) olive oil-capped β-In_2S_3 nanoparticles fabricated from (**13D**) at (a) 200 °C, (b) 250 °C and 300 °C.

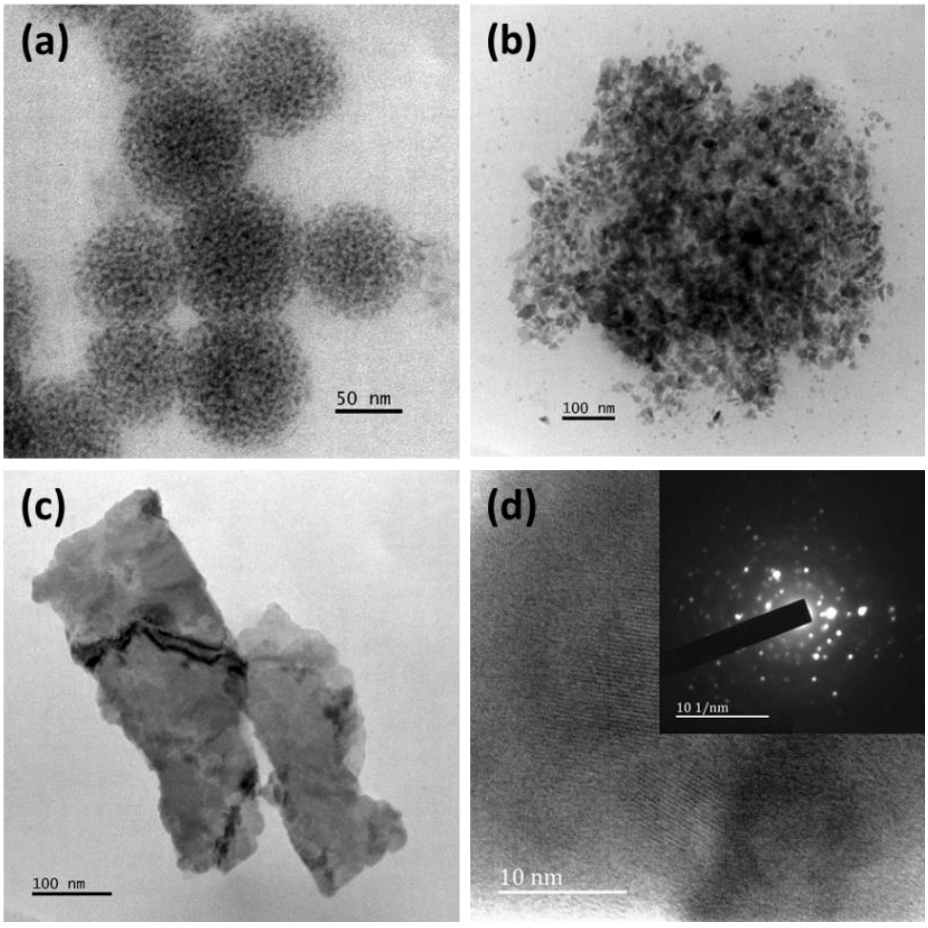

Figure 4.14: The TEM images of the castor oil-capped In_2S_3 nanoparticles obtained using (**13D**) at (a) 200 °C, (b) 250 °C, (c) 300 °C, and the high resolution TEM image of the nanosheets obtained at 300°C (inset: SAED image).

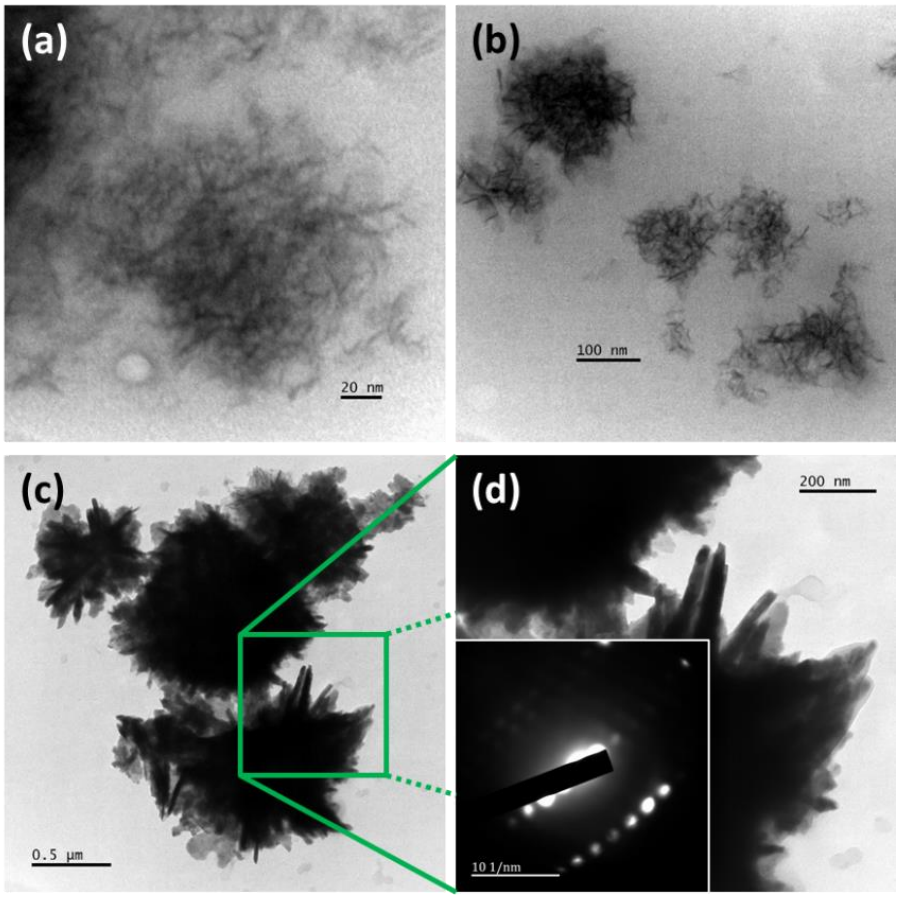

Figure 4.15: The TEM images of the olive oil-capped In_2S_3 nanoparticles obtained using (**13D**) at (a) 200 °C, (b) 250 °C, (c) 300 °C, and the (d) high magnification TEM image of 300 °C (inset: SAED image).

Interestingly, the crystallographic phase changes to wurtzite $CuInS_2$ (Card no.: 01-077-9459) when the DTC system is employed, in comparison to chalcopyrite obtained from the XAN system. The observation was independent of the coordinating solvent used, Figure 4.16 and 4.17. Sakamoto *et al*.[56] also made similar phase change observation, where the spherical nanoparticles were identified as chalcopyrite $CuInS_2$ and hexagonal nanodiscs as wurtzite $CuInS_2$, when using a three-component system, i.e. different metal and sulfur sources. This prompted a pilot evaluation of the oleylamine coordinating solvent used in their study, specifically on the DTC system also used in this work. The DTC system was preferred for this investigation, owing to the additional unindexed peaks. This was indicative of either phase or material impurity, which was observed with an increase in reaction temperature on both castor oil and olive oil-mediated reactions. The additional unindexed peaks observation was pronounced in the olive oil-mediated reaction. The unidentified species may be multi

phases of copper sulfide material, since the common growth mechanism is reported to be initiated by the formation of copper sulfide nanoparticles which then become templates to which $CuInS_2$ nanoparticles grow from. Thus, oleylamine was investigated as an alternative coordinating solvent for the DTC system. Interestingly, the oleylamine-capped $CuInS_2$ nanoparticles obtained from this work, at all temperatures, were matched to chalcopyrite $CuInS_2$ (Figure 4.18), as opposed to the wurtzite phase from castor oil and olive oil-capped counterparts. This is additional evidence that crystallographic phase change is also influenced by the type of the coordinating solvent, in addition to the type of precursors used.

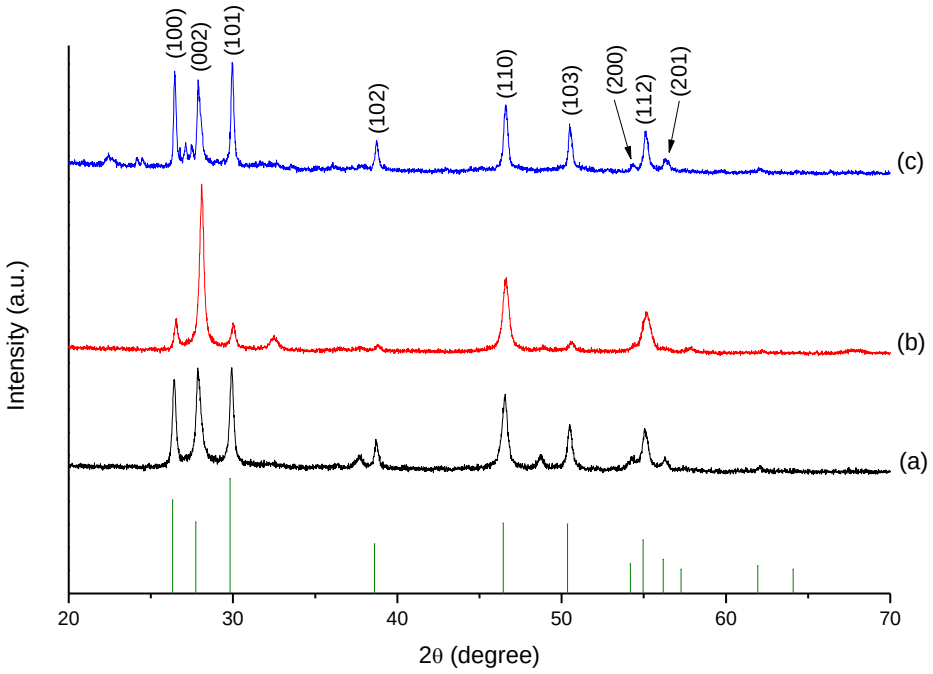

Figure 4.16: The p-XRD patterns for castor oil-capped wurtzite $CuInS_2$ nanoparticles (Card no.: 01-077-9459) synthesized from (**13D**) + (**14D**) at (a) 200 °C, (b) 250 °C and 300 °C.

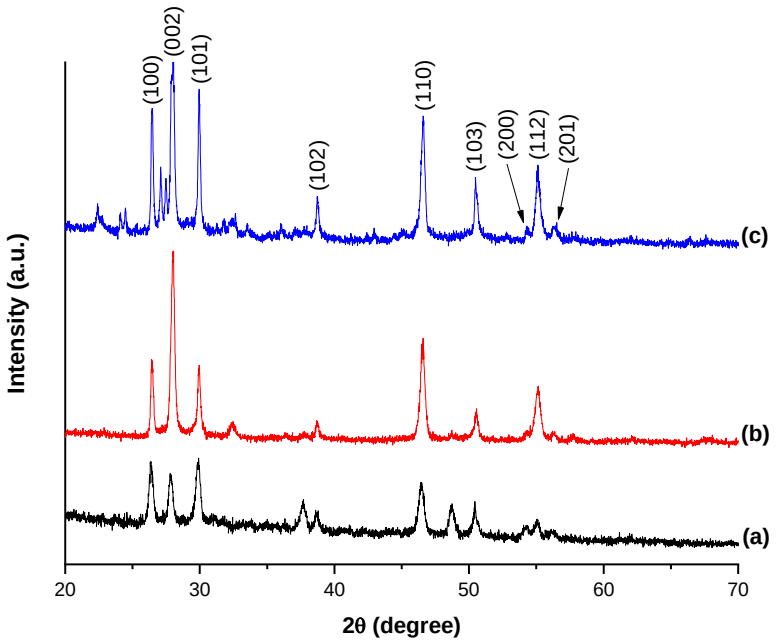

Figure 4.17: The p-XRD patterns for olive oil-capped wurtzite $CuInS_2$ nanoparticles (Card no.: 01-077-9459) synthesized from (**13D**) + (**14D**) at (a) 200 °C, (b) 250 °C and 300 °C.

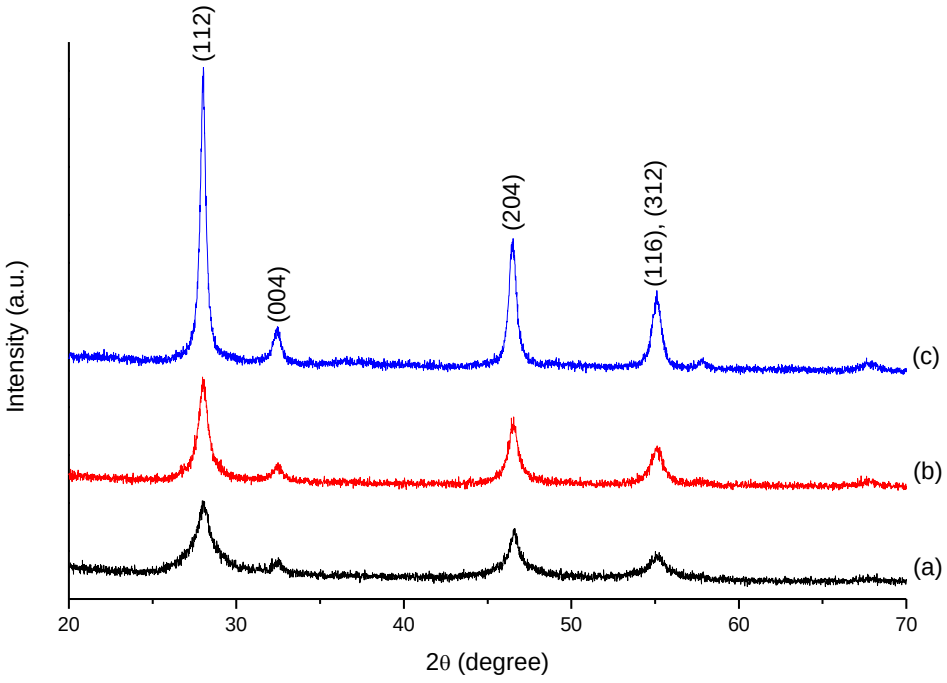

Figure 4.18: The p-XRD patterns for oleylamine-capped chalcopyrite $CuInS_2$ nanoparticles (card no.: 01-075-0106) synthesized from (**13D**) + (**14D**) at (a) 200 °C, (b) 250 °C and 300 °C.

The particle size and shape became more defined when the DTC system was employed in place of the XAN system, Figure 4.19. The particle sizes are relatively bigger compared to those from the XAN system. The particle shapes are mostly cubic-like. Castor oil-capped nanoparticles have particles with average sizes of 43.5 ± 5.01 nm, 84.0 ± 13.4 nm and 167 ± 21.0 nm obtained at 200 °C, 250 °C and 300 °C, respectively. Average particle sizes of 25.0 ± 1.67 nm, 275 ± 48.4 nm and 312 ± 47.1 nm for olive oil-capped nanoparticles obtained at 200 °C, 250 °C and 300 °C, respectively. Irregular sphere-like oleylamine-capped nanoparticles exhibited average particle sizes of 4.66 ± 0.49 nm, 11.7 ± 2.39 nm and 19.1 ± 2.91 nm obtained at 200 °C, 250 °C and 300 °C, respectively (Figure 4.20).

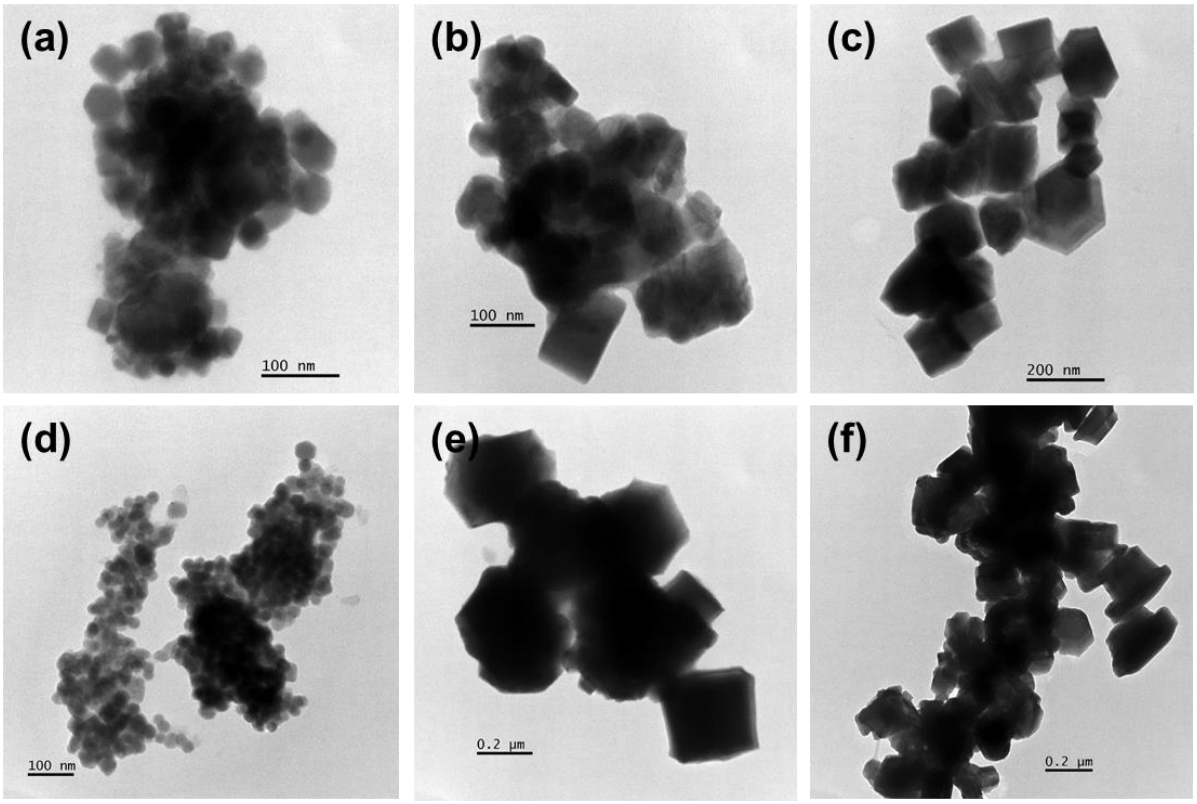

Figure 4.19: The TEM images of castor oil-capped wurtzite $CuInS_2$ nanoparticles obtained at (a) 200 °C, (b) 250 °C, and (c) 300 °C. Olive oil-capped wurtzite $CuInS_2$ obtained at (d) 200 °C, (e) 250 °C, and (f) 300 °C.

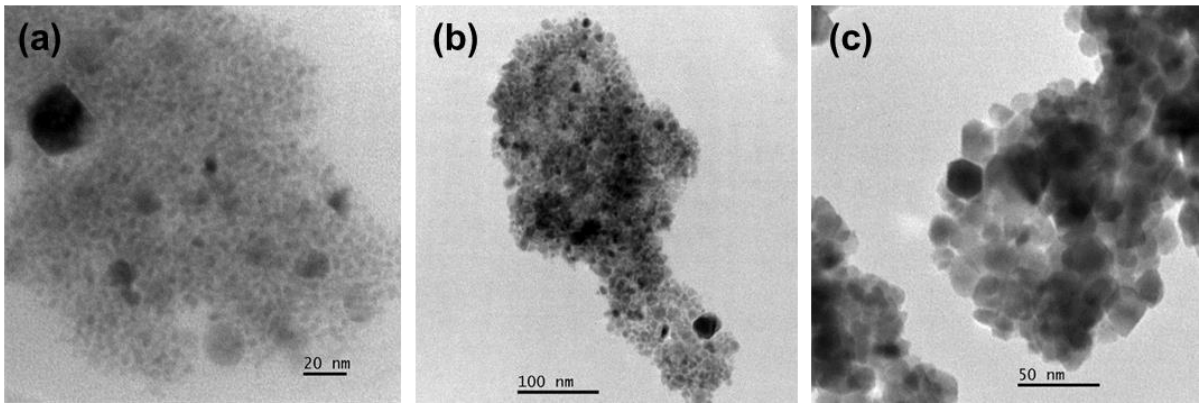

Figure 4.20: The TEM images of oleylamine-capped chalcopyrite $CuInS_2$ nanoparticles obtained at (a) 200 °C, (b) 250 °C, and (c) 300 °C.

Although the UV-Vis-NIR absorption measurements for the β-In_2S_3 nanoparticles presented a challenge, the $CuInS_2$ nanoparticles displayed different absorption curves across the Vis-NIR region, complimentary to the difference in crystallographic phases observed in their p-XRD patterns. The DTC system shows castor oil-capped nanoparticles exhibiting estimated band gaps of 1.0 eV, 0.88 eV and 1.18 eV (Figure 4.21), while olive oil-capped nanoparticles show 1.92 eV, 0.75 eV and 1.08 eV (Figure 4.22) at fabrication temperatures of 200 °C, 250 °C and 300 °C, respectively.

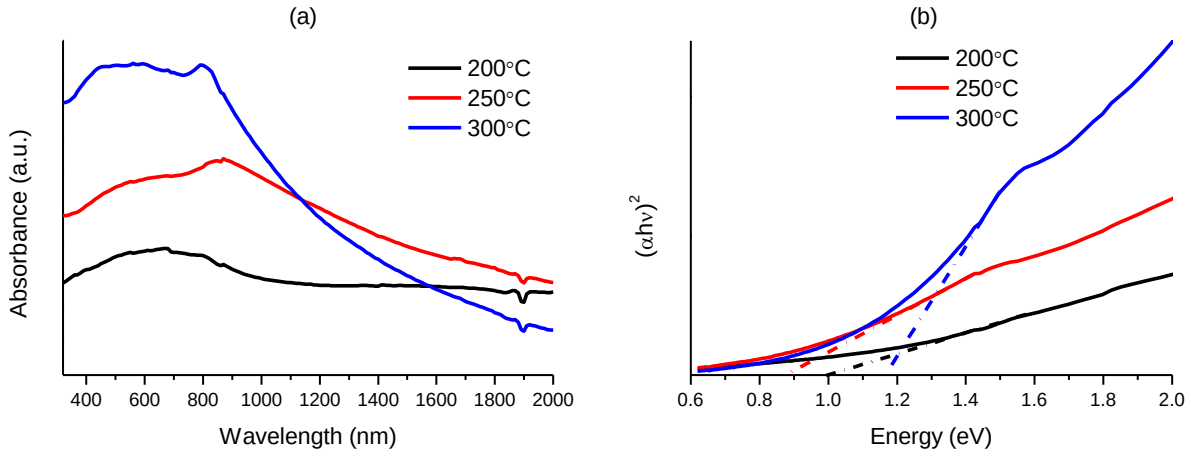

Figure 4.21: The (a) UV-Vis-NIR spectra and the corresponding (b) Tauc plots for the castor oil-capped $CuInS_2$ nanoparticles synthesized from (**13D**) + (**14D**).

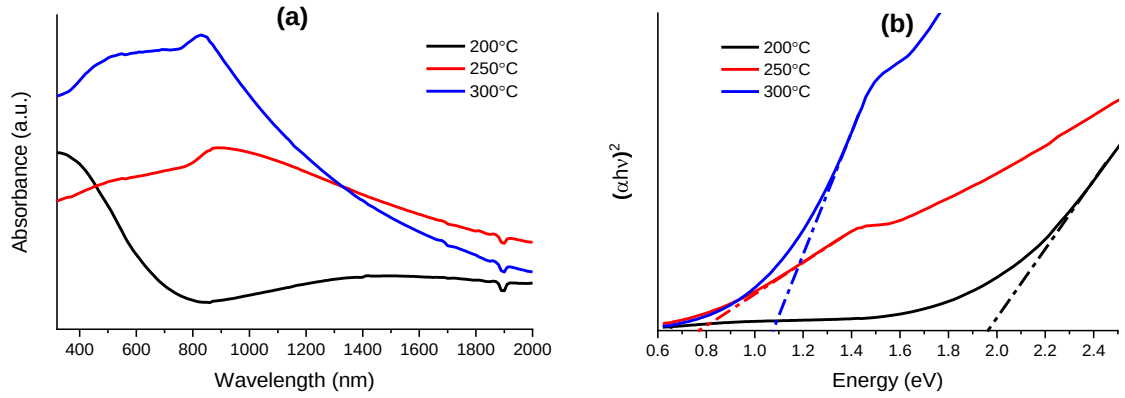

Figure 4.22: The (a) UV-Vis-NIR spectra and the corresponding (b) Tauc plots for the olive oil-capped $CuInS_2$ nanoparticles synthesized from (**13D**) + (**14D**).

4.4 Conclusion

Castor oil and olive oil were used as green capping agents for nontoxic β-In_2S_3 and $CuInS_2$ nanoparticles. The nanoparticles were synthesized by a hot-injection method, using In(III) and Cu(II) ethyl xanthate complexes as molecular precursors. The reaction temperature and type of the coordinating solvent used have a significant influence in determining the particle size and shape, as well as the optical properties of the as-prepared nanoparticles. The β-In_2S_3 nanoparticles predominantly exhibit a rod-like morphology where the average sizes of castor oil-capped nanoparticles are relatively smaller (12.2–14.5 nm) compared to the olive oil-capped nanoparticles (30.1–35.1 nm). The band gaps of the nanoparticles increase with a decrease in particle sizes due to the quantum confinement effect; 4.0–4.3 eV and 3.5–3.7 eV for the castor and olive oil-capped nanoparticles respectively. The band gaps were estimated from solution-based absorbance measurements as opposed to the normal practice, transmittance measurements. As such, there is some degree of uncertainty in the estimated values, arising from various factors such as solvent and excess capping agent interferences. The dual-precursor approach, i.e. (**13**) + (**14**) in a 1:1 (In:Cu) precursor mole ratio, afforded roquesite mineral (chalcopyrite $CuInS_2$). Predominantly irregular sphere-like nanoparticles are obtained, with band gaps ranging between 1.15–1.50 eV.

Castor oil and olive oil further displayed their capping efficacies when a different class of precursors, dithiocarbamates (**13D**) and (**14D**), were used. In the case of β-In_2S_3 nanoparticles, different morphologies (rods, sheets and urchin-like) were observed and influenced by reaction parameters (temperature and type of capping agent). The $CuInS_2$ nanoparticles showed larger particle sizes with a predominantly cubic morphology and were matched to wurtzite $CuInS_2$ compared to chalcopyrite obtained from the xanthate precursors.

References

[1] M. Green, *J. Mater. Chem*. **2010**, *20*, 5797.

[2] G.B. Shombe, E.B. Mubofu, S. Mlowe, N. Revaprasadu, *Mater. Sci. Semicond. Process*. **2016**, *43*, 230.

[3] L.D. Nyamen, N. Revaprasadu, P.T. Ndifon, *Mater. Sci. Semicond. Process*. **2014**, *27*, 191.

[4] J.W. Kyobe, E.B. Mubofu, Y.M.M. Makame, S. Mlowe, N. Revaprasadu, *Phys. E*, **2016**, *76*, 95.

[5] S. Mlowe, R. Pullabhotla, E. Mubofu, F. Ngassapa, N. Revaprasadu, *Int. Nano. Lett*. **2014**, *4*, 106.

[6] S. Iravani, *Green. Chem*. **2011**, *13*, 2638.

[7] A.Y. Zavrazhnov, A.V. Naumov, P.V. Anorov, E.G. Goncharov, V.I. Sidei, V.S. *Pervov, Inorg. Mater*. **2006**, *42*, 1294.

[8] A.V. Kosyakov, A.Y. Zavrazhnov, A.V. Naumov, *Inorg. Mater*. **2010**, *46*, 343.

[9] M.I. Hossain, P. Chelvanathan, M. Zaman, M.R. Karim, M.A. Alghoul, N. Amin, *Chalcogenide Lett*. **2011**, *8*, 315.

[10] S. Cingarapu, M.A. Ikenberry, D.B. Hamal, C.M. Sorensen, K. Hohn, K.J. Klabunde, *Langmuir* **2012**, *28*, 3569.

[11] R. Sumi, A.R. Warrier, C. Vijayan, *J. Phys. D: Appl. Phys*. **2014**, *47* 105103.

[12] N. Barreau, *Sol. Energy* **2009**, *83*, 363.

[13] S. Lugo-Loredo, Y. Peña-Méndez, M. Calixto-Rodriguez, S. Messina-Fernández, A. Alvarez-Gallegos, A. Vázquez-Dimas, T. Hernández-García, *Thin Solid Films* **2014**, *550*, 110.

[14] Y. Sharma, P. Srivastava, *Mater. Phys. Chem.* **2012**, *135*, 385.

[15] R. Diehl, R. Nitsche, *J. Cryst. Growth* **1973**, *20*, 38.

[16] X. Chen, Z. Zhang, X. Zhang, J. Liu, Y. Qian, *Chem. Phys. Lett*. **2005**, *407*, 482.

[17] S. Acharya, M. Dutta, S. Sarkar, D. Basak, S. Chakraborty, N. Pradhan, *Chem. Mater*. **2012**, *24*, 1779.

[18] S. Acharya, S. Sarkar, N. Pradhan, *J. Phys. Chem. Lett.* **2012**, *3*, 3812.

[19] N. Revaprasadu, M.A. Malik, J. Carstens, P. O'Brien, *J. Mater. Chem.* **1999**, *9*, 2885.

[20] S.W. Haggata, M.A. Malik, M. Motevalli, P. O'Brien, *Chem. Mater*. **1995**, *7*, 716.

[21] P. O'Brien, D.J. Otway, J.R. Walsh, *Thin Solid Films* **1998**, *515*, 57.

[22] A.N. MacInnes, M.B. Power, A.F. Hepp, A.R. Barron, *J. Organomet. Chem*. **1993**, *449*, 95.

[23] M. Afzaal, M.A. Malik, P. O'Brien, *Chem. Commun*. **2004**, 334.

[24] D.P. Dutta, G. Sharma, S. Ghoshal, N.P. Kushwah, V.M. Jain, *J. Nanosci. Nanotechnol*. **2006**, *6*, 235.

[25] V.G. Bessergenev, E.N. Ivanova, Yu.A. Kovalevskaya, S.A. Gromilov, V.N. Kirichenko, S.V. Larionov, *Inorg. Mater*. **1996**, *32*, 592.

[26] V.G. Bessergenev, A.V. Bessergenev, E.N. Ivanova, Y.A. Kovalevskaya, *J. Solid State Chem*. **1998**, *137*, 6.

[27] D.P. Dutta, G. Sharma, A.K. Tyagi, S.K. Kulshreshtha, *Mater. Sci. Eng. B* **2007**,*138*, 60.

[28] E. Quiroga-González, L. Kienle, C. Nather, V.S.K. Chakravadhanula, H. Luhmann, W. Bensch, *J. Solid State Chem*. **2010**, *183*, 2805.

[29] R. Nomura, K. Konishi, H. Matsuda, *Thin Solid Films* **1991**, *198*, 339.

[30] S.K. Batabyal, S.E. Lu, J.J. Vittal, *Cryst. Growth Des*. **2016**, *16*, 2231.

[31] P. Bera, S.I. Seok, *J. Nanopart. Res*. **2011**, *13*, 1889.

[32] A.L. Abdelhady, K. Ramasamy, M.A. Malik, P. O'Brien, *Mater. Lett.* **2013**, *99*, 138.

[33] M. Afzaal, D. Crouch, P. O'Brien, J.-H. Park, *J. Mater. Sci. Mater. Electron*. **2003**, *14*, 555.

[34] T.C. Deivaraj, J.-H. Park, M. Afzaal, P. O'Brien, J.J. Vittal, *Chem. Mater*. **2003**, *15*, 2383.

[35] G. Shang, K. Kunze, M.J. Hampden-Smith, E.N. Duesler, *Chem. Vap. Depos*. **1996**, *2*, 242.

[36] J. Kolny-Olesiak, H. Weller, *ACS Appl. Mater. Interfaces* **2013**, *5*, 12221.

[37] S.K. Batabyal, L. Tian, N. Venkatram, W. Ji, J.J. Vittal, *J. Phys. Chem. C*. **2009**, *113*, 15037.

[38] C. Sun, J.S. Gardner, E. Shurdha, K.R. Margulieux, R.D. Westover, L. Lau, G. Long, C. Bajracharya, C. Wang, A. Thurber, A. Punnoose, R.G. Rodriguez, J.J. Pak, *J*. *Nanomater*. **2009**, *2009*, 748567.

[39] C. Sun, J.S. Gardner, G. Long, C. Bajracharya, A. Thurber, A. Punnoose, R.G. Rodriguez, J.J. Pak, *Chem. Mater*. **2010**, *22*, 2699.

[40] (a) S.L. Castro, S.G. Bailey, R.P. Raffaelle, K.K. Banger, A.F. Hepp, *J. Phys*. *Chem*. *B* **2004**, *108*, 12429; (b) S.L. Castro, S.G. Bailey, R.P. Raffaelle, K.K. Banger, A.F. Hepp, *Chem. Mater*. **2003**, *15*, 3142.

[41] J.J. Nairn, P.J. Shapiro, B. Twamley, T. Pounds, R. Wandruszka, T.R. von Fletcher, M. Williams, C. Wang, M.G. Norton, *Nano Lett*. **2006**, *6*, 1218.

[42] J.S. Gardner, E. Shurdha, C. Wang, L.D. Lau, R.G. Rodriguez, J.J. Pak, *J*. *Nanopart*. *Res*. **2007**, *10*, 633.

[43] H. Zhong, Y. Zhou, M. Ye, Y. He, J. Ye, C. He, C. Yang, Y. Li, *Chem. Mater*. **2008**, *20*, 6434.

[44] A. Kharkwal, K. Jain, S.B. Tyagi, A.K. Singh, S.N. Sharma, M. Kharkwal, *Colloid Polym*. *Sci*. **2014**, *292*, 2913.

[45] C. Buchmaier, T. Rath, F. Pirolt, A.-C. Knall, P. Kaschnitz, O. Glatter, K. Wewerka, F. Hofer, B. Kunert, K. Krenn, G. Trimmel, *RSC Adv*. **2016**, *6*, 106120.

[46] D.P. Dutta, G. Sharma, *Mater. Lett*. **2006**, *60*, 2395.

[47] S. Link, M.A. El-Sayed, *J. Phys. Chem. B* **1999**, *103*, 8410.

[48] B.M.I. van der Zande, M.R. Böhmer, L.G.J. Fokkink, C. Schönenberger, *Langmuir* **2000**, *16*, 451.

[49] J.A. Creighton, D.G. Eadon, *J. Chem. Soc. Faraday Trans.* **1991**, *87*, 3881.

[50] J.A. Marqusee, J. Ross, *J. Chem. Phys*. **1984**, *80*, 536.

[51] Y. Wang, N. Herron, *J. Chem. Phys*. **1991**, *95*, 525.

[52] N. Barreau, S. Marsillac, J.C. Bernède, T. Ben Nasrallah, S. Belgacem, *Phys*. *Stat*. *Sol*. *(a)* **2001**,*184*, 179.

[53] A.D.P. Leach, J.E. Macdonald, *J. Phys. Chem. Lett.* **2016**, *7*, 572.

[54] S.T. Connor, C.-H. Hsu, B.D. Weil, S. Aloni, Y. Cui, *J. Am. Chem. Soc*. **2009**, *131*, 4962.

[55] R. Xie, M. Rutherford, X. Peng, *J. Am. Chem. Soc*. **2009**, *131*, 5691.

[56] M. Sakamoto, L. Chen, M. Okano, D.M. Tex, Y. Kanemitsu, T. Teranishi, *J. Phys. Chem. Lett.* **2015**, *119*, 11100.

CHAPTER 5

5 Solventless synthesis of indium sulfide nanoparticles and aggregates from the thermal decomposition of indium(III) complexes

5.1 Introduction

The indium-sulfur (In-S) binary metal chalcogenide system is of interest in optoelectronics[1, 2] and catalysis[3, 4] due to attractive properties such as various crystallographic phases[5, 6] and band gap of ~2 eV.[7] The most easily accessed and found phases are InS, In_3S_4, In_6S_7 and In_2S_3.[2] Indium sulfide semiconductors are classified as non-toxic and have potential as an alternative to the toxic cadmium sulfide as used in buffer in cadmium gallium indium selenide/sulfide solar cells.[8] More recently in the search for 2D materials beyond graphene, the InS phase, in the form of a two atom-thin layered material or two-dimensional (2D) nanomaterial has gained attention.[9] However, synthetic chemical routes rarely afford crystalline InS, and any heating usually induces a phase change to the thermodynamically stable In_2S_3 species.[10] The In_2S_3 phase exists in α (cubic), β (tetragonal) and γ (trigonal) polymorphic forms as a result of defects responsible for vacancies within the structure.[11] The widely reported β-In_2S_3 and the less reported γ-In_2S_3, a layered material with similar potential to InS for forming 2D materials, are stable at room temperature.[12]

Access to thin films and nanoparticles of β-In_2S_3 through a synthetic approach, can follow either the multiple precursor route or single source molecular precursor (SSP) route. Since control over phase is a common challenge to both routes, the former is usually chosen due to compatibility with various synthetic approaches such as chemical bath deposition[4, 6, 13–15] and spray pyrolysis.[16–20] However, a variety of In(III) complexes as SSPs for the preparation of β-In_2S_3 and related nanostructures have been explored. Dithiocarbamates, among other classes of SSPs, have largely contributed towards the literature coverage on indium sulfide materials mainly due to the flexibility in designing and derivatizing the ligands using vast possibilities of moieties. The nature of the ligand, choice of synthetic method, as well as tweaking reaction parameters has been identified to have a significant influence on the

crystallographic and morphological preference of the indium sulfide material produced. In(III)-trisdiethyldithiocarbamate, [$In(S_2CNEt_2)_3$], has been demonstrated to produce β-In_2S_3 urchin-like microspheres composed of nanoflakes through the hydrothermal route,[21] nanometer to micrometer β-In_2S_3 sheets through the long alkyl chain amine-mediated thermolysis route,[22, 23] and InS quantum dots through the TOPO-mediated thermolysis route.[24] The organo-In complexes with the same diethyldithiocarbamate ligand, [$RIn(S_2CNEt_2)$] where R = dimethyl, diethyl and neopentyl produce films exhibiting different phases (InS, In_6S_7 and β-In_2S_3) which result from the influence of both type of ligand and temperature used in the low-pressure metal organic chemical vapour deposition (LP-MOCVD) reaction.[25] In another instance, the mixed alkydithiocarbamates of the formula [$In(S_2CNMeR)_3$] where R = *n*-Butyl and *n*-Hexyl, produce α-In_2S_3 thin films by LP-MOCVD.[26] An example of organo-In complexed with a mixed alkydithiocarbamate ligand, [$Et_2In(S_2CNMe^nBu)$], produces β-In_2S_3 thin films using standard MOCVD method.[10, 27] Alkyl thiolates,[28–30] thiobenzoates,[31] thiocarbazates,[32] thiobiurets,[33] thiophosphinates[34] and thiocarboxylates[35, 36] have also been reported in literature for the fabrication of indium sulfide nanoparticles and thin films exhibiting different phases and morphologies.

Xanthate metal complexes are a class of dithiolates with breakdown temperatures typically lower than that of dithiocarbamates and a decomposition pathway which results in volatile bi-products. Metal xanthate complexes have been explored to produce thin films and nanoparticles of a variety of metal chalcogenides at low temperatures ideal for large scale industrial processes where energy use is a major factor.[37–43] By choice of xanthate ligand, O'Brien and co-workers[40,41] demonstrated size control of PbS within melts and when mixed in polystyrene. Variation of xanthate ligand length was also explored in CuxSy demonstrating a similar effect on particle size.[39] Ternary phases of $Cd_xZn_{1-x}S$ and PbS_xSe_{1-x} have also be accessed using metal xanthate complexes.[38, 44] In contrast, very few indium xanthate complexes have been prepared and used as molecular precursors to afford indium sulfide and related nanocomposites.[45, 46] Interest has mainly been on thin films.[47, 48]

In this chapter, a series of In(III) xanthate complexes, [$In(S_2COR)_3$] where R = Me, Et, ^{i}Pr and ^{s}Bu, respectively, have been prepared and evaluated as potential

precursors for In_xS_y materials through a solventless pyrolysis method at different decomposition temperatures.

5.2 Experimental

5.2.1 Materials

Indium(III) chloride (98%, Aldrich), potassium ethyl xanthogenate (96%, Aldrich), 1-propanol (anhydrous 99.7%, Aldrich), methanol (≥99.9%, Aldrich), 2-butanol (anhydrous, 99.5%), potassium hydroxide, sodium hydride (dry 95%, Sigma-Aldrich), carbon disulfide (low benzene ≥99.9%, Sigma-Aldrich), diethylether (≥99.8%, Sigma-Aldrich), chloroform (≥99.5%, Sigma-Aldrich), and magnesium sulfate (anhydrous, ≥99.5%, Sigma-Aldrich) were used as received.

5.2.2 Synthesis of complexes

The potassium salts of xanthate ligands were synthesized by previous methods outlined in references, where an excess alcohol is reacted with equimolar potassium hydroxide and carbon disulfide in an ice bath.[39] The sodium *S*-(+)-sec-butyl xanthogenate ligand was prepared from the sodium hydride route reported elsewhere.[40]

5.2.2.1 Preparation of tris-ethyl xanthato indium(III) (13)

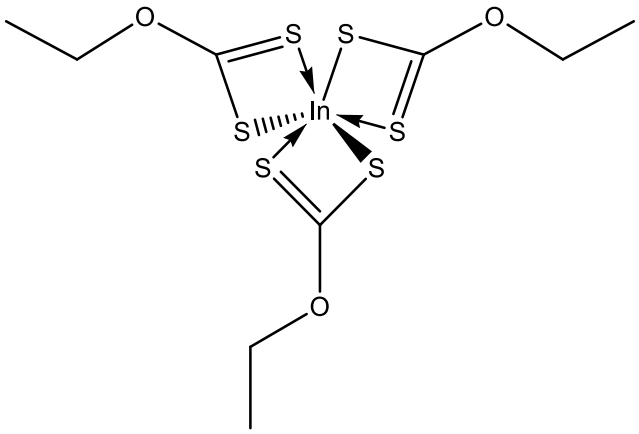

The complex was prepared in chapter 4 (section 4.2.2.1). In this chapter, the preparation protocols were modified as follow: indium(III) chloride (1.00 g, 4.52 mmol) was dissolved in dry tetrahydrofuran (100 mL). A solution of potassium

diethylxanthogenate (2.18 g, 13.6 mmol) in tetrahydrofuran was added to indium chloride solution forming a colourless precipitate. The white precipitate was collected by filtration and the indium ethyl xanthate was extracted by dissolving in chloroform. Residual water was removed by an organic workup prior to slow evaporation of chloroform in open air resulting in colourless crystals; Yield: 1.30 g, 60%.

Anal. Calc. % (Obtained) for $C_9H_{15}S_6O_3In$: C, 22.60 (22.95); H, 3.16 (2.94); S, 40.21 (39.84); In, 24.00 (23.64).

^1H NMR δ: 4.51 ($CH_3C\underline{H}_2$-, q), 1.49 ($C\underline{H}_3CH_2$-, t). $^{13}C\{^1H\}$ δ: 229.82, 76.13, 14.01.

5.2.2.2 Preparation of tris-methylxanthato indium(III) (15)

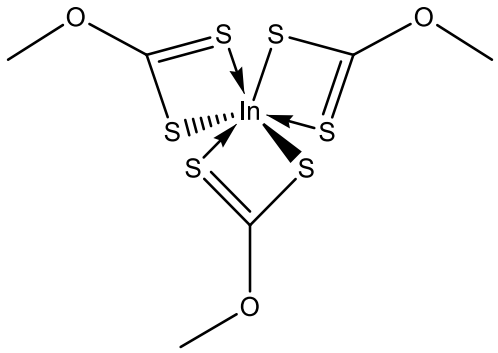

The synthesis of (**15**) followed the same procedure as for (**13**) except potassium methylxanthogenate (1.99 g, 13.6 mmol) was used in place of potassium diethylxanthogenate. Yellow crystals were obtained; Yield: 906 mg, 46%.

Anal. Calc. % (Obtained) for $C_6H_9S_6O_3In$: C, 16.52 (16.83); H, 2.08 (2.00); S, 44.09 (43.97); In, 26.31 (26.33).

^1H NMR δ: 4.19 (CH_3-, s). $^{13}C\{^1H\}$ δ: 231.47, 65.83.

5.2.2.3 Preparation of tris-isopropylxanthato indium(III) (16)

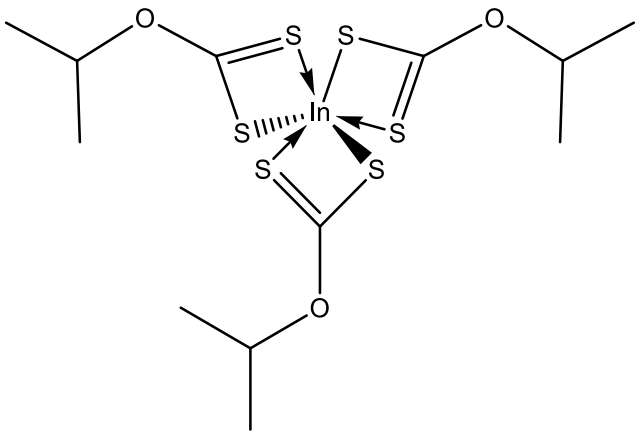

The synthesis of (**16**) followed the same procedure as for (**13**) except that potassium isopropylxanthogenate (2.37 g, 13.6 mmol) was used in place of potassium ethyl xanthogenate. Colourless crystals were obtained using cyclohexane for recrystallisation; Yield: 1.69 g, 72%.

Anal. Calc. % (Obtained) for $C_6H_9S_6O_3In$: C, 27.69 (28.01); H, 4.07 (4.01); S, 36.96 (36.99); In, 22.06 (21.96).

^{1}H NMR δ: 5.16 ($(CH_3)_2C\underline{H}$-, sep), 1.48 ($(C\underline{H}_3)_2CH$-, d). $^{13}C\{^1H\}$ δ: 229.04, 86.16, 21.79.

5.2.2.4 Preparation of tris-2-butylxanthato indium(III) (17)

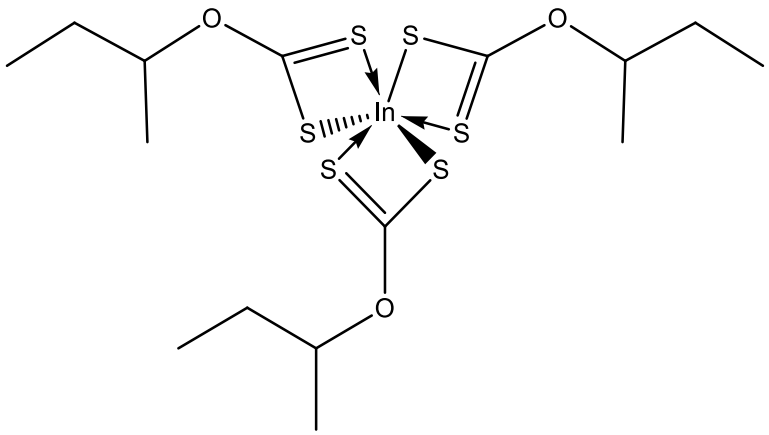

The synthesis of (**17**) followed the same procedure as for (**13**) except potassium 2-butylxanthogenate (4.77 g, 17.5 mmol) was used in place of potassium ethyl xanthogentate. Colourless oily product was obtained; Yield: 3.75 g, 79%.

Anal. Calc. % (Obtained) for $C_6H_9S_6O_3In$: C, 32.02 (32.21); H, 4.84 (4.76); S, 34.20 (34.05); In, 20.41 (20.23).

^{1}H NMR δ: 4.97 ($CH_3CH_2(C\underline{H}\text{-})CH_3$, sextet), 1.94, 1.79 ($CH_3C\underline{H}(CH\text{-})_6CH_3$, each m), 1.44 ($CH_3CH_2(CH\text{-})C\underline{H}_3$, d), 1.00 ($C\underline{H}_3CH_2(CH\text{-})CH_3$, t). $^{13}C\{^1H\}$ δ: 229.08, 90.79, 28.77, 18.86, 9.59.

5.2.3 Decomposition experiments

In a typical experiment, under Schlenk conditions, 0.5 mmol of the complex was placed in a ceramic boat under a nitrogen atmosphere at 50 °C. The furnace was then heated at 10 °C min^{-1} and held at the target temperature (200-600 °C) for an hour. The reaction was stopped by quickly cooling the reaction vesicle to room temperature.

5.2.4 Characterisation techniques

The characterisation techniques and instrument specifications used in this chapter are outlined in detail in section 2.2.4 of chapter 2, with minor modifications as follows:

- Powder X-ray diffraction patterns were indexed using standard diffraction patterns simulated online using the single-crystal diffraction data from http://www2.fiz-karlshuhe.de/icsd_web.htlm, using Cu Kα source (λ = 1.54184 Å) and 2θ range of 10°-80° parameters.
- Microelemental analyses were conducted on a Carlo Erba EA 1108 elemental analyzer attached to an Edwards E2M8 vacuum pump.
- The NMR spectra were recorded on a Bruker 500 spectrometer.
- Optical absorbance measurements were conducted at the UV-Vis-NIR spectral range on a Perkin-Elmer Lambda 1050 NIR UV-Visible spectrophotometer.
- The SEM imaging was used to determine the surface morphology of the nanoparticles. The nanoparticles sprinkled on a carbon tape prior to analyses. Imaging was conducted on a FEI Quanta 200 SEM equipped with an EDAX Genesis spectrometer.

5.2.4.1 Single-crystal X-ray crystallography (XRD)

The single-crystal XRD was used to elucidate the chemical structure of the complexes from their crystals. The diffractions were performed using a Bruker diffractometer equipped with a Cu Kα source (λ = 1.5418 Å) and Agilent diffractometer equipped with a Mo Kα source (λ = 0.71073 Å), at various temperatures.

5.3 Results and discussion

The nature of the study required that the complexes, herein used as single-source molecular precursors (SSPs), should be obtained as crystalline materials, making it easy to trail the mechanism by which the In_xS_y materials are formed. Among the SSPs used in this work (Figure 5.1), two have crystal structures known in literature, Et (**13**)[49] and ^{i}Pr (**16**)[50]. These complexes exhibit a geometry typical for trivalent In and Ga complexes incorporating bidentate ligands. The chemical structures exhibit a distorted geometry between trigonal prismatic octahedral, owing to the restricted bite angle of the xanthate ligands. The crystals of the former complex obtained from this work have identical features to those reported in literature, while the latter has been obtained as a cyclohexane solvate, where an asymmetric unit cell consists of a pair of complex and solvent compounds as opposed to a pair of isomeric complexes reported

by Jain and co-workers.[50] Regardless of this, both structures exhibit Z = 4 with two pairs existing as rotational isomers (*i.e.* Δ and Λ isomers).

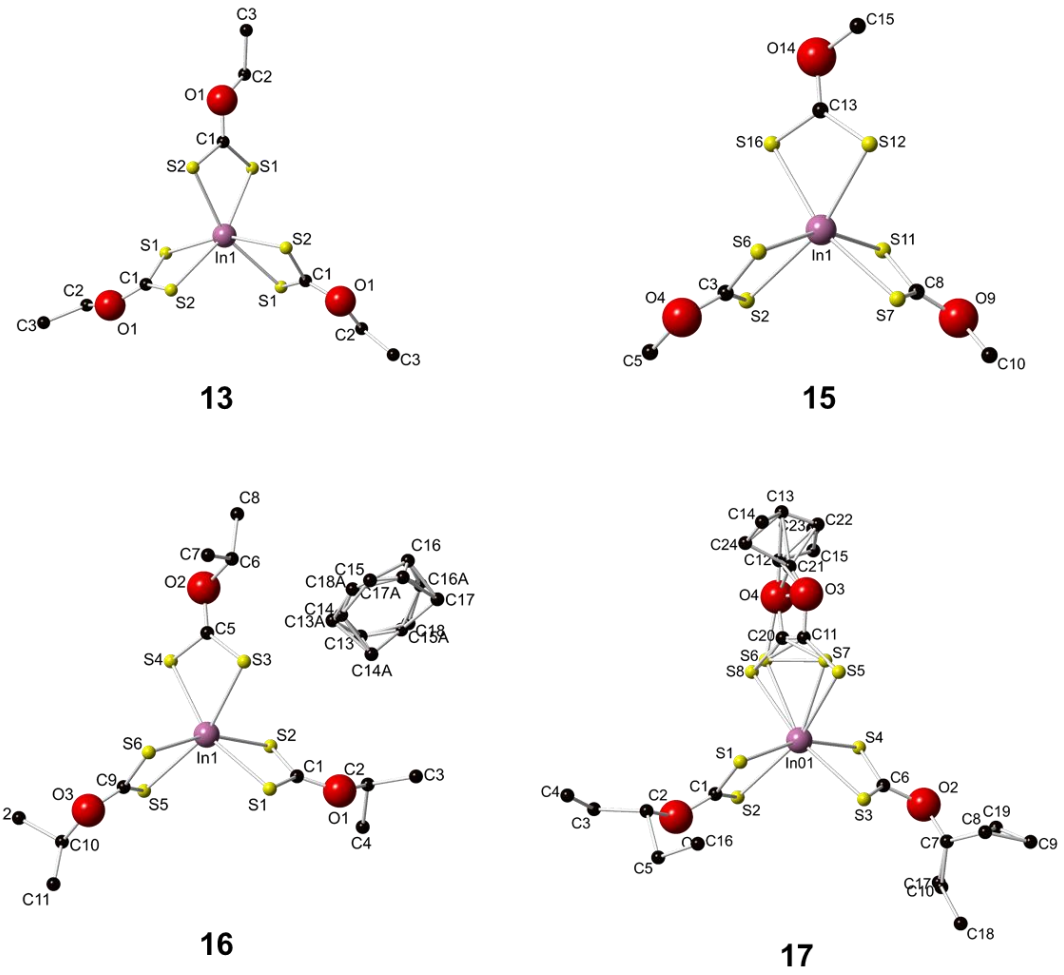

Figure 5.1: The asymmetric units of [In($S_2COEt)_3$] (**13**), [In($S_2COMe)_3$] (**15**) CCDC 1875344, [In($S_2CO^iPr)_3$] (**16**) CCDC 1875347 and [In($S_2CO^sBu)_3$] (**17**) CCDC 1875345 crystal structures. Black = C, yellow = S, red = O, purple = In.

Similar symmetry observation was made on the [In($S_2CO^sBu)_3$] SSP, although they have different Z values and space groups. The first [In($S_2CO^sBu)_3$] (**17**) complex was synthesized from racemic sec-butyl xanthate ligand, as a result, a disordered structure was obtained. The disorder is considered random by means of crystal packing and a contribution mostly arising from the racemic nature of the ligand which influences the rotational isomerism of the structure. This was corroborated by a complex synthesized from enantiomerically pure counterpart ligand, *S*-(+)-sec-butyl xanthate (Figure 5.2). All three ligands retained the parent stereochemistry and the

structure did not show signs of distortions. Furthermore, the asymmetric unit contains a pair of isomers, similarly to the [In($S_2CO^iPr)_3$] structure by Jain and co-workers.[50] The crystallographic data for the new structures are provided in Table 5.1. The selected bond lengths and angles are provided in Table A1 and A2 Appendix section, respectively.

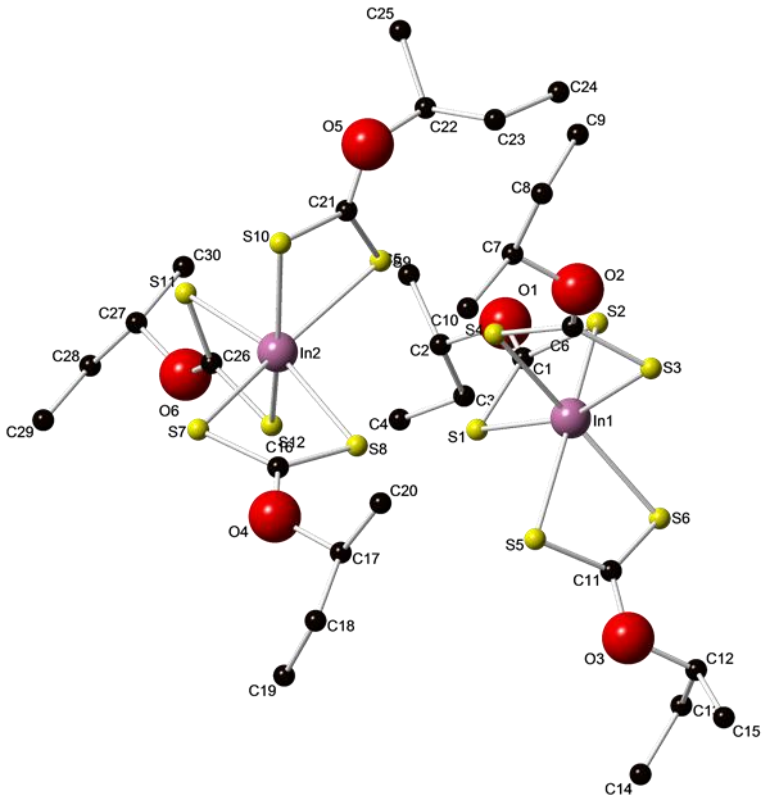

Figure 5.2: The asymmetric unit of the (+)-^{s}Bu CCDC 1875346 crystal structure.

Table 5.1: Crystal structure and structure refinement for $[In(S_2COR)_3]$ where R = Me (**15**), ^{i}Pr (**16**), ^{s}Bu (**17**) and (+)-^{s}Bu, respectively.

Parameter	Me (**15**)	^{i}Pr (**16**)	^{s}Bu (**17**)	(+)-^{s}Bu
Empirical formula	$C_6H_9InO_3S_6$	$C_{12}H_{21}InO_3S_6$, C_6H_{12}	$C_{15}H_{26}InO_3S_6$	$C_{15}H_{27}InO_3S_6$
Formula weight	436.31	604.62	561.54	562.55
Temperature/K	293	150	293	150
Wavelength/Å	1.54184	1.54184	1.54184	0.71073
Crystal system	Monoclinic	Monoclinic	Orthorhombic	Orthorhombic
Space group	P21/n	P21/n	Pna21	P212121
a/Å	9.6364(1)	14.3780(1)	11.7522(5)	10.8724(3)
b/Å	14.6235(1)	10.9636(1)	19.7056(4)	11.2857(3)
c/Å	11.0022(1)	17.9856(2)	10.3925(2)	38.3026(13)
α/°	90	90	90	90
β/°	109.133(1)	105.160(1)	90	90
γ/°	90	90	90	90
Volume/Å^3	1464.76(2)	2736.49(5)	2406.74(12)	4699.8(2)
Z	4	4	4	8
Density calculated/Mg m^{-3}	1.979	1.468	1.550	1.590
Absorption coefficient/mm^{-1}	20.830	11.310	12.814	1.551
F(000)	856.0	1240.0	1140.0	2288.0
Reflections collected	3041	5689	4748	12125
Final *R* indices [*I* > 2sigma(*I*)]	R_1 = 0.0240, wR_2 = 0.0668	R_1 = 0.0302, wR_2 = 0.0741	R_1 = 0.0662, wR_2 = 0.2310	R_1 = 0.0599, wR_2 = 0.0958

The thermogravimetric analysis (TGA) of the SSPs has been reported; the profiles were however not provided.[46] The physico-chemical properties were not disseminated in-depth. This experimental data becomes crucial as both TGA and melt method exhibit similar procedural protocols, as opposed to the solvothermal route chosen by the authors which follows a different decomposition pathway. Regardless of this, the authors report a single-step decomposition profile for all SSPs. To the contrary, the profiles in Figure 5.3 show 4-step, 2-step, 3-step and 4-step decomposition curves for $[In(S_2COR)_3]$ where R = Me, Et, ^{i}Pr and ^{s}Bu, respectively. The anticipated inflection point for ^{i}Pr (**16**) corresponding to the loss of cyclohexane solvent of crystallisation was not observed since the mother liquor was removed completely to obtain dry sample prior to microelemental and thermogravimetric analyses, the contrary procedure to the single crystal X-ray analysis. A plausible explanation for the difference observed between the decomposition profiles by Dutta *et al*.[46] and ours is a slower heating rate (5 °C min^{-1}) versus faster heating rate (10 °C min^{-1}) used, respectively. The phenomenon of an inflection point levelling off into a plateau at slower heating rate is explained in a TGA-themed review by Coats and Redfern.[51] Thus, this demonstrates the importance of adjusting the heating rate especially when an intricate system such as indium sulfide is a subject of study. The TGA profiles from this work exhibited two plateaus which, interestingly, become less resolved in the order of SSP alkyl chain length of ^{s}Bu<^{i}Pr<Et<Me and with a decrease in decomposition temperature. The data provided in Table 5.2 clearly indicates that TGA might not be a reliable tool to identify/match the weight percentage of the residue with those of known indium sulfide compounds. Dutta *et al*.[46] made a deduction that all the residues match to the anticipated In_2S_3, they however did not account for the discrepancies in the obtained and calculated weight percentages. Thus, the current approach rather explored the appropriate identification of the materials obtained at selected regions of the TGA curves.

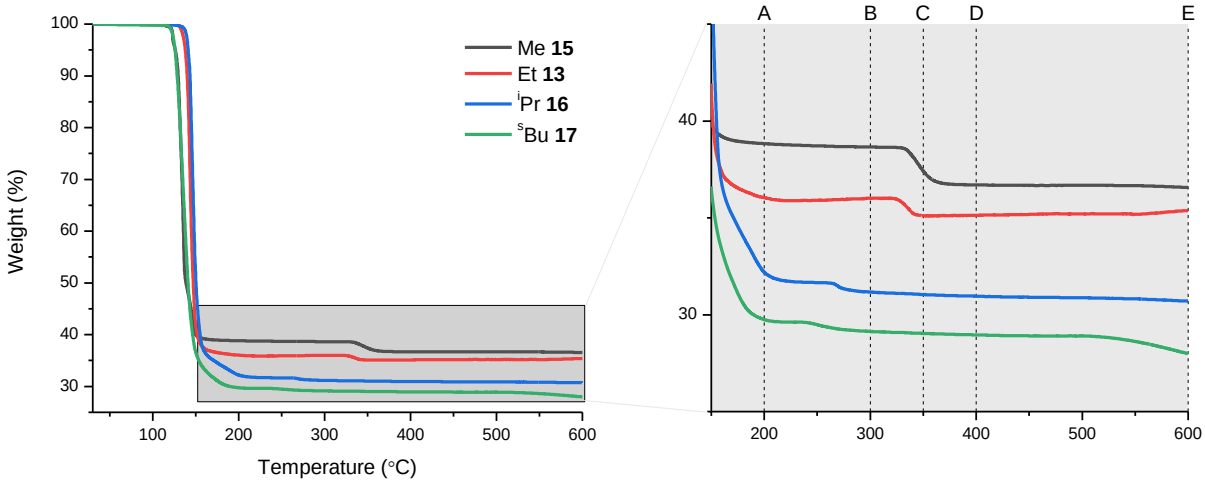

Figure 5.3: The TGA profiles of the In(III) xanthate SSPs from 30 °C to 600 °C at a heating rate of 10 °C min^{-1}. The vertical lines represent the chosen temperatures for the melt reactions.

Table 5.2: The residue weight percentages obtained from TGA of the SSPs and the corresponding weight percentages of the common indium sulfide phases.

	Isotherm					Compound				
SSP	A	B	C	D	E	InS	In_2S_3	In_3S_4	In_6S_7	In_5S_4
(**15**)	-	38.54	37.42	36.63	-	33.66	37.34	36.11	34.89	32.19
(**13**)	35.99	35.82	35.04	35.04	35.19	30.70	34.05	32.94	31.82	29.36
(**16**)	-	31.05	30.90	30.99	-	28.22	31.30	30.27	29.25	26.99
(**17**)	-	29.31	28.99	28.82	-	26.11	28.96	28.01	27.06	24.97

Evaluation of the DTA in Figure 5.4 and Table 5.3 also provides additional information pertaining to the decomposition pathway of the SSPs. Single curves observed for Me (**15**) and Et (**13**) SSPs are typical of a simultaneous melting with decomposition. A similar observation was made during the traditional melting point determination experiments; no melting was observed, instead change in colour signifying decomposition was observed. This nature of decomposition was also observed at a larger scale when crystals of Et (**13**) were decomposed in a furnace with the fully decomposed product retaining a similar shape of the crystals, Figure 5.5. Therefore, this suggested that the inorganic residue formed is obtained through

solventless thermolysis pathway. The tailing observed in the DTA curves for Et (**13**) and Me (**15**) is attributed to the possible strong adsorption of the volatile by-products on the formed residue.[42] The volatile by-products expected from the decomposition experiments of the xanthate SSPs prepared from this work are alkenes, carbonyl sulfide and hydrogen sulfide, assuming a breakdown mechanism following the Chugaev elimination process.[43]

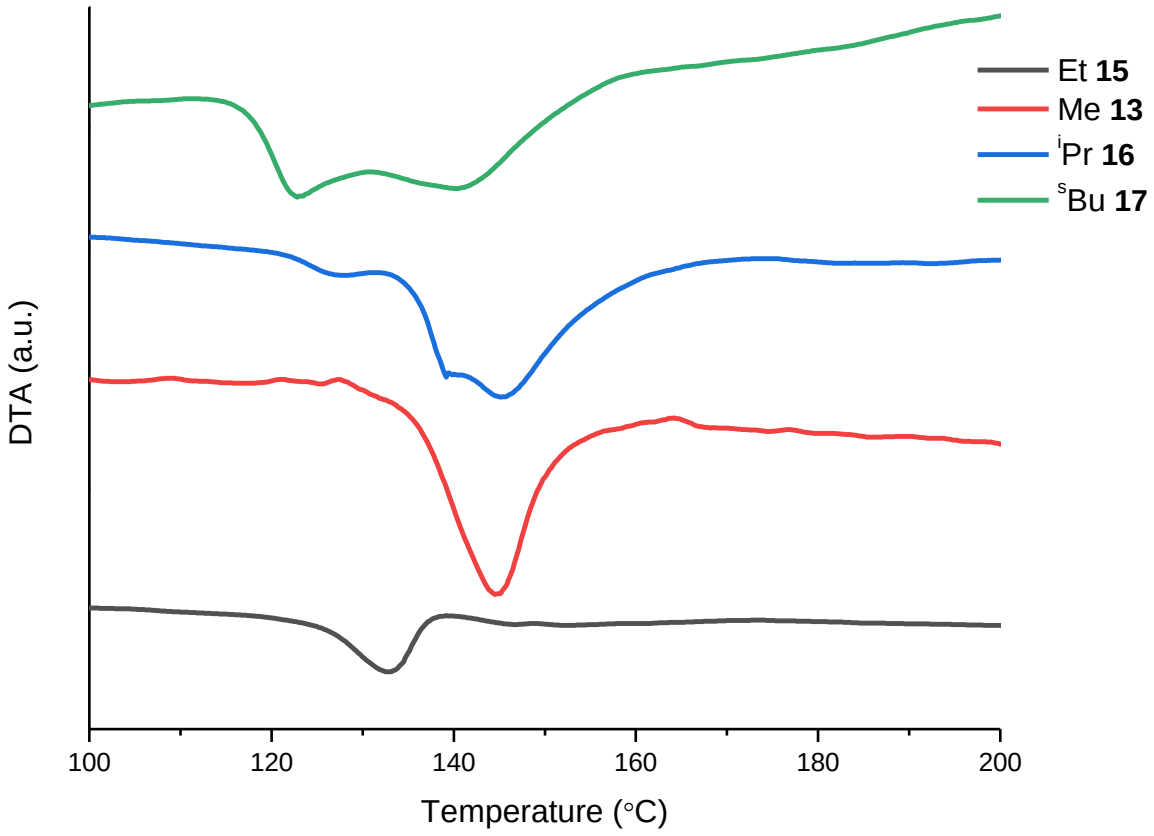

Figure 5.4: The DTA profiles of the In(III) xanthate SSPs from 30°C to 600°C at a heating rate of 10 °Cmin^{-1}.

Table 5.3: Decomposition temperatures from DTA curves and experimental melting points. Data recorded in degrees Celsius (°C).

SSPs	Decomposition onset	Decomposition offset	1st turning point	2nd turning point	3rd turning point	Experimental melting point
Me (**15**)	119.7	140.3	133.0	-	-	-
Et (**13**)	126.2	166.7	144.8	-	-	-
iPr **(16**)	120.8	176.3	127.2	139.5	145.5	127-129
sBu (**17**)	111.7	165.2	122.7	140.8	-	117-118

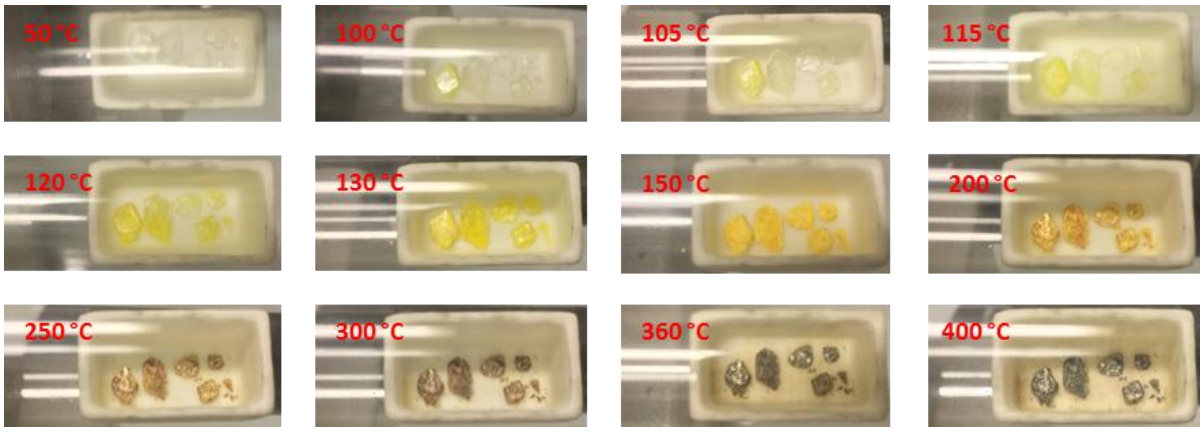

Figure 5.5: Thermal decomposition study of Et (**13**) crystals in a tubular furnace, at a heating rate of 10 °C min and 5 min hold at a desired temperature.

The lower temperature peak from the ^{i}Pr (**16**) and ^{s}Bu (**17**) DTA profiles are assumed to be melting curves; the corresponding experimental melting point temperatures match the DTA. The samples exhibited a slight yellow colour during the experimental melting point determinations, suggesting a melting point temperature in close vicinity of the decomposition temperature. Evidence to this is observed where the melting curve overlaps with the decomposition curve. It was further observed that when fully decomposed ^{i}Pr (**16**) and ^{s}Bu (**17**) afford red-coloured crystalline flakes compared to orange to brown-coloured residue obtained from Et (**13**) and [In(S$_2$COMe)$_3$] (**15**), Figure 5.6.

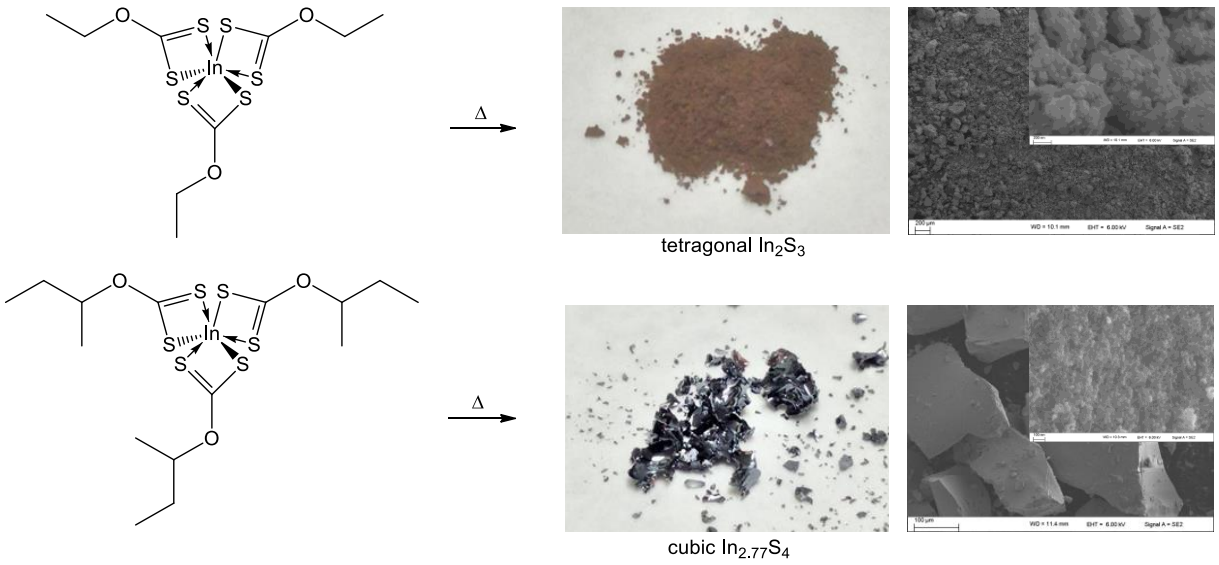

Figure 5.6: The physical features of the pyrolysis products obtained from Et (**13**) (powdery, brown colour) and ^{s}Bu (**17**) (crystalline, red colour) SSPs at 350 °C.

The melt reaction conditions were optimised using Et (**13**) due to the clear steps in the decomposition profile, Figure 5.3. Exploration of the phases produced was based on the temperatures of the two final plateaus and the temperature of the final decomposition step midpoint. The heated samples showed three prominent colour transitions from orange, brown to dark grey, with increasing decomposition temperature. The powder XRD pattern of the solid formed from Et (**13**) at 200 °C displayed highly broadened and overlapped peaks which is typical of sub 5 nm nanocrystal formation unlike the well-defined patterns observed at higher decomposition temperatures, Figure 5.7. The powders obtained at 300, 350, 400 and 600°C exhibit diffraction patterns typical of In_2S_3 phases; as expected, the crystallinity and crystallite sizes increase with an increase in annealing temperature as shown in Figure 5.7b. The observed diffraction patterns from Et (**13**) heated at 350 °C and 400 °C were matched and indexed to tetragonal In_2S_3 (PDF no. 00-025-0390).[52] However, the absence of the (112) reflection peak when heating Et (**13**) at 300°C and 600 °C diffraction patterns were in line with cubic In_2S_3 (PDF no. 03-065-0459) calculated from the single crystal data collected by Adenis *et al*.[53] Figure 5.9b.

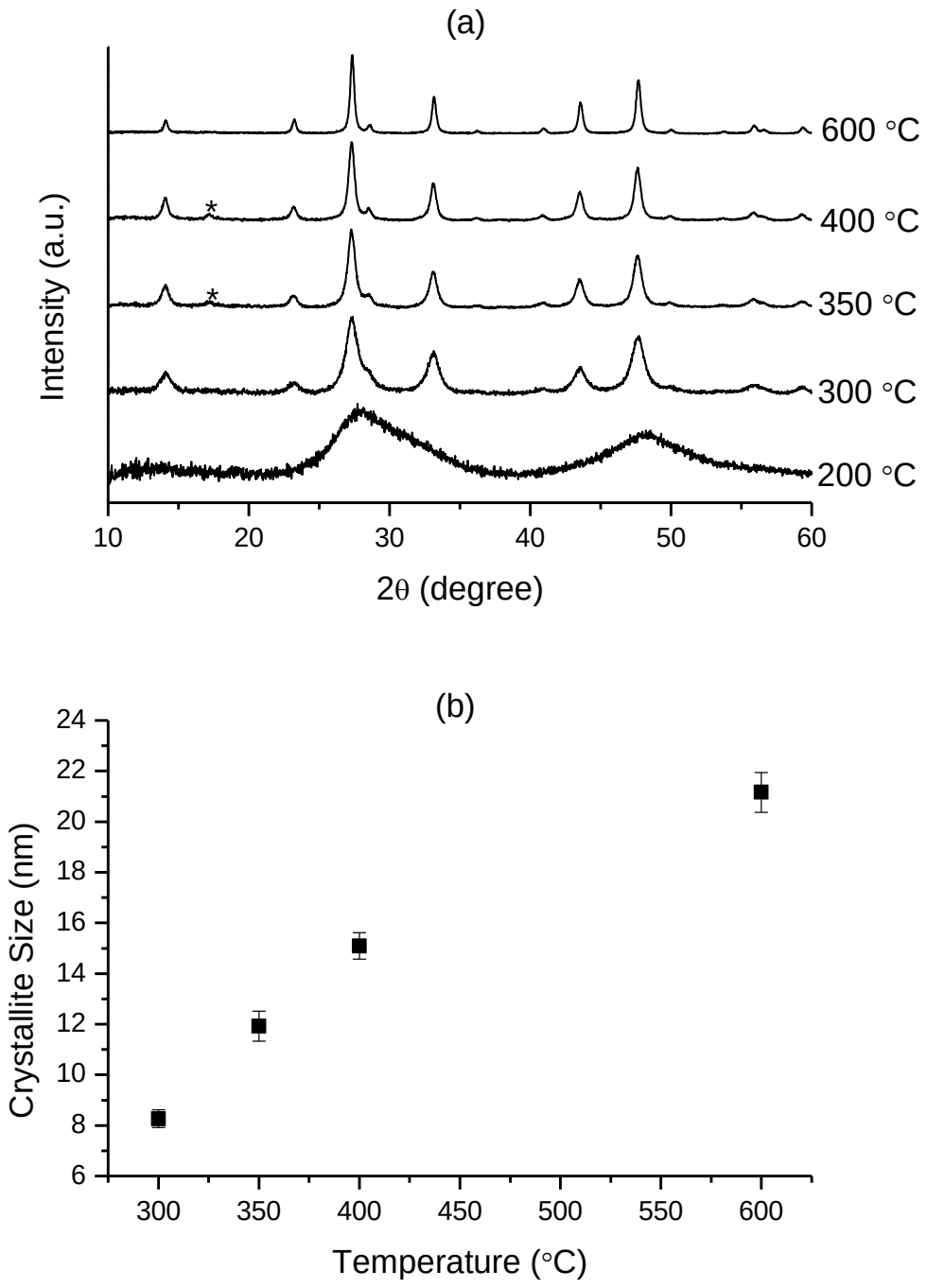

Figure 5.7: The (a) p-XRD patterns and (b) crystallite sizes for In_2S_3 obtained from Et (**13**) SSP heated for 1 h at the stated temperatures under an N_2 atmosphere. Peak indices are provided in Figure 5.11 and Figure 5.12.

$[In(S_2COR)_3]$ where R = Me, ^{i}Pr and ^{s}Bu were decomposed at 300 °C, 350 °C and 400°C. The indium sulfide phases obtained from all precursors are summarized in Figures 5.8 and Figure 5.9. The p-XRD for the material obtained from Me (**15**) at 300 °C was also characteristic of very small nanocrystals, similarly to that obtained at

200 °C for Et (**13**), regardless that the former SSP had a lower decomposition temperature than the latter. The p-XRD patterns from Me (**15**) heated at 350 °C and 400 °C, as well as those from ^{i}Pr (**16**) at all temperatures were also matched to tetragonal In_2S_3 (PDF no. 00-025-0390 and pattern simulated from ICSD 183879), Figure 5.9a. Whereas decomposition of the ^{s}Bu (**17**) SSP yielded a material matching to cubic $In_{2.77}S_4$ from ICSD 41680, Figure 5.9c.

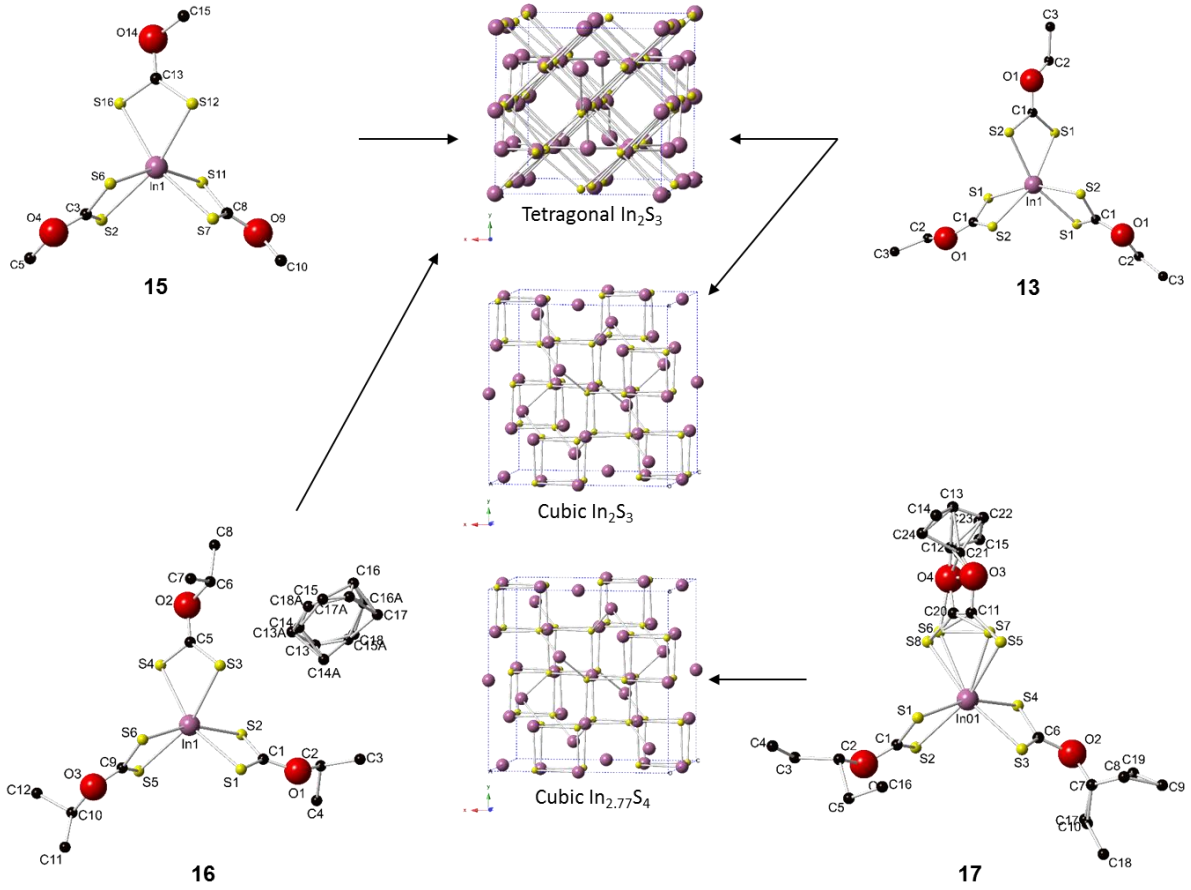

Figure 5.8: SSPs and the corresponding In_xS_y materials formed from solventless decomposition reactions.

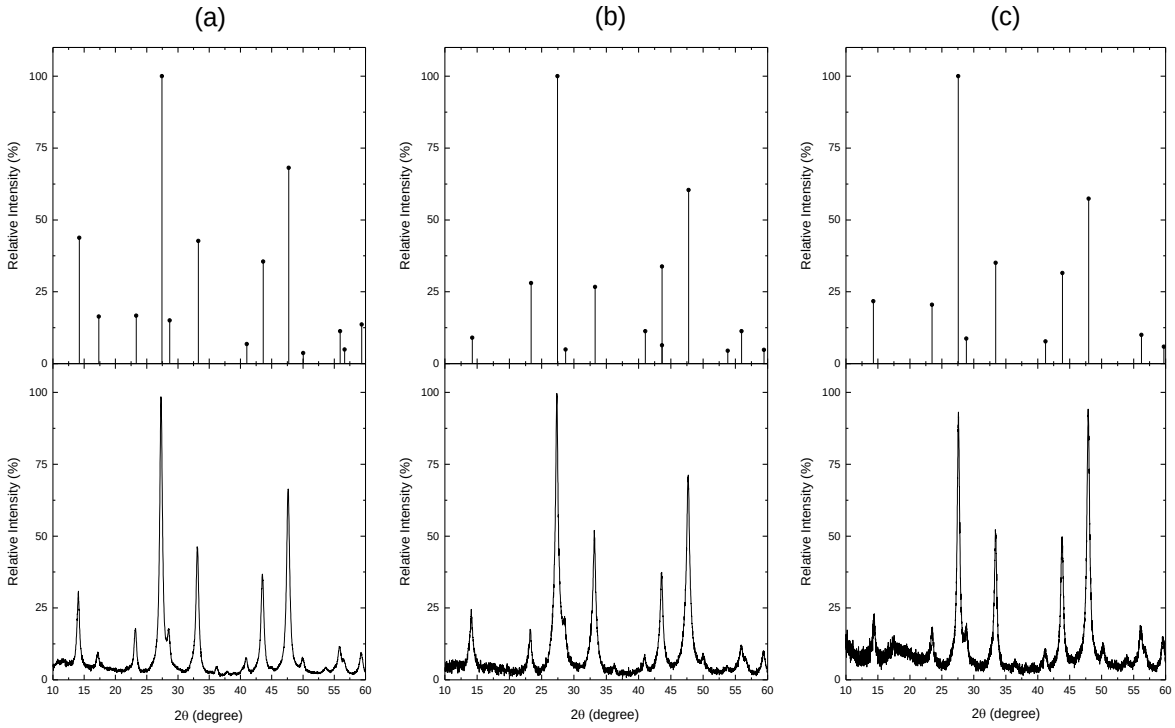

Figure 5.9: Average patterns matching to (a) tetragonal In_2S_3 (ICSD 183879), (b) cubic In_2S_3 (ICSD 202353) and (c) cubic $In_{2.77}S_4$ (ICSD 41680). Top plots are standard patterns, while bottom plots are averaged p-XRD patterns matching to the standard pattern. Peak indices are provided in Figures 5.11-5.13.

To support the phase identification by matching peak positions, the peak intensities were also compared to the powder diffraction patterns generated from previously reported single crystals structures, Figure 5.10. A linear plot of observed pattern intensity vs intensity from previously reported powder pattern indicates a strong match with the reference In_xS_y phase. Phase identification across all three phases undoubtedly displays a linear trend. To the contrary, the phase purity comparable to the single crystal materials does not display a perfect linear trend. This can be ascribed to contributing factors such as background noise on the patterns as a function of crystallinity, as observed from inconsistencies in the magnitude of errors. Furthermore, it does not rule out the possibility of mixed phases, especially in the case of tetragonal and cubic In_2S_3 materials where the difference in reference patterns is not only the absence of the (112) reflection peak as stated earlier, but also difference in intensities of other peaks. The error was better understood by examining the intensity of the peaks on individual patterns, in relation to SSP type and reaction

temperature. In both tetragonal and cubic In_2S_3-matched patterns (Figure 5.11 and Figure 5.12, respectively) there is clear evidence of inverse proportion trend between peak intensities and reaction temperature. The cubic $In_{2.77}S_4$ series displayed an interesting temperature-dependant behaviour. The inverse proportion trend is observed in most of the reflection peaks, however, a significant discrepancy is observed in the (311) and (440) reflection peaks which appear interlinked (Figure 5.13). The intensities of the two peaks are nearly equal at 300 °C reaction temperature. An increase to 350 °C results to a significant drop in the intensity of the (311) peak relative to the (440) peak, while vice versa is observed at 400 °C. This observation is generally explained as preferred growth orientation being strongly dependant on reaction parameters.

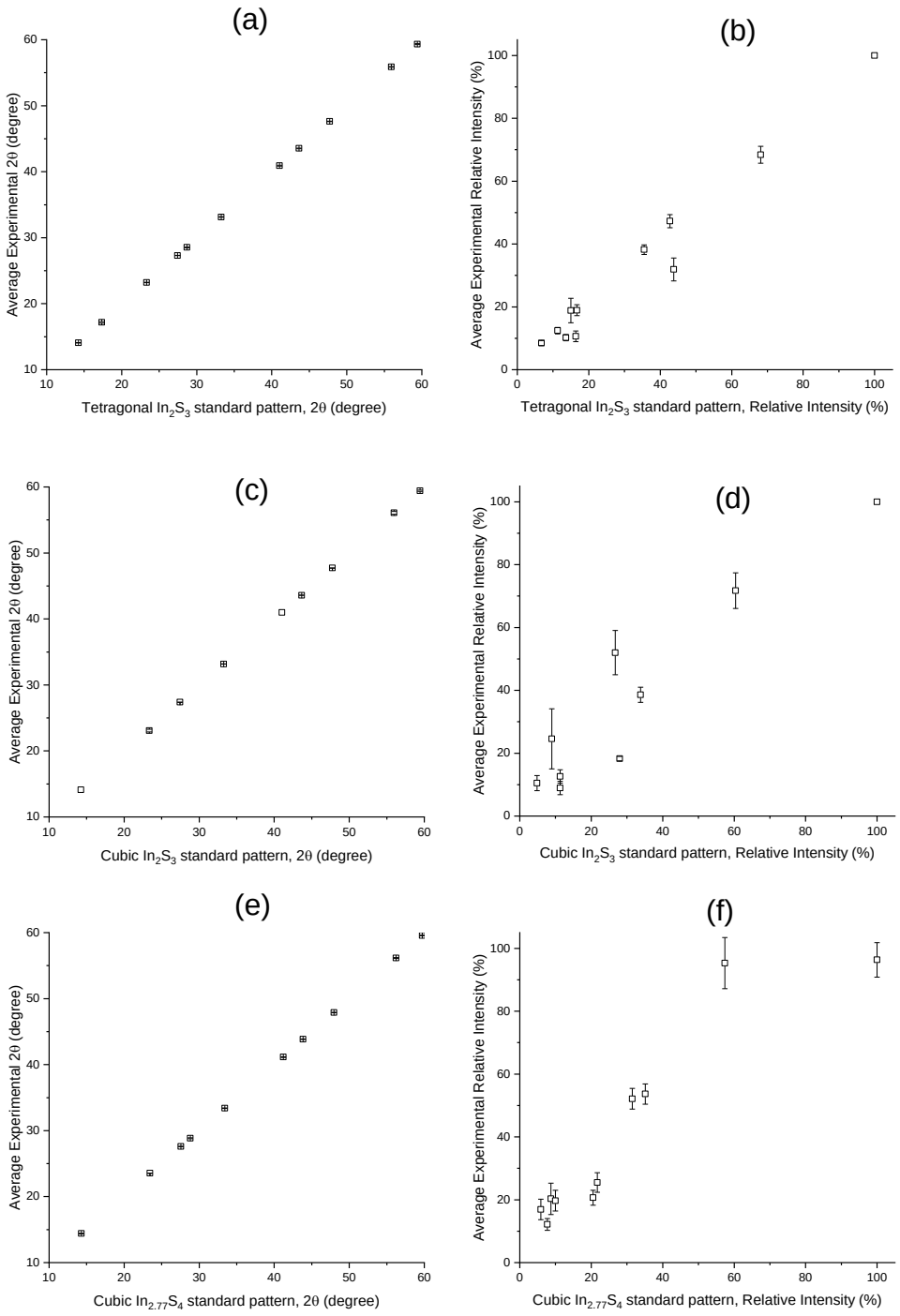

Figure 5.10: Phase identification by peak positions for (a) tetragonal In_2S_3 (ICSD 183879), (c) cubic In_2S_3 (ICSD 202353) and (e) cubic $In_{2.77}S_4$ (ICSD 41680) matched decomposition products, with phase purity determination through their relative intensities (b), (d) and (f), respectively.

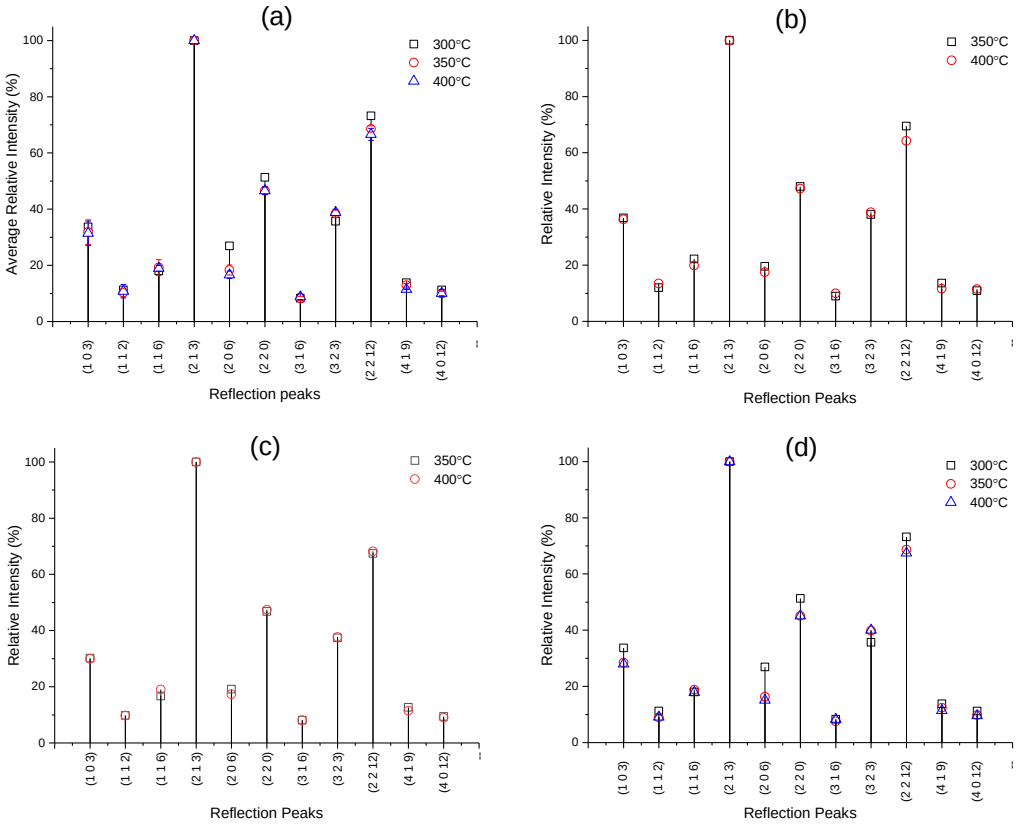

Figure 5.11: Correlation of peak positions and relative intensities between experimental and simulated standard patterns for tetragonal In_2S_3.

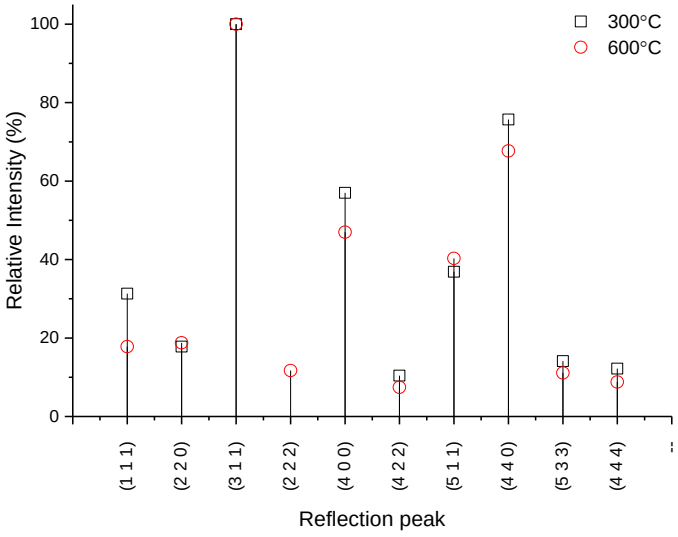

Figure 5.12: Correlation of peak positions and relative intensities between experimental and simulated standard patterns for cubic In_2S_3.

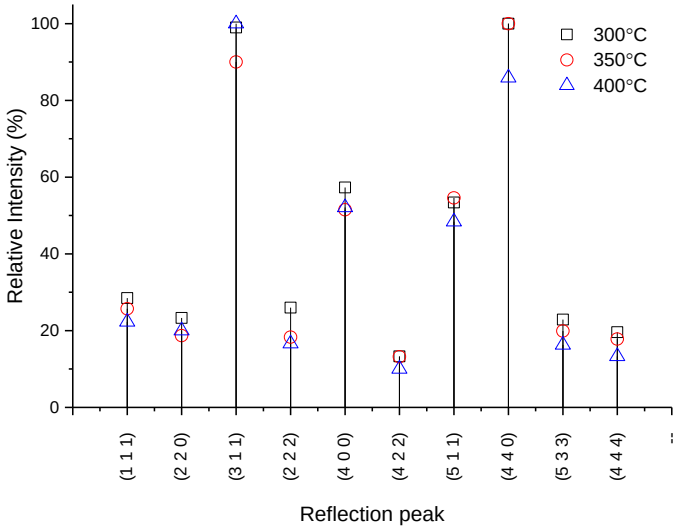

Figure 5.13: Correlation of peak positions and relative intensities between experimental and simulated standard patterns for cubic $In_{2.77}S_4$.

5.4 Conclusion

The solventless thermolysis of crystalline powders of $[In(S_2COR)_3]$, where R = Me, Et, ^{i}Pr and ^{s}Bu, resulted in crystalline In_xS_y materials. Four novel structures have been elucidated by single crystal X-ray crystallography. By choice of complex and temperature, different phases of pure In_xS_y were obtained. Three phases, namely, tetragonal In_2S_3, cubic In_2S_3 and cubic $In_{2.77}S_4$ are obtained demonstrating the ease of access to these phases through this simple, cost-efficient and scalable method.

References

[1] N. Barreau, *Sol. Energy*, **2009**, *83*, 363.

[2] S. Lugo-Loredo, Y. Peña-Méndez, M. Calixto-Rodriguez, S. Messina-Fernández, A. Alvarez-Gallegos, A. Vázquez-Dimas, T. Hernández-García, *Thin Solid Films*, **2014**, *550*, 110.

[3] S. Cingarapu, M. A. Ikenberry, D.B. Hamal, C. M. Sorensen, K. Hohn, K. J. Klabunde, *Langmuir*, **2012**, *28*, 3569.

[4] R. Sumi, A.R. Warrier, C. Vijayan, *J. Phys. Appl. Phys.*, **2014**, *47*, 105103.

[5] A.Y. Zavrazhnov, A.V. Naumov, P.V. Anorov, E.G. Goncharov, V.I. Sidei, V.S. Pervov, *Inorg. Mater.*, **2006**, *42*, 1294.

[6] A.V. Kosyakov, A.Y. Zavrazhnov, A.V. Naumov, *Inorg. Mater.*, **2010**, *46*, 343.

[7] P.D. Matthews, P.D. McNaughter, D.J. Lewis, P. O'Brien, *Chem. Sci.*, **2017**, *8*, 4177.

[8] M.I. Hossain, P. Chelvanathan, M. Zaman, M. Karim, M. Alghoul, N. Amin, *Chalcogenide Lett*, **2011**, *8*, 315.

[9] U. Schwarz, H. Hillebrecht, K. Syassen, *Z. Für Krist.*, **1995**, *210*, 494.

[10] A.N. MacInnes, M.B. Power, A.F. Hepp, A.R. Barron, *J. Organomet. Chem.*, **1993**, *449*, 95.

[11] Y. Sharma, P. Srivastava, *Mater. Chem. Phys.*, **2012**, *135*, 385.

[12] R. Diehl, R. Nitsche, *J. Cryst. Growth*, **1973**, *20*, 38.

[13] S.B. Bansode, R.S. Kapadnis, V.G. Wagh, S.S. Kale, H.M. Pathan, *AIP Conf. Proc.*, **2013**, *1536*, 455.

[14] R. Sumi, A.R. Warrier, C. Vijayan, *AIP Conf. Proc.*, **2014**, *1576*, 141.

[15] A.C. Dhanya, K. Deepa, T.L. Remadevi, *Appl. Phys. A*, **2014**, *117*, 1161.

[16] A.V. Sergeeva, A.V. Naumov, V.N. Semenov, Y.V. Sokolov, *Inorg. Mater.*, **2007**, *43*, 1046.

[17] K. Otto, A. Katerski, A. Mere, O. Volobujeva, M. Krunks, *Thin Solid Films*, **2011**, *519*, 3055.

[18] F. Rahman, J. Podder, M. Ichimura, *Surf. Rev. Lett.*, **2013**, *20*, 1350014.

[19] T. Sall, A. Nafidi, B.M. Soucase, M. Mollar, B. Hartitti, M. Fahoume, *J. Semicond.*, **2014**, *35*, 063002.

[20] S. Elfarrass, B. Hartiti, A. Ridah, P. Thevenin, *J Mater Env. Sci*, **2015**, *6*, 487.

[21] X. Chen, Z. Zhang, X. Zhang, J. Liu, Y. Qian, *Chem. Phys. Lett.*, **2005**, *407*, 482.

[22] S. Acharya, M. Dutta, S. Sarkar, D. Basak, S. Chakraborty, N. Pradhan, *Chem. Mater.*, **2012**, *24*, 1779.

[23] S. Acharya, S. Sarkar, N. Pradhan, *J. Phys. Chem. Lett.*, **2012**, *3*, 3812.

[24] N. Revaprasadu, M.A. Malik, J. Carstens, P. O'Brien, *J. Mater. Chem.*, **1999**, *9*, 2885.

[25] S.W. Haggata, M.A. Malik, M. Motevalli, P. O'Brien, J.C. Knowles, *Chem. Mater.*, **1995**, *7*, 716.

[26] P. O'Brien, D.J. Otway, J.R. Walsh, *Thin Solid Films*, **1998**, *315*, 57.

[27] M. Afzaal, M.A. Malik, P. O'Brien, *Chem. Commun.*, **2004**, *0*, 334.

[28] D.P. Dutta, G. Sharma, A.K. Tyagi, S.K. Kulshreshtha, *Mater. Sci. Eng. B*, **2007**, *138*, 60.

[29] E. Quiroga-González, L. Kienle, C. Näther, V.S.K. Chakravadhanula, H. Lühmann, W. Bensch, *J. Solid State Chem.*, **2010**, *183*, 2805.

[30] R. Nomura, K. Konishi, H. Matsuda, *Thin Solid Films*, **1991**, *198*, 339.

[31] S.K. Batabyal, S.E. Lu, J.J. Vittal, *Cryst. Growth Des.*, **2016**, *16*, 2231.

[32] P. Bera, S.I. Seok, *J. Nanoparticle Res.*, **2011**, *13*, 1889.

[33] A. Lutfi Abdelhady, K. Ramasamy, M.A. Malik, P. O'Brien, *Mater. Lett.*, **2013**, *99*, 138.

[34] M. Afzaal, D. Crouch, P. O'Brien, J.-H. Park, *J. Mater. Sci. Mater. Electron.*, **2003**, *14*, 555.

[35] T.C. Deivaraj, J.-H. Park, M. Afzaal, J.J. Vittal, *Chem. Mater.*, **2003**, *15*, 2383.

[36] G. Shang, K. Kunze, M.J. Hampden-Smith, E.N. Duesler, *Chem. Vap. Depos.*, **1996**, *2*, 242.

[37] P.D. McNaughter, J.C. Bear, A.G. Mayes, I.P. Parkin, P. O'Brien, *R. Soc. Open Sci.*, **2017**, *4*, 170383.

[38] S.A. Saah, P.D. McNaughter, M.A. Malik, J.A.M. Awudza, N. Revaprasadu, P. O'Brien, *J. Mater. Sci.*, **2018**, *53*, 4283.

[39] M. Al-Shakban, P.D. Matthews, G. Deogratias, P.D. McNaughter, J. Raftery, I. Vitorica-Yrezabal, E.B. Mubofu, P. O'Brien, *Inorg. Chem.*, **2017**, *56*, 9247.

[40] P.D. McNaughter, S.A. Saah, M. Akhtar, K. Abdulwahab, M.A. Malik, J. Raftery, J.A.M. Awudza, P. O'Brien, *Dalton Trans.*, **2016**, *45*, 16345.

[41] E.A. Lewis, P.D. McNaughter, Z. Yin, Y. Chen, J.R. Brent, S.A. Saah, J. Raftery, J.A.M. Awudza, M.A. Malik, P. O'Brien, S.J. Haigh, *Chem. Mater.*, **2015**, *27*, 2127.

[42] P.S. Nair, T. Radhakrishnan, N. Revaprasadu, G. Kolawole, P. O'Brien, *J. Mater. Chem.*, **2002**, *12*, 2722.

[43] N. Pradhan, B. Katz, S. Efrima, *J. Phys. Chem. B*, **2003**, *107*, 13843.

[44] A.A.K. Bakly, B.F. Spencer, P. O'Brien, *J. Mater. Sci.*, **2018**, *53*, 4360.

[45] (a) S. Ghoshal, V.K. Jain, *J. Chem. Sci.*, **2007**, *119*, 583. (b) V.G. Bessergenev, A.V. Bessergenev, E.N. Ivanova, Y.A. Kovalevskaya, *J. Solid State Chem.*, **1998**, *137*, 11.

[46] D.P. Dutta, G. Sharma, S. Ghoshal, N.P. Kushwah, V.K. Jain, *J. Nanosci. Nanotechnol.*, **2006**, *6*, 235.

[47] V. Bessergenev, E. Ivanova, Y.A. Kovalevskaya, S. Gromilov, V. Kirichenko, S. Larionov, *Inorg. Mater.*, **1996**, *32*, 592.

[48] D. Reishofer, T. Rath, H.M. Ehmann, C. Gspan, S. Dunst, H. Amenitsch, H. Plank, B. Alonso, E. Belamie, G. Trimmel, S. Spirk, *ACS Sustain. Chem. Eng.*, **2017**, *5*, 3115.

[49] B.F. Hoskins, E.R.T. Tiekink, R. Vecchiet, G. Winter, *Inorganica Chim. Acta*, **1984**, *90*, 197.

[50] S. Ghoshal, A. Wadawale, V.K. Jain, *Anal. Sci. X-Ray Struct. Anal. Online*, **2008**, *24*, x15.

[51] A.W. Coats, J.P. Redfern, *Analyst*, **1963**, *88*, 906.

[52] H.E. Swanson, H.F. McMurdie, M.C. Morris, E.H. Evans, B. Paretzkin, *Natl. Bur. Stand. U.S. Monogr*, **1974**, *25*, 30.

[53] C. Adenis, J. Olivier-Fourcade, J.-C. Jumas, E. Philippot, *Rev. Chim. Minérale*, **1987**, *24*, 10.

CHAPTER 6

6 Summary and future work

Different metal-organic compounds have been used as molecular precursors for the fabrication of the corresponding binary and ternary metal sulfide nanoparticles.

Although thiosemicarbazone compounds are well known for their biological application, in this work, they have shown efficiency in manipulating the optical and morphological properties of oleylamine-capped CdS and PbS nanoparticles when complexed to CdX_2 and PbX_2, respectively, where X = Cl^-, I^- and Br^-. Prior to the fabrication of the nanoparticles by the solvent thermolysis route, a clear distinction on the thermogravimetric analysis of the complexes suggested a major influence of the halide ligands on their thermal stability. This prompted some hypothetical differences in the nanoparticles expected from the halide classes. For the first time, in consideration of the current knowledge, the influence of halide ligands on the formation of nanoparticles is reported, in the context of single-source precursors. Blueshifted absorptions were consistently observed in particles prepared from CdI_2 more than from $CdCl_2$ complexes, analysis of which revealed quantum confinement phenomena of the CdS particles. A similar observation was made on the particle sizes, corroborated by powder X-ray diffraction and transmission electron microscopy techniques. Furthermore, predominant dendrite-like and cubic/spheres/rod-like morphologies were obtained from CdI_2 and $CdCl_2$ complexes, respectively. Particle shape transformation was also found to be temperature-dependent.

The influence of the halide ligands on the PbS nanoparticles was also observed in their optical and morphological properties. Interestingly, significant amounts of the bromide and iodide elements were detected in nanoparticles obtained from the corresponding complexes using the energy dispersive X-ray spectroscopy. Average particle sizes were found to be in the 50-400 nm range, were estimated using transmission electron microscopy imaging; increase in reaction temperature results in an increase in particle size. Furthermore, the dominant cubic-shape morphology becomes less pronounced down the halogen series. The bromide-incorporated complex, however, produced truncated cube-shaped nanoparticles at relatively lower temperatures. The optical absorbance of all PbS nanoparticles were found to be blue-

shifted when compared to the bulk material; band gaps of between 1.08 eV to 3.18 eV were obtained.

As already known in literature that In_2S_3 and $CuInS_2$ materials are non-toxic alternatives to CdS and PbS materials, this study further attempted to devise greener reaction protocols without compromising the sought-after properties of the semiconductors. Castor oil and olive oil were then identified and demonstrated as green capping agents for non-toxic β-In_2S_3 and $CuInS_2$ nanoparticles. The nanoparticles were synthesized by a hot-injection method, using In(III) and Cu(II) ethyl xanthate and diethyldithiocarbamate complexes as molecular precursors. The reaction temperature, type of the coordinating solvent and type of the ligand used had a significant influence in determining the particle size and shape, as well as the optical properties of the as-prepared nanoparticles. The β-In_2S_3 nanoparticles predominantly exhibit a rod-like morphology from the In(III) ethyl xanthate complex, whereas nanosheets and urchin-like microstructures were obtained from the diethyldithiocarbamate counterpart. Castor oil-capped nanoparticles were relatively smaller compared to the olive oil-capped β-In_2S_3 nanoparticles from both xanthate and dithiocarbamate complexes. The band gaps of the nanoparticles obtained from the xanthate complex increased with a decrease in particle sizes due to the quantum confinement effect; 4.0-4.3 eV and 3.5-3.7 eV for the castor and olive oil-capped nanoparticles respectively. The band gaps were estimated from solution-based absorbance measurements as opposed to the normal practice, transmittance measurements. As such, there is some degree of unreliability in the estimated values, arising from various factors such as solvent and excess capping agent interferences. The $CuInS_2$ nanoparticles were prepared using a dual-precursor approach, i.e. InL_3 + CuL_2 in a 1:1 (In:Cu) precursor mole ratio, where L = ethyl xanthate or diethyldithiocarbamate. The xanthate system afforded the chalcopyrite phase, while a wurtzite phase was obtained from the dithiocarbamate system. The green capping agent did not have any influence on the crystallographic phases, however, a chalcopyrite phase was obtained when oleylamine was used in the dithiocarbamate system. The xanthate system showed relatively higher energy band gaps compared to the dithiocarbamate system.

In light of the xanthate complexes exhibiting desirable properties, the study was extended to devise an alternative greener route to synthesize high quality In_2S_3 nanoparticles. The low decomposition temperature of xanthate complexes, identified them as suitable candidates for a solventless synthetic route to indium sulfide material. The thermogravimetric and differential thermogravimetric analysis revealed that the alkyl backbone of the ligands influences the chemical behaviour of the complexes. The combination of temperature and alkyl backbone of the ligands efficiently manipulated the physical texture and crystallographic phases of the indium sulfide materials. It was observed that the indium sulfide materials (tetragonal In_2S_3, cubic In_2S_3 and cubic $In_{2.77}S_4$) were obtained through solventless thermolysis and melt reaction mechanisms. Thus, the study confirmed that the route is capable of producing high quality material from the crystalline powders of complexes, in the absence of solvents as stabilizers.

The overall work reported in this thesis has demonstrated the use of biologically-active thiosemicarbazone compounds as ligands for single source precursors, the use of abundant naturally occurring castor oil and olive oil as capping agents, and a solventless route in preparing semiconductor materials. The design of the study focused on the green chemistry theme, towards the implementation of eco-friendly synthetic protocols with aims of obtaining high quality non-toxic nanomaterials.

Future work, as per demand of functional nanomaterials exhibiting interesting properties, will entail the development of novel and or improved synthetic protocols. The protocols will focus on preparing and evaluating novel halogen-incorporated complexes as single source precursors for nanomaterials fabrication. The study would extend to thin films for next generation solar cells, gas sensing and water splitting potential applications. The solventless thermolysis method can find future use and/or exploitation in the preparation of various classes of nanomaterials (e.g. ternary and quaternary systems) and nanocomposites (e.g. polymer-nanoparticle composites. The studies would focus on nanomaterials of significant importance (i.e. eco-friendly nature and abundant starting materials) such as iron chalcogenide system.

Appendix: supplementary data, list of publications and conferences

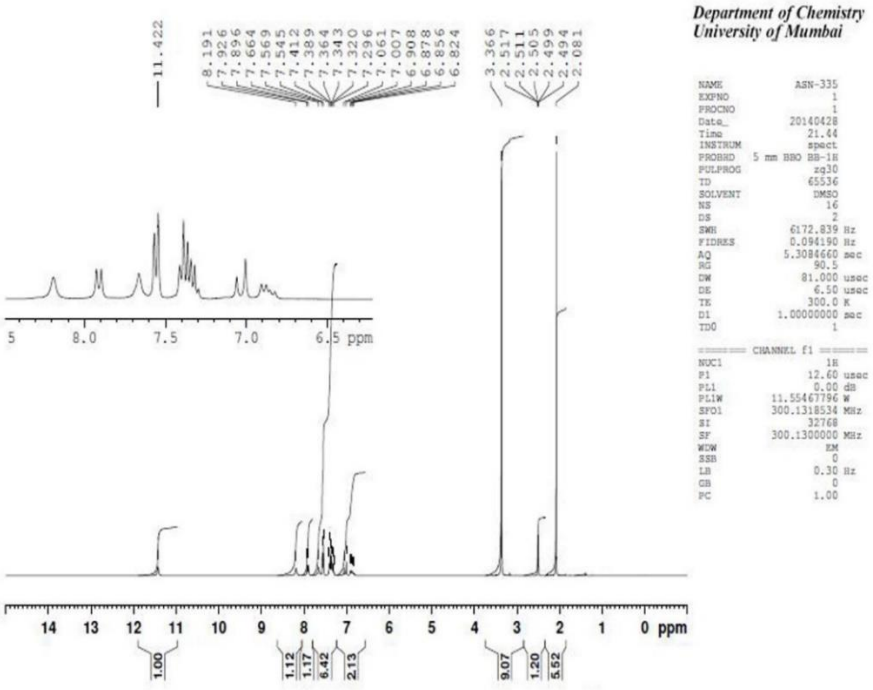

Figure A1: The ^{1}H NMR spectrum of precursor (**1**).

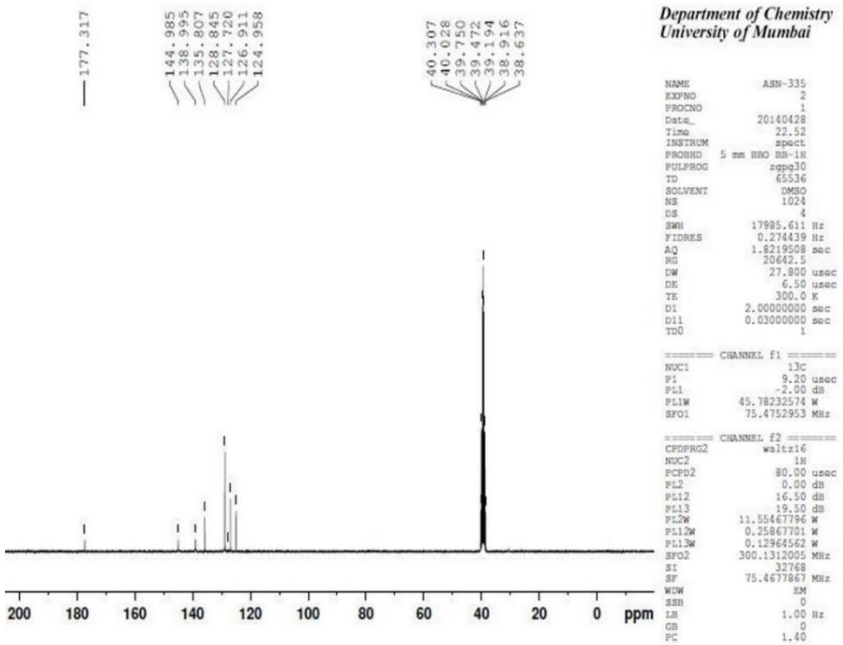

Figure A2: The ^{13}C{^{1}H} NMR spectrum of precursor (**1**).

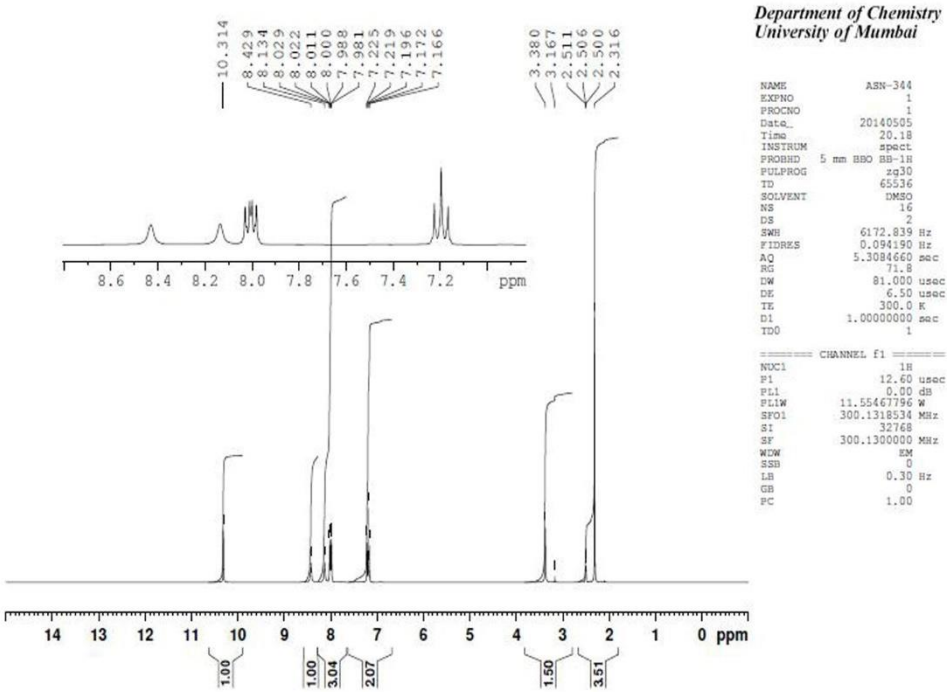

Figure A3: The ^{1}H NMR spectrum of precursor (**2**).

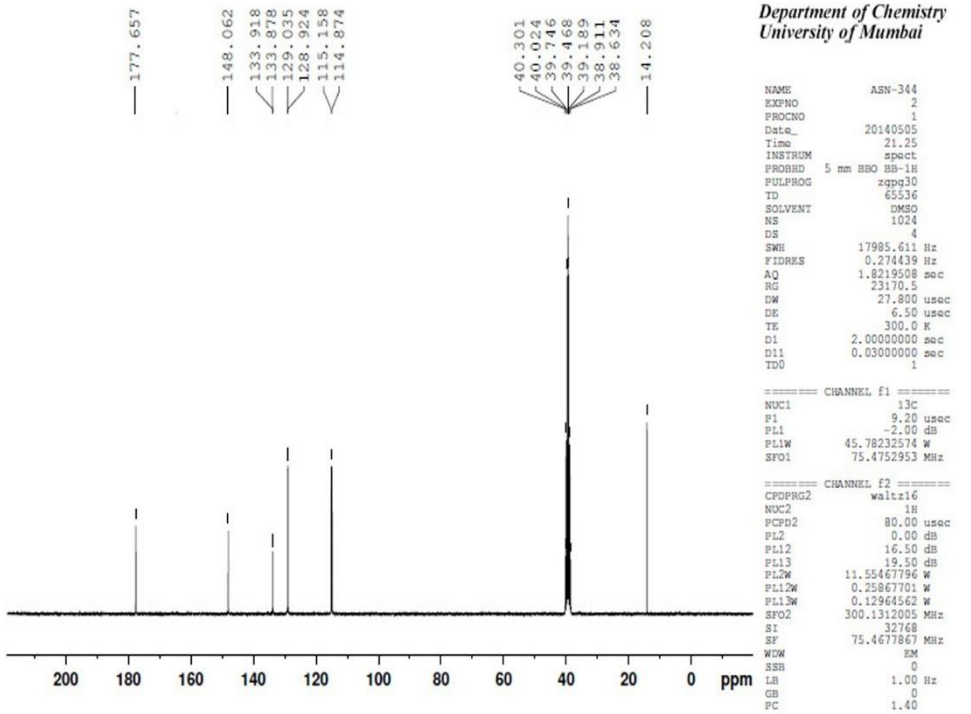

Figure A4: The ^{13}C{^{1}H} NMR spectrum of precursor (**2**).

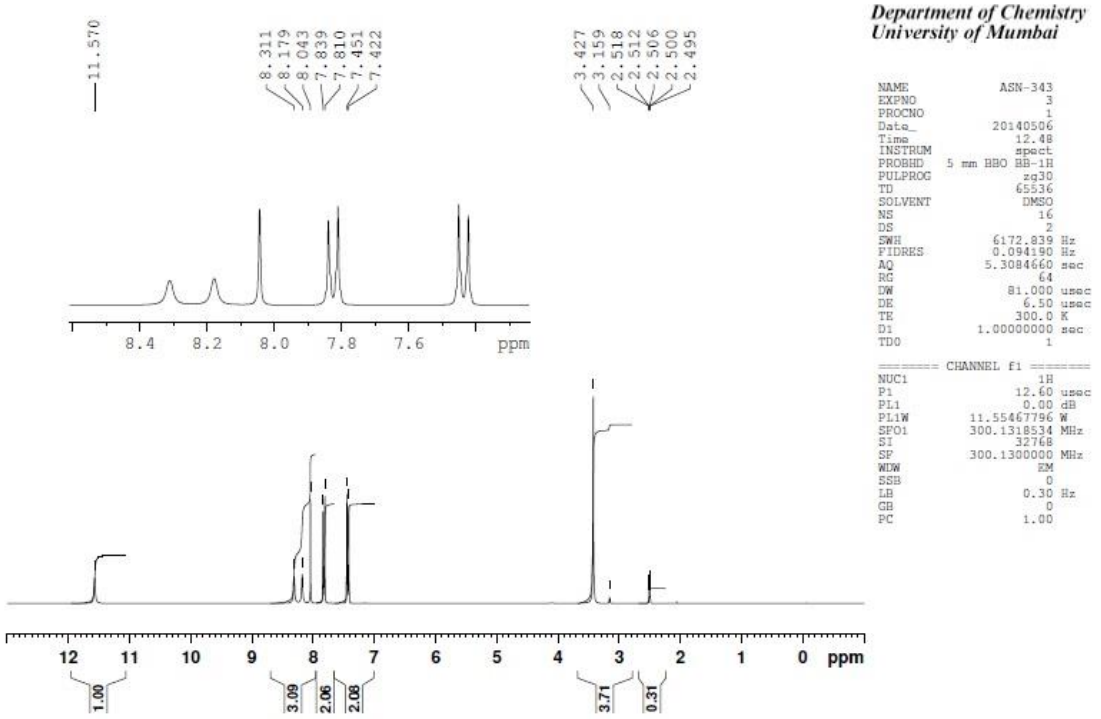

Figure A5: The ^{1}H NMR spectrum of precursor (**3**).

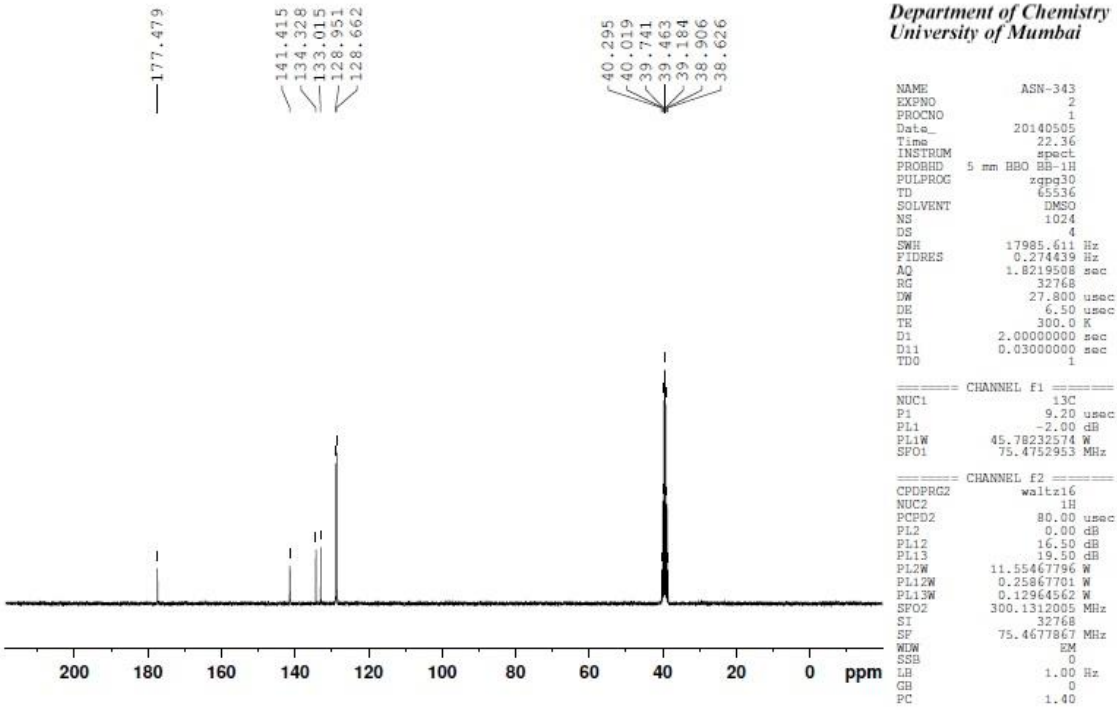

Figure A6: The $^{13}C\{^{1}H\}$ NMR spectrum of precursor (**3**).

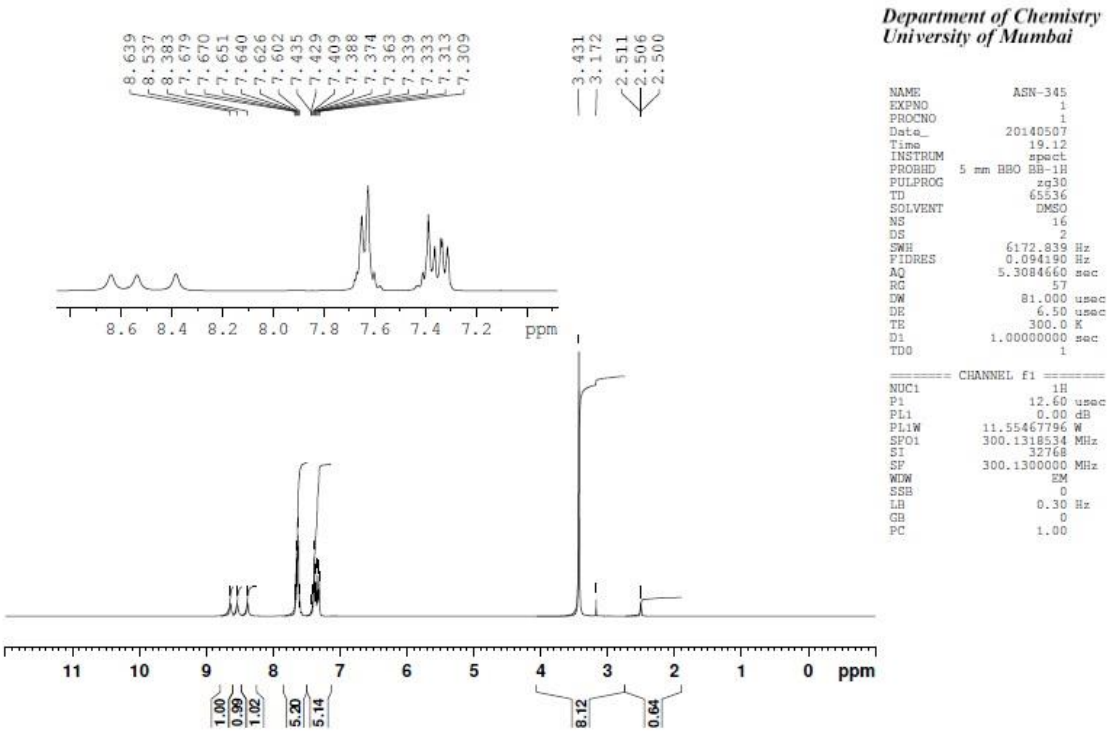

Figure A7: The ^{1}H NMR spectrum of precursor (**4**).

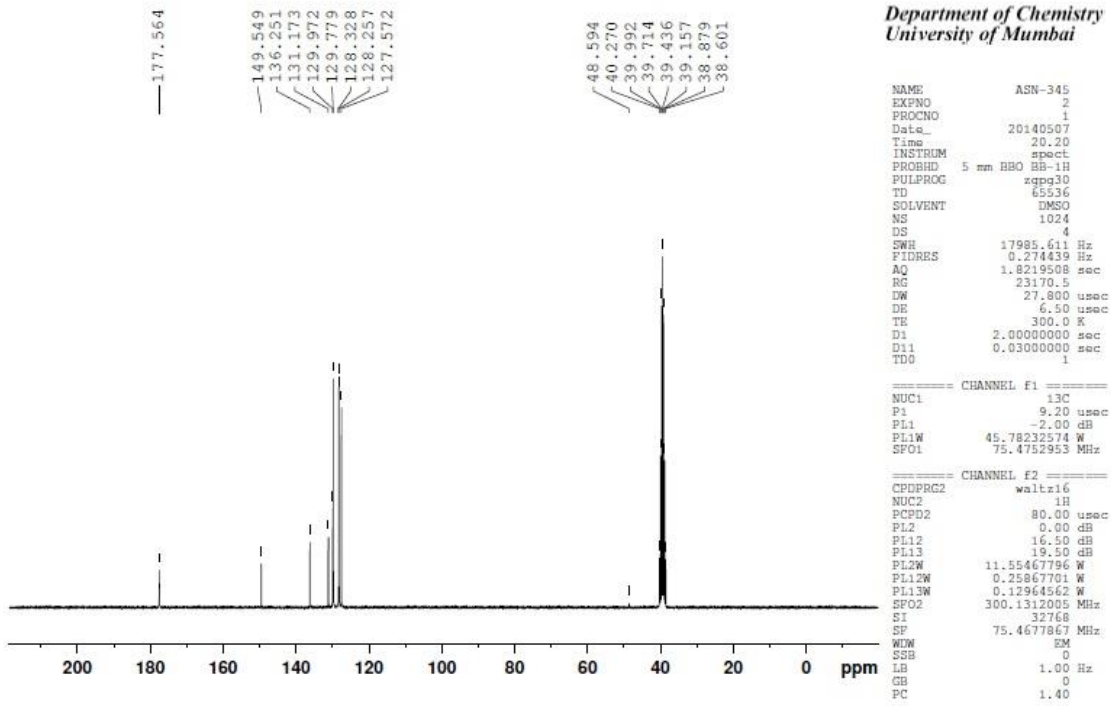

Figure A8: The ^{13}C{^{1}H} NMR spectrum of precursor (**4**).

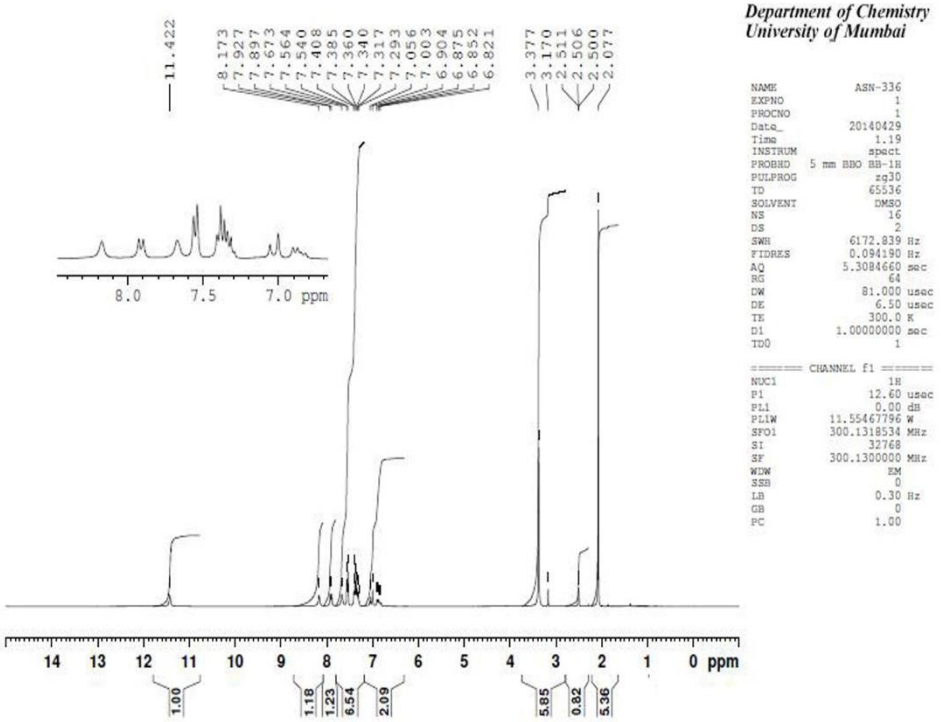

Figure A9: The ^{1}H NMR spectrum of precursor (**5**).

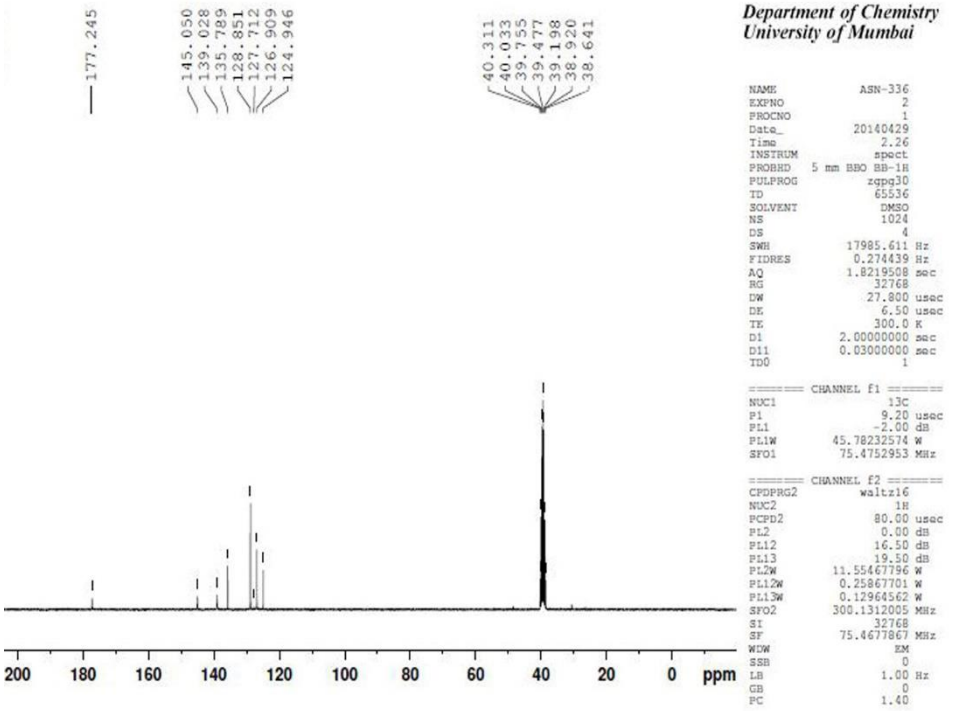

Figure A10: The ^{13}C{^{1}H} NMR spectrum of precursor (**5**).

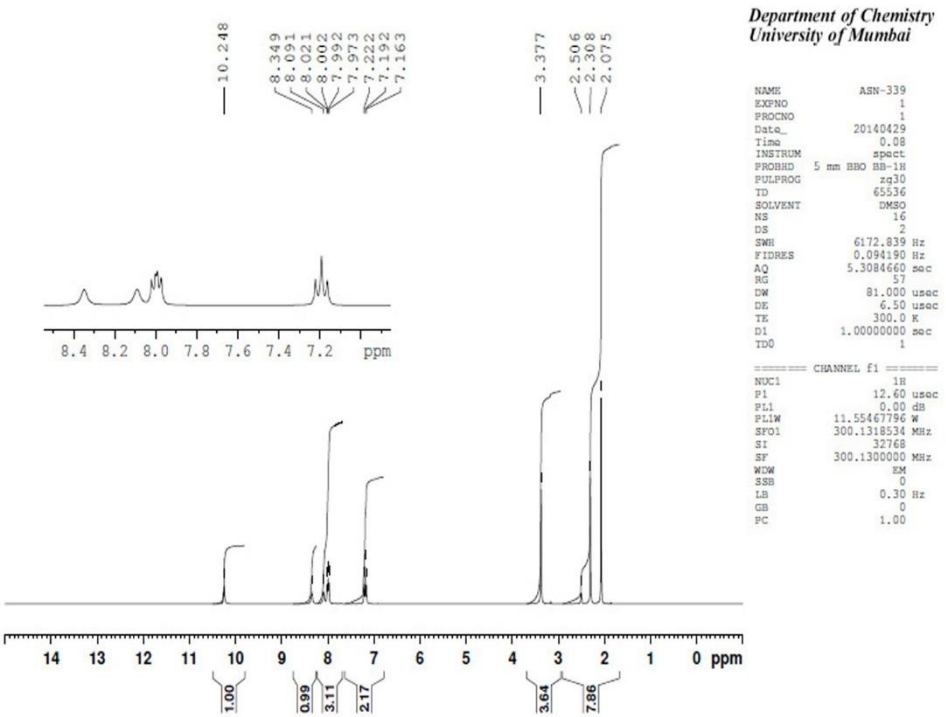

Figure A11: The ^{1}H NMR spectrum of precursor (**6**).

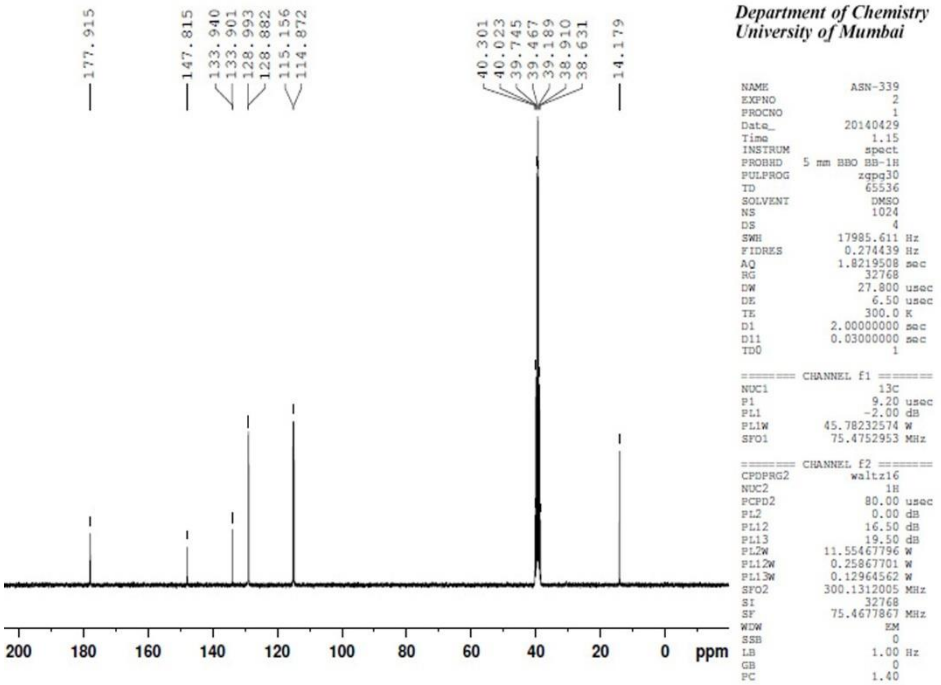

Figure A12: The $^{13}C\{^{1}H\}$ NMR spectrum of precursor (**6**).

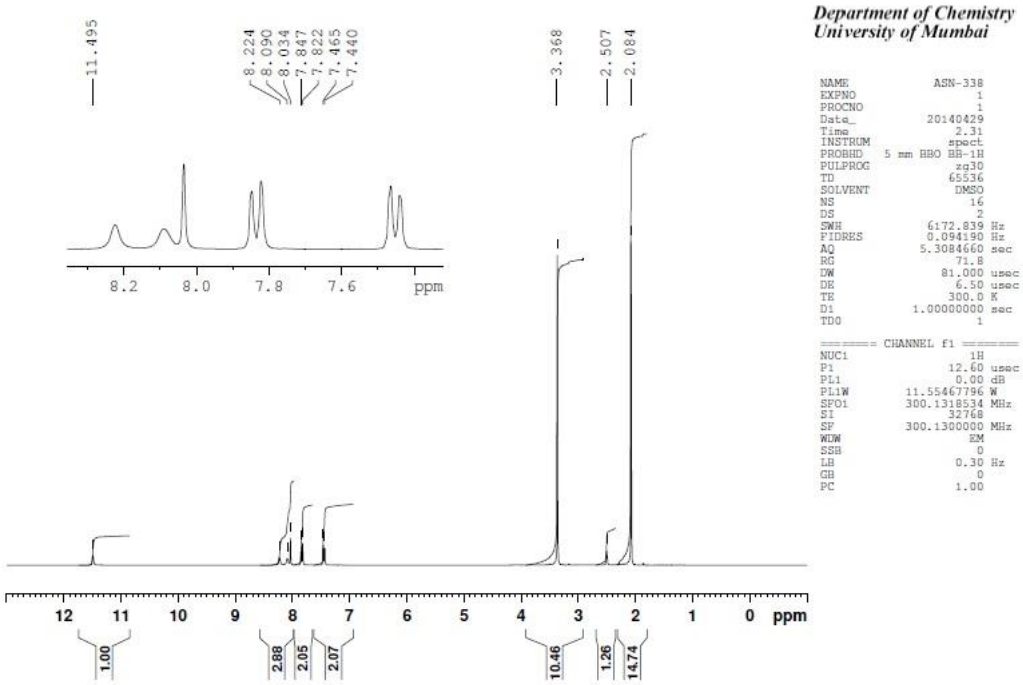

Figure A13: The ^{1}H NMR spectrum of precursor (**7**).

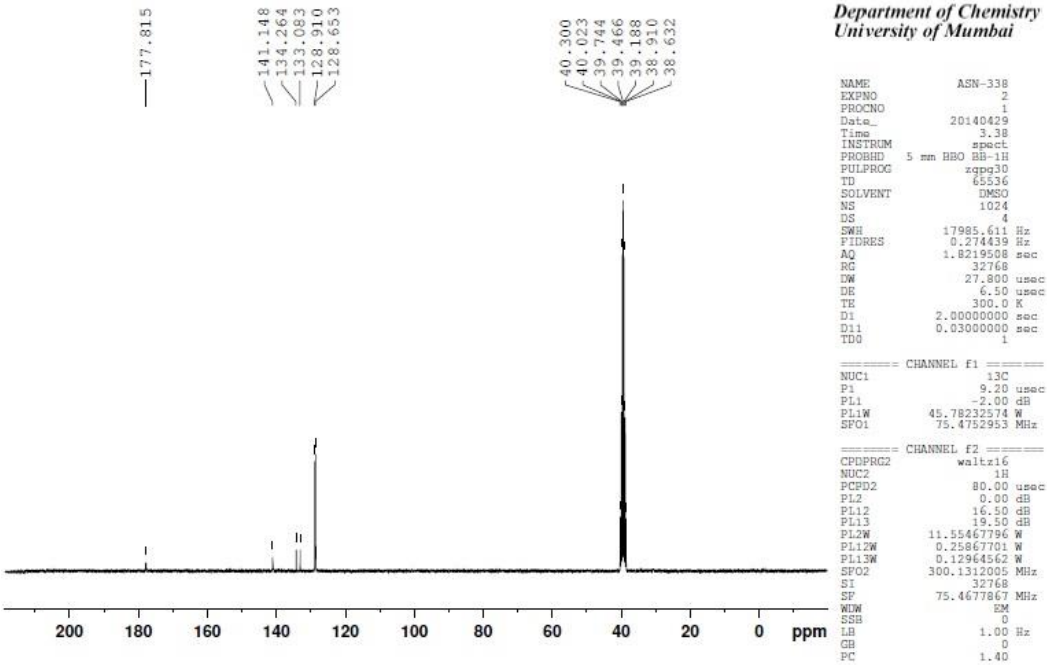

Figure A14: The $^{13}C\{^{1}H\}$ NMR spectrum of precursor (**7**).

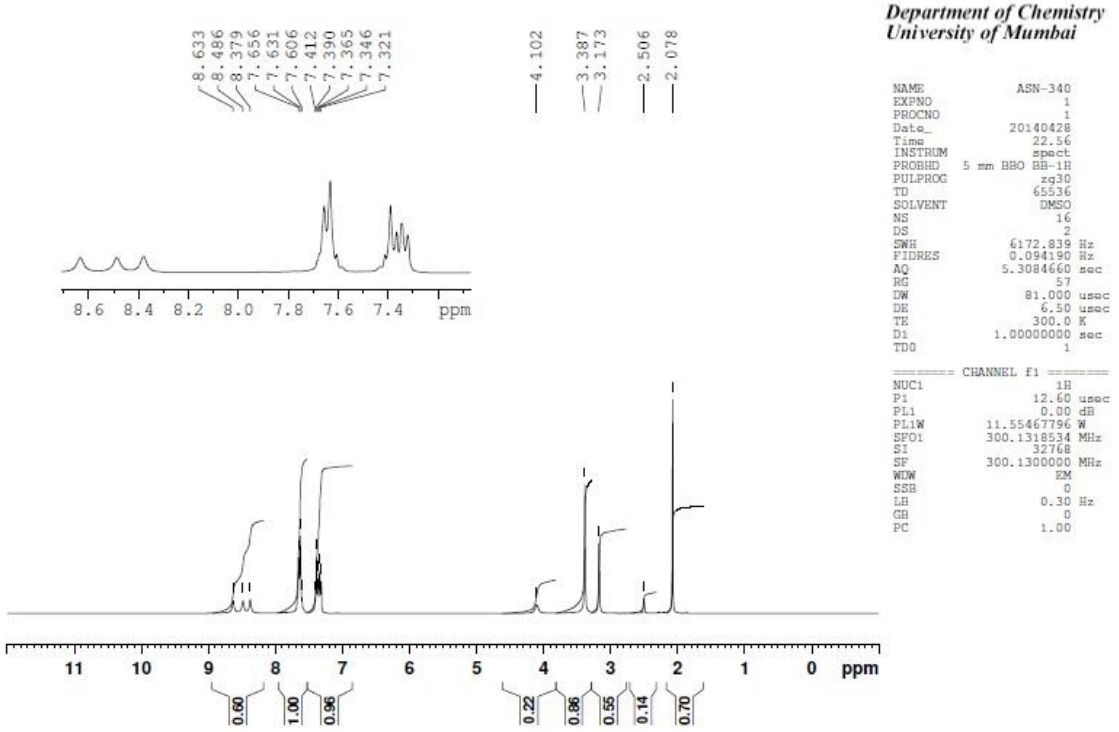

Figure A15: The ^{1}H NMR spectrum of precursor (**8**).

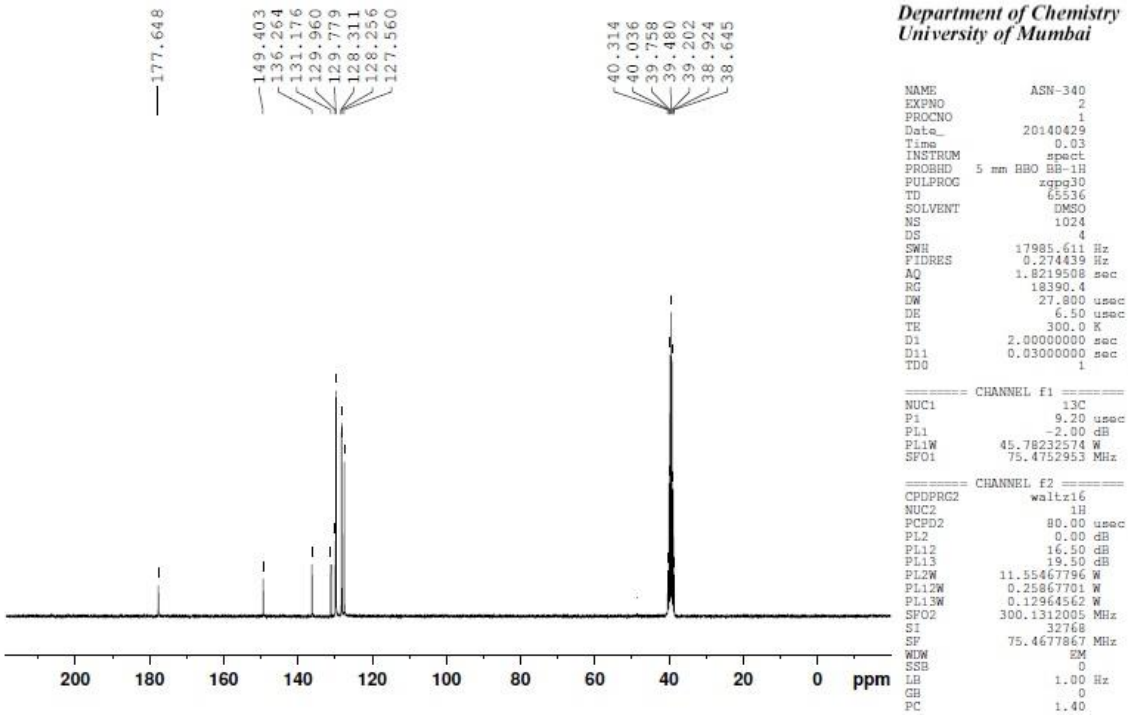

Figure A16: The $^{13}C\{^{1}H\}$ NMR spectrum of precursor (**8**).

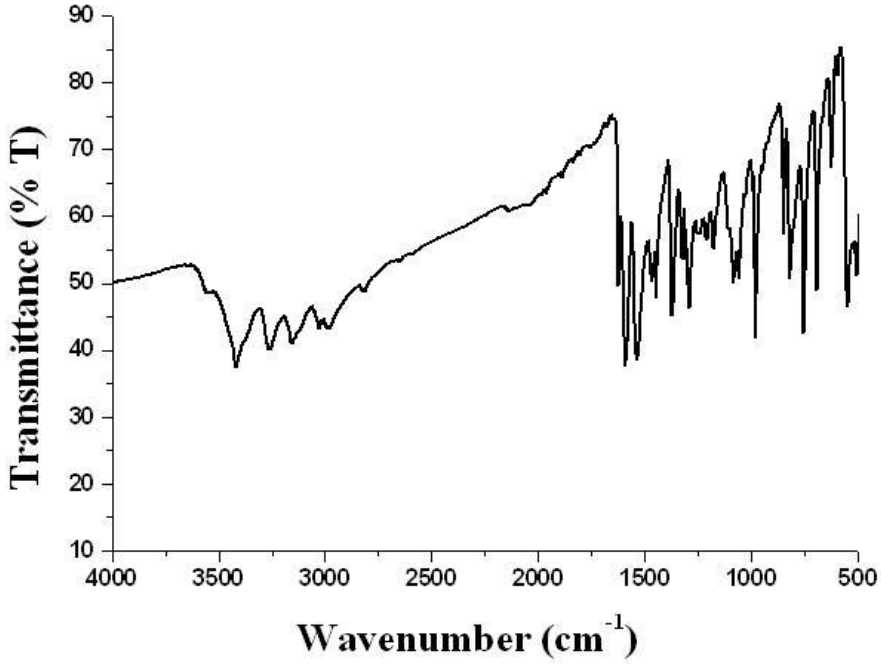

Figure A17: The FTIR spectrum of cinnamaldehyde thiosemicarbazone ligand.

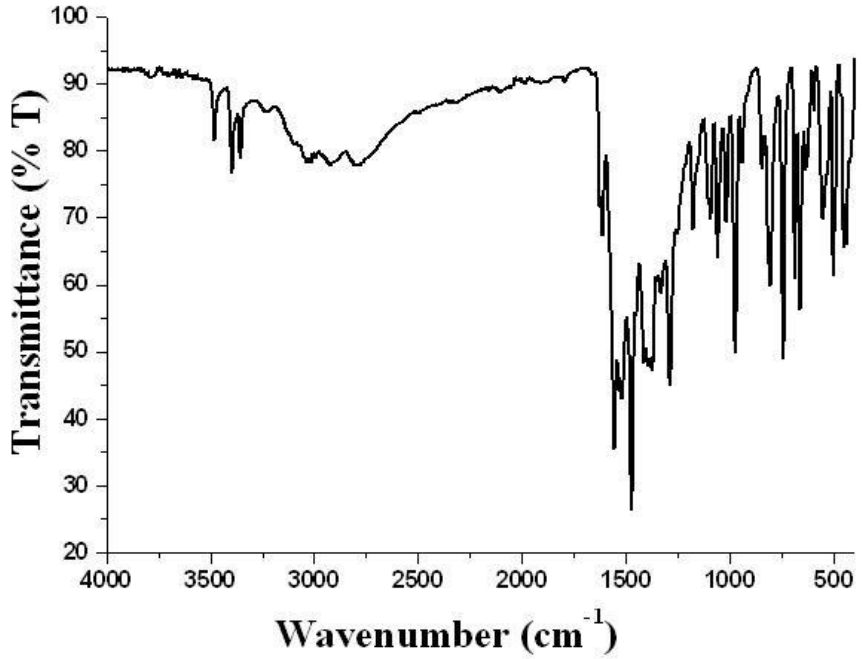

Figure A18: The FTIR spectrum of precursor (**9**).

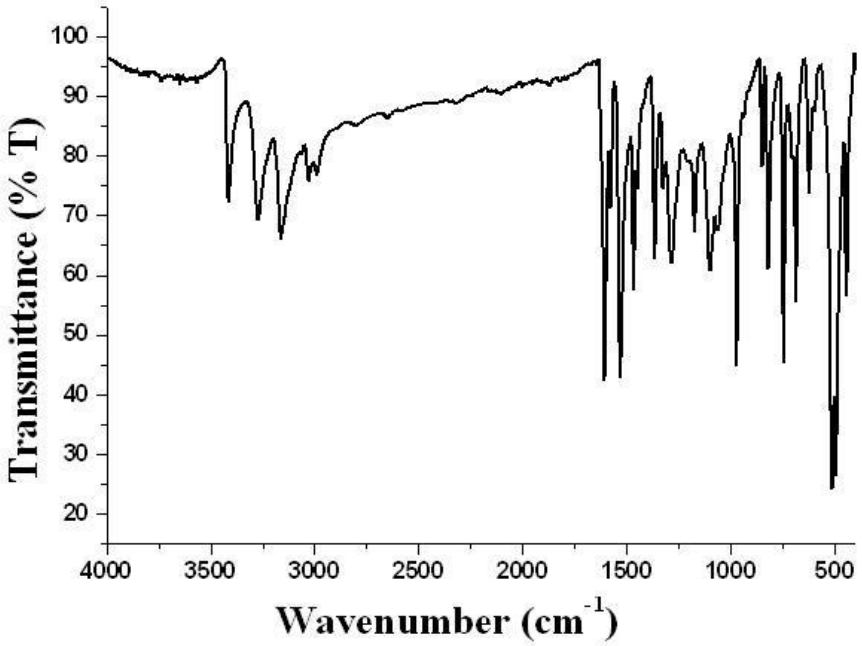

Figure A19: The FTIR spectrum of precursor (**10**).

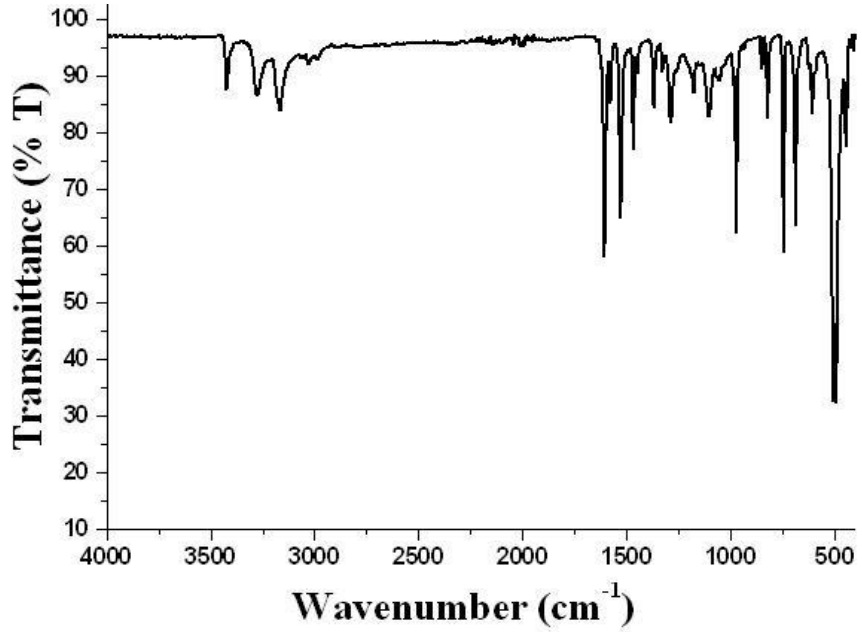

Figure A20: The FTIR spectrum of precursor (**11**).

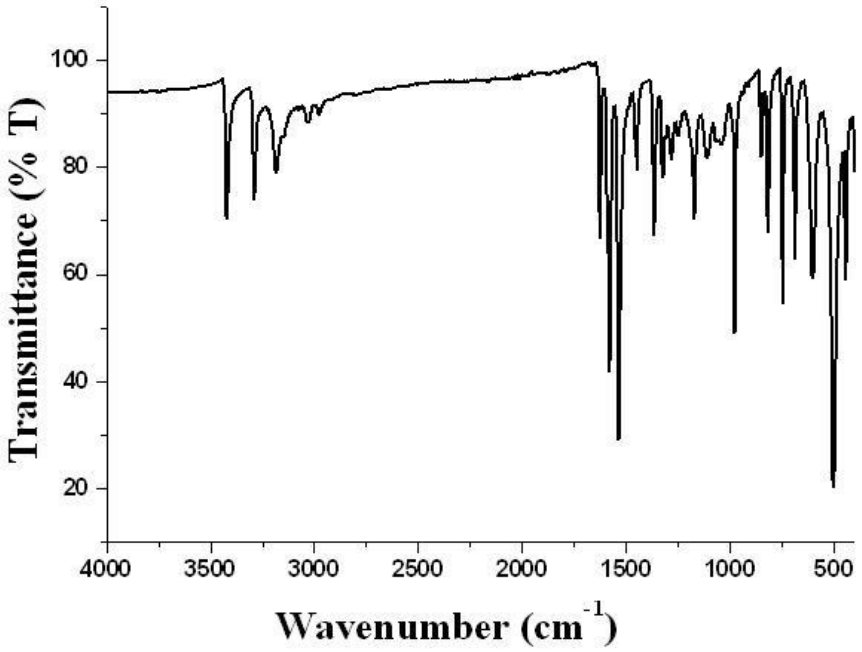

Figure A21: The FTIR spectrum of precursor (**12**).

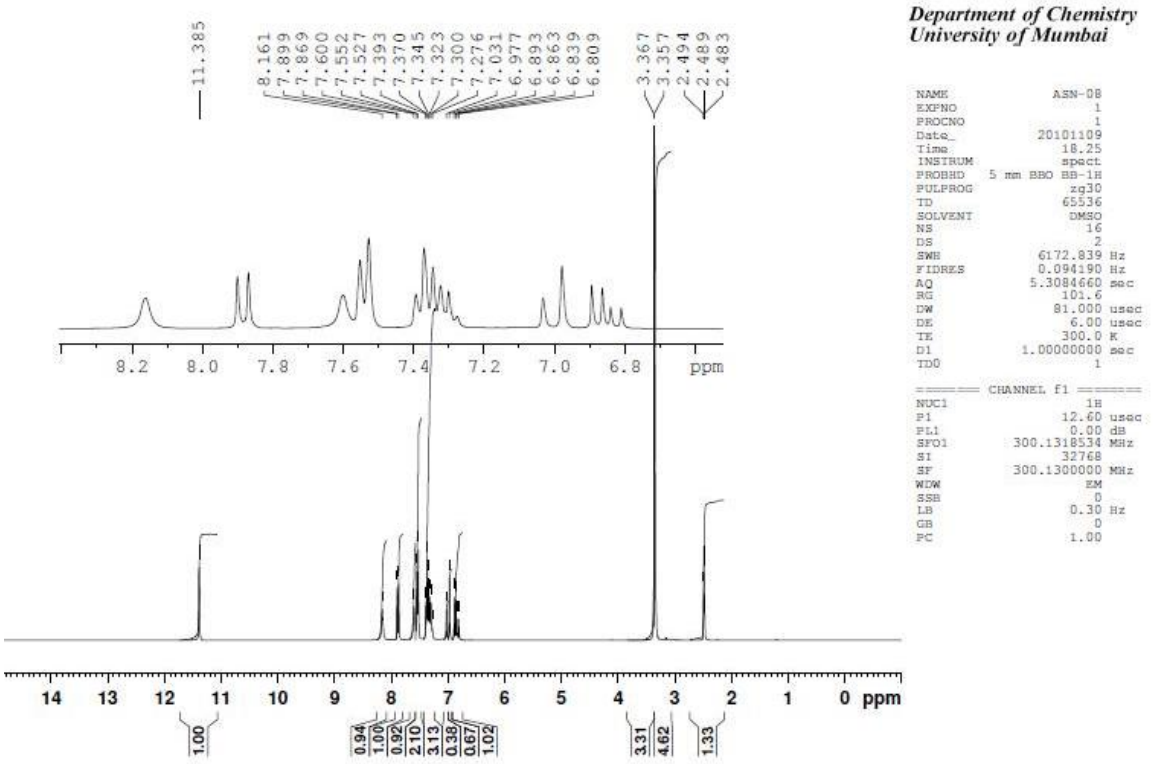

Figure A22: The ^{1}H NMR spectrum of cinnamaldehyde thiosemicarbazone ligand.

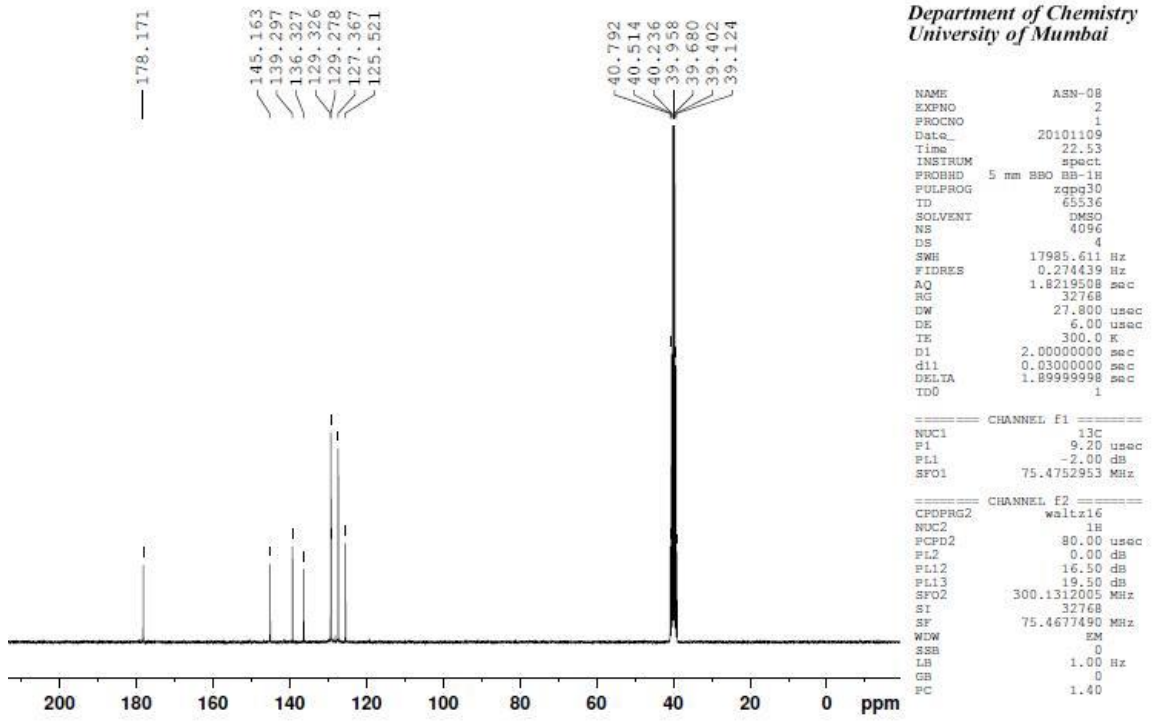

Figure A23: The $^{13}C\{^{1}H\}$ NMR spectrum of cinnamaldehyde thiosemicarbazone ligand.

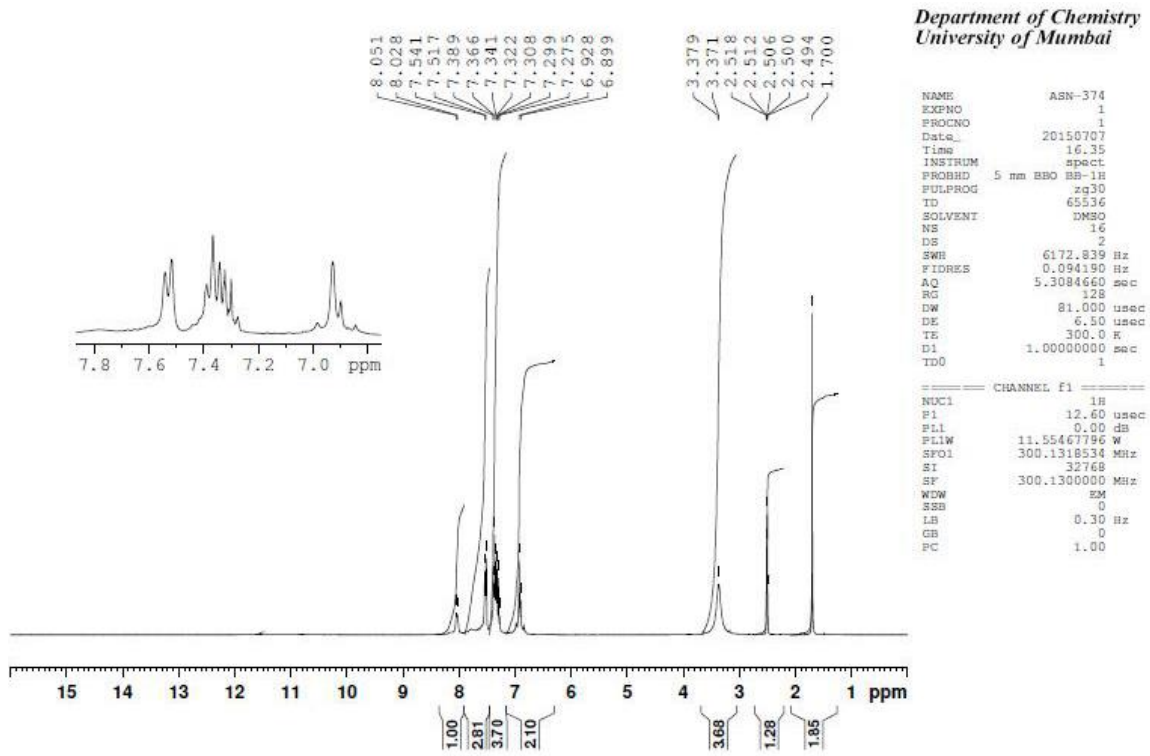

Figure A24: The ^{1}H NMR spectrum of precursor (**9**).

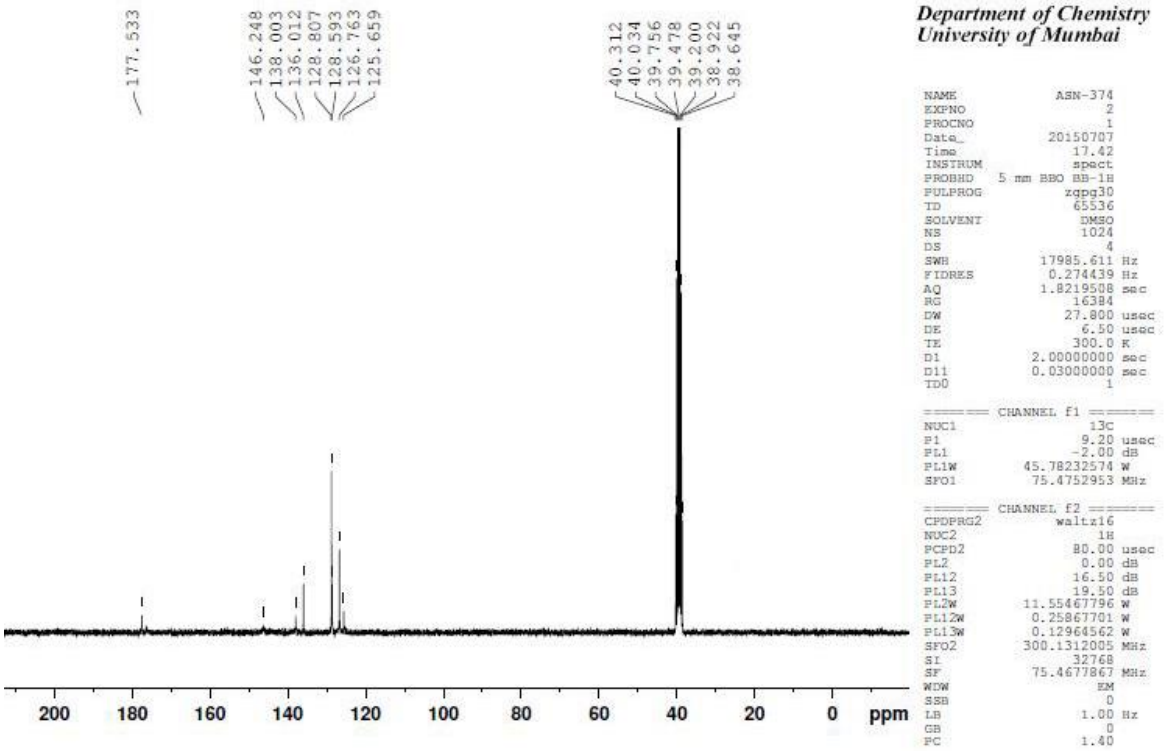

Figure A25: The ^{13}C{^{1}H} NMR spectrum of precursor (**9**).

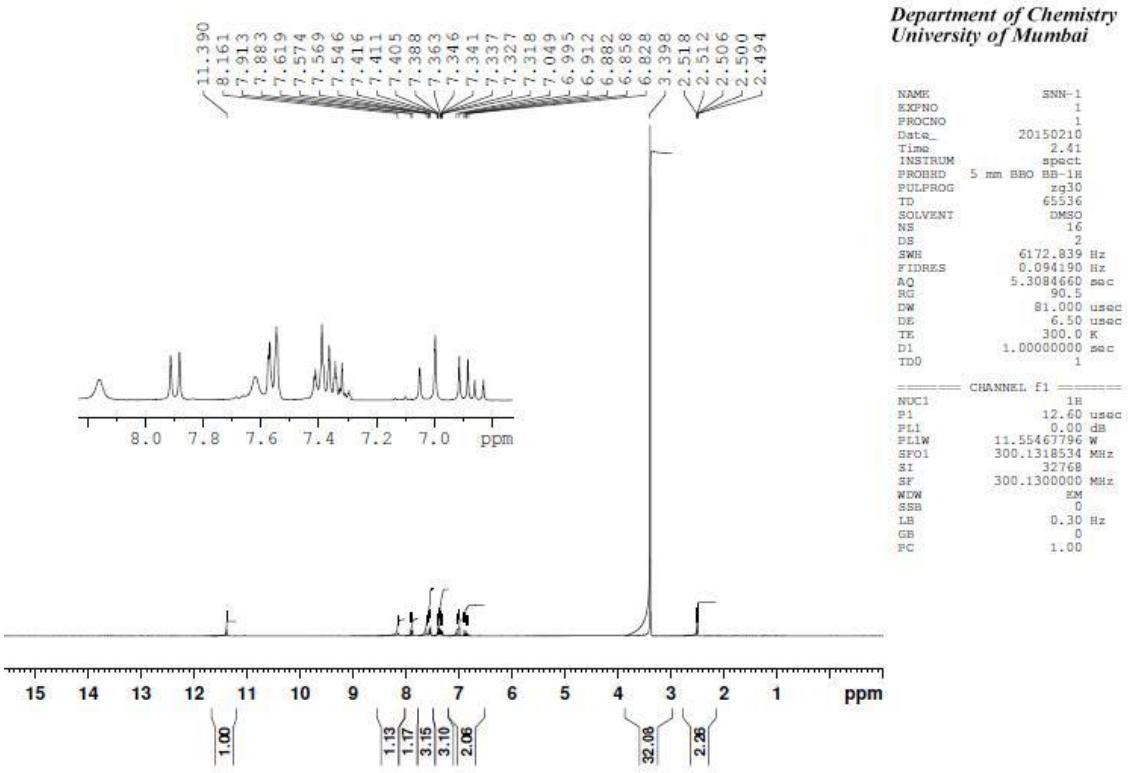

Figure A26: The ^{1}H NMR spectrum of precursor (**10**).

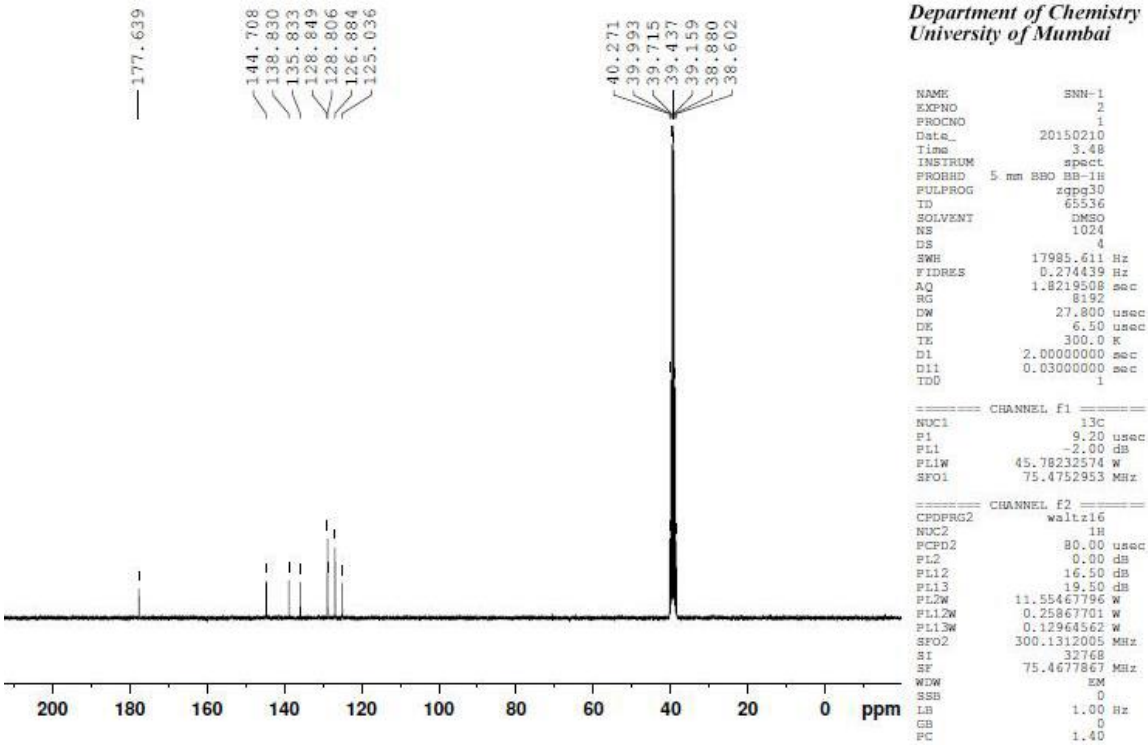

Figure A27: The ^{13}C{^{1}H} NMR spectrum of precursor (**10**).

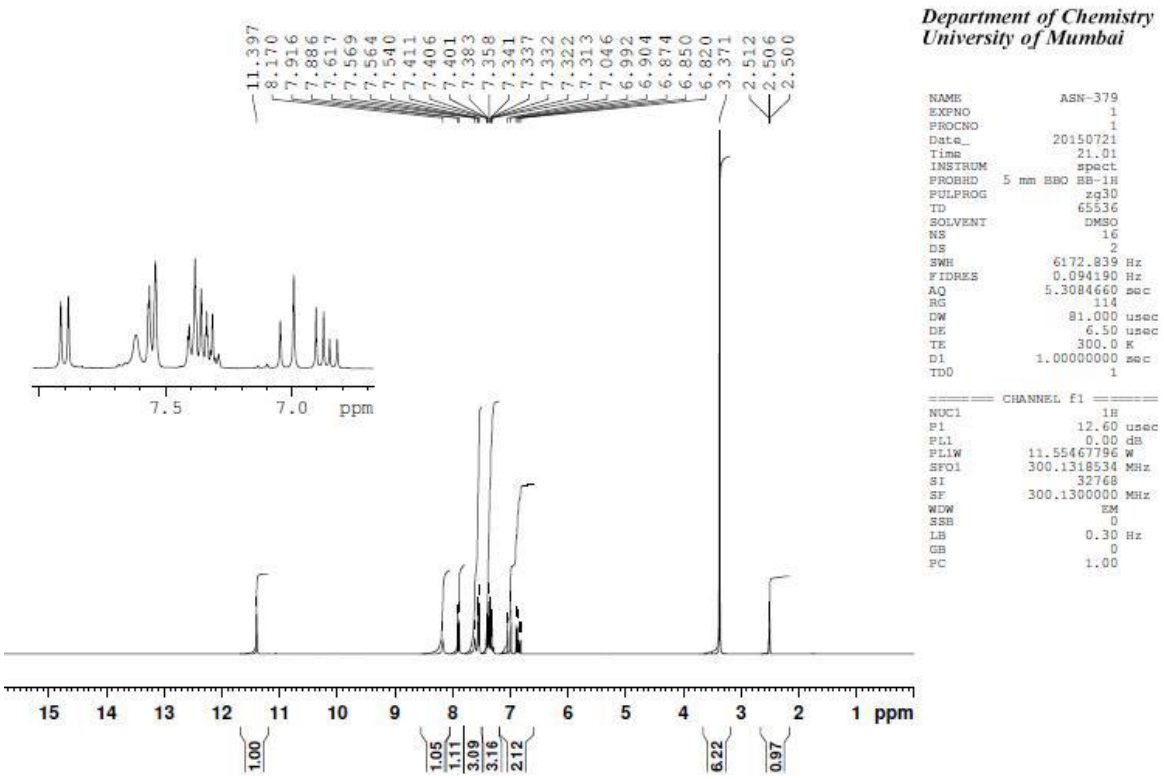

Figure A28: The ^{1}H NMR spectrum of precursor (**11**).

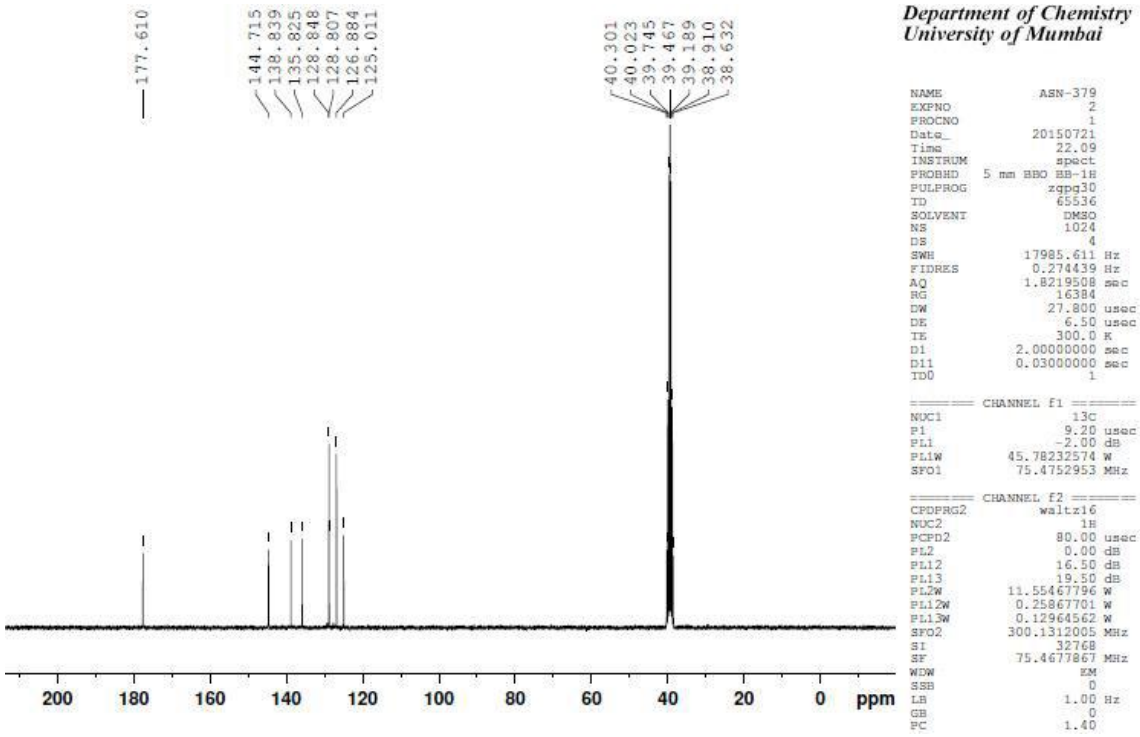

Figure A29: The ^{13}C{^{1}H} NMR spectrum of precursor (**11**).

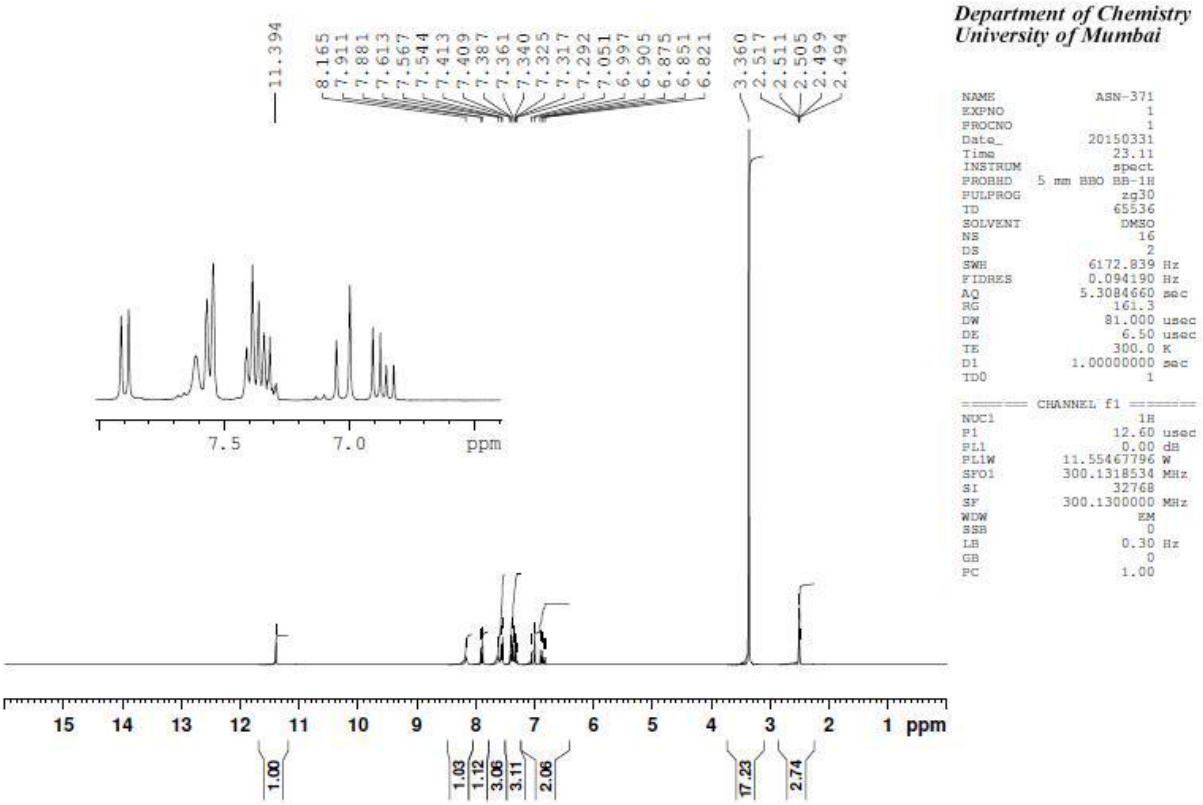

Figure A30: The ^{1}H NMR spectrum of precursor (**12**).

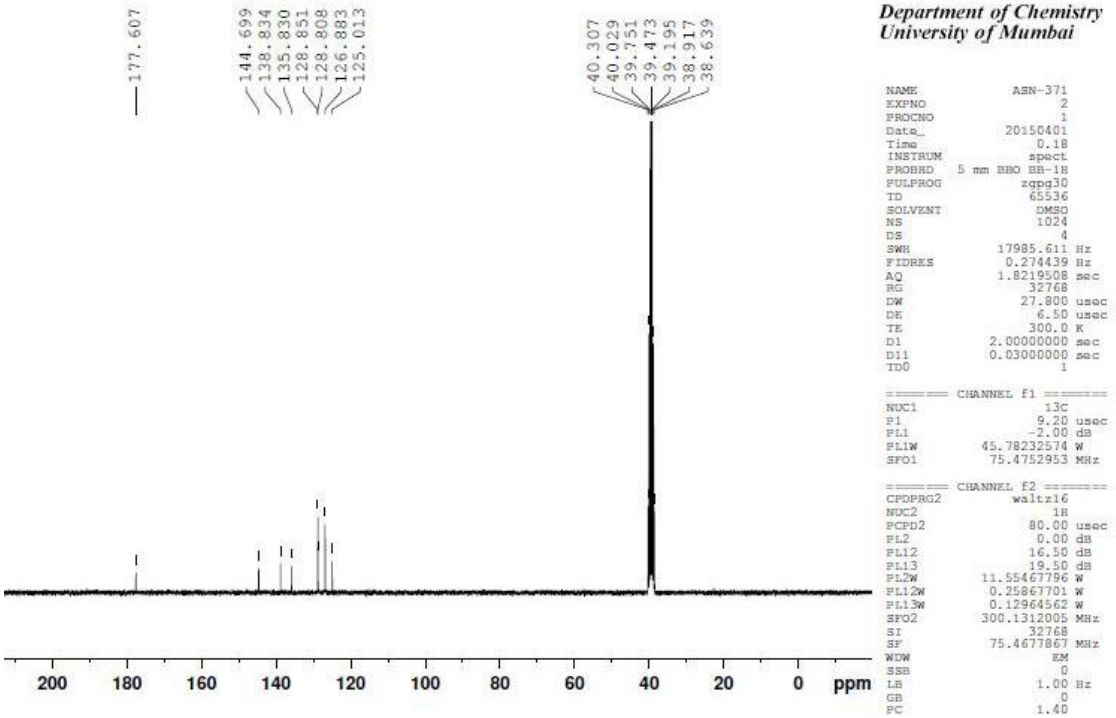

Figure A31: The ^{13}C{^{1}H} NMR spectrum of precursor (**12**).

Table A1: Selected bond lengths from Me (**15**), ^{i}Pr (**16**), ^{s}Bu (**17**) and (+)-^{s}Bu structures.

Me (**15**)		^{i}Pr (**16**)		^{s}Bu (**17**)		(+)-^{s}Bu (Δ)		(+)-^{s}Bu Bu (Λ)	
	Length (Å)		Length (Å)		Length (Å)		Length (Å)		Length (Å)
In1-S2	2.6126(6)	In1-S1	2.5764(8)	In1-S4	2.581(5)	In1-S1	2.644(2)	In2-S7	2.601(2)
In1-S7	2.6171(7)	In1-S3	2.6391(9)	In1-S3	2.597(4)	In1-S2	2.582(2)	In-S8	2.590(2)
In1-S12	2.5859(7)	In1-S4	2.5625(7)	In1-S5	2.61(1)	In1-S3	2.597(2)	In2-S9	2.649(2)
In1-S11	2.5862(8)	In1-S2	2.6187(7)	In1-S6	2.59(1)	In1-S4	2.594(2)	In2-S10	2.565(2
In1-S6	2.5959(8)	In1-S5	2.6015(9)	In1-S1	2.616(6)	In1-S5	2.591(2)	In2-S11	2.631(2)
In1-S16	2.5793(7)	In1-S6	2.5720(7)	In1-S2	2.566(4)	In1-S6	2.588(2)	In2-S12	2.581(2)
S2-C3	1.696(4)	S1-C1	1.707(3)	S4-C6	1.64(2)	S1-C1	1.696(8)	S7-C16	1.692(8)
S7-C8	1.692(3)	S3-C5	1.691(3)	S3-C6	1.68(1)	S2-C1	1.713(8)	S8-C16	1.705(8)
S12-C13	1.702(3)	S4-C5	1.711(3)	S5-C11	1.70(2)	S3-C6	1.722(9)	S9-C21	1.698(8)
S11-C8	1.708(3)	S2-C1	1.700(3)	S6-C11	1.64(2)	S4-C6	1.701(9)	S10-C21	1.704(8)
S6-C3	1.708(3)	S5-C9	1.703(3)	S1-C1	1.73(2)	S5-C11	1.713(8)	S11-C26	1.710(9)
S16-C13	1.713(2)	S6-C9	1.707(3)	S2-C1	1.62(2)	S6-C11	1.697(8)	S12-C26	1.684(9)
O9-C10	1.456(3)	O2-C5	1.314(3)	O1-C1	1.33(2)	O1-C1	1.32(1)	O4-C16	1.334(9)
O9-C8	1.321(4)	O2-C6	1.484(4)	O2-C7	1.38(3)	O1-C2	1.48(1)	O4-C17	1.488(9)
O14-C15	1.456(3)	O3-C9	1.309(4)	O1-C2	1.46(3)	O2-C6	1.316(9)	O5-C21	1.321(9)
O14-C13	1.310(3)	O3-C10	1.479(5)	O2-C6	1.39(2)	O2-C7	1.49(1)	O5-C22	1.47(1)
O4-C3	1.317(3)	O1-C1	1.315(4)	O3-C11	1.27(3)	O3-C11	1.317(9)	O6-C26	1.34(1)
O4-C5	1.453(3)	O1-C2	1.476(4)	O3-C12	1.51(4)	O3-C12	1.50(1)	O6-C27	1.46(1)

Table A2: Selected bond angles from Me (**15**), ^{i}Pr (**16**), ^{s}Bu (**17**) and (+)-^{s}Bu structures.

Me (**15**)		^{i}Pr (**16**)		^{s}Bu (**17**)		(+)-^{s}Bu (Δ)		(+)-^{s}Bu Bu (Λ)	
	Angle (°)		Angle (°)		Angle (°)		Angle (°)		Angle (°)
S2-In1-S6	69.93(2)	S6-In1-S5	70.34(2)	S2-In1-S1	69.3(2)	S3-In1-S4	70.19(7)	S12-In2-S11	69.31(7)
S7-In1-S11	69.95(2)	S1-In1-S2	69.80(2)	S3-In1-S4	69.4(1)	S2-In1-S1	69.48(6)	S8-In2-S7	70.07(6)
S12-In1-S16	70.64(2)	S4-In1-S3	69.58(2)	S5-In1-S6	68.0(4)	S6-In1-S5	70.14(6)	S9-In2-S10	69.38(7)
S2-In1-S12	162.93(2)	S6-In1-S2	160.73(3)	S1-In1-S4	161.5(2)	S3-In1-S1	163.50(7)	S11-In2-S8	161.91(7)
S6-In1-S11	156.89(2)	S3-In1-S5	159.99(3)	S2-In1-S5	161.4(2)	S2-In1-S5	160.50(7)	S12-In2-S10	159.79(7)
S7-In1-S16	162.11(2)	S1-In1-S4	158.17(3)	S3-In1-S6	155.8(3)	S6-In1-S4	160.12(7)	S9-In2-S7	157.70(7)

List of publications

- Journal article: Masikane, S. C., Mlowe, S., Gervas, C., Revaprasadu, N., Pawar, A. S. and Garje, S. S. *Lead (II) halide cinnamaldehyde thiosemicarbazone complexes as single source precursors for oleylamine-capped lead sulfide nanoparticles*. Journal of Materials Science: Materials in Electronics, (2018) 29: 1479-1488. http://dx.doi.org./10.1007/s10854-017-8056-2.
- Journal article: Masikane, S. C. and Revaprasadu, N. *Castor Oil and Olive Oil: Towards the Green Synthesis of In_2S_3 and $CuInS_2$ Nanoparticles from Xanthate Complexes*. Material Science in Semiconductor Processing, (2018) 76: 73-79. https://doi.org/10.1016/j.mssp.2018.01.002
- Journal article: Pawar, A. S., Masikane, S. C., Mlowe, S., Garje, S. S. and Revaprasadu, N. (2016), *Preparation of CdS Nanoparticles from Thiosemicarbazone Complexes: Morphological Influence of Chlorido and Iodido Ligands*. European Journal of Inorganic Chemistry, (2016): 366–372. http://dx.doi.org/10.1002/ejic.201501125.
- Journal article: Khoza, S. H., Masikane, S. C., Mlowe, S., Ezekiel, I. P., Moyo, T. and Revaprasadu, N. Turkish Journal of Chemistry. Accepted.
- Book chapter: Castor and Lesquerella Oils: Production, Composition and Uses; Chapter 7. *Castor Oil Production and Applications*; Sixberth Mlowe, Siphamandla C. Masikane, Joseph W. Kyobe, Egid B. Mubofu and Neerish Revaprasadu; ISBN: 978-1-53612-972-4.
- Book chapter: Recent Advances in Ionic Liquids; *Progress in Green Solvents for the Stabilisation of Nanomaterials: Imidazolium Based Ionic Liquids*; Zikhona Tshemese, Siphamandla C. Masikane, Sixberth Mlowe and Neerish Revaprasadu; ISBN: 978-953-51-6705-1.
- Journal article: Masikane, S. C., Mlowe, S., Pawar, A. S., Garje, S. S. and Revaprasadu, N. *Cadmium chloride and cadmium iodide thiosemicarbazone complexes as single source precursors for CdS nanoparticles*. Accepted.
- Journal article: Masikane, S. C., McNaughter, P. D., Lewis, D. J., Vitorica-yrezabal, I., Revaprasadu, N. and O'Brien, P. Important Phases of Indium

Sulfide Through Melt Reactions of Indium (III) Xanthate Precursors. European Journal of Inorganic Chemistry, (2019): 1421–1432. http://dx.doi.org/10.1002/ejic.201900007.

List of conferences

- Oral presentation “**From Crystalline Indium(III) Xanthate Complexes to Indium Sulfide Nanocrystals Through a Solventless Decomposition Route**” in the 7th International Conference on Nanoscience and Nanotechnology in Africa (NanoAfrica2018) on 22-25 April 2018 at the Salt Rock Hotel in Durban north. Organized by the University of KwaZulu-Natal (UKZN), South Africa.
- Poster presentation "**Preparation of heterocyclic dithiocarbamate nickel complexes as single source precursors for nickel sulfide nanomaterials**” in the 13th International Conference on Materials Chemistry (MC13) on 10-13 July 2017 at the ACC Liverpool. Organized by the Materials Chemistry Division of the Royal Society of Chemistry, United Kingdom.
- Oral presentation “**Castor oil and olive oil**: Towards a greener synthesis of nanostructured In_2S_3” in the Pan African Chemistry Network (PACN) International Conference on 03-05 October 2016. Organized by KNUST, Kumasi, Ghana.